Two-dimensional Spin Ice and the Sixteen-Vertex Model
Demian Levis

▶ To cite this version:

Demian Levis. Two-dimensional Spin Ice and the Sixteen-Vertex Model. Statistical Mechanics [cond-mat.stat-mech]. Université Pierre et Marie Curie - Paris VI, 2012. English. NNT : . tel-00763350

HAL Id: tel-00763350
https://theses.hal.science/tel-00763350

Submitted on 10 Dec 2012

UPMC
PARISUNIVERSITAS

Ecole Doctorale de Physique de la Région Parisienne - ED107

Thèse en vue d'obtenir le grade de

DOCTEUR DE L'UNIVERSITÉ DE PIERRE ET MARIE CURIE

Discipline : Physique Théorique

Realisée au

Laboratoire de Physique Théorique et Hautes Energies

Two-dimensional Spin Ice and

the Sixteen-Vertex Model

presentée par

Demian LEVIS

dirigée par

Leticia F. CUGLIANDOLO

Soutenue le 26 Octobre 2012 devant le jury composé de :

M. Olivier BABELON	Examinateur
M. Claudio CASTELNOVO	Rapporteur
Mme. Leticia CUGLIANDOLO	Directrice
M. Peter HOLDSWORTH	Rapporteur
M. Will BRANFORD	Examinateur

A las hermanitas Roehrich, Maria y Hanna.

Two-dimensional spin ice and the sixteen-vertex model

Abstract

In this thesis we present a thorough study of the static and dynamic properties of the $2D$ sixteen-vertex model or, in other words, a simplified version of the dipolar spin-ice model. After a general discussion on frustrated magnets, and spin-ice in particular, we motivate the introduction of our model in order to study the collective behaviour of spin-ice.

We use a rejection-free continuous-time Monte Carlo algorithm with local spin-flip updates to analyse the equilibrium phases and the critical properties of the $2D$ model. We compare our results with the integrable cases. We extend the model to be defined on carefully chosen trees and employ a Bethe-Peierls approximation to study its equilibrium properties. The range of validity of the approximation is discussed by comparing the results obtained analytically for the model defined on trees with the exact and numerical results obtained for the $2D$ model. Motivated by advent of artificial spin-ice realisations, we set the parameters of the model in order to reproduce the experimental situation. We show that the sixteen-vertex model gives an accurate description of the thermodynamics of artificial spin-ice samples. Our theoretical results are in quasi-quantitative agreement with experimental data obtained in as-grown samples away from the expected critical point. The phase diagram of the sixteen-vertex model and the nature of the equilibrium phases is presented in detail.

Our model is build as a stochastic extension of the integrable six-vertex model in order to include thermal fluctuations in the form of defects. We study the ordering dynamics of the system following different kind of quenches by means of Monte Carlo simulations. We analysed the evolution of the density of defects and we identified the dynamical mechanisms leading the different ordering processes. We showed that the dynamics proceed through coarsening accordingly to the dynamical scaling picture. The interplay between localised and extended topological defects is discussed. We study in detail the existence of a dynamical arrest following a quench as observed in $3D$ dipolar spin-ice.

Keywords Spin ice ; Geometrical frustration ; Topological defects ; Phase transitions ; Hard constraints ; Out-of-equilibrium dynamics ; Monte Carlo ; Cavity method ; Integrability.

Glace de spin bidimensionnelle et le modèle à seize vertex

Résumé

Cette thèse présente une étude complète des propriétés statiques et dynamiques du modèle à seize vertex en $2D$, une version simplifiée de la glace de spin avec interactions dipolaires. Après une discussion générale sur le magnétisme frustré, et la glace de spin en particulier, on justifie l'introduction de notre modèle pour étudier le comportement collectif de la glace de spin.

On utilise un algorithme de Monte Carlo à temps continu avec une dynamique locale qui nous permet d'analyser les phases d'équilibre et les propriétés critiques du modèle $2D$. On compare nos résutats avec les resultats obtenus dans les cas où le système est intégrable. On définit ensuite le modèle sur des arbres orientés et on applique une approximation du type Bethe-Peierls. Afin de discuter le domaine de validité de cette approche, on compare les résultats ainsi obtenus avec les résultats exacts et numériques obtenus pour le modèle $2D$. L'apparition récente des glaces de spin artificielles suggère un certain choix des paramètres du modèle. On montre que le modèle à seize vertex décrit de façon précise la thermodynamique de la glace de spin artificielle. On présente en détail le diagramme de phase et la nature des phases d'équilibre du modèle à seize vertex.

Afin d' inclure l'effet des fluctuations thermiques responsables de apparition de défauts ponctuels dans la glace de spin, on construit une extension stochastique du modèle intégrable à six vertex. On étudie, par l'intermédiaire de simulations Monte Carlo, comment le système s'ordonne dans le temps après différentes trempes. On analyse l'évolution de la densité de défauts et on identifie les mécanismes dynamiques qui pilotent la relaxation vers ses différentes phases d'équilibre. On montre ainsi que la dynamique donne lieu à du "coarsening" et qu'elle vérifie l'hypothèse de "scaling" dynamique. On discute le rôle des défauts topologiques étendus et ponctuels présents dans le système au cours de l'évolution. Finalement, on étudie la présence d'un régime dynamique où le système reste gelé pendant de longues périodes de temps, ce qui à été observé dans la glace de spin dipolaire en $3D$.

Mots-clefs Glace de spin ; Frustration géométrique ; Défauts topologiques ; Transitions de phase ; Contraintes dures ; Dynamique hors-équilibre ; Monte Carlo ; Méthode de cavité ; Intégrabilité.

Acknowledgments

Mes premiers remerciements vont à ma directrice de thèse, Leticia Cugliandolo. Elle a su attirer mon attention sur des sujets fascinants et guider mon travail d'un oeil critique, tout en me laissant la liberté nécessaire pour devenir autonome et être capable de développer et mener à bout mes propres idées. Sa bonne humeur et son enthousiasme à l'égard de la physique ont rendu ces années de travail à ses côtés aussi agréables qu'enrichissantes. Muchas gracias Leticia por tu apoyo y por tu simpatía.

Je tiens à remiercier Laura Foini et Marco Tarzia avec qui j'ai eu le plaisir de collaborer. J'espère on trouvera une autre occasion de travailler ensemble sur des sujets aussi passionants.

I would like to thank Claudio Castelnovo and Peter Holdsworth to have accepted to write a report on my thesis and come to Paris for the defence. I am also very grateful to Olivier Babelon and Will Branford for being part of my jury.

All along these three years I had the opportunity to meet different researchers from different horizons and benefit of their knowledge. I would like to express my gratitude to Claudio Castelnovo, Olivier Cepas, Malte Henkel, Anthony Maggs, Marco Picco and Yair Shokef (and certainly more people) for their advices and suggestions.

Ces trois années de thèse ont aussi été marqués par mon 'initiation à l'enseignement'. J'ai eu la chance de travailler aux côtés de Jean-Bernard Zuber et profiter de son expérience (et sympathie!). À lui, et à toute l'équipe de LP207, merci.

Un grand merci à Gautier et Thibault pour ses 'conseils *geek*': ils m'ont fait gagner un temps précieux dans l'avancement de ma thèse grâce à toute sorte de *scripts* et commandes bizarres dont j'ignorais l'existence... J'en profite pour remercier 'les jeunes du labo' que j'ai rencontré au cours de ces années et ont rendu mon séjour au LPTHE fort agréable. Ils ont participé à créer une ambiance conviviale et symapathique dans un laboratoire de physique théorique, tâche 'hautement non-triviale'. Je pense à Alberto, Ana-Carolina, Camille, Gautier, João, Laura, Nicolas's (grand et petit), Paloma, Tiago, Thibault et Thomas, avec une mention spéciale à Herr Bonart et ses *very useful discussions*.

Je voudrais remercier le ministère de la recherche pour financer ma thèse, et d'un point de vue plus vaste, la France, ce pays qui m'a accueilli chaleureusement et instruit gratuitement. Je pense à tous mes amis parisiens qui m'ont accompagné depuis que je suis arrivé. Je tiens à remercier particulièrement mes amis physiciens, Charles-Alexandre, Emmanuel, Karim et Maxime. Nos interminables discussions ont sans doute nourri davantage mon esprit que la plupart des cours suivis à l'Université.

Le agradezco a Daniel todo su apoyo, sin él no solo no podría haber realizado esta tesis sino tampoco haber estudiado física. Tengo la suerte de tener una familia que siempre ha apoyado mis proyectos, y por ello les doy las gracias a los tres: a mi hermano, a mi madre y a mi padre.

No puedo no concluir sin agradecerle a Maria todo lo que ha hecho por mi estos últimos años. Me ha querido y ha estado siempre a mi lado; y no se sabe como, ha sabido iluminarme incluso en los momentos mas oscuros de mi vida. A ti mi amor te dedico esta tesis.

Paris, le 16 octobre 2012

Contents

Introduction

Make things as simple as possible, but not simpler.

Albert Einstein

In a broad class of condensed-matter systems, the tendency to local ordering is hampered by constraints. This leads to frustration, with the impossibility of satisfying all competing forces simultaneously. Hard local constraints lead to a rich variety of collective behaviours such as the splitting of phase space into different topological sectors and the existence of "topological phases", which cannot be described with conventional order parameters [14]. In geometrically frustrated magnets, the local minimisation of the interaction energy on a frustrated unit gives rise to a macroscopic degeneracy of the ground state [188], unconventional phase transitions [130, 163], long-range correlations in the "Coulomb" phase [278, 115] and slow dynamics [95, 65] in both $2D$ and $3D$ systems.

The prototypical example is *water ice* for which this zero point entropy has been measured in the 30s [103]. Pauling explained this feature with a model in which the O atoms occupy the vertices of a coordination four lattice. Two H atoms are near while the other two H atoms are shifted away from each vertex [215]. This is encoded in the so-called *ice-rules*. The large degeneracy of such locally electro-neutral ground states gives rise to the zero point entropy.

A residual entropy has also been measured in frustrated magnets such as $Ho_2Ti_2O_7$ [113]. In these *spin-ice* samples, magnetic ions form a tetrahedral structure in $3D$, i.e. a pyrochlore lattice [45]. This is the case, for instance, of the Dy^{+3} ions in the $Dy_2Ti_2O_7$ compound. Their f-electron spins are large and can be taken as classical variables at, say, $T < 10$ K. They behave as Ising doublets, forced to point along the axes joining the centres of the tetrahedra shared by the considered spin. Geometric frustration arises from the non-collinear Ising-like anisotropy and the effective exchange and long-range coupling between the spins. In a simplified description, only short-range ferromagnetic exchanges are retained [113]. Frustration is due to the different Ising axes of the spins on the unit cell. The configurations that minimise the energy of each tetrahedron

are the six states with two-in and two-out pointing spins.

The system is more easily visualised by realising that each tetrahedron in $3D$ space can be considered as a vertex taking one out of six possible configurations in a coordination four lattice. The magnetic problem just described becomes the analog of the earlier model of water ice. In this context, the entropy of the ground state satisfying the ice-rules, with all vertices taken as statistically equivalent, was estimated by Pauling with a simple counting argument [215]. The result is very close to the earlier measurements performed by Giauque and Stout [103] on water ice; and to the ground-state entropy of the magnetic spin-ice sample measured in the late 90s [224]. Experimentally, the Boltzmann weights of the vertices can be tuned by applying pressure or magnetic fields along different crystallographic axes. Indeed, the extensions of Pauling's ice model to describe more general ferroelectric systems lead to 'ice-type models' [243].

The local constraint leads to many peculiar features that have been studied experimentally and analytically. The total spin surrounding a lattice point is conserved and constrained to vanish according to the two-in – two-out rule. This fact has been interpreted as a zero-divergence condition on an emergent vector field [124]. Spins are interpreted as fluxes and, quite naturally, an effective fluctuating electromagnetism emerges with each equilibrium configuration made of closed loops of flux. This analogy can be used to derive power-law decaying spatial correlations of the spins [278], with a parameter dependent exponent, that were recently observed experimentally with neutron scattering [93]. The criticality of the disordered or spin-liquid phase had been first observed in a simulation [247], and it has been more recently discussed in general in [122]. A detailed description of this also called Coulomb phase can be found in [115].

Thermal (or other) fluctuations are expected to generate defects, in the form of vertices breaking the ice rules. In the electromagnetic analogy a defect corresponds to a charge, defined as the number of outgoing minus ingoing arrows. As such, a tetrahedra with three-out and one-in spins contains a positive charge q, and the reversed configuration a negative charge $-q$ of the same magnitude. The four-out units carry a charge $2q$ and the four-in ones a charge $-2q$. Such vertices should be present in the samples under adequate conditions. The possibility of observing magnetic monopoles and Dirac strings as being associated to defects has been proposed by Castelnovo *et al.* [58] and investigated experimentally by a number of other groups [94, 198, 44].

Spin ice can be projected onto $2D$ Kagome planes by applying specially chosen magnetic fields. Recently, interest in $2D$ spin-ice physics has been boosted by the advent of artificial samples [264] on square lattices that are stable at room temperature. These artificial materials have magnetic moments that are large enough to be easily observed in the laboratory.

Following the same line of reasoning exposed in the previous paragraphs, such $2D$ ice-type systems should be modelled by a *sixteen-vertex model* on a square lattice. The exact solution of the ice model [165], and the generalisation of it in which a different statistical weight is given to the six allowed vertices [248] were given by Lieb and Sutherland using the Bethe *Ansatz*. A few years later, Baxter developed a more powerful method to treat the generic eight- vertex models [22] and founded in this way the modern theory of integrable systems (in the eight-vertex model vertices with four in-going or four out-going arrows are allowed).

The presence of a hard constraint in the problem makes $2D$ vertex models and $3D$ spin-ice share several important physical properties. For instance, the ice rules lead to a zero-point entropy measured in the $3D$ spin-ice material $Dy_2Ti_2O_7$ ($S_{exp}^{3D} \approx 1.86$ mol^{-1} K^{-1}) [224] which is very close to the exact value computed for the $2d$ ice-model on a square lattice ($S_{exact}^{2D} \approx 1.79$ mol^{-1} K^{-1}) [165]. Vertex models then appear as good candidates to study spin-ice systems.

Much less is known about the static and dynamic properties of the unconstrained sixteen-vertex model in two and three dimensions. As the experimental interest in classical frustrated magnets of spin-ice type is now cantered on the understanding of defects and their effects on the samples'

macroscopic properties, it seems timely to complete the analysis of the generic model. The special experimental simplicity of two dimensional samples suggests starting from the $2D$ case. Moreover, it seems worth trying to extend at least part of the very powerful analytic machinery to the models with defects.

Bi-dimensional Ising-like ice-models had no experimental counterpart until recently when it became possible to manufacture artificial samples made of arrays of elongated ferromagnetic nano-islands. The beauty of artificial spin-ice (ASI) is that the interaction parameters can be precisely controlled - by tuning the distance between islands or applying external fields - and the state of a single degree of freedom can be directly visualised by microscopy [264]. The system sets into different phases depending on the island length l, the lattice constant a_0, and the height h between layers [190]. The main drawback of these materials had been the lack of thermal fluctuations and the ensuing difficulty to observe the expected ground state. Lately, these problems have been overcome by (i) applying an external drive [206], (ii) using materials with a lower Curie temperature [136], (iii) thermalising the system during the slow growth of the samples [197]. The study of the equilibrium phases and critical behaviour of ASI has thus become possible on rather large samples with up to 10^6 vertices.

In this thesis we show that the *sixteen-vertex model*, a simplified version of the more realistic dipolar spin-ice model in $2D$, is an accurate model for the collective behaviour of artificial spin-ice samples. During the past thirty years a great effort has been put into the study of the mathematical properties of constrained vertex models [25]. The here proven relevance of more generic vertex models for ASI and the intriguing excitation properties of spin-ice (emergence of magnetic monopoles and attached Dirac strings [58]) should encourage their study from a novel and more phenomenological perspective. The work done during this thesis goes in this direction.

In recent years, research in this field has been boosted by the exciting proposal that topological defects, in the form of magnetic monopoles and their attached Dirac strings, could be observed in spin-ice samples [58, 132, 44, 59, 198, 178]. Spin-flips due to thermal fluctuations are responsible for the emergence of these defects. The presence of frustration gives rise to unusually large equilibration time scales in real spin-ice materials. Moreover, $2D$ artificial spin ice samples are a-thermal, hence fundamentally out-of-equilibrium. For these reasons, the study of the leading dynamical mechanisms are of prior importance in order to understand spin-ice's collective behaviour. Reaction-diffusion arguments have been used to estimate the time-dependent density of defects in the disordered phase of $3D$ spin ice [59]. The dynamics induced by the presence of a time-dependent magnetic field on arrays of large ferromagnetic islands has been studied by a mean field approach [51]. As far as we know, no studies of dynamics towards the ordered phases nor beyond these simple modellings has yet been performed.

Here we choose a different approach to address the dynamics of spin-ice models. For the sake of simplicity we focus on thermal quenches in the $2D$ square lattice spin ice model built as a stochastic extension of the celebrated *six-vertex model* of statistical mechanics [25]. We use a rejection-free continuous-time Monte Carlo (MC) algorithm [17], with local spin-flip updates and non-conserved order parameter. This algorithm allows us to identify the equilibrium phase diagram and to analyse different dynamic regimes.

In this thesis we study both the equilibrium and out-of-equilibrium properties of $2D$ spin-ice. In order to do so we consider a sixteen-vertex model defined on an $L \times L$ square lattice. Each edge is occupied by an arrow modelled as a binary variable $S = \pm 1$. Then we assign a Boltzmann weight $\omega_k \propto e^{-\beta \epsilon_k}$ to each of the $k = 1, \ldots, 2^4$ vertex configurations shown in Fig I.1 and we assume symmetry under spin-reversal. We set the energies of all vertices with three-in and one-out
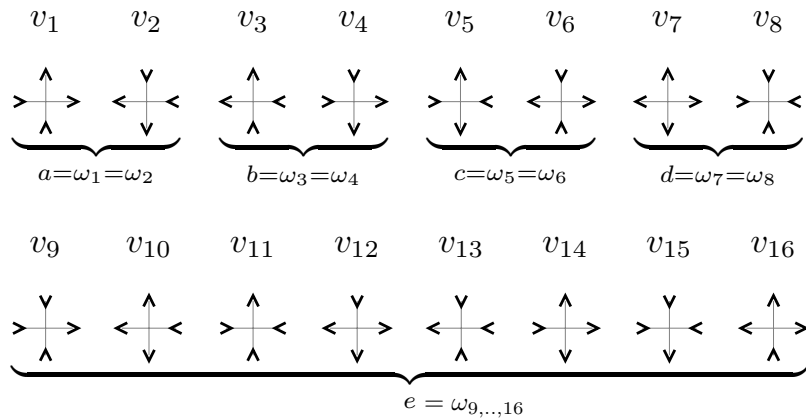
Figure I.1: The sixteen possible vertex configurations in the square lattice.

arrows (and their spin reversed) to be equal. As depicted in Fig. I.1 these assumptions leave us with five different statistical weights (or fugacities) a, b, c, d and e: the parameters in the model. In experimental samples, interactions between arrows favour vertices verifying the ice-rule, then: $\min(a, b, c) > e > d$.

The manuscript is organised as follows:

Chapter II starts by a general introduction on geometrically frustrated magnets to then move to spin-ice in particular. We briefly review the main experimental realisations of spin-ice like systems in order to motivate the introduction of our model. We stress, when possible, the relationship between different frustrated systems with a macroscopic degeneracy of the ground state. Some theoretical models used to compute their thermodynamic quantities are presented and compared with the relevant experimental results.

In chapter III we present some useful concepts from the theory of phase transitions and critical phenomena: modern classification of phase transitions, scaling and universality. Then, we describe the numerical methods used in order to investigate the collective behaviour of the system (Monte Carlo, finite size scaling, non-equilibrium relaxation method). This chapter has been included for clarity and completeness. If readers are quite familiar with phase transitions and the numerical methods used to tackle them, they may skip this chapter and proceed to the next.

In chapter IV we collect the available exact results on $2D$ vertex models. Although this is not a thesis in mathematical physics, we are dealing with extensions of the six- and eight-vertex models, hence some comments about integrability should be included. The exact phase diagram of the six- and eight-vertex models is presented. We discuss the quantum representations of vertex models and the relationship between Quantum Monte Carlo and loop algorithms for classical constrained models. We introduce the unifying concept of height function for the six-vertex model and hardly constrained models in general. This leads us to a general definition of topological sectors in this context.

In chapter V we obtain the equilibrium phases and critical properties of the symmetric sixteen-vertex model.We proceed in two directions. On the one hand, we study the static properties of the sixteen vertex model on a square lattice with Monte Carlo simulations. We establish the phase diagram and critical properties, that we compare to the ones of the integrable cases. On the other hand, we adapt the cavity (Bethe-Peierls) method to treat the same problem on a well-chosen tree and we thus access all the expected phases in the model. We discuss the range of validity of this

approximation. We compare the results obtained analytically to the numerical ones for the finite dimensional system. We then apply the same strategy to the model for a special choice of the parameters closer to the experimental set-up. We compare the predictions of our vertex model with the measurements and find quantitative agreement away from the critical point. Our results prove the relevance of the vertex model as a simple model system for the study of ASI samples, and more generally $2D$ spin-ice. After giving the few exact results available for the sixteen-vertex model, we present our attempts to generalise the height function framework and the quantum mapping into a spin chain to our unconstrained generic model. The work presented in this section has benefit from close collaboration with Laura Foini and Marco Tarzia.

Finally, in chapter VI we analyse the out-of-equilibrium dynamics of the model following different kind of quenches: from a fully disordered initial condition (equilibrium at infinite temperature) into its disordered, ferromagnetic and anti- ferromagnetic phases. We analyse the evolution of the density of topological defects and we identify the leading mechanisms for the growth of domains in the ordered phases. We compare our results with known facts of the dynamics of spin ice samples.

Experimental realisations: Frustrated magnets and artificial spin-ice

II.1 Geometrical frustration

In systems with a large number of interacting degrees of freedom the tendency to order locally cannot always be fully satisfied. The impossibility to simultaneously minimize the interaction energy at each point of the system is called *frustration*, a concept which covers a broad class of very different situations in condensed matter physics. Frustration arises when there is a competition between different interactions and/or when the lattice structure prevents the simultaneous minimization of the local interaction energy.

II.1.1 Definitions and ground-state manifold

There are two main sources of frustration in condensed matter systems: (i) the presence of strong disorder or (ii) the geometry of the lattice combined with the specific nature of the interactions (usually antiferromagnetic). In this section, we first discuss briefly the main features related to frustration to then discuss in more detail its origin in spin-ice. We present some representative examples of frustrated systems to illustrate general concepts and motivate their study, with no attempt to give a review on this vast research domain. For a recent general introduction on the subject the reader may consult [188]. A more detailed review of the field is given in [84]. For a more specific review dedicated to frustrated Ising systems see [167]. We refer the interested reader to [226] for an experimental review.

II.1.1.1 Disordered systems

In the context of disordered systems frustration arises from the randomness of the interactions between the different degrees of freedom. One can introduce disorder in the $O(n)$ model by considering a random exchange interaction J_{ij} between two nearest-neighbours (NN) spins on sites i and j of a $d-$dimensional lattice. This class of models is described by the following

Hamiltonian

$$H = - \sum_{\langle i,j \rangle} J_{ij} \, \mathbf{S}_i . \mathbf{S}_j \tag{II.1}$$

where $\{J_{ij}\}$ is a set of independent 'quenched' random variables (time independent) with mean $\langle J_{ij} \rangle = 0$; $\mathbf{S}_i$ are n-component vectors such that $\mathbf{S}_i^2 = 1$, $\forall i$. For $n = 1$ this model corresponds to the canonical *spin-glass* model: the D-dimensional Edwards-Anderson model. It models the presence of magnetic impurities located randomly in 'dirty' materials. Since the interaction between them is well captured by the RKKY mechanism the strength and orientation of the exchange coupling is randomly distributed.

As shown in Fig. II.1(a) the spin located on site i cannot simultaneously satisfy the antiferromagnetic bond $J_{ij} > 0$ and the ferromagnetic one $J_{ik} < 0$. In $3D$, this model is expected to undergo a spin-glass transition at a finite temperature T_g [170]. The low temperature glassy phase is characterized by a vanishing magnetization and an extremely slowing down of the dynamics. The ground state of the Edwards-Anderson model is not only characterised by the symmetry of the Hamiltonian, on the contrary to its non-frustrated counterpart, the Ising model. Therefore, the nature of the low temperature phase is radically modified by the inclusion of frustrated interactions. Despite the existence of several mean field models which reproduce some characteristic features of 'real' glassy systems, the nature of the glass transition in finite dimensions is still a matter of debate [184]. The question of whether the glass transition is a true phase transition or just a non-equilibrium effect is far from being solved. This is a formidable theoretical problem which will not be treated in the following pages. Instead, we will focus on the effects of frustration in the absence of disorder.
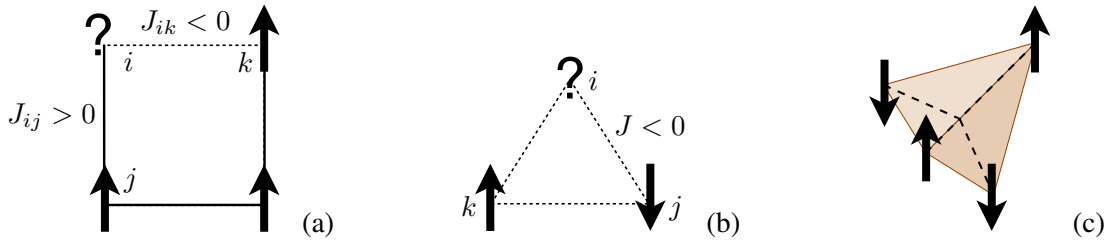
Figure II.1: Frustrated units with Ising spins. (a) The Edwards-Anderson's model on the square lattice. The dashed bond corresponds to AF exchange and plane bonds correspond to FM exchange. (b) The AF Ising model on an equilateral triangular lattice. (c) The AF Ising model on a lattice of corner-sharing tetrahedra.

II.1.1.2 Clean systems

In a large class of condensed-matter systems without disorder the tendency to order is hampered by constraints. These are due to the nature of the interactions and the geometry (or topology) of the space where the relevant degrees of freedom are defined. The combination of these two elements gives rise to the so-called *geometrical frustration*.

In order to illustrate the latter definition we consider the antiferromagnetic (AF) Ising model defined on the $2D$ triangular lattice. This model was originally introduced in 1950 by Wannier [265] and Houtappel [118] who computed the exact partition function and recognized the absence of long range order at any temperature. It has been largely studied since then and has become the text-book example of geometrical frustration. As shown in Fig. II.1 (b) the three antiferromagnetic bonds around a triangle cannot be satisfied simultaneously. The third spin sitting

on site i can be equivalently 'up' or 'down' such that each plaquette contains at least one pair of parallel spins. This limitation is due to the particular geometry of the lattice. Hence, all the configurations verifying

$$\sum_{i \in \mathcal{T}} S_i = \pm 1 \tag{II.2}$$

on each triangular plaquette $\mathcal{T}$ are energetically equivalent. Meaning that there is a 'frustrated' bond of parallel spins per triangle, even thought the interaction is antiferromagnetic. The latter equation (II.2) can be seen as a local *constraint* defining the ground state of the system. Among the $2 \times 2 \times 2 = 8$ possible configurations for an elementary triangle there are six verifying the constraint, leading to an extensive degeneracy of the ground-state which diverges in the thermo-dynamic limit. The phase space submanifold defined by the constraint eq. (II.2) will be called the *ground-state manifold* of the model. The exact value of the associated ground state entropy was computed by Wannier and Houtappel [265, 118] . It is given by

$$\frac{S_{2D}}{N k_B} = \frac{3}{\pi} \int_0^{\pi/6} \ln(2 \cos x) \, dx \approx 0.323 \tag{II.3}$$

where N is the number of spins in the system. This calculation shows that the system is disordered even at $T = 0$. The calculation of the pair correlation function $C(r)$ confirms this scenario [246]. Indeed, it has been shown that, for $T \to 0$ the correlations decay algebraically as

$$C(r) \sim r^{-1/2} \tag{II.4}$$

where r is the distance between two spins in the lattice. The above constraints impose long-range correlations between the spins. In analogy with molecular liquids this kind of collective paramagnets are called classical *spin-liquids*.

For reasons that will become clear in the following section, lets consider the $3D$ version of the previous model: the AF Ising model on a pyrochlore lattice (see Fig II.2) introduced by Anderson [7] six years after the work of Wannier and Houtappel. Similarly to the $2D$ case, he found a macroscopic degeneracy of the ground state on a $3D$ lattice. As shown in Fig. II.1 (c), the number of satisfied bonds on an elementary tetrahedron cannot be larger than two. All the configurations $\{S_i\}_{i=1}^N$ with two spins up and two spins down per tetrahedron are equivalent and constitute the ground state of the system. In a more formal way, the ground state manifold $\mathcal{G}$ is defined by the local constraint

$$\mathcal{G} = \left\{ \{S_i\} \ : \sum_{i \in \mathcal{T}} S_i = 0, \ \forall \, \mathcal{T} \right\} \tag{II.5}$$

where here the *elementary frustrated unit* $\mathcal{T}$ is a tetrahedron.

The models we have discussed above include only NN interactions such that each link of the lattice can be seen as a two-body interaction (a bond). From Fig. II.1 one can be easily convinced that, since the AF order is staggered, the interacting spins must be defined on a bipartite lattice in order to be able to accommodate into its Néel ground state and avoid geometrical frustration. In $1D$ systems, further neighbours interactions are needed in order to have frustration. Indeed, geometrical frustration comes from the presence of *closed loops* of an odd number of degrees of freedom with antiferromegnetic interactions. This can be summarised by Toulouse's criterion [259]: the plaquette or unit $\mathcal{T}$ is frustrated if the parameter $\mathcal{W}_{\mathcal{T}}$ defined as

$$\mathcal{W}_{\mathcal{T}} = \prod_{\langle i,j \rangle \in \mathcal{T}} \frac{J_{ij}}{|J_{ij}|} \tag{II.6}$$
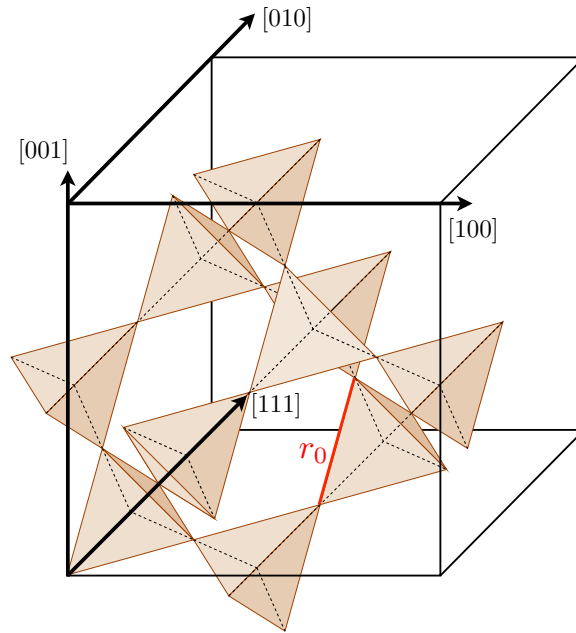
Figure II.2: **The pyrochlore lattice** made by corner-sharing tetrahedra. The cube represents a unit cell. The three crystallographic directions [001], [010] and [001] are shown together with the [111] direction. The spacing between nearest neighbours is denoted by r_0 (shown in red).

is equal to -1. The product in the equation above runs over all the NN pairs around an elementary frustrated unit $\mathcal{T}$. Since this criterion can be generalised to a product over all the bonds along any closed loop we will call it *loop product*. To illustrate this concept let us consider the AF Ising model on the triangular lattice. Since all the plaquettes are made of three bonds, elementary loops are made of an odd number of bonds (see Fig. II.3 (a)). Therefore $\mathcal{W}_{\mathcal{T}} = -1$ for any loop $\mathcal{T}$. As shown in Fig. II.3 (b), this does not apply to the AF Ising model on the Kagome lattice. In this system all the triangles are frustrated but not all loop products give a negative result because of the presence of hexagonal plaquettes. The latter remarks lead us to a concise definition of geometrical frustration:

A system is geometrically frustrated if a negative loop-product exists.

The existence of a ground state manifold with an extensive number of states (diverging in the thermodynamic limit) is a central feature of geometrical frustration but not all frustrated systems display this property. For continuous spins ($n > 1$) placed on the vertices of frustrated lattices the ground state is usually long-range ordered but no longer made by parallel or antiparallel spins. This is the so-called non-collinear order. The canonical example is the AF XY model on a triangular lattice whose ground states give rise to the ' 120 º structure' [84]. In the ground state, the spins accommodate such that their orientations form an angle of $2\pi/3$, or equivalently, the sum of the three spins around an elementary plaquette is zero.

So far, we have only considered lattice systems with interacting spin variables. Even though it usually appears in the context of magnetic systems, geometrical frustration plays a fundamental role in the understanding of the structural aspects of solids and complex media [233]. In such systems, the tendency to grow a local ordered structure with some symmetry is hampered by the topology of the space to fill (e.g. the 3D Euclidean space cannot be filled by tetrahedral packing of spheres) [258].
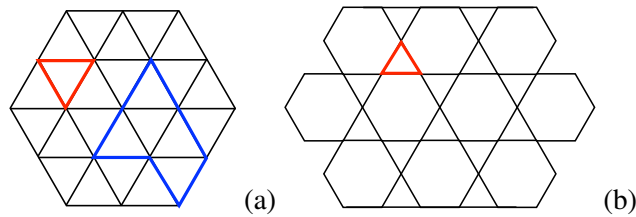
Figure II.3: Examples of $2D$ frustrated lattices and their corresponding loop products. (a) **The triangular lattice**. The loop product $\mathcal{C}_{\mathcal{T}_1} = (-1)^3$ around a single frustrated unit $\mathcal{T}_1$ made by 3 bonds shown in red and $\mathcal{C}_{\mathcal{T}_2} = (-1)^7$ around the loop $\mathcal{T}_2$ made by five plaquettes and 7 bonds shown in blue. (b) **The Kagome lattice** made by corner sharing triangles has a negative loop product around a triangular plaquette (shown in red).

At this stage one should try to answer the following question: Is the lack of long range order robust to small perturbations? Strictly speaking, the above arguments leading to the macroscopic degeneracy of the ground state were based on: (i) the equivalence of all the bonds around a frustrated unit (ii) the lack of thermal fluctuations breaking the constraint. The inclusion of anisotropy [118], range of the interactions [181] and lattice deformations [69] break the first before mentioned argument and order becomes possible in a frustrated system. The second argument breaks down at any non zero temperature. Then, *defects* breaking the constraint defining the ground state manifold must be considered. Thermal fluctuations in frustrated magnets can give rise to 'exotic' excitations such as fractional excitations [14] or unconventional superconductivity [9]. It might explain the enthusiasm of condensed matter physicists in studying these systems.

A subtle ground state selection mechanism occurring in strongly frustrated systems was identified by Villain et al. [262]. The authors considered a frustrated Ising system (the domino model) without long range order at zero temperature. They showed that thermal fluctuations order the system at any finite temperature below T_c. At T_c the system undergoes a continuous phase transition to a disordered phase. This intriguing phenomenon was hence termed 'order as an effect of disorder'. Similarly, it has been shown in the Kagome and triangular Heisenberg AF models that quantum fluctuations at zero temperature can also select a ground state [232]. In its usual form, the third law of thermodynamics is violated in geometrically frustrated systems with a hard constraint and discrete degrees of freedom. Strictly speaking, one must take into account the presence of quantum fluctuations at low temperature. It is not clear how these could affect the ground state degeneracy of water ice. The interplay between quantum fluctuations and geometrical frustration leads to the so-called *quantum spin liquids* [14]. Theories like resonance valence bonds [8, 9] predict the existence of 'exotic' excitations in connection with high temperature superconductivity, explaining the huge amount of recent works in the field. For recent reviews in the subject I would recommend [158, 186, 14] .

II.1.2 Water Ice

Back in the thirties, physicists and chemists where confronted for the first time to the unexpected consequences of frustration when studying ordinary *water ice*. Even though the concept of frustration was not used yet, everyday's water ice is indeed the prototypical example of geometrical frustration. This section is devoted to a brief review on this system.

II.1.2.1 Zero-point entropy

The emergence of a macroscopic degeneracy of the ground state is the main characteristic of geometrically frustrated systems. Even down to zero temperature, the entropy does not vanish and the system fluctuates, in apparent contradiction with the third law of thermodynamics. As a result, there is an absence of long-range order at $T = 0$ and the corresponding *zero-point entropy* or *residual entropy* can be measured. This was done for water ice in 1936 by Giauque and Stout [103]. The authors performed heat capacity measurements on water from 273 K down to 10 K. They computed the entropy between 10 K and 273 K by integrating the heat capacity measurements shown in Fig. II.4. They found

$$\Delta S = \int_{10}^{273} C_p \, d\ln T \approx 9.081 \text{ cal.mol}^{-1}.\text{K}^{-1}. \tag{II.7}$$

The entropy of the lower temperature regime, between 0 K and 10 K, was extrapolated using Debye's model [141]. Then, by adding the latent heat contributions, accurately measured in the past, they found $\Delta S_1 = 44.28 \pm 0.05 \text{ cal.mol}^{-1}.\text{K}^{-1}$. This measurement was compared with the entropy calculated by Giauque and Ashley using spectroscopic data $S_{273} \approx 45.10$ cal.mol^{-1}.K^{-1} [104]. This value is larger than the one obtained by calorimetric measurements. The discrepancy between these two values gives an experimental evidence of a zero-point entropy of $S_{3D} = S(273) - \Delta S_1 = 0.82 \pm 0.05 \text{ cal.mol}^{-1}.\text{K}^{-1}$ ($\approx 3.4 \text{ J.mol}^{-1}.\text{K}^{-1}$). By introducing a simple model, Pauling explained and gave an excellent estimation of this value [215].
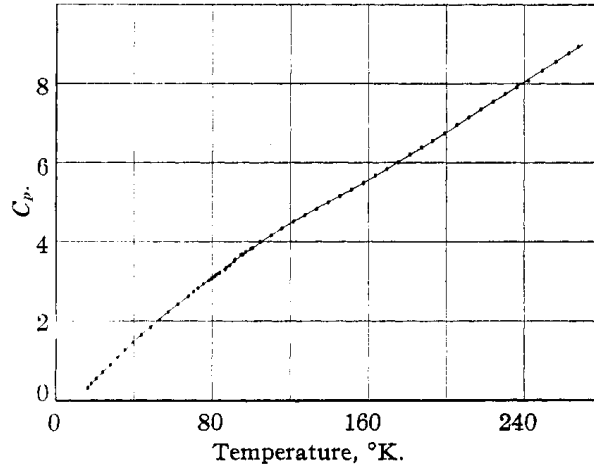
Figure II.4: Heat capacity of water ice measured by Giauque and Stout (from [103]). The structure of water ice I$_h$ is shown in Fig. II.7.

II.1.2.2 Pauling's Ice model

The following quote from Giauque and Stout's seminal paper [103] presents in a concise way the essence of Pauling's model:

> *During the course of the present investigation, Pauling offered an alternative explanation based on the random orientation of hydrogen bonds in ice. [...] The spectroscopic value is 45.10 leading to a discrepancy of 0.82 cal./deg./mole. This is in excellent agreement with the theoretical discrepancy 0.806 calculated by Pauling on the assumption of random orientation of hydrogen bond directions in ice.*

Pauling's model [215] predicts the before mentioned zero-point entropy as arising from the intrinsic disorder of hydrogen ions (H^+) in water ice. Oxygen ions (O^{2-}) occupy the vertices of a coordination number four lattice and protons are located on its edges. At each oxygen-oxygen link there is only one proton with two possible equivalent positions: close or distant to an oxygen ion (covalent or hydrogen bond respectively). Water molecules are polar, hence each edge of the lattice carries an electric dipole moment ($\vec{\mu} \equiv O^{2-} \to H^+$). The two possible positions for the proton correspond to a dipole pointing towards one of its two adjacent vertices. This is summarized in the so called Bernal-Fowler's *ice-rules* defining the ground state of the model: at each vertex two dipoles must point inward and two outward [30]. These rules are equivalent to the discrete local constraint,

$$\vec{\nabla}_i . \vec{\mu}_i = 0, \ \ \forall i \tag{II.8}$$

where the index i denotes a site (i.e. vertex) of the lattice. All the configurations verifying that constraint are energetically equivalent. Even though Pauling's model was originally proposed to study $3D$ water ice, it can be defined in any coordination four lattice. As the reader will remark, all the discussions and results that follow in this section are independent of the dimensionality of the lattice as soon as a the relevant unit is a vertex with four equivalent edges attached to it. On a square lattice, six configurations among the $2^4 = 16$ possible local arrangements verify the ice-rule (see Fig. II.5). The system is geometrically frustrated: each frustrated unit (made by a vertex and its four edges) carries a degeneracy of six, leading to the extensive degeneracy of the ground state measured by Giauque and Stout.

Pauling computed approximately the number of configurations verifying the ice-rules. Consider a lattice with N vertices (O atoms) and $2N$ edges (H atoms). There are 2 possible configurations for each edge, which gives $\Omega_0 = 2^{2N}$ possible configurations. This gives the entropy of the model if the ice-rules are omitted. The number of configurations must then be reduced. In order to do so, Pauling considered each vertex as an independent object. Then the number of allowed configurations is reduced by multiplying by N factors $6/16$. These factors are the probability that the vertices verify the ice-rule (six allowed configurations among the sixteen possible ones). One should note that the hypothesis of independence between vertices is a huge approximation (of the 'mean-field' kind) and has, *a priori*, no reason to give accurate results. The number of ground state configurations is therefore $\Omega_\infty = 2^{2N}(6/16)^N = (3/2)^N$ and the residual entropy

$$\frac{S_\infty}{Nk_B} = \ln(3/2) \approx 0.405 \ . \tag{II.9}$$

This value is remarkably close to the experimental value $S_{3D} = 0.82 \pm 0.05$ cal.mol^{-1}.K^{-1} ($\approx 0.41R \approx 3.4$ J.mol^{-1}.K^{-1}, where $R \approx 8.314$ J.mol^{-1}.K^{-1} is the gas constant). This approximation can be applied to any model where the extensive degeneracy of the ground state comes from a local constraint. For the AF triangular Ising model the probability to find a triangle in its ground state [i.e. verifying eq. (II.2)] is $6/8$. Since there are two triangles per spin, one finds $\Omega_\infty = 2^N(6/8)^{2N}$, where N is the number of spins in the system. Hence,

$$\frac{S_\infty}{Nk_B} = \ln(9/8) \approx 0.118 \ . \tag{II.10}$$

Pauling's approximation gives neither an upper nor a lower bound of the zero point entropy. The exact value of the zero point entropy of the model was given in eq. (II.3). This result shows that, for the AF Ising model on the triangular lattice, Pauling's method is unsatisfactory (see Table II.1). However, for the AF Kagome lattice and the ice problem this approximation turns out to be extremely accurate. Magnetic specific heat measurements show the agreement between the theoretical result and experiments [225].

The energy of the ice model is minimised when all the vertices verify the ice rule. Protons can only be in two different positions per bond, which is equivalent to a binary variable attached to each edge. The model is then defined by giving the same energy to all the configurations verifying the ice-rule and an infinite one to all the other ones. The exact solution of the ice model on the square lattice was given by Lieb using transfer matrix techniques [165]. The ground state degeneracy is given by the so-called Lieb's square ice constant W and the residual entropy is

$$S_{2D} = N\,k_B\,\ln W, \quad W = \left(\frac{4}{3}\right)^{\frac{3}{2}} = \frac{8\sqrt{3}}{9}\,. \tag{II.11}$$

Its numerical value is $S_{2D} \approx 0.43R$. The ice problem is closely related to many other problems in mathematical physics and Lieb's constant is now extensively used in combinatorics.
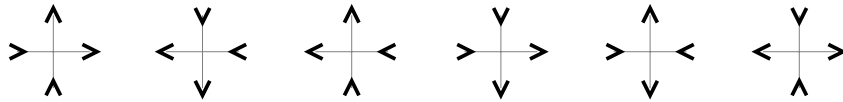
Figure II.5: The six vertex configurations verifying the ice rule in the square lattice.

II.1.3   Generalised 'ice-type' models

The extension of Pauling's ice model to include more general ferroelectric systems led to the so called 'ice-type models' and then 'vertex models'. Vertex models consist in some degree of freedom (Ising spins, q-valued variables, etc.) sitting on the *edges* of a lattice where interactions are defined on the *vertices* (contrary to 'edge' models, as $O(n)$ models, where interactions are explicitly written in terms of variables on the edges). The many-body interaction between the variables sharing a vertex is then encoded by the energy of a local configuration.

The theoretical solution of the ice model [165], and some generalizations of it in which a different statistical weight is given to the six allowed vertices [163, 248] were given by Lieb and Sutherland in the late 60s using the transfer matrix technique with the Bethe Ansatz. Soon after, Baxter introduced the Yang-Baxter equation to treat the generic *six-* and *eight-vertex model* [25]. The eight-vertex model is an extension of the six-vertex model. It includes all the vertices with an odd number of incoming and outgoing arrows on each vertex, leading to the eight configurations shown in Fig. II.6. Their equilibrium phase diagrams are very rich: depending on the weight of the vertices the system sets into a quasi long-range ordered spin liquid phase (SL) and several ferromagnetic (FM) and antiferromagnetic (AF) phases separated by different types of transition lines. In the six vertex case the SL phase is critical in a similar way to what is observed in $3D$ spin-ice.

In these models a local constraint makes them integrable, meaning that the Yang-Baxter equations are verified (see Chapter IV), and many of its equilibrium properties can be derived exactly. From a theoretical perspective integrable vertex models are of particular interest. The static properties can be mapped onto spin models with many-body interactions [166], loop models [205, 125], three-coloring problems [165], random tilings [281], surface growth [26], alternated sign matrices [281] and quantum spin chains [249]. A comprehensive discussion of some of these mappings will be made in the text, mainly in Chapter IV.

The critical properties and the nature of the phase transitions in frustrated spin systems are difficult to treat with the standard methods of modern statistical mechanics. Although largely studied, the collective behaviour of frustrated systems is still a matter of debate. Renormalisation group

studies of Heisenberg frustrated magnets support the existence of scaling laws with continuously varying exponents [54, 82], similarly to what happens in the eight-vertex model (see chapter IV). Well established approaches must be improved in order to capture the essence of these new phenomena. It is then of great interest to develop simple theoretical models to describe these systems. Frustrated spin models, and vertex models in particular, seem to be a good playground to start with.

$$a=\omega_1=\omega_2 \qquad b=\omega_3=\omega_4 \qquad c=\omega_5=\omega_6 \qquad d=\omega_7=\omega_8$$
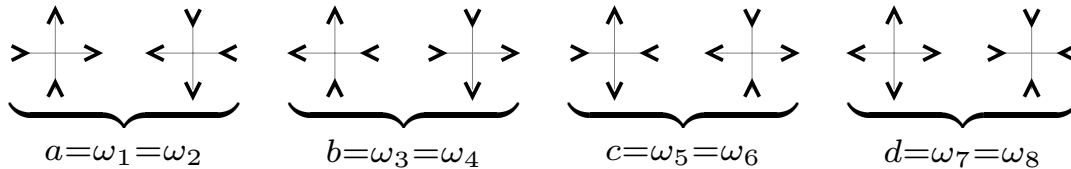
Figure II.6: Vertex configurations of the eight vertex model on the square lattice.

The latter remarks make the study of frustrated systems interesting by itself from the theoretical point of view. Experimentally, frustrated magnetic materials can be engineered and studied in the laboratory using a large variety of different techniques. The control of magnetic materials has been crucial for technological issues during the last decades and we could expect that frustrated magnetism will also become a source of new technological development. As shown all along the coming sections, spin ice in $2D$ is a good candidate both for the theoretical understanding of geometrical frustration and for potential technological applications. In particular, the ability to manipulate magnetic monopoles in spin ice would lead to magnetic analogs to electric circuits.

II.2   Spin-ice materials

II.2.1   Rare-earth pyrochlores with residual entropy

This section is devoted to *spin ice*, a classical frustrated spin system realised in a family of rare-earth pyrochlore oxides such as $Ho_2Ti_2O_7$ or $Dy_2Ti_2O_7$. Since the pioneering work of Harris and co-workers [113] spin ice has been the subject of a great deal of work and has become one of the most studied frustrated systems. This has been driven by the remarkable and unexpected properties observed in these materials. Spin-ice belongs to the more general family of pyrochlore oxides of the type $A_2B_2O_7$. For a review dedicated to magnetic pyrochlore oxides in general and spin-ice in particular see [102] and [43], respectively. In spin-ice 'A' is a rare-earth magnetic ion (such as Ho^{3+} or Dy^{3+}) and 'B' is a non-magnetic ion (such as Ti^{4+}).

The only magnetic ions in spin-ice come from rare-hearth elements (Ho^{3+} or Dy^{3+}). They carry a large magnetic moment located on the sites of a lattice made by corner-sharing tetrahedra forming a pyrochlore lattice. The surrounding crystal field acting on the magnetic ions gives rise to a strong single ion anisotropy that forces the magnetic moments to be aligned along their local $\langle 111 \rangle$ direction connecting the centres of their two corner-sharing tetrahedra (see Fig. II.2). At low temperature, the magnetic moments are well described by classical Ising spins with a large magnetic moment ($\approx 10\mu_B$), in such a way that they can only point inward or outward from the centre of a tetrahedron. Each tetrahedron can be seen as a vertex in a $3D$ lattice taking one out of sixteen possible configurations (see Fig. II.10).

As suggested by its name, spin ice is the magnetic analog of water ice. Magnetic moments in spin ice play an equivalent role to that of the proton position, i.e. dipolar moment, in water ice. In ordinary ice I_h the oxygens are located at the centre of the tetrahedra forming a pyrochlore lattice

as shown in Fig. II.7. Electric dipoles are then located on the sites of a pyrochlore lattice [1], such that the correspondence between a water ice configuration and a spin ice one is straightforward: when there is only one proton per edge, one can identify an electric dipole with a spin.
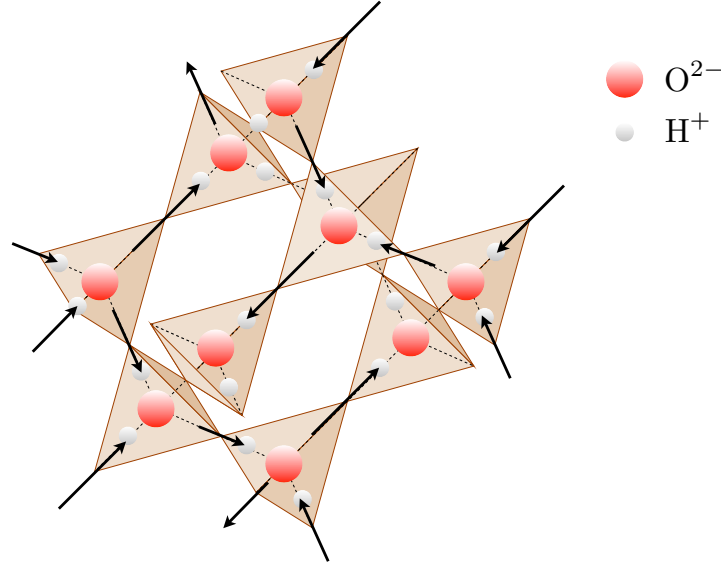
Figure II.7: Equivalence between the crystalline structure I_h of water ice and spin-ice on a pyrochlore lattice. The oxygens form a diamond lattice, the coordination number four lattice made by the centers of the tetrahedra. The middle points of the edges where the arrows sit form a pyrochlore lattice, the dual of the diamond lattice. A spin (black arrows) pointing inside a tetrahedron occupied by an oxygen corresponds to a hydrogen closer to it.

A few years after Harris et al. reported the absence of long-range order in $Ho_2Ti_2O_7$, Ramirez and collaborators measured a residual entropy close to the one predicted by Pauling now using $Dy_2Ti_2O_7$ [224]. Similarly to what Giauque and Stout did sixty years before, these authors extracted the entropy at very low temperature from heat capacity measurements between $T = 0.2$ K and $T = 12$ K (see Fig. II.8). As shown in Table II.1 this measurement is remarkably close to the entropy of water ice and, interestingly, to analytical calculations in $2D$ and making use of the Pauling approximation (mean-field like models). From this observation one would like to conclude that spin ice is geometrically frustrated and that, at low enough temperatures, it verifies some kind of hard constraint such as the ice-rules.

	S_{exp}	S_{2D}	S_∞
Water ice	$0.41R$ [103]	$0.43R$ [165]	$0.40R$
Spin ice	$0.46R$ [224]	$0.43R$	$0.40R$
Kagome AF	$0.5018R$ [225]	$0.5018R$ [135]	$0.5014R$
Ising AF	$0.36R$ [202]	$0.323R$ [265]	$0.118R$

Table II.1: **Zero point entropy**. First column S_{exp}: experimental results with the corresponding references for different frustrated materials. Second column S_{2D}: exact computations in $2D$ lattice models. Third column S_∞: approximate results applying Pauling's method. Where $R \approx 8.314$ J.mol^{-1}.K^{-1} is the gas constant.

---

1. The diamond and the pyrochlore lattice are dual.
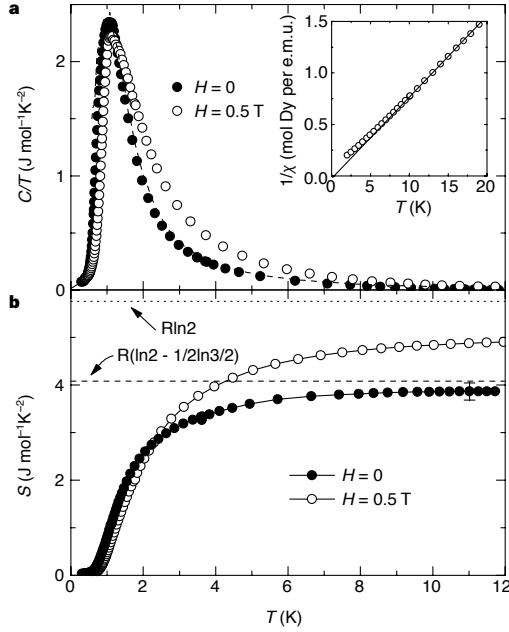
Figure II.8: Specific heat and entropy measurement in $Dy_2Ti_2O_7$ from [224]. (a) Heat capacity divided by temperature of $Dy_2Ti_2O_7$ in an external field $H = 0$ and $H = 0.5$ T. The dashed line is a Monte Carlo simulation of the dipolar spin-ice model in a finite lattice made by $8 \times 8 \times 8$ tetrahedra at zero field. The inset shows the inverse susceptibility of $Dy_2Ti_2O_7$ in an external field $h = 0.02$ T. (b) Entropy of $Dy_2Ti_2O_7$ in an external field $H = 0$ and $H = 0.5$ T. The entropy of a random arrangement of spins $R \ln 2$ and the one computed by Pauling $R(\ln 2 - (1/2)\ln(3/2))$.

II.2.2 Dipolar spin-ice model

In order to further understand the analogies between water and spin ice behaviour one should first understand the origin of frustration in spin ice. In these materials the exchange coupling between rare-earth ions (≈ 1 K) is weaker that in an usual ferromagnet (≈ 300 K for Co). Moreover, the magnetic moments carried by the magnetic ions are large ($\approx 10\mu_B$) such that dipolar interactions cannot be neglected [112]. Dipolar and exchange interactions are of the same order of magnitude in spin ice materials. The best suited microscopic model to describe spin ice is the so called dipolar spin ice (DSI) model [240]. Its Hamiltonian is given by

$$H_{DSI} = -J \sum_{\langle ij \rangle \in \mathcal{P}} \mathbf{S}_i.\mathbf{S}_j + Dr_0^3 \sum_{i<j\in\mathcal{P}} \left(\frac{\mathbf{S}_i.\mathbf{S}_j}{||\vec{r}_{ij}||^3} - 3\frac{(\mathbf{S}_i.\vec{r}_{ij})(\mathbf{S}_j.\vec{r}_{ij})}{||\vec{r}_{ij}||^5} \right) \qquad \text{(II.12)}$$

where the magnetic moments $\mathbf{S}_i = S_i\vec{z}_i$ are Ising spin variables ($S_i = \pm 1$) along the local $\langle 111 \rangle$ axis $\vec{z}_i$[2]. The separation between spins is given by $\vec{r}_{ij} = \vec{r}_i - \vec{r}_j$ and $\mathcal{P}$ denotes the set of sites of the pyrochlore lattice. The first sum runs over all the edges $\langle ij \rangle$ of $\mathcal{P}$. The exchange coupling $J > 0$ is ferromagnetic and the dipole strength $D = \mu_0\mu^2/4\pi\vec{r}_0^3$ where r_0 is the distance between two nearest-neighbours, μ the net magnetic moment carried by magnetic ions and μ_0 the magnetic

---

2. In the crystallographic basis $\{[100], [010], [001]\}$ the four local directions of a tetrahedra are

$$\frac{1}{\sqrt{3}}(1,1,1), \frac{1}{\sqrt{3}}(1,-1,-1), \frac{1}{\sqrt{3}}(-1,1,-1), \frac{1}{\sqrt{3}}(-1,-1,1)$$

permeability of vacuum [3].

Let us focus first on the local interaction energy coming from H_{DSI}. Consider two nearest-neighbours spins located on sites i and j. We introduce a new set of binary variables σ_i on each site where $\sigma_i = \pm 1$ if the spin points into or out of the center of a considered tetrahedron. The scalar product $\mathbf{S}_i.\mathbf{S}_j = -\frac{1}{3}\sigma_i\sigma_j$ and $(\mathbf{S}_i.\vec{r}_{ij})(\mathbf{S}_j.\vec{r}_{ij}) = -\frac{2}{3}\sigma_i\sigma_j r_0^2$. At the nearest-neighbour (NN) level approximation the DSI Hamiltonian reads

$$H_{DSI} \approx H_{NN} = J_{eff} \sum_{\langle ij \rangle \in \mathcal{P}} \sigma_i\sigma_j \tag{II.13}$$

where

$$J_{eff} = \frac{J}{3} + \frac{5D}{3} > 0. \tag{II.14}$$

One obtains a short range antiferromagnetic model where only nearest neighbours (NN) $\langle ij \rangle$ interact. The NN Hamiltonian eq. (II.13) is equivalent to the $3D$ AF Ising model in the pyrochlore lattice introduced earlier (see Fig. II.9). As already mentioned, this system is geometrically frustrated, the ground-state corresponds to all the configurations with two $\sigma = 1$ and two $\sigma = -1$ per tetrahedron. It corresponds to two spins pointing in and two pointing out of each tetrahedron ($2\,in - 2\,out$ rule). Meaning that spin ice obeys the same ice rules as water ice in terms of spins instead of dipole moments. The centre of each tetrahedron in spin-ice can be considered as a vertex sitting on the dual lattice (i.e. the diamond lattice) taking one out of the sixteen possible configurations. As shown in Fig. II.10, all the vertices verifying the ice rule are degenerate. The ground state manifold of the system can then be formally written

$$\mathcal{G} = \left\{ \{S_i\} : \sum_{i \in \mathcal{T}} \sigma_i = 0, \ \forall\, \mathcal{T} \right\} \tag{II.15}$$

where the sum is over the four spins which belong to the same tetrahedron $\mathcal{T}$. The interactions split the sixteen vertices into three categories labelled a, e and d. The reasons for this labelling will become clear in the following sections, after projecting spin ice in the $2D$ plane and making the link with vertex models.

The interaction energy is minimised when the number of satisfied bonds on each tetrahedra is maximal under the constraint imposed by the lattice geometry. This mapping between the ferromagnetic interactions in terms of $\vec{S}_i$ in spin-ice and the antiferromagnetic interactions in terms of σ_i in the AF Ising model shows clearly why spin-ice is frustrated at the nearest-neighbour level. As pointed out originally [113], frustration in spin ice arises through the combination of the ferromagnetic character of the interactions and the local easy-axis anisotropy on the pyrochlore lattice, being the first example of *frustrated ferromagnetism*.

The NN model explains the emergence of the ice rules in spin ice and the agreement between calorimetric measurements and Pauling's calculation. However, it does not explain why the inclusion of long range interactions does not break the ground-state degeneracy imposed by ice-rules. We should emphasize that this is a very non-trivial feature of spin-ice: for other frustrated systems it has been shown that the inclusion of interactions beyond nearest neighbours selects a unique ground state [181, 228, 214]. The reason why DSI obeys the ice rules comes from the self screening of the dipolar long range interactions, hence needed in order to investigate the phases and excitations in spin ice. The relevance of the full long-range dipolar Hamiltonian became uncontested after the experimental work of Bramwell and collaborators [46]. By numerical simulations using both the DSI and the NN model, they showed that DSI reproduces correctly neutron scattering data in $Ho_2Ti_2O_7$ while the NN model fails. Dipolar interactions are crucial for the understanding of the phase diagram and the nature of the excitations in spin ice.

---

3. With $r_0 \approx 3$ Å and $\mu \approx 10\mu_B$ we get $D \approx 1.5$ K. This value is of the same order of magnitude as the Curie temperature measured in spin ice materials.
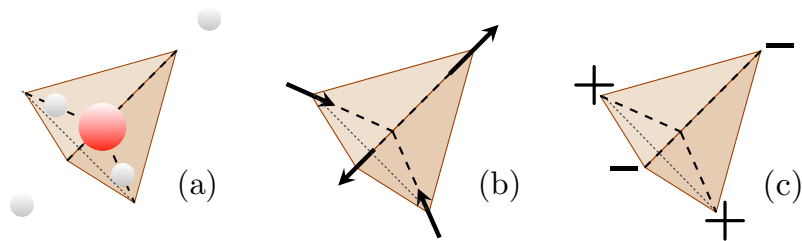
Figure II.9: Equivalent representations of spin ice. (a) Arrangement of oxygens (red) and hydrogens (white) in water ice. (b) Corresponding configuration in spin ice in term of spins pointing inwards or outwards the center of the tethrahedron. (c) Corresponding configuration in the AF Ising model.
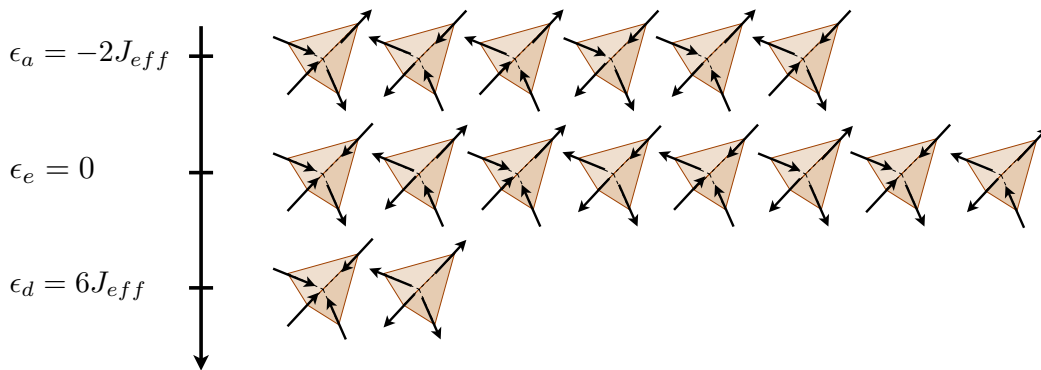
Figure II.10: **Energy levels in spin ice**. The sixteen possible configurations of a tetrahedron with their corresponding energy.

II.2.3 Phase diagram

The strength of the dipolar interaction at a NN level is denoted D_{nn}. Depending on the relative strength of dipolar $D_{nn} = 5D/3$ and exchange $J_{nn} = J/3$ interactions, spin ice can set into different ordered thermodynamic phases. These have been studied in detail by means on numerical simulations of the DSI model in [175]. In this work, the whole long range dipolar interaction is simulated using the Ewald summation method [78]. Their results are summarised in the phase diagram shown in Fig. II.11. For $J_{nn}/D_{nn} < 0$ small enough compared to T/D_{nn} the system sets into a staggered long-range ordered d-AF phase dominated by d-vertices, i.e. 4 *in* or 4 *out* configurations (see Fig. II.10) and denoted $q = 0$ in Fig. II.11. At low temperatures there is a region of the phase diagram where the ice-rules are verified. By lowering the temperature within this region the system undergoes a first order phase transition into a long-range ordered phase denoted $\vec{q} = (0, 0, 2\pi/a)$. This phase verifies the ice rules and is characterised by a striped order: all the spins located in the same (001) layer are parallel (see [175] for further details). A ground state without zero point entropy is then found in DSI.

External magnetic fields in different directions can couple with the Ising spins and lift the degeneracy between states depicted in Fig. II.10. The phase diagram of spin ice in the presence of fields is very rich and a full discussion goes beyond the scope of this thesis. We refer the interested reader to Bramwell, Gingras and Holdsworth's review [45]. We should, however, say a

few words about the particular field direction [111]. The effect of a strong field in this direction is to effectively project the system onto $2D$ Kagome layers. The spins pointing in the [111] direction are oriented with the field direction while the three others do not interact enough with the field to order. Each tetrahedron should verify the ice rules at low temperature and the direction of the spins along the [111] direction is fixed. For some range of temperature and magnetic field strength, an ice rule like constraint arises on the Kagome layers: each triangular plaquette has one spin pointing in and two out or the opposite [173]. As the reader may have noticed this so-called *Kagome ice* is isomorphic to the AF Ising model on the Kagome lattice mentioned in the previous section. At high enough magnetic field the Kagome planes order across a first order phase transition [116, 58, 93].
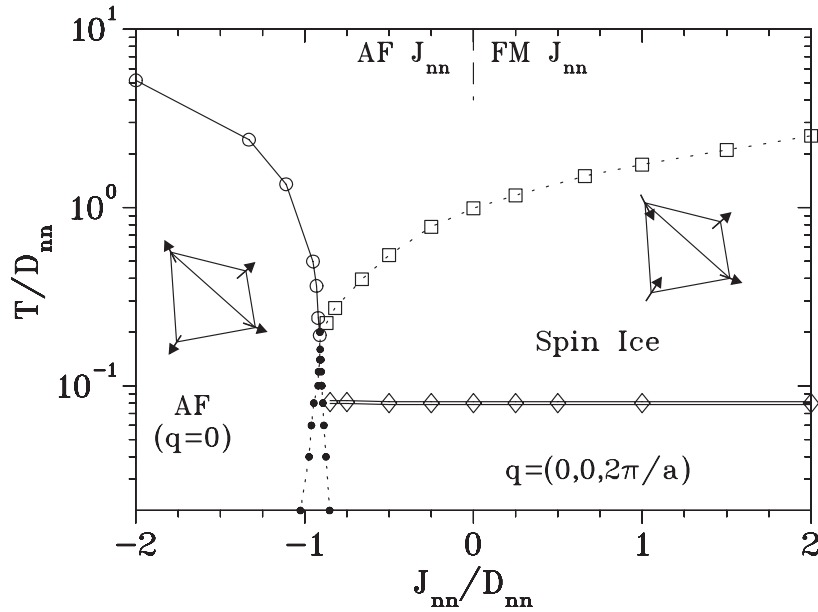
Figure II.11: **Phase diagram of DSI in zero field** from [175]. Open circles denote a second order phase transition between the ordered AF phase (4 *in* - 4 *out* staggered order $\vec{q} = \vec{0}$) and the disordered paramagnet. Open squares denote a cross over between the disordered paramagnet and the collective paramagnet (SL) verifying the ice-rules. The line of open diamonds represents the first order phase transition between the SL and the $\vec{q} = (0, 0, 2\pi/a)$ ordered phase. The region in between the black dotted lines displays hysteresis as J_{nn}/D_{nn} is varied at fixed temperature.

II.2.4 Magnetic monopoles

Four years ago, Castelnovo, Moessner and Sondhi proposed an alternative picture to explain the emergence of the ice-rules in spin-ice compounds [58]. In this 'dumbbell picture', spins are thought as two separated and oppositely charged *magnetic monopoles*. As shown in Fig. II.12 (a), there are four charges at the center of each tetrahedron. The ice-rules are then equivalent to a local magnetic charge neutrality. At finite temperature, spin fluctuations create pairs of *defects* breaking the ice-rule [see Fig. II.12 (b)]. They carry a net magnetic charge defined by

$$q = \frac{1}{2} \sum_{i \in \mathcal{T}} \sigma_i \ \in \{0, \pm 1, \pm 2\}. \tag{II.16}$$

Two types of defects are possible: tetrahedra breaking the ice-rule once - with three spins pointing inwards or outwards ($3\ in - 1\ out$ or $1\ in - 3\ out$) - or twice - with all the spins pointing inwards or outwards ($4\ in$ or $4\ out$). Defects create a default or an excess of magnetic charges on the sites of the diamond lattice (see Fig. II.7).

We can push forward this picture and rewrite the DSI Hamiltonian eq. (II.12) in terms of interacting monopoles and write

$$H_{DSI} = \sum_{(\alpha,\beta)\in\mathcal{P}^*} V(\alpha,\beta) + O(r_{ij}^{-5}) \tag{II.17}$$

where the sum here runs over all the pairs of sites (α,β) of the diamond lattice denoted by $\mathcal{P}^*$, the dual of the pyrochlore lattice. Since spins interact through a dipolar term, their magnetic charges interact via a Coulomb potential. From any distribution of charges creating a field which strength decays as r^{-2}, one can perform a multipole expansion. The spins in this picture are equivalent to dipole moments $\vec{d} = q_i\vec{r}_i$. The multipole expansion assumes that dipoles are far from each other. It then gives the same potential as the DSI model with corrections $O(r^{-5})$. In order to be able to take into account the nearest neighbour exchange in H_{DSI} one must add a self interaction term which gives

$$V(\alpha,\beta) = \begin{cases} \frac{\mu_0}{4\pi}\frac{Q_\alpha Q_\beta}{r_{\alpha\beta}} & \text{if } \alpha \neq \beta \\ \frac{1}{2}v_0 Q_\alpha^2 & \text{otherwise} \end{cases}, \tag{II.18}$$

where the charges are $Q_\alpha = q_\alpha\mu/a_d$, a_d the nearest-neighbours distance on the diamond lattice and v_0 a function of the parameters of the system μ, μ_0, r_0, J and D [58]. In this picture the ice-rules emerge naturally from locally neutral configurations. Flipping a single spin in the ice-rule manifold generates a $3\ in - 1\ out$ and a $1\ in - 3\ out$ defect. Then these two defects can be moved apart from each other by flipping one spin among the three ones responsible of the ice-rule breaking. By repeating this procedure, the monopoles separate leaving behind a *string* connecting them, reminiscent of a Dirac string [85]. Since all the configurations verifying the ice rule are equivalent, the string carries no tension and monopoles can move with the only energy cost coming from the $1/r$ Coulomb interaction. In this regime monopoles are *deconfined* and spin ice behaves as an effective Coulomb gas.

The equilibrium phases of this ionic gas model explains nicely the first order phase transition observed in spin ice compounds in the presence of an external magnetic field $H_{[111]}$ in the [111] direction. As already mentioned, applying such a field selects a single configuration of the spins along the [111] direction. At $H_{[111]} = H_c$ the system undergoes a first order phase transition between the Kagome ice phase (at $H_{[111]} < H_c$) and the ordered phase (at $H_{[111]} > H_c$) made by $3\ in - 1\ out$ (or $1\ in - 3\ out$) vertices. In the magnetic monopoles language, this transition corresponds to a liquid-gas transition where the magnetic field plays the role of the chemical potential and the magnetisation plays the role of the density of monopoles. This transition terminates in a critical point like the liquid-gas transition. The dumbbell picture gives a very useful understanding of the low temperature behaviour of spin ice (when a small density of monopoles is present). Moreover, several recent experiments have given support to this picture [244, 132, 198, 44, 105].

Magnetic monopoles are predicted by Grand Unified Theories tempting to describe electroweak interactions and strong nuclear forces by a single unified quantum field theory [255, 219]. Despite the efforts to reveal their existence, no magnetic monopoles have been observed yet (the reader will find a recent review on the subject in [185]). The closest realisation of magnetic charges might be in spin-ice materials.

A Dirac string is a line of singularities of the vector potential linking two oppositely charged magnetic monopoles. The choice of this branch cut is arbitrary and cannot therefore be measurable. In spin ice, a string can be defined by identifying the reversed spins in relation to some initial

configuration verifying the ice rules. By forcing the system to be in a polarised initial configuration aligned with a strong [001] field, strings of reversed moments can be observed by magnetic neutron scattering [198]. When the field is turned off spin flips create pairs of monopoles connected by Dirac-like strings. The neutron scattering data is well reproduced if one considers strings as $2D$ random walks $\eta(x, y, t)$ in the $(x, y) \equiv (001)$ plane where the third [001] direction acts like time.

A few years ago, Bramwell, Giblin and collaborators applied the theory of electrolytes to the study of spin-ice materials [44, 105]. They realised transport measurements by applying small magnetic fields to the spin ice material $Dy_2Ti_2O_7$. They addressed for the first time "the question of whether such magnetic charges and their associated-'magnetricity'-can be measured directly in experiment" (quoted from [44]). Onsager's theory of electrolytes [209] describes transport properties of ionic systems in the presence of a small electric field E. It gives the dissociation constant of the ions $K(E)$ perturbatively in $b \propto e^3 E/(k_B T)^2$. The elementary charge e can then be determined by measuring the conductivity of the material. Bramwell and collaborators applied these ideas to spin-ice to measure the charge of a single magnetic monopole Q. This was done by measuring the demagnetisation on the samples with muon spin rotation. The experimental value turns out to be in agreement with the dumbbell model in the range of temperatures $0.3 < T < 0.07$K where the Onsager's arguments are justified. Quasi-stationary currents of magnetic monopoles have been measured recently and show the 'symmetry' between electrolytes and 'magnetolytes' made by oppositely charged magnetic charges [105]. Therefore, the description of spin ice in terms of magnetic monopoles is specially well suited for the investigation of transport and dynamical phenomena. An exceptional increase of the magnetic relaxation times at low temperatures has been observed in $Dy_2Ti_2O_7$ [244]. A phenomenological Arrenhuis argument based on the presence of thermally activated monopoles reproduces this behaviour [132].

The emergence of magnetic monopoles in spin-ice has attracted a great deal of attention since it is the first example of $3D$ *fractionalisation* in condensed matter. This phenomenon gives its name to its most mentioned and studied example where fractionalisation plays a central role: the fractional quantum Hall effect. In these systems the excitations are non integer parts of the constituents of the systems, here electrons, and carry a fraction of the elementary charge e. In spin-ice thermal fluctuations breaking the ice rule give rise to fractional excitations, magnetic monopoles. Classical spins can be though of as an ordinary dipole made by two opposite charges at its extremities. Magnetic monopoles are then 'one half' of a spin, the 'real' constituent of the system.
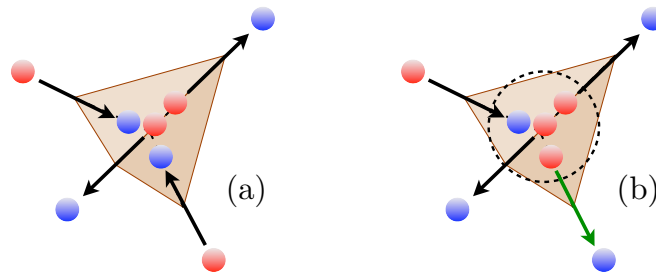
Figure II.12: **The dumbbell picture**. Each magnetic moment is replaced by a negative (blue) and a positive (red) magnetic charge. (a) The ice rules are obeyed and the tetrahedron is neutral. (b) After flipping a spin (green) we break the ice rule and create a pair of oppositely charged monopoles. The positive monopole is represented by the dotted circle at the center of the tetrahedron.

II.3   Artificial spin-ice samples

For many decades, condensed matter systems have been, and still are, built by combining different chemical compounds. Thanks to the expertise of chemists and material scientists, the interacting constituents of condensed matter systems can be manipulated. Then materials can be designed in order to fulfil the requirements that are expected to lead to some interesting behaviour. A large variety of collective phenomena such as the above mentioned zero point entropy in rare-earth pyrochlores has been discovered in such a way.

Frustration can be responsible for a large degeneracy of the ground state, associated with long range correlations and the presence of dynamical obstructions which can give rise to glassy physics [229, 65]. The study of thermal excitations and defects are then crucial for the understanding of frustrated systems. Local probes are needed to characterise these objects, which is clearly a difficult task to achieve in real materials. A way to solve this problem is to manufacture a frustrated system which allows the direct observation of a single constituent. This can be achieved in nano-arrays of ferromagnetic islands and, as briefly presented at the end of the following section, in colloidal systems. Using well established tools from nanotechnology, it has become possible to control magnetic degrees of freedom in a very precise way. The lattice geometry and the interaction strength between constituents become adjustable parameters and the magnetic configurations can be imaged directly by different microscopic techniques such as MFM (magnetic force microscopy) [264, 207, 206, 197] and PEEM (photoemission electron microscopy) [177, 178]. This allows the 'artificial' realisation of microscopic models of frustration with the possibility of reading directly its micro-states. In particular, two-dimensional analogues of pyrochlore spin-ices can now be produced in the laboratory. These *'artificial spin-ice'* (ASI) systems constitute an ideal playground to investigate the excitations and the local dynamics of highly frustrated systems and $2D$ vertex-models in particular.

II.3.1   Experimental set-up

In 2006, using electron beam lithography, Wang, Nisoli and collaborators [264] constructed an artificial analog of spin-ice on a $2D$ square lattice made by elongated ferromagnetic (made by permalloy) islands. Each island carries an intrinsic single-domain magnetic moment collinear to its long axis. In this set up, the size of the islands is fixed to $80 \times 220 \times 25$ nm^3 in such a way that the moment of each island is $\mu \sim 10^7$ Bohr magnetons. The strong shape anisotropy and the large magnetic moment carried by the islands makes them behave as classical Ising spins. The arrays are made by $\sim 10^4$ islands separated by a lattice parameter r_0 ranging from 320 nm to 880 nm. Therefore, the energy barrier to flip a spin is too high to be overcome by thermal fluctuations (typically equivalent to temperatures $\sim 10^4 - 10^5$ K). The system is then a-thermal and fundamentally out-of-equilibrium, which in some sense reminds a usual situation in the context of granular matter [174]. With this approach individual islands can be directly visualised by MFM or PEEM as shown in Fig II.13. The size and the shape of the nano-arrays just described are rather typical and do not differ significantly between different realisations [4].

In order to understand the similarities between these artificial square ices , real spin-ice materials and general vertex models, it is convenient to focus on the vertices where four islands meet. Since each island is modelled as an Ising spin, there are $2^4 = 16$ possible vertex configurations shown in Fig II.13. In the artificial spin-ice literature, the vertices are divided into four categories I-IV of increasing interaction energy. In order to make the link with the theory of integrable vertex models, we also show in Fig II.13 a different classification for the vertices divided into five

---

4. In Morgan et al. 's [197] the permalloy islands are $85 \times 280 \times 26$ nm^3 and a lattice spacing $r_0 = 400$ nm. In Mengotti et al. 's [178] the permalloy islands are $160 \times 470 \times 20$ nm^3 and a lattice spacing $r_0 = 500$ nm.
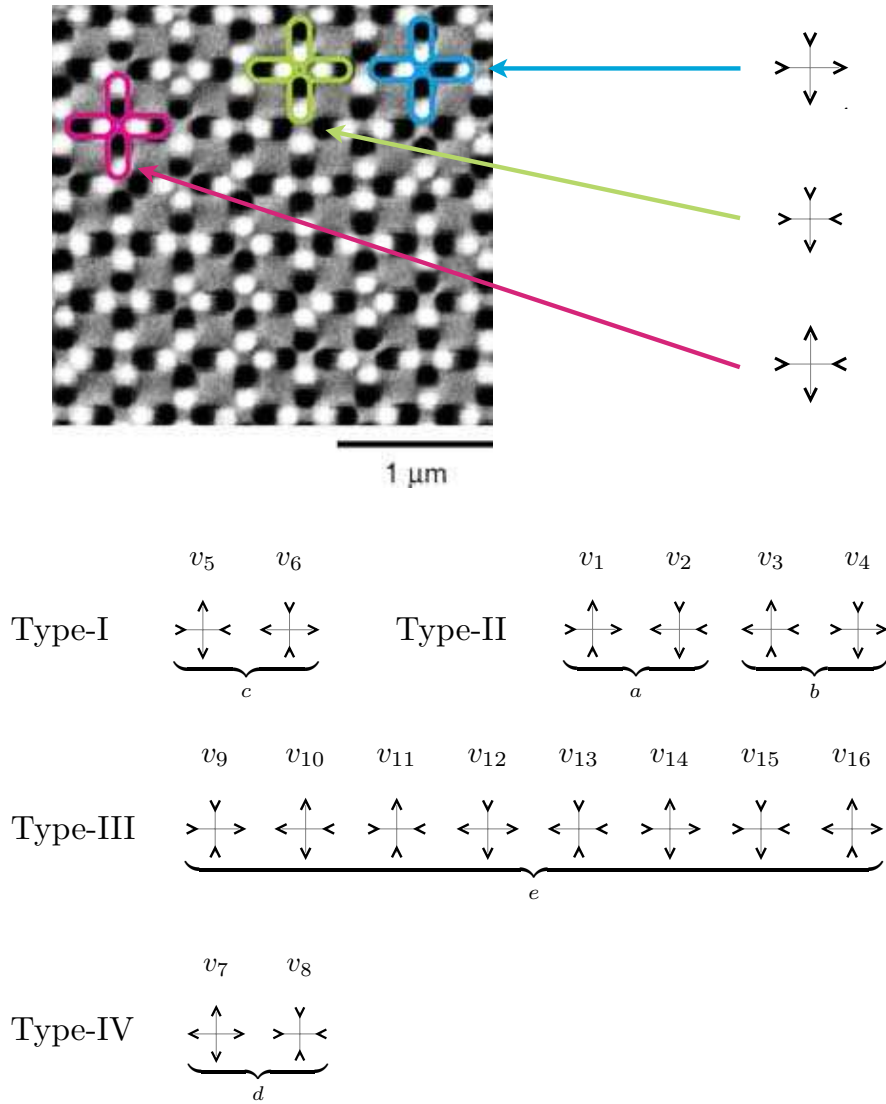
Figure II.13: Top: MFM image from Wang et al.'s realisation of artificial spin ice in the square lattice [264]. Each island in the lattice carries a single magnetic moment. Black and white dots correspond to its positive and negative poles. The color lines indicate a vertex of type I (pink), II (blue) and III (green). Vertices of type IV are extremely rare and are not shown in this picture. Bottom: The sixteen possible vertex configurations. Ferromagnetic islands are represented by an arrow. The configurations are labeled I,II,III and IV in the artificial spin-ice literature. The corresponding Boltzmann weights of each configuration a, b, c, d and e are also shown.

categories labeled by its Boltzmann weights a, b, c, d and e. In artificial square ice samples $a = b$, such that the vertices are indeed divided into four different types with different energy. Although it has not been realised yet, it should be possible to construct artificial samples such that $a \neq b$ by introducing a height offset between islands pointing in different directions [190]. This will become clearer after the following discussion.

In these samples, the interactions between magnetic islands are dipolar, hence described by

the Hamiltonian

$$H = Dr_0^3 \sum_{i<j\in\mathcal{P}} \left(\frac{\mathbf{S}_i.\mathbf{S}_j}{||\vec{r}_{ij}||^3} - 3\frac{(\mathbf{S}_i.\vec{r}_{ij})\,(\mathbf{S}_j.\vec{r}_{ij})}{||\vec{r}_{ij}||^5} \right) \tag{II.19}$$

where $\vec{S}_i = S_i\vec{z}_i$ are Ising spins, i.e. $S_i = \pm 1$, along the orthogonal principal axes of the lattice $\langle 1, 0 \rangle$ and $\langle 0, 1 \rangle$ of the island located at $\vec{r}_i$. The vector $\vec{r}_{ij} = \vec{r}_i - \vec{r}_j$ denotes the spacing between moments, r_0 is the lattice constant and D the dipole strength proportional to the intrinsic moment μ_0 of the islands. Note that this Hamiltonian becomes identical to the $3D$ dipolar spin-ice Hamiltonian (II.12) by removing the exchange term and replacing the sum over the pyrochlore lattice by a sum over the square lattice. Therefore, dipoles in artificial spin ice are $3D$ objects embedded in a $2D$ lattice. We will show the importance of this remark when discussing the nature of the excitations (magnetic monopoles) in the coming section. Following the same strategy we used to deduce a short range antiferromagnetic Hamiltonian for pyrochlore spin-ice, we consider the variables $\sigma_i = \pm 1$ depending on whether the magnetic dipole points inwards or outwards a given vertex. The Hamiltonian (II.19) gives an effective antiferromagnetic (AF) interaction between the variables σ_i sharing a vertex. We note the nearest-neighbour and the next-nearest-neighbour contribution J_1 and J_2 respectively with $J_1, J_2 > 0$.

A prior goal of these systems is to reproduce the ice-rules and mimic the prototypical example of geometrical frustration, i.e. the ice model. However, contrarily to its $3D$ counterpart, the ground state of these artificial arrays is not the ice-rule manifold. The six bonds around a vertex are not equivalent since the distances between spins adjacent to the same vertex are not equal: orthogonal spins sharing a vertex are at a distance $r_0/\sqrt{2}$ whereas collinear ones are separated by r_0. The typical AF nearest-neighbour interaction strength J_1 between orthogonal spins is larger than the next-to-nearest-neighbour one J_2 (see Fig. II.15). The six vertices verifying the ice rules split into two different categories. Among them, c-vertices (or type-I) are energetically favoured. The energy of each vertex in terms of these two inequivalent bonds J_1 and J_2 is shown in Fig. II.14.
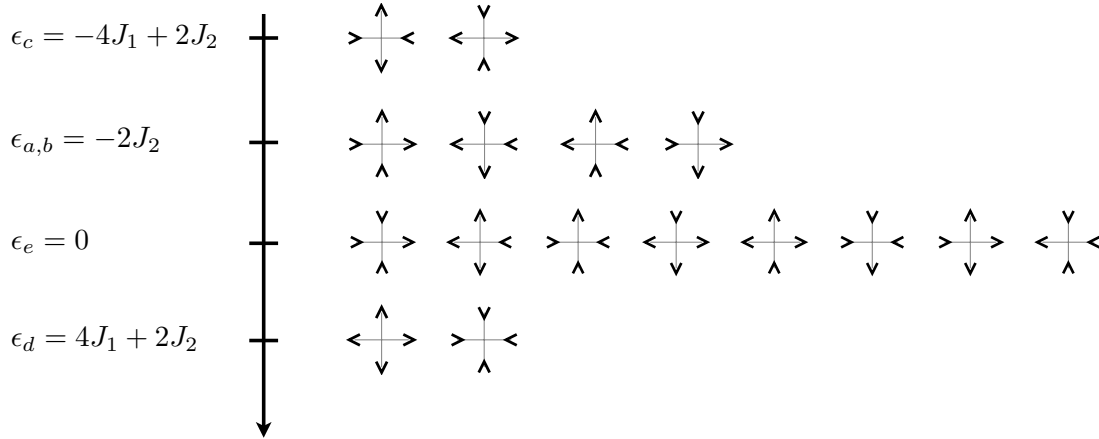
Figure II.14: The sixteen possible vertex configurations classified by their energy in terms of the first and second-neigbour interaction strength.

Although c-vertices are favoured, all the bonds around a vertex cannot be simultaneously satisfied and the system is 'weakly' frustrated. From Fig. II.14, it is clear that the degree of frustration depends on the ratio J_2/J_1. All the vertices verifying the ice-rule are degenerate when $J_1 = J_2$. Based on this observation, Möller and Moessner proposed a slight modification of the experimental set up to restore the ice-rules degeneracy [190]. One can fix the horizontal islands on

a square array which is slightly above the array of vertical islands. By including a height difference h between the layers where the horizontal and vertical spins lie, we change the original distance between the spins around a vertex. Therefore, the ratio J_2/J_1 can be tuned and set equal to one by choosing the appropriate height offset denoted h_c [5]. Then the interaction parameters can be controlled by the lattice constant r_0, the length of the ferromagnetic islands l and the height shift between layers h.
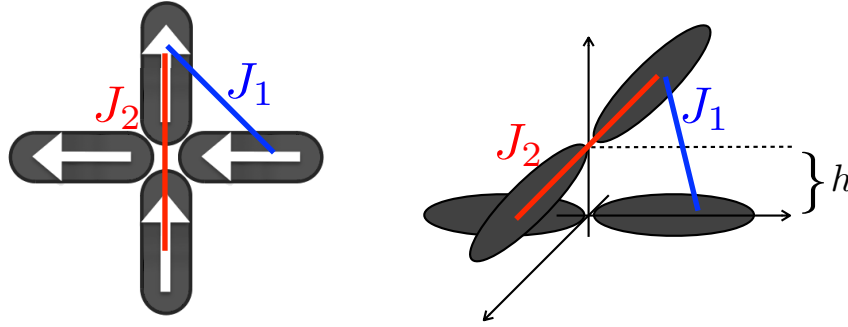
Figure II.15: Interactions between spins around a vertex. Left: In the original set-up with no height shift ($h = 0$) $J_1 > J_2$. Right: The relative strength of J_1 and J_2 is modified by the height shift. The ice-rules degeneracy can be recovered by a suitable choice of h.

The possibility to tune the vertex weights by introducing this extra control parameter h makes this set-up very appealing. However, the experimental realisation becomes rather involved and, as far as we know, it has not been achieved yet. Another possible route to investigate the physics related with an ice-rule like constrained ground state is to manufacture a different artificial geometry, the so-called *artificial Kagome spin-ice* [177, 178, 154]. Similarly to artificial square ice, these samples are made by elongated ferromagnetic islands in an hexagonal lattice [6] as shown in Fig. II.16. In this geometry the interactions between the three moments around a vertex are equivalent. There are only two type of energetically different vertices among the $2^3 = 8$ possible configurations. In this lattice a modified ice-rule defines the ground state: all the configurations with two spins pointing in and one out (or the opposite) are degenerate.

Recent experiments realised in colloidal systems offer an alternative approach to realise artificial frustrated materials [111]. Numerical simulations with Brownian dynamics have shown that artificial spin ice can be realised with charged colloids on a square and hexagonal lattice of optical traps [162, 227] . A vertex consist of four orthogonal traps meeting in a point (see Fig. II.17) The repulsive Coulomb interactions of the colloids trapped in a double-well favour vertices with four arrows pointing out of it, but this local minimisation of the energy cannot be satisfied by its neighbouring vertex. The collective arrangement of colloids should be considered. The ice rules can arise as a collective effect and the vertex weights can be tuned by the charge of the colloids, the lattice spacing and the screening length.

II.3.2 Monopoles and strings

In the dumbbell picture, thermal excitations breaking the ice rules are associated with effective magnetic monopoles in $3D$ dipolar spin-ice. Similarly, in $2D$ spin ice in the square lattice, flipping

---

5. In Wang's el al. realisation $l/r_0 \approx 0.7$ giving $h_c/r_0 \approx 0.2$ [190].

6. The Kagome lattice is the medial graph of the hexagonal lattice: the ferromagnetic islands sit on the sites of the Kagome lattice which are identical to the mid points of the edges of the hexagonal lattice.
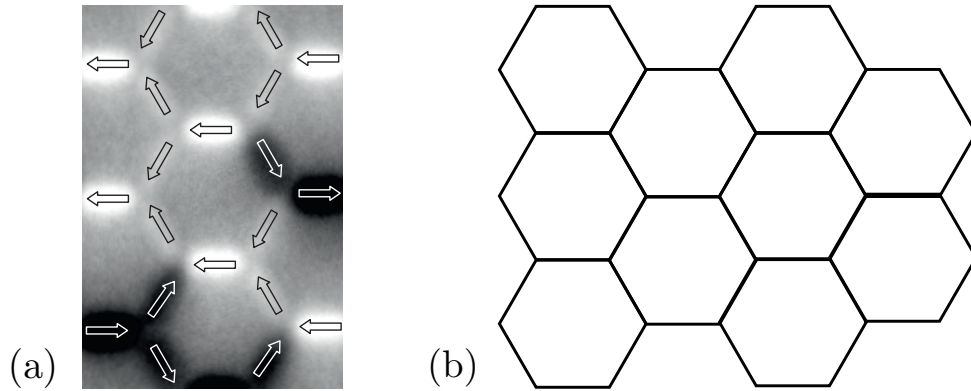
Figure II.16: **Artificial Kagome ice** (a) X-ray magnetic circular dichroism (XMCD) images of the lithographic array of permalloy islands (from [178]). The contrast associated with each island in the hexagonal lattice indicates that they analog to the Ising spins represented by the white arrows. The colour in the image is a measure of the orientation of the spin. (b) The hexagonal lattice.
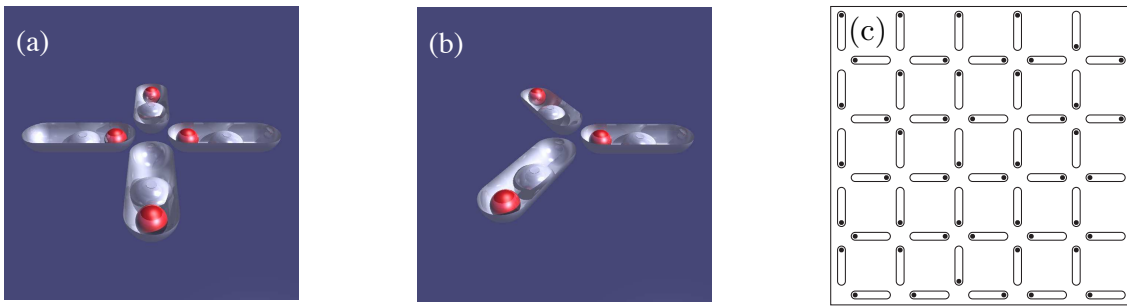
Figure II.17: Artificial spin ice made by charged colloidal particles confined in a double well potential (from [227]). (a) One among the six possible vertices occurring in the square lattice verifying the ice rules. (b) One among the eight vertices occurring in artificial Kagome ice. The ice rules here corresponds to two particles close to the vertex and one further, or the opposite. (c) Artificial square ice ground state.

a single spin in an ice-rule configuration leads to the creation of a pair of *defects* with a non-zero opposite charge in adjacent sites (see Fig II.18). As for its $3D$ counterpart, the charge of a vertex is defined by

$$q_v = \frac{1}{2} \sum_{i \in v} \sigma_i \ \in \ \{0, \pm 1, \pm 2\}. \qquad (II.20)$$

where the sum runs over the four spins sharing a vertex v in the square lattice. Defects are divided into two categories depending on the absolute value of their charge: d-vertices (Type-IV) carrying a double charge $q_d = \pm 2$ and e-vertices (Type-III) with a single charge $q_e = \pm 1$. In artificial spin ice, and spin ice-like systems in general, vertices breaking the ice rule are much more energetic than the six 2-in–2-out ones (hence called defects).

Interactions between defects in $2D$ are not simply given by a $1/r$ Coulomb interaction by extension of what happens in $3D$ pyrochlores. This comes from the fact that not all the configurations verifying the ice-rules are equivalent in the square lattice as dictated by the Hamiltonian II.19. Although as in $3D$ defects can be separated without creating any extra defects, they can create ex-

citations verifying the ice-rules, i.e. a- and b-vertices. Besides the $1/r$ Coulomb energy coming from the dipolar interactions, the strings carry a tension associated with the creation of a- and b-vertices. Numerical simulations of the dipolar model in the square lattice have shown evidences for a string tension proportional to its length X [189]. In this work, the energy computed for different configurations seems consistent with an interaction between defects of the form

$$V(r) = -\frac{Q}{r} + \kappa X(r) + C \tag{II.21}$$

where r is given in units of the lattice spacing, $\kappa > 0$ is the effective strain of the string and Q and C are adjustable parameters[7]. The interaction between monopoles has been evaluated numerically at zero temperature by computing the energy of different configurations with two defects at a given distance attached by a string of spins with a given shape. The energy cost of a pair of defects is given by the sum of a $3D$ Coulomb interaction and a potential $\kappa X(r)$ which diverges with the length of a string and the monopoles remain confined. Magnetic monopoles in $2D$ artificial spin ice are '$3D$ objects' embedded in a lattice. It is a particularity of dipolar interactions in $3D$ spin ice that both electrostatic and entropic interactions are $1/r$.
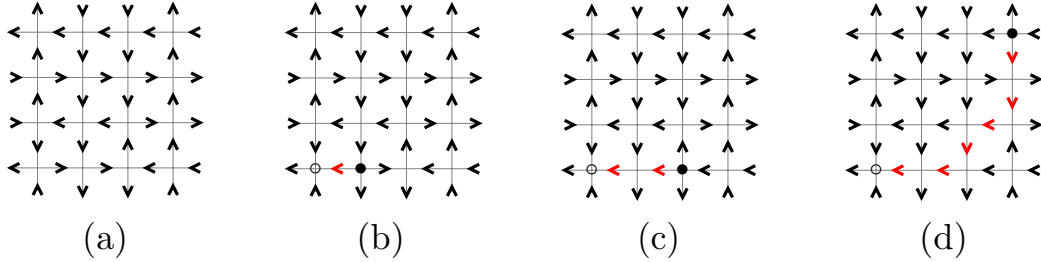
Figure II.18: (a) Initial configuration verifying the ice-rules. (b) Creation of two oppositely charged defects (open and black circles) by flipping the spin shown in red. (c) Displacement of the positively charged defect by flipping one among its three outgoing spins. (d) Configuration after six spin-flips without creation of an extra defect. The positively charged defect has moved apart leaving behind a string of red spins.

So far, we have only considered artificial spin ice at zero temperature. At finite temperature, effective entropic $2D$ Coulomb interactions $\propto T \ln r$ must be added to the previous potential. The free energy of the system made by two monopoles distant of r is $F(r) = V(r) - TS(r)$. The energy is given by eq. II.21 and the entropy associated to the number of ways of connecting two monopoles by a string of length X is approximated by

$$S(r) \approx k_B \ln\left(3^{X(r)}\right) . \tag{II.22}$$

This result is obtained by considering the strings as self-avoiding random walks in the $2D$ square lattice. Then, the string's contribution to the free energy $F_s(r) = \kappa X(r) - k_B T \ln(3) X(r)$ includes a confining term $\propto k_B T X(r)$. At high temperatures the configurational entropy of the string makes the string tension vanish, and at low temperatures the entropic interaction between monopoles confines them. Making use of an argument *à la* Kosterlitz-Thouless [149], one would expect a transition to occur at $k_B T_c = \kappa / \ln(3)$. Although the above 'heuristic' argument is appealing, it only considers the free energy cost of an isolated string and do not take into account

---

7. The value of Q extracted from the fitting of the numerical data should be compared with $\frac{\mu_0 \mu^2}{4\pi} q^2$ and C should be associated with an 'ionization' energy of a pair of defects.

the effective interactions between defects, neither the energy associated with a single defect. It is however not clear whether there is a *deconfinement transition* in artificial spin ice coming from the competition between these effects. A more careful analysis is needed to describe the situation at high enough temperatures, when the string losses its tension. A non negligible density of defects will then populate the system and intersections between strings make the definition of X ambiguous. Subtle many-body effects as self-screening can take place in the system.

A modified artificial square ice system with a height shift h can remove the inconveniences caused by the emergence of the string tension [190, 191]. If h is chosen in such a way that the ice rule degeneracy is restored, the strings carry no tension and the interaction energy between defects would be simply given by a $3D$ Coulomb potential.

A statistical approach has been used by Silva et al. in order to link oppositely charged defects and define an effective string length [242]. In this approach, the strings are defined by identifying, among all the possible ways to link n positive charges to n negative charges, the one which minimises the total distances between them. The average distance between defects is maximum at a given temperature T_d where the specific heat exhibits a logarithmic divergence. It has been argued that this temperature corresponds to a transition temperature between a confined and a deconfined phase of magnetic monopoles in artificial spin ice.

Recently, Morgan and co-workers have identified and classified defects and string excitations in artificial spin ice on square arrays of elongated ferromagnetic islands [197]. They have observed that the excitations should be classified by the number of a- and b-vertices and the number of defects involved. More recently, magnetic monopoles motion with the proliferation of attached strings have been visualized in artificial square ice by microscopy [218]. Similarly to what was done for $3D$ spin ices, the samples were initially prepared in a polarized configuration by applying a strong magnetic field in the [11] direction, then switched to the opposite orientation. Strings of flipped spins are then identified from their background with the corresponding motion of monopoles induced by the field reversal.

Most of the work in artificial spin-ices focus on the square and hexagonal arrangements. The interest on the square geometry finds its roots in the physics of spin-ice and $2D$ vertex models. In the honeycomb lattice, also known as artificial Kagome ice, the zero divergence constraint cannot be satisfied. Instead, the minimisation of the local charge on each site yields to a modified ice rule: on each vertex two arrows point in and one out, or the opposite (see Fig. II.16). The Kagome lattice is then highly frustrated and has two main advantages over the square geometry: (i) all the bonds around a vertex are equivalent; (ii) defects dynamics are induced naturally by the presence of an external field since all the vertices carry a non negative charge $q = \sum_{i \in v} \sigma_i = \pm 1, \pm 3$ [176]. Kagome artificial spin ice verifying the ice rule degeneracy has been realised by lithographic techniques [177, 223, 153, 178, 70]. Although an ordered GS is expected to occur in dipolar Kagome spin ice [175], none experiment has been able to accesses it.

Strings associated with the motion of defects, i.e. vertices with $q = \pm 3$, have been directly observed by PEEM in these systems [153, 178]. This has been done by preparing the samples in a polarised state align with an external magnetic field H. Then the field is reversed, creating strings of spins in a background of opposite orientation. Below a certain critical field H_c the defects are free to move. Instead, they become trapped for higher fields. The orientation and strength of an external magnetic field applied to these samples alters considerably the configuration and the dynamics of the system. The possibility to control defects' motion and manipulate states in Kagome spin ice motivates its study for potential applications in spintronics and computer science.

II.3.3   Ordering protocols

Artificial spin ices built by nano-lithography are a-thermal. A usual method one would like to apply is to thermally anneal the system to its ground state by heating and cooling the material. This, however, is not possible in spin ice since the energy barriers involved are of the order of 10^4-10^5K (the system would melt during the procedure). We discuss in the following lines the alternative protocols which have been proposed to overcome this difficulty.

II.3.3.1   External drive

Several works have reported the use of time-varying external fields to order artificial spin ice samples [264, 177, 223, 139, 230]. The expected ground state in artificial spin ice is non magnetized. A way to demagnetise the system is to rotate the sample in a time-dependent magnetic field, a method which was already used in nano-technology [123]. The sample rotates at a frequency of $2\pi/\Delta t$ while the magnetic field $H(t)$ decreases by a step H_s after each period Δt. In Wang et al.' s realisation the magnetic field also changes its polarity at each step, i.e. $H(n\Delta t) = (-1)^n (H_o - nH_s)$. The initial value of the magnetic field H_o should be chosen much larger than the coercive field of the ferromagnetic islands. Then, vertex populations are measured after the demagnetisation protocol, when $H(t_{final}) = 0$ and the islands are in a frozen configuration. As we will show in the next section, an effective statistical ensemble describing the outcomes of this demagnetisation procedure can be constructed [207, 206] (see Section II.3.4). Indeed, the demagnetisation protocol described above will lower energy states but does not reach the staggered ground state of the system [206].

II.3.3.2   Material selection

In order to achieve thermal ordering, an alternative approach is to reduce the energy barriers between different configurations. One can select a material to build the nano-islands in such a way that the energy cost for a single spin flip is reduced enough to allow thermal activation. This can be achieved by using a material with lower Curie temperature [136]. The selected material is made of δ-doped Pd(Fe) thin films instead of permalloy. It has the important advantage that the Curie temperature and the magnetisation can be tuned by the thickness of the Fe layer. The energy barrier to reverse the magnetisation of an island is now strongly temperature dependent [8]. Thermal fluctuations in the sample become relevant if not too small compared with the Curie temperature of the islands. The equilibrium thermodynamics of artificial spin ice can then be investigated. By increasing the temperature from a magnetised state, the samples loose their magnetisation. The mechanisms taking place in this realisation and leading to such ordering are, however, difficult to analyse. One should be able to 'decouple' what comes from the artificial spin ice problem and can give us some insights on spin ice like systems, and what comes from the internal behaviour of the islands.

II.3.3.3   Thermal annealing during fabrication

Two years ago, Jason P. Morgan and colleagues reported for the first time the role of real thermodynamics in artificial spin ice [197]. In this experiment, spin configurations are visualised at the

---

8. The energy barrier to flip the magnetisation of the island depends on temperature in Wang et al.'s realisation as well. However, the magnetisation of the permalloy islands is not very sensitive to temperature changes in this range and can be considered constant.

end of a sample preparation process in which the thickness of the magnetic islands grows by deposition onto pre-patterned substrates. During a limited time, the permalloy islands are small enough to reverse they magnetic moment by thermal fluctuations during the growth process. However, as the time scales for these moves increase with the growing size of the islands, once a certain thickness is reached the flipping times become too large and the effective spins *freeze*. Therefore, the blocked configurations are reached by thermal annealing. Using this different approach they find large domains of staggered order regions containing c-vertices only (see Fig. II.19). This allowed the visualisation of artificial spin ice very close to its ground state. Frozen thermal excitations as domain walls and charged defects can be visualised after the growing process. No information about the actual thermal dynamics occurring during the annealing is available, only the frozen states at the end of the experiment can be analysed. These authors also measured the frequency of occurrence for a large number of local excitations and they find that they can be reproduced by a Boltzmann distribution.
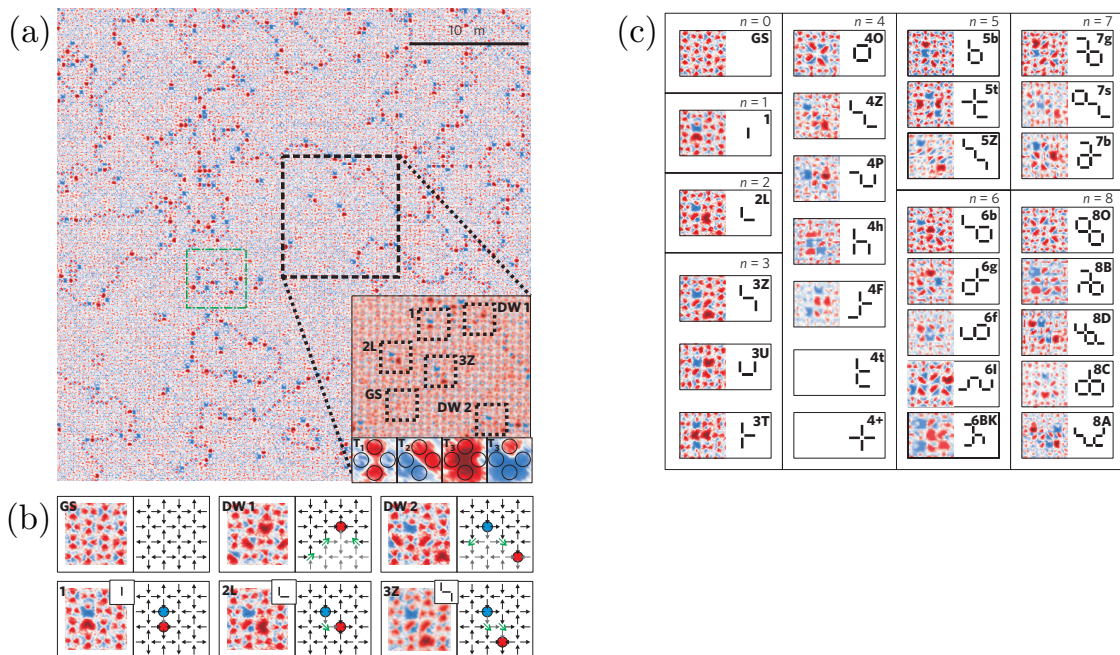
Figure II.19: Extacted from Morgan et al. 's publication [197]. (a) MFM Image of a frozen configuration displaying large domains of ground-state order. The domains are separated by domain walls made by a- and b-vertices. Localised excitations are shown in the inset. (b) Different arrangements of islands with their corresponding vertex configuration. The flipped spins are shown in grey. (c) Visualisation of different local excitations. A mnemonic labelling based on the shape and size of the excitations has been introduced.

II.3.4   Statistical mechanics of a-thermal systems

The methods of statistical mechanics to study a large number of 'individuals' differ fundamentally if these individuals are *microscopic* or *macroscopic*. By microscopic individuals we mean physical degrees of freedom which are subject to thermal noise (e.g.: particles, spins, etc.). Systems of this kind are the object of classical equilibrium statistical physics and thermodynamics. On the contrary, by macroscopic individuals we mean physical bodies which are large enough to avoid thermal fluctuations and hence canonical equilibration (e.g.: grains, ferromagnetic nano-

islands, etc.). Artificial spin ice on arrays of elongated ferromagnetic nano-islands fall in the category of a-thermal systems. Following Edwards' ideas [87, 88], a micro-canonical ensemble can be constructed for such systems under some assumptions. These notions can then be applied to the artificial spin ice problem.

II.3.4.1 Edward's measure in granular matter

The fundamental quantity that makes the connection between the statistical micro-canonical ensemble and thermodynamics is the entropy S. In order to give a thermodynamic meaning to an a-thermal system one should first of all define its entropy. For convenience we focus here on granular materials [174, 127] for which this approach was first introduced to then move our attention to artificial spin ice.

In order to allow a statistical description, the number N of individuals in the system must me large. The fundamental postulate of statistical mechanics asserts that all the accessible configurations of an isolated system in a volume V and energy E have equal probability. The set of micro-states with given E, V and N (called external parameters) constitute the *micro-canonical ensemble* [119]. This implies a uniform probability in the ensemble:

$$P(\mu) = \begin{cases} \Omega(E,V,N)^{-1} & \text{if } E \leq H(\mu) \leq E + \Delta E \\ 0 & \text{otherwise} \end{cases} \tag{II.23}$$

where μ denotes a micro-state of the system and $\Omega(E,V,N)$ the volume of the phase space occupied by the micro-canonical ensemble: $\Omega(E,V,N) = \sum_\mu \delta_{E,H(\mu)}$, i.e. the number of states with an energy between E and $E + \Delta E$ (with $\Delta E \ll E$). The entropy S and temperature T are defined by

$$S(E,V,N) = k_B \ln \Omega(E,V,N), \quad \frac{1}{T} = \frac{\partial S(E,V,N)}{\partial E}. \tag{II.24}$$

The construction of a statistical ensemble can be viewed as an optimisation problem under some constraints. The microcanonical distribution can be derived by maximising the entropy $S = -k_B \sum_\mu P(\mu) \ln P(\mu)$ under the constraint $\sum_\mu P(\mu) = 1$. We present this method for the construction of the *canonical ensemble* with a Botzmann-Gibbs measure. Consider a Lagrange multiplier λ_1 associated to the constraint $\sum_\mu P^c(\mu)H(\mu) = E$ and a second one λ_2 associated to the normalisation of the probability distribution $\sum_\mu P^c(\mu) = 1$. Then we should extremise the entropy $S = -k_B \sum_\mu P^c(\mu) \ln P^c(\mu)$ under these constraints, i.e. we need to solve

$$\frac{\delta}{\delta P^c(\mu)} \left(S[\{P^c(\mu)\}] - \lambda_1[\sum_\mu P^c(\mu)H(\mu) - E] - \lambda_2[\sum_\mu P^c(\mu) - 1] \right) = 0, \tag{II.25}$$

which leads to

$$P^c(\mu) = e^{-1-\frac{\lambda_2}{k_B}} e^{-\frac{\lambda_1}{k_B}H(\mu)}, \ \forall \mu. \tag{II.26}$$

Then we impose the normalization of $P^c(\mu)$ and we define $Z = \sum_\mu e^{-\frac{\lambda_1}{k_B}H(\mu)}$ to obtain the canonical distribution

$$P^c(\mu) = \frac{e^{-H(\mu)/k_B T}}{Z} \tag{II.27}$$

where we have identified $T = \lambda_1^{-1}$. Note that this is consistent with the previous definition of the temperature since $\lambda_1 = \partial S/\partial E$. The second Lagrange multiplier is associated with $Z = \exp(1 + \lambda_2/k_B)$. The same method will be applied to construct an effective temperature for artificial spin ice samples.

In granular matter, the energy does not characterize configurations with different macroscopic arrangements and the temperature can be ignored (effectively $T = 0$). The volume though depends on the configuration and suggests that it is the relevant variable to describe granular matter. The starting point to construct a statistical mechanics description is the fundamental postulate: all the blocked configurations with the same number of grains formed by manipulations which do not act on individual grains (shearing, shaking, compressing, etc.) and occupying the same volume V are equally probable. An important assumption has been done here: we consider that an enormous number of configurations are available to the grains and that the system is ergodic. Under this assumptions the probability density is

$$P(\mu) = \begin{cases} \Omega(V, N)^{-1} & \text{if } V \leq W(\mu) \leq V + \Delta V \\ 0 & \text{otherwise} \end{cases} \tag{II.28}$$

We have introduced a function W which gives the occupied volume of a given configuration. The log of $\Omega(V, N)$ gives the 'Edwards's entropy' S_E of grain configurations with given volume and satisfying stability conditions. The configurational entropy is sometimes called 'complexity' in the context of glassy systems. For a recent review on the subjects I refer the reader to [62] and [31]. From this central quantity an effective thermodynamics can be constructed.

The volume plays here the same role as the energy for a thermal system where the function W is analog to the Hamiltonian H. We should also introduce an 'indicating' function Q which is equal to one or zero weather the configuration is stable or not. The function Q imposes an extra condition in the phase space volume of this Edwards' micro-canonical ensemble. In this construction, a mechanically stable configuration of macroscopic objects is the analog of a micro-state in usual thermal statistical mechanics. We introduce the new variable X defined by

$$\frac{1}{X} = \frac{\partial S_E(V, N)}{\partial V}. \tag{II.29}$$

X is the analog of the temperature and it is called 'compactivity'. For $X = 0$ the system is 'compact' (analog to a frozen state at $T = 0$) and for $X \to \infty$ the system is 'loose' (analog to a random state at $T \to \infty$). It measures the ability of the system to be more or less 'compact' in a way analog of what temperature measures in terms of energy. As the temperature, the variable X controls the equilibrium between different subsystems. We can also introduce the thermodynamic potential $Y(X, N) = V - X S_E(V, N)$, the analog of the free energy $F(T, V, N)$ in statistical mechanics which extends this construction into the canonical ensemble. In order to study the packing and the effective thermodynamics of grains one has to start by defining the W and Q of the model, as one usually does in statistical mechanics via the Hamiltonian of the system. Note that, in the previous discussion we considered two external parameters V and N and we derived an analog of the temperature in terms of entropic variation with V. We can pursue the same strategy and define a 'configurational' temperature T_E defined by the derivative of the Edward's entropy as a function of the energy. Depending on the system we are dealing with, one can define 'two different temperatures', X and T_E, the Lagrange multipliers associated with volume and energy conservation in the Edwards' ensemble. None of them is equivalent to the 'thermal' temperature T of the environment.

Edward's measure has become a systematic tool to study glassy dynamics. One has to decide which configurations are considered as being blocked and belonging to the Edwards's ensemble. In particular, it is quite natural to define blocked configurations in the context of kinetically constrained lattice models displaying glassy-like behaviour [229]. In has been shown that an Edwards' entropy can be defined in a systematic way for these systems and reproduces different dynamical observables in the aging regime of the Kob-Andersen model [18]. It has also been proposed to

extend Edwards's construction to general glassy systems in finite dimensions with thermal fluctuations [37].

Several studies have demonstrated the usefulness of Edwards' construction. An effective temperature can be extracted from violations of the fluctuation-dissipation theorem [77] in a granular system under compaction [72]. This dynamical effective temperature T_{eff} turns out to coincide with the Edwards' compactivity X. The introduction of a dynamical effective temperature is theoretically justified for mean-field models but beyond the situation is less clear. Similarly, numerical simulations on slowly sheared grains have extracted a dynamical effective temperature T_{eff} in agreement with the configurational temperature T_E [169]. It is however a very difficult task to sample the blocked configurations experimentally. It is far from being clear whether a perturbation or procedure is appropriate in order to generate configurations in the blocked manifold in an ergodic way.

II.3.4.2   Configurational temperature in artificial spin-ice

Edwards' ideas have recently been applied to artificial spin ice samples under a rotating magnetic field [207, 206]. Similarly to grains in granular materials, magnetic moments in artificial spin ice are frozen. There are mainly two experimental procedures to drive the system into a lower energy state: (i) by rotating the sample in a decreasing magnetic field [206]; (ii) by thermal annealing during the growth of the islands [197]. The first procedure is analog to shearing and shaking in granular matter language. The second procedure is somehow similar to compaction: if we identify a grain with a dipole the annealing procedure corresponds to start by a microscopic particle, subject to thermal fluctuations, and make it grow until it freezes.

In order to construct an Edwards' measure for artificial spin ice one should identify the blocked configurations of a given volume/energy and assume their are equiprobable. The micro-state of the samples can be directly visualise such that one can extract the number of vertices of each type. One needs an experimental control function, as an applied oscillatory field $H(\omega, H_s)$. Then one should assume that, once this function has been fixed, the 'ergodic' hypothesis of Edwards' construction is fulfilled. Meaning that all the possible blocked configurations of the system are generated by applying the demagnetisation protocol $H(\omega, H_s)$ in an equiprobable manner. Then the set of blocked configurations reached in this way can be described by a canonical ensemble with a configurational temperature T_E. This temperature would a priori depend on the control parameters H_s and ω. For a given choice of H_s and ω one can run the experiment, count the number of vertices, and extract T_E from eq. (II.40) and then plot how the temperature depends on the external drive (see Fig. II.20).

Nisoli and collaborators [264, 207, 206] used a vertex model to describe their samples. The interaction energy per vertex can be approximated by:

$$\varepsilon = \sum_{i=1}^{16} \epsilon_i n_i \tag{II.30}$$

where n_i is the density of vertices of type i (see Fig. II.13) and ϵ_i their corresponding energies. In this description, we are only considering the interactions occurring around a vertex, i.e. the nearest and next-nearest neighbour interactions. This model is an unconstrained sixteen-vertex model with

$$\epsilon_1 = \epsilon_2 = \epsilon_3 = \epsilon_4 = \epsilon_{a,b} = \epsilon_{II}$$
$$\epsilon_5 = \epsilon_6 = \epsilon_c = \epsilon_I$$
$$\epsilon_8 = \epsilon_9 = \epsilon_d = \epsilon_{IV}$$
$$\epsilon_9 = ... = \epsilon_{16} = \epsilon_e = \epsilon_{III} \tag{II.31}$$

We use the notations: $i = 1...16$ or $\alpha = I, II, III, IV$ to label the vertices according to Fig. II.13. The value of the vertex energies can be computed using the dumbbell picture introduced in section II.2.4 eq. (II.18) in the square lattice. If one considers the interactions between the charges around a vertex one gets: $\epsilon_c/\epsilon_e \approx 0.453$. One could also make a next-to-nearest neighbours approximation of the dipolar Hamiltonian (II.19). Meaning that only the spins around a vertex are considered and longer range interactions are neglected. This yields to $\epsilon_c/\epsilon_e \approx 0.692$.

Initially the samples are prepared in a completely polarised state made exclusively by a- or b-vertices. This can be achieved by applying a strong magnetic field in the [11] direction. In a background of one type of polarised vertices, lets say v_1, the rotating magnetic field will create all other kinds of vertices. The density of vertices different from v_1 is given by $\rho = D/N$ where D is the total number of vertices that are different from the initial one created during the protocol and N the total number of vertices in the sample. The density of vertices of type $i \neq 1$ relative to the density of non-polarised vertices created during this process is denoted ν_i and reads

$$\nu_i = \frac{n_i}{\rho} \tag{II.32}$$

for the vertex types which were absent in the initial configuration. For v_1 vertices we have

$$n_1 = 1 - \rho \tag{II.33}$$

which accounts for the density of vertices which remain identical after the demagnetisation protocol.

In order to compute a configurational entropy Nisoli and collaborators assumed that vertices are *independent*. Thus, the volume of the phase space $\Omega(\varepsilon, N)$ is simply the number of ways of choosing D objects among N divided into four categories $\alpha = I, II, III, IV$ (c, $a(b)$, e and d respectiveley), and within each category the objects are considered indistinguishable. Hence,

$$\Omega(\varepsilon, N) = \frac{1}{\prod_\alpha N_\alpha!} \frac{N!}{(N - D)!} \tag{II.34}$$

where, in order to make the link with the usual conventions,

$$N_I/N = n_5 + n_6 = n_I$$
$$N_{II}/N = n_1 + n_2 + n_3 + n_4 = n_{II}$$
$$N_{III}/N = n_9 + n_{10} + ... + n_{16} = n_{III}$$
$$N_{IV}/N = n_7 + n_8 = n_{IV}. \tag{II.35}$$

The configurational entropy is given by $S(\varepsilon, N) = k_B \ln \Omega(\varepsilon, N)$ which for N large enough it is well approximated by

$$\frac{S(\varepsilon, N)}{N k_B} = -\rho \sum_i \nu_i \ln \nu_i - (1 - \rho) \ln(1 - \rho) - \rho \ln \rho . \tag{II.36}$$

In order to define a configurational temperature we look for extremes of this function under the energy constraint

$$\varepsilon = \sum_i \epsilon_i n_i = \epsilon_{a,b} \equiv \text{ct} . \tag{II.37}$$

The energy ε can be measured after running the demagnetisation protocol from a completely polarised sample. The main experimental observation justifying the Edwards' construction is that this energy constraint is verified after a cycle [207], i.e. the external drive does not reduce the total energy (similarly to shearing and shaking grains in a fixed container conserves the volume). This

immediately implies that the ground state of the system cannot be reached using this procedure. The demagnetised field creates different type of vertices, some of them more or less energetic than a- and b-vertices, and experimentally the energetic contribution of the new vertices created during the demagnetization compensate each other.

We introduce the Lagrange multiplier λ associated to it. The optimisation equation reads

$$\delta\left(\rho\sum_i \nu_i \ln\nu_i - (1-\rho)\ln(1-\rho) - \rho\ln\rho - \lambda(\rho\sum_i \epsilon_i\nu_i - \varepsilon)\right) = 0. \qquad \text{(II.38)}$$

Once solved we obtain the canonical distribution for vertices $i \neq 1$

$$\nu_i = \frac{\exp\left(-\beta_E \epsilon_i\right)}{Z(\beta_E)} \qquad \text{(II.39)}$$

where $\beta_E = \lambda/k_B$ is equivalent to an inverse temperature in the canonical formalism and $Z(\beta_E) = \sum_i \exp(-\beta_E \epsilon_i)$ to the partition function. This configurational temperature can be extracted from measurements by counting vertices of each kind and averaging over all the configurations obtained with the same procedure. Then, the predictions of the canonical measure can be compared with the experiments. In particular

$$\ln\frac{4(\nu_5 + \nu_6)}{(\nu_9 + \nu_{10} + ... + \nu_{16})} = \ln\frac{4n_I}{n_{III}} = \beta_E(\epsilon_e - \epsilon_c) \qquad \text{(II.40)}$$

allows β_E to be determined. As shown in Fig. II.20 (a), the experimental data of is well reproduced by this canonical distribution. Moreover, the configurational temperature derived above can be controlled during the demagnetisation via H_s. As also shown in Fig. II.20 (b), Nisoli and collaborators found a linear dependence of β_E in the magnetic step size, meaning that the rotating magnetic field behaves as an effective thermal bath. Note that negative temperatures are possible when $4n_I < n_{III}$. These are highly energetic states with a very low entropy.
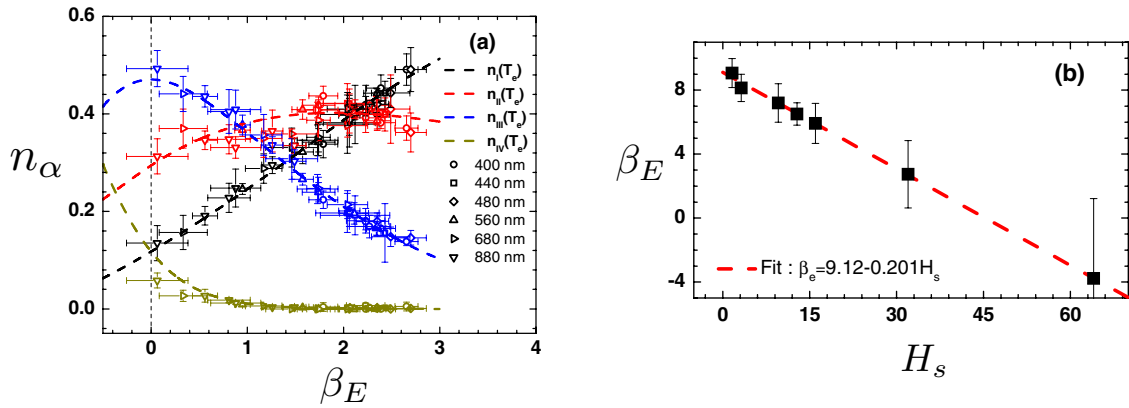
Figure II.20: Experimental data extracted from [206]. (a) Density of vertices from arrays with different lattice constants (shown in the key) and magnetic step H_s (in Oersted). Dotted lines are obtained from eq. II.39. The configurational inverse temperature β_E is given in units of ϵ_e. (b) Dependence of β_E in the magnetic step H_s confronted to a linear decay $\beta_E = \gamma - \kappa H_s$.

Note that the same group studied in detail the effect of different demagnetisation protocols on the correlations between islands and the energy of the system [139]. In this paper, they show that

the correlations and energy of the system are dependent of H_s. Although for a given step size the total energy can remain roughly constant during the procedure, its not equal to ϵ_a in general. It is not very clear whether the constraint $\varepsilon \equiv$ cte actually holds or under which experimental conditions.

II.3.5 Artificial spin ice and computer science

Artificial arrays of nano-scale ferromagnetic materials can be produced by nanolitographic techniques. Apart from the fundamental physics interests, they constitute promising candidates to improve the performances of data storage devices [71, 280] and data processing [75, 123, 13]. Ferromagnetic islands have typically an elongated shape that make them behave as a large Ising spin. Usual nowadays data storage technology is based on the manipulation of magnetic domains used to store a single bit of information. The control of the interactions in these materials and the associated excitations opens the possibility of increasing the limits of data storage and conceive electronic devices with greater processing capacity. Modern nanotechnology allows us to write and read the state of a nano-array. Therefore, the work on artificial spin ice is also motivated by the hope of being able to manipulate precisely the spins such that we can use them to perform calculations. Some work has been done very recently in artificial spin ice in this direction by Branford, Ladak and collaborators [153, 156, 47] who have found a possible way to precisely manipulate states in artificial Kagome ice by applying magnetic fields.

III

Some concepts about phase transitions

Nature uses only the longest threads to weave her patterns, so that each small piece of her fabric reveals the organization of the entire tapestry.

Richard Feynman

Matter appears to us in a rich variety of different thermodynamic states called *phases*. When dealing with systems with a large number of degrees of freedom (infinite for practical purposes), a thermodynamic state is the set of points of the phase space which share some extended physical quantity (e.g. the global magnetisation of an usual ferromagnet). Statistical mechanics makes the connection between these macroscopic phases and the microscopic constituents of the system. Different phases arise from some particular collective arrangement of the elementary building blocks of the macroscopic system. A system in contact with an environment can display different phases depending on the thermodynamic conditions of the latter (also called external parameters such as the temperature, the pressure, an external field, etc.). A familiar example is given by the different phases of water.

The phenomenon of transformation that takes brutally a system from one phase to another is called a *phase transition*, such as melting and condensation in water. In order to get a deeper understanding of the system under study, one should characterise quantitatively its different phases as a function of the external parameters, i.e. establish the *phase diagram*, and identify the location and the properties of the different phase transitions taking place. For a more detailed discussion on the subject I refer to reader to the classical textbooks [79, 107].

Ideally, one would like to start from the fundamental interactions between the elementary building blocks of the system and 'zoom out' to deduce the collective behaviour of the system (e.g. given the atomic interactions between water molecules in the continuum, deduce the quantitative behaviour of water). This is however an impossible task and a different theoretical route has to be taken. The first step is to construct a *model system* which reproduces the behaviour of a 'real' physical one. Since the introduction of the Ising model [235], the study of simple lattice models

which keep what is thought to be the 'main ingredients' of a physical problem has proven to be a very fruitful approach.

We shall use the Ising model, the simpler system with a phase transition, to illustrate the general concepts presented here. The model is defined by a set of N spin variables $\sigma_i = \pm 1$ ('up' or 'down') sitting on the sites i of a d-dimensional lattice $\mathcal{G}$ and interacting via the following Hamiltonian:

$$H(\{\sigma\}) = -J \sum_{\langle i,j \rangle} \sigma_i \sigma_j - h \sum_{i=1}^{N} \sigma_i \tag{III.1}$$

where the first sum runs over all the edges $\langle i,j \rangle$ of the lattice $\mathcal{G}$, $J > 0$ favours the alignment between the spins and h is an external field.

A phase transition is characterised by a singular behaviour of the free energy at the thermodynamic limit. They are usually classified by the nature of the singularities of the free energy. Phase transitions pertaining to different categories can exhibit very different collective behaviour and their study demands the introduction of specific methods. In the coming sections a brief description of the different kind of transitions we encounter in the study of spin ice is presented, together with the methods we used for their investigation.

III.1   Continuous phase transitions

III.1.1   Second order phase transitions

Phase transitions can change the symmetry of the thermodynamic state. Consider the magnetisation $m(T)$ as a function of temperature in the Ising model. At fixed T, lower h until zero. If the system remains magnetised it is said to have a *spontaneous magnetisation*. At low temperature, the model exhibits a non-zero spontaneous magnetisation. The interaction energy aligns the spins and the system develops large domains of parallel spins. Since the system is invariant under global spin reversal, one has to apply an external field h in order to select a given magnetisation in one among the two degenerate orientations. This is called a ferromagnetic (FM) phase. Above a critical temperature T_c, the entropic tendency to randomly distribute the spins dominates over the tendency to align them, such that the system is not magnetised when the field is switched to zero. This is called a paramagnetic (PM) phase. At T_c the system experiences a phase transition between an equilibrium state which does not respect the Z_2 symmetry of the Hamiltonian (FM phase) and a PM phase which does. Below T_c the symmetry is said to be *spontaneously broken* and m is used as an *order parameter* which labels the phases by their symmetry or degree of order.

For $h = 0$, the spontaneous magnetisation is a continuous function of T. The transition is therefore said to be *continuous* or *second order*[1]. But one should ask the following question: where does the singular behaviour of the free energy comes from? Let us consider the spin-spin connected correlation function

$$G(r_{ij}) = \langle \sigma_i \sigma_j \rangle - \langle \sigma_i \rangle \langle \sigma_j \rangle \tag{III.2}$$

where r_{ij} denotes the lattice distance between sites i and j. At high temperature, thermal fluctuations ensures the de-correlation of distant spins. One finds that G decreases exponentially at large distances:

$$\lim_{r \to \infty} G(r) \sim \exp(-r/\xi(T)). \tag{III.3}$$

---

1. The name 'second-order' comes from the old-fashioned Ehrenfest's classification of phase transitions [126]: the second derivative of the free-energy displays a singular point at T_c. The concept of continuity of the transition is more general since it also refers to higher-order transitions in Ehrenfest's scheme and, in particular, to the Kosterlitz-Thouless phase transitions. The scaling theory developed three decades later suggests to adopt a more modern terminology and divide phase transitions into two categories: 'continuous' and 'first-order'.

Here we introduced a characteristic *correlation length* $\xi(T)$ which quantifies the typical size of clusters made by strongly correlated spins. For temperatures $T < T_c$, the connected correlation function also falls off exponentially. A phase with a finite correlation length is called *disordered* if the magnetisation is zero and *long range ordered* if the magnetisation is non-zero (corresponding here to the high and low temperature regime respectively). The most interesting situation occurs at T_c where the correlations decay algebraically:

$$\lim_{r\to\infty} G(r) \sim \frac{1}{r^{d-2+\eta}} \tag{III.4}$$

where η is a *critical exponent*. The correlation function varies with temperature, and in order to connect this form with the one found away from T_c in eq. (III.3) one must set $\xi(T_c) \equiv \infty$. Precisely at the critical point the system has *long-range correlations*. The FM-PM transition point in the Ising model is a *critical point*, defined by a divergent correlation length. A phase with an infinite correlation length is said to be *quasi long-range ordered*. A thermodynamic phase should be characterised by its symmetry, leading to both the value of an order parameter and the nature of the correlations. By the fluctuation-dissipation theorem the correlation function must be proportional to the susceptibility:

$$k_B T \chi(T) = \sum_{i,j} G(r_{ij}), \qquad \chi(T) = \frac{1}{N} \left[\frac{\partial^2 F(T,h)}{\partial h^2} \right]_{h=0} . \tag{III.5}$$

At the critical point the system has long-range correlations then χ diverges, meaning that the second derivative of the free energy is singular (see footnote 1).

III.1.2   Universality of equilibrium critical phenomena

At a critical point, clusters made of parallel spins of *any* size are present and the system looks statistically identical on all length scales. This means that the critical point is *scale invariant*. A scale transformation should then leave the free energy invariant, meaning that its singular part, denoted f_s, defines a generalised homogeneous function. This is usually called the '*scaling hypothesis*' introduced by Widom in 1964 [268]. Using this single statement one can show that the associated thermodynamic quantities at the vicinity of a critical point are characterised by a set of critical exponents α, β and γ defined by:

$$C(t) \sim t^{-\alpha} \tag{III.6}$$

$$m(t) \sim t^{\beta} \tag{III.7}$$

$$\chi(t) \sim t^{-\gamma} \tag{III.8}$$

where $t = (T - T_c)/T$ goes to zero. The exponent α can be also be defined as [25]:

$$f_s(t) \sim t^{2-\alpha}, \text{ as } t \to 0. \tag{III.9}$$

The definition of α in eq. (III.6) is problematic when the specific heat has a jump or a logarithmic discontinuity. Instead, eq. (III.9) allows for a non ambiguous determination of α. When the discontinuity of C manifests through a divergence below and above T_c both definitions are equivalent. In a ferromagnet at the critical point the behaviour of the magnetisation in the presence of a small external field h defines a critical exponent δ:

$$m(t=0, h) \sim h^{1/\delta} . \tag{III.10}$$

The correlation function G is a generalised homogeneous function at the vicinity of a scale invariant point as well. The divergence of the spatial correlations can then be characterised by two other exponents, η (already introduced in eq. (III.4)) and ν defined by:

$$G(r) \sim r^{-(d-2+\eta)} \tag{III.11}$$

$$\xi(t) \sim t^{-\nu} \tag{III.12}$$

From the homogeneity form of the correlation function G and the free energy f_s at the vicinity of a critical point, one can show the following *scaling relations* between critical exponents:

$$\alpha + 2\beta + \gamma = 2 \tag{III.13}$$

$$\gamma = \nu(2 - \eta) \tag{III.14}$$

$$d\nu = 2 - \alpha \tag{III.15}$$

$$\delta = \frac{d + 2 - \eta}{d - 2 + \eta} \tag{III.16}$$

Therefore, there are only two independent critical exponents, for instance η and ν. Equations (III.14), (III.15) and (III.16) are usually referred to as *hyperscaling relations* since they link singularities in the global thermodynamic quantities with singularities related to the spatial correlations. Note that, however, the scaling hypothesis on the correlation function is only valid if the dimension the system is smaller than a certain value called the upper critical dimension d_c. Above d_c spatial correlations become irrelevant (mean-field like) and the system's dimension d becomes meaningless. The values of all the critical exponents are independent of d for $d > d_c$. The scaling relations can be precisely proven from the scale invariance by a renormalisation group (RG) approach [96].

Critical phenomena display a remarkable fact: a wide class of different physical systems have the same critical exponents (such as the 'historical' identification of the liquid-gas critical point and the ferromagnetic transition [159]). A set of critical exponents is also called a *universality class* verifying the universal scaling relations eq (III.13), (III.14) and (III.15). The critical behaviour of macroscopic systems seems then to be independent on the microscopic details of system. This phenomenon is extremely appealing from the theoretical point of view: one can describe a physical problem by a simple mathematical model belonging to the same universality class and forget about the microscopic complexity of the 'real world'. One should ask the following question: What are the main ingredients that make different systems belong to the same universality class? The answer is given by the renormalisation group theory. Suppose we have two different systems described in the continuum by two different statistical field theories. If the action of these two theories is the same up to some irrelevant terms, it will be described by the same fixed points and then the same critical behaviour. The *universality hypothesis* asserts that different systems with the same symmetry, dimensionality and range of the interactions should belong to the same universality class.

However, as we will see in chapter IV and V, vertex models appear as counterexamples of this claim. The exact solution of the eight-vertex model [22] showed that the value of the critical exponents depend continuously on the microscopic interaction parameters. This observation shows that a deeper understanding of the theories used until then to describe critical phenomena was needed. In particular, a rigorous renormalisation group construction has been applied to the eight-vertex model reformulated as a fermionic field theory [235, 171]. The formulation of vertex models as a field theory is already quite subtle. Then, in such cases, the fermionic interactions can be marginal in the RG sense and the RG transformation has a line of fixed points with different critical exponents associated to each of them. Non-universal exponents are thought to come from

the emergence of 'hidden' symmetries and marginal terms which are not apparent in the original formulation of the model in terms of Ising spins or vertex variables [27, 172]. Kadanoff and Wegner [133] pointed out that the eight-vertex model presents more symmetries that the just the Z_2 symmetry of the Ising model. Then they argued that the presence of four-spin interactions around a plaquette can explain the continuous variation of critical exponents verifying scaling. A few years after Kadanoff and Wagner's work van Leeuwen [260] proposed a real-space RG procedure in order to show the emergence of a marginal scaling field indicating the existence of a line of fixed points along which the exponents vary. However, the exact value of the exponents found by Baxter were not reproduced.

III.1.3 Landau's classification

The main idea behind *Landau theory* is that an effective thermodynamic potential $\mathcal{F}$ can be constructed in order to describe phase transitions, on the unique basis of symmetry considerations. This potential is expressed as an analytic function of the order parameter m which must respect the symmetry of the problem. Equilibrium thermodynamic states are then given by the minimisation of $\mathcal{F}$. The theory is constructed under some important assumptions: thermal and spatial fluctuations of the order parameter are negligible and the parameters in $\mathcal{F}$ are analytic functions of the microscopic parameters of the system (e.g. J, T and h for the Ising model). For a system with the Z_2 symmetry of the Ising model, the Landau potential has the general form:

$$\mathcal{F}(m, \mathbf{g}) = \sum_{n \geq 0} \frac{1}{n} c_n(\mathbf{g}) m^{2n} = \text{ct} + \frac{1}{2} a(\mathbf{g}) m^2 + \frac{1}{4} b(\mathbf{g}) m^4 + O(m^6) \,. \tag{III.17}$$

where $\mathbf{g}$ denotes a set of external parameters (e.g. $\mathbf{g} = (t, J, h)$). This model considers a global non-fluctuating order parameter and then it is of the mean-field kind. With this model Landau suggested that the phenomenon of spontaneous symmetry breaking is the crucial ingredient for the understanding of phase transition. However, the theory neglects another central point of critical phenomena: fluctuations. Therefore it does not give a correct description of critical phenomena at low dimensions. For dimensions above the *upper critical dimension d_c* fluctuations can indeed be neglected.

The extension of Landau's symmetry arguments to include fluctuations in a systematic way is known as the Ginzburg-Landau-Wilson theory. It is a field theory where the spatial fluctuations of a local order parameter are included in the action and departures from the mean field behaviour can be evaluated[2]. Together with the RG and other field theoretical techniques, it constitutes the 'canonical' approach to study critical phenomena.

The function in eq. (III.17) can describe a variety of different situations depending on the nature of the order parameter (scalar, tensor, etc.) and the expression of the functions a, b, etc. Although a more careful treatment has to be done to study the critical properties of a system, Landau theory allows for a simple phenomenological description of multi-critical points and first-order phase transitions. We introduced it here for this reason.

III.1.4 Kosterlitz-Thouless phase transition

So far, we were only concerned with phase transitions with a discrete symmetry breaking. The Mermin-Wagner theorem [180] states that in a system with *continuous symmetry* in a space of dimension $d \leq 2$, fluctuations are strong enough to avoid the establishment of a long-range order at any temperature. However, the theorem does not prevent the emergence of phase transitions.

---

2. For the Ising model one replaces m by a local field $m(\mathbf{x})$ in eq. (III.17) and includes terms in even powers of $\nabla m(\mathbf{x})$.

Indeed, this interesting situation occurs in the case of a planar model (e.g. $O(2)$ or XY model) in $d = 2$. This system experiences a phase transition due to the unbinding of *topological defects*: the so-called *Kosterlitz-Thouless phase transition* (KT) [29, 150, 148]. Although the 'order parameter' m is identically zero at all temperatures, the behaviour of the spatial correlation function changes abruptly from an exponential decay at high temperature (disordered phase) to an algebraic decay at low temperature (quasi-long range ordered phase).

The prototypical example displaying a KT transition is the classical XY model described by the following Hamiltonian

$$H\{\theta\} = -J \sum_{\langle i,j \rangle} \mathbf{S}_i \mathbf{S}_j = -J \sum_{\langle i,j \rangle} \cos(\theta_i - \theta_j) \tag{III.18}$$

where the sum runs over all the links of a square lattice and θ_i is an angle defined by: $\mathbf{S}_i = (\cos\theta_i, \sin\theta_i)$. At very low temperature, one can approximate this Hamiltonian by a quadratic form: $H \approx -J/2 \sum_{\langle i,j \rangle} (\theta_i - \theta_j)^2$. This leads to a *Gaussian field theory* in the continuum . The thermodynamics of the Gaussian model are obtained from the action:

$$S_{sw}[\theta] = \frac{1}{2} K \int d\vec{r}\, [\vec{\nabla}\theta(\vec{r})]^2 \tag{III.19}$$

where $K = \beta J$ is sometimes called the stiffness of the field. In the context of magnetic systems, this theory is usually referred to as spin-wave approximation. The equilibrium configurations are given by the extrema of the action, i.e. solutions of the Poisson equation $\nabla^2 \theta = 0$. The function θ is 2π-periodic such that the solutions of the Poisson equation can be written as

$$\oint_\Gamma \vec{\nabla}\theta(\vec{r}).d\vec{l} = 2\pi q, \ q \in \mathbb{Z} \tag{III.20}$$

where the integration is done along a closed path Γ. Configurations with $q \neq 0$ are called *vortices*. Along any close loop surrounding a vortex, θ goes from some value $\theta(\vec{r})$ to a different value $\theta(\vec{r}) + 2\pi q$, meaning that the function θ is *multivalued*. In order to define θ in the presence of vortices, one should fix a *branch cut* starting at a singularity and going to infinity, or ending at a different vortex. Vortices are an example of topological defects indexed by an integer number called *vorticity* or *winding number* or *topological charge*. A topological defect is a singularity of the field, θ here, characterised by, as the name suggests, the topology of the order parameter manifold. Topological defects cannot be destroyed by continuous deformations of the system: they are said to be *topologically stable*. Homotopy theory is the natural language to describe these objects. One can classify the possible stable topological defects of a system by looking at the homotopy groups of the order parameter manifold. Vortices in the XY model are the easiest non-trivial example: the order parameter manifold is the $1D$ sphere S^1 and its unique non-trivial homotopy group is the set of integers $\mathbb{Z}$ (the winding numbers). For a detailed and pedagogical introduction on the subject see [179].

The Gaussian approximation allows for the calculation of the correlation functions. One finds the following asymptotic behaviour:

$$G(r) = \langle \mathbf{S}(r)\mathbf{S}(0) \rangle = \exp[-(g(0) - g(r))] \sim \left(\frac{1}{r}\right)^{\frac{1}{2\pi K}} \quad \text{for } |\vec{r}| = r \to \infty \tag{III.21}$$

where g is the Green function of the Gaussian field theory

$$g(r) = \langle \theta(r)\theta(0) \rangle \underset{r \gg a}{\sim} \frac{1}{2\pi K} \ln\left(\frac{r}{a}\right) \ . \tag{III.22}$$

The correlation function decays as a power law with a critical exponent $\eta = 1/(2\pi K)$. It depends explicitly on the external parameters and is hence non-universal. The low temperature phase is then critical, which is the extreme situation allowed by the Mermin-Wagner theorem.

This simple low temperature approximation suggests that the model has two different phases: a quasi-long range ordered phase and a disordered one. A simple heuristic argument was provided by Kosterlitz and Thouless [149] to justify the existence of a rather special phase transition between these two phases. Then, using the Gaussian theory, one can determine the energy carried by a vortex: $E_{1v} = \pi K q^2 \ln(R/a)$, where R is the linear dimension of the $2D$ lattice and a the lattice spacing. One can estimate the importance of these excitations as a function of the temperature by considering the free energy associated to a single vortex. A free vortex can be in $(R/a)^2$ different states (i.e. the number of sites in the lattice). Then, the free energy of a single vortex is:

$$F_{1v} = (\pi J - 2k_B T) \ln\left(\frac{R}{a}\right) . \tag{III.23}$$

The competition between the tendency to order and the entropy indicates a critical value $T_c = \pi J/2k_B$. At low temperature the creation of vertices is suppressed. At high temperature $F_{1v} < 0$ and vortices are created spontaneously. Once vertices are created the above arguments based on small perturbations over a uniform field configuration are not justified.

In the Gaussian theory, one can compute the interaction energy between two vortices of vorticity q_1 and q_2 located at $\vec{r}_1$ and $\vec{r}_2$:

$$E_{2v} = E_{1v}^{(1)} + E_{1v}^{(2)} - 2\pi J q_1 q_2 \ln\left(\frac{|\vec{r}_1 - \vec{r}_2|}{a}\right) . \tag{III.24}$$

A pair of isolated vortices interact via an effective $2D$ Coulomb potential arising as a many body effect. At low enough density of vortices one can describe the system by the effective action:

$$S[\theta, \rho] = S_{sw}[\theta] + S_v[\rho] \tag{III.25}$$

$$S_v[\rho] = -\pi K \int \int d\vec{r} d\vec{r}' \rho(\vec{r}) \ln\left(\frac{|\vec{r} - \vec{r}'|}{a}\right) \rho(\vec{r}') + \beta E_c \int d\vec{r} \rho^2(\vec{r}) \tag{III.26}$$

where ρ is the vorticity density and E_c is the energy needed to create a vortex. This theory is a $2D$ Coulomb gas of positive and negative charges with a spin-wave term. The emergence of such long-range interaction between defects is a subtle effect and one should study more carefully with an RG approach. This was done by Kosterlitz [148], who used the Coulomb gas representation of the model. He showed that a *screening length* is generated along the RG flow and vortices cannot be considered as independent excitations. In the high temperature phase vortices are free to move: it corresponds to a conducting phase. Below T_c vortices of opposite charge are bound together: it corresponds to a dielectric phase.

Using RG arguments Kosterlitz found the following critical singularities associated with the KT transition:

$$G(r) \sim r^{-\eta}, \quad \eta = 1/4 \tag{III.27}$$

$$\xi(t) \sim \exp(a/\sqrt{t}), \quad t > 0 \tag{III.28}$$

$$f_s(t) \sim \xi^{-2}, \quad t > 0 \tag{III.29}$$

$$\chi(t) \sim \xi^{2-\eta}, \quad t > 0 \tag{III.30}$$

Below the critical temperature the correlation length and hence the susceptibility are infinite. The correlation length has an essential singularity at $t = 0$, meaning that, in the Ehrenfest classification, it corresponds to an *infinite order phase transition*. In this case, a new set of critical

exponents $\hat{\alpha}$, $\hat{\beta}$ and $\hat{\gamma}$ should be introduced [148]. These are defined in terms of the divergence of the correlation length at the KT transition point:

$$C \sim \xi^{\hat{\alpha}}, \quad m \sim \xi^{-\hat{\beta}}, \quad \chi \sim \xi^{\hat{\gamma}}. \tag{III.31}$$

They are related to the usual critical exponents previously defined by:

$$\hat{\phi} = \frac{2-\alpha}{\nu}, \quad \hat{\alpha} = \frac{\alpha}{\nu}, \quad \hat{\gamma} = \frac{\gamma}{\nu} = 2 - \eta, \quad \hat{\beta} = \frac{\beta}{\nu}. \tag{III.32}$$

The scaling relations are obeyed by these exponents. Their numerical values are:

$$\hat{\phi} = 2, \quad \hat{\gamma} = 7/4, \quad \hat{\beta} = 1/8, \quad \eta = 1/4, \tag{III.33}$$

which defines the KT universality class.

III.1.5   Topological defects

Topological defects are the key ingredient of the KT transition. They also play a central role in the theory of melting in solids. The field θ in the XY model can represent a large variety of different physical systems. For example, θ might represent the phase of the macroscopic wave function in liquid helium. The KT ordering is in this context a transition into superfluid phase. The XY model in its Coulomb gas representation is dual to the Gaussian approximation of the *absolute solid-on-solid* model (ASOS). The angular variable θ can then be mapped onto a *height function* h describing a solid-fluid interface or the shape of a growing crystal. The duality transformation maps the low temperature behaviour of the XY model into the hight temperature behaviour of the surface model (and viceversa). The transition point can then be located by identifying the fixed point of such transformation and the critical singularities of both models are the same. In this context, the KT transition corresponds to a *roughening transition*. As we will show in chapter IV, this duality property and the roughening transition are closely related to the critical properties of spin-ice. The six-vertex model in its antiferromagnetic regime (i.e. the F model) can be one-to-one mapped anto a SOS model. We should postpone this discussion to the section devoted to hardly constrained models.

Halperin, Nelson and Young [203, 277] proposed a generalisation of the Kosterlitz-Thouless theory in order to describe melting in $2D$ solids. In this so-called *dislocation mediated melting* in $2D$, usually referred to as Kosterlitz-Thouless-Halperin-Nelson-Young (KTHNY) transition, the displacement field **u** plays the role of θ. The Burgers vector **b** is the topological charge characterising a dislocation, a vectorial analog to the winding number of a vortex in the XY model. In the theory of dislocations [199, 143, 157] the Burgers vector is defined by:

$$\oint_\Gamma \vec{\nabla} \mathbf{u}(\vec{r}).d\vec{l} = \mathbf{b} = (k_x, k_y)a, \quad k_x, \; k_y \in \mathbb{Z}. \tag{III.34}$$

The vector **b** is a measure of the strength of the dislocation. Just as θ around a vertex, it is a natural consequence of eq. (III.34) that the displacement field is a multivalued function. In order to give a meaning to this function one should arbitrarily fix a branch cut going from the singularity to infinity (or to an other singularity) and defining the dislocation line. The problem of definiteness of a field and the need for a branch cut is a general fact associated with the presence of a topological defect. In electrodynamics, the presence of a Dirac monopole of charge q makes the vector potential singular, and the *Dirac string* is the branch cut associated to it [85]. The circulation of the vector potential around a monopole is given by its charge:

$$\oint_\Gamma \mathbf{A}(\vec{r}).d\vec{l} = 4\pi q. \tag{III.35}$$

Therefore, a Dirac string can be thought of as a 'dislocation' of the electromagnetic field.

Using similar arguments that the ones used by Kosterlitz and Thouless, one can show that the interaction between dislocations leads to the following contribution to the effective action [203]:

$$S_d[\mathbf{d}] = -\frac{1}{8\pi} K \int d\vec{r} \int d\vec{r}' \left[\mathbf{d}(\vec{r}) \cdot \mathbf{d}(\vec{r}') \ln\left(\frac{|\vec{r} - \vec{r}'|}{a} \right) \right.$$
$$\left. - \frac{[\mathbf{d}(\vec{r}) \cdot (\vec{r} - \vec{r}')] \, [\mathbf{d}(\vec{r}') \cdot (\vec{r} - \vec{r}')]}{|\vec{r} - \vec{r}'|^2} \right] + \beta E_c \int d\vec{r} \, \mathbf{d}^2(\vec{r}) \qquad \text{(III.36)}$$

where $\mathbf{d}$ is the density of dislocations. This should be compared with eq. (V.119). A review on KTHNY theory can be found in Nelson's book [204]. Note that a *2D dipolar interaction* emerges as a many-body effect. A detailed discussion on the KT transition in the XY model, in $2D$ solids and liquid helium can be found in Chaikin and Lubensky's book [64] and Kleinert's book [143].

III.2 Discontinuous phase transitions

III.2.1 First order phase transitions

In this section we describe briefly, on the basis on Landau mean field theory, the main features of the 'usual' first order phase transitions which differ from the ones of the 'unusual' discontinuous FM transition of the six-vertex model. A much detailed and precise presentation of first-order phase transitions beyond mean field arguments can be found in the review by Binder [35].

Landau theory predicts a first-order phase transition if the symmetry of the system imposes the presence of a cubic term in the expansion eq. (III.17)(used in the context of liquid crystals [80]). Consider

$$\mathcal{F}(m, T, h) = \text{ct} + \frac{1}{2} a_1 \, (T - T_c) \, m^2 - \frac{1}{3} a_2 \, m^3 + \frac{1}{4} b \, m^4 \qquad \text{(III.37)}$$

where a_1, a_2 and b are all positive constants. As shown in Fig. III.1 this function might have two minima of different nature depending on the range of temperature. The thermodynamic state is given by the minimisation of $\mathcal{F}$ which leads to a second order equation in m. The solutions depend on the sign of the parameter $\Delta = a_2^2 - 4a_1(T - T_c)b$. This leads to three different regimes:

– High temperature regime:

For $T \geq T_+ > T_c$ the function $\mathcal{F}$ has a single global minimum at $m_0 = 0$.

– Metastable regime:

(i) For $T_+ > T \geq T_c$ the function $\mathcal{F}$ has a global minimum at $m_0 = 0$ and a local minimum at $m_0 = m_+ \neq 0$. The limit temperature T_+ separating a *pure phase* and a *mixed phase* is thus the *limit of metastability* of the disordered state. It is identified by an inflexion point: $(\partial^2 \mathcal{F} / \partial m^2)_{T_+} = 0$. Local minima of the Landau potential are interpreted as *metastable states*. Such that, in this regime, ordered and disordered regions coexist.

(ii) For $T_c > T > T_-$ the function $\mathcal{F}$ has a global minimum at m_+ and a local minimum at $m_0 = 0$. Both phases coexist until the temperature T_- is reached when cooling. The minimum associated to the ordered phase is deeper than the one associated with the disordered one. When cooling, regions of non-negative order parameter grow until the limit of metastability T_- is reached.
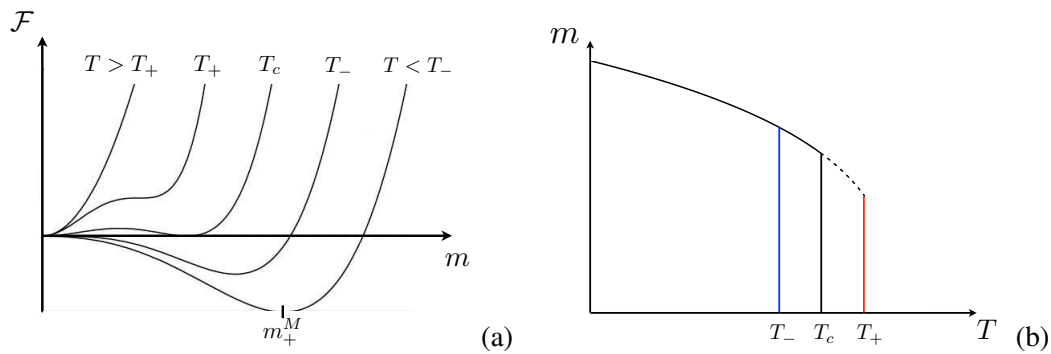
Figure III.1: (a) Landau potential with a cubic term in m for different temperatures. The limits of metastability are indicated. For clarity we only show here the positive m-axis. (b) Order parameter as a function of temperature. Depending on the cooling (blue) or heating (red) procedure, the system can avoid the transition at T_c and set in a supercooled of superheated phase between the metastability limits. Metastable states coexisting with the equilibrium stable phase are present between the blue and the red lines.

    – Low temperature regime:

        For $T < T_-$ the function $\mathcal{F}$ has a single global minima at $m_0 = m_+$ and the ordered phase is stable.

At T_c the two minima $m_0 = 0$ and $m_0 = m_+$ are equally deep. The concavity of $\mathcal{F}$ changes abruptly at that point, leading to a discontinuous phase transition: the spontaneous magnetisation given by the deeper minima jumps from a strictly positive value m_+ to zero. The emergence of metastable states is responsible for the *hysteresis* phenomenon. Starting from a high temperature state one can 'supercool' the system and obtain a metastable disordered state below the critical temperature. This needs cooling procedures faster than the microscopic kinetics of the system (see Fig. III.1). The phenomena of hysteresis and phase coexistence characterising a first-order phase transition might be familiar from everyday's observation of boiling water: the formation of bubbles of vapour coexisting with liquid water above 100°C.

Some important remarks should be done about the meaning of metastability. Usually, one refers implicitly to the dynamical properties of the system when discussing metastability and hysteresis (which depends on the cooling rate and it is hence a non-equilibrium phenomenon). The minima of $\mathcal{F}$ is related to the probability of finding an equilibrium configuration with a given value of m. In this mean field picture we neglected fluctuations, which turn out to be crucial for a precise characterisation of coexistence phases. When one includes fluctuations all possible configurations can be observed with a given probability. One can think of a metastable state as being a state, among all the possible ones, where the system spends a long macroscopic time. In an ordered phase, such as the FM phase of the Ising model, the same argument applies. The system spends a huge time $\sim \exp N$ close to one of its two valleys $m = \pm m_0$ and a very little time far from them. Fluctuations and dynamics should be taken into account in order to get a complete understanding of first order phase transitions. The existence of long-lived metastable states (such as in supercooled liquids [81]) and the dynamical mechanisms responsible for the equilibration of a system close to a first order phase transition are interesting but rather complicated issues which are not completely understood yet. First-order phase transitions constitute a difficult situation to handle theoretically even though it is a phenomenon we encounter more usually than critical phenomena.
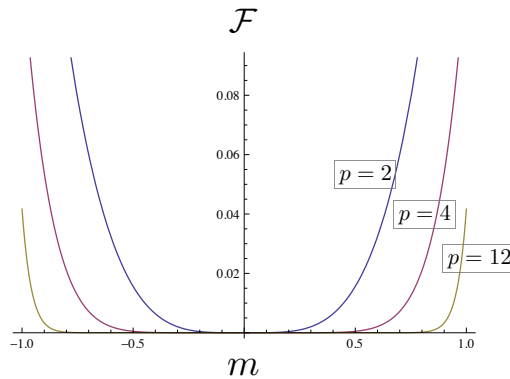
Figure III.2: Landau potential at a critical point corresponding to $p = 2$ (in blue) and at a multi-critical point of order $p = 4$ and $p = 12$.

III.2.2 Multi-criticality

The stability of the equilibrium solutions of the Landau theory eq. (III.17) is guaranteed by the positivity of the parameter b. The Ising second-order transition in this theory is due to the change of sign of $a(\mathbf{g}) = a_1(T - T_c)$ at T_c. If one includes the next term $c(\mathbf{g})m^6$ in the development of $\mathcal{F}$ the stability condition is $c(\mathbf{g}) > 0$, i.e. the positivity of the factor in front of the term with the largest power. The transition comes from the change of sign of the terms with lower power. If $b(\mathbf{g}) > 0$ there is a 'lambda line' of second order phase transitions at $(\mathbf{g}_t) = 0$ (the name lambda line comes from the phase diagram of liquid helium where this kind of behaviour was first observed [108]). If $b(\mathbf{g}) < 0$ the system experiences a first order phase transition $a(\mathbf{g}_c) = 0$. At $b(\mathbf{g}_t) = a(\mathbf{g}_t) = 0$ the system is said to be on a *tricritical point*. The system responds in a qualitatively different manner to changes along different directions in the parameter space. Depending on the relative sign of $a(\mathbf{g})$ and $b(\mathbf{g})$ the system undergoes a first order or second order phase transition. At a *multi-critical point*, the system has more than one relevant external parameters.

In general, one can consider a Landau potential including all the even powers of the order parameter:

$$\mathcal{F}(m, \mathbf{g}) = \sum_{n>0} \frac{1}{2n} c_{2n}(\mathbf{g}) m^{2n} . \tag{III.38}$$

A multi-critical point of order p is defined by: (i) the stability condition: $c_{2p}(\mathbf{g}) > 0$, $\forall \mathbf{g}$ (higher order terms are neglected), (ii) the 'meeting' point of all the critical surfaces: $c_{2n}(\mathbf{g}_t) = 0$, $\forall n < p$. Note that $\mathbf{g}$ must be, at least, a $(p-1)$-dimensional vector. As shown in Fig. III.2 the mean-field probability of an equilibrium state becomes flatter as p increases.

III.2.3 The 'Frozen-to-Critical' KDP transition

So far, we distinguished transitions for which: (i) the order parameter is continuous, there is a diverging correlation length at the critical point and a set of exponents characterising the singularity; (ii) the order parameter is discontinuous, there is no divergent length scale in the system at the transition point and no critical exponents associated to it. This classification into first and second order is mainly based on general arguments coming from Landau's ideas and the more precise Ginzburg-Landau-Wilson formulation. The conjectures made by field theory approaches should be confronted with the few exact results available in statistical mechanics [25]. The exact solu-

tion of the dimer model by Kasteleyn [137, 138] [3] and the solution of the KDP model by Lieb in 1967 [163] show that this classification is not exhaustive. As we will show in a second, these simple lattice models cannot be described by the Ginzburg-Landau-Wilson framework. Constrained models, and in particular vertex models, exhibit phase transitions that do not fit into the standard classification.

The dimer model is meant to describe the absorption of a diatomic gas on a substrate. Each diatomic molecule is modelled as a rigid *dimer* (or domino) occupying two neighbouring sites of a lattice. A recent review on dimer models in $2D$ can be found in [269]. Here we focus on *perfect matchings*, i.e. configurations where all the sites are occupied by exactly one dimer. These models defined on general bipartite graphs are largely studied in mathematics as well, where there are known as domino tilings. But let us focus here on the interesting collective phenomena arising in these systems and leave the discussion of more formal aspects to the next chapter. Consider dimers on an hexagonal lattice and give a Boltzmann weight to the three possible configurations of a dimer (the three orientations of the hexagonal lattice) denoted $z_1 = e^{-\beta\epsilon_1}$, $z_2 = e^{-\beta\epsilon_2}$ and $z_3 = e^{-\beta\epsilon_3}$. The partition function of the model is

$$Z(z_1, z_2, z_3) = \sum_{N_1, N_2, N_3} g(N_1, N_2, N_3) z_1^{N_1} z_2^{N_2} z_3^{N_3} \tag{III.39}$$

where $g(N_1, N_2, N_3)$ is a combinatorial factor which counts the number of dimer coverings using N_1, N_2 and N_3 dimers along the three directions of the hexagon. This model experiences a phase transition when one of the weights is equal to the sum of the other two, for example $z_1 = z_2 + z_3$. In the ordered phase $z_1 > z_2 + z_3$ and $Z(z_1, z_2, z_3) = \sqrt{z_1}$. Meaning that the only allowed configuration is the one where all the dimers are z_1 (see Fig. III.3). The system shows a perfect order in this phase. The only excitations that could introduce some orientational disorder in the system involve an extensive number of dimers and are hence suppressed in the thermodynamic limit. This ordered phase is said to be *frozen*.

(a)   (b)
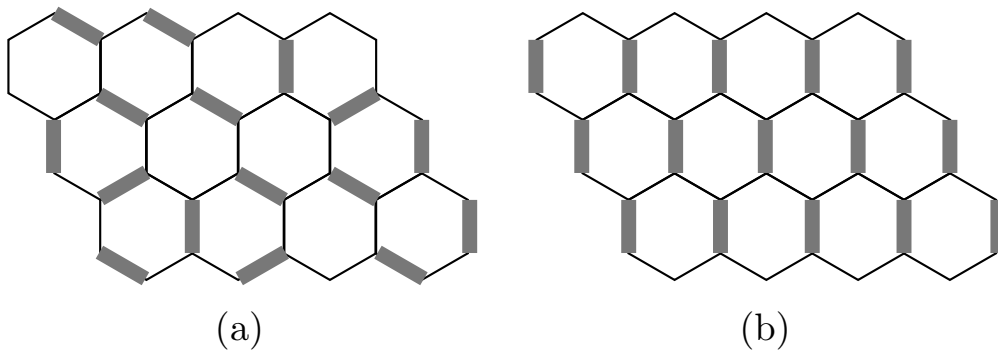
Figure III.3: **The dimer model on the hexagonal lattice.** (a) A particular isotropic dimer covering. (b) Ground state of the system when dimers in the vertical direction are favoured. Below T_c, the system is frozen in this configuration.

A phenomenological picture of this transition mechanism arises as follows. Consider the ground state shown in Fig. [III.3 (b)] and, for simplicity, let us fix $\epsilon_1 = 0$ and $\epsilon_2 = \epsilon_3 = \epsilon > 0$. In order to excite the system one would try to shift a vertical dimer into one among the two non-vertical positions. By doing so, one creates a pair of topological defects called *monomers* at an

---

3. Although the solution of the dimer model is commonly attributed to Kasteleyn, the problem was solved almost simultaneously in 1961 by two other 'big names' of statistical physics, namely Fisher [97] and Temperley [256].

energy cost ϵ. Monomers are strictly forbidden in this model and one must then shift dimers in order to eliminate them. As shown in Fig. III.4, one must shift an extensive number of vertical dimers forming a *string* in order to avoid the presence of monomers. This can be done at an energy cost of $L\epsilon$. Since there are two possible choices for the shift of a dimer during the construction of the string, the free energy of one '*string excitation*' is

$$F_{1s} = L(\epsilon - k_B T \ln 2). \tag{III.40}$$

Then, a simple argument *à la* Kosterlitz-Thouless (see eq. (III.23)) locates the transition temperature at $k_B T_c = \epsilon/\ln 2$. It turns out that this simple estimation gives the *exact* transition temperature: $z_1 = z_2 + z_3$. At $T > T_c$ string excitations populate the system. At $T < T_c$ the system freezes since thermal fluctuations are not strong enough to create a string.

(a)   (b)

(c)   (d)
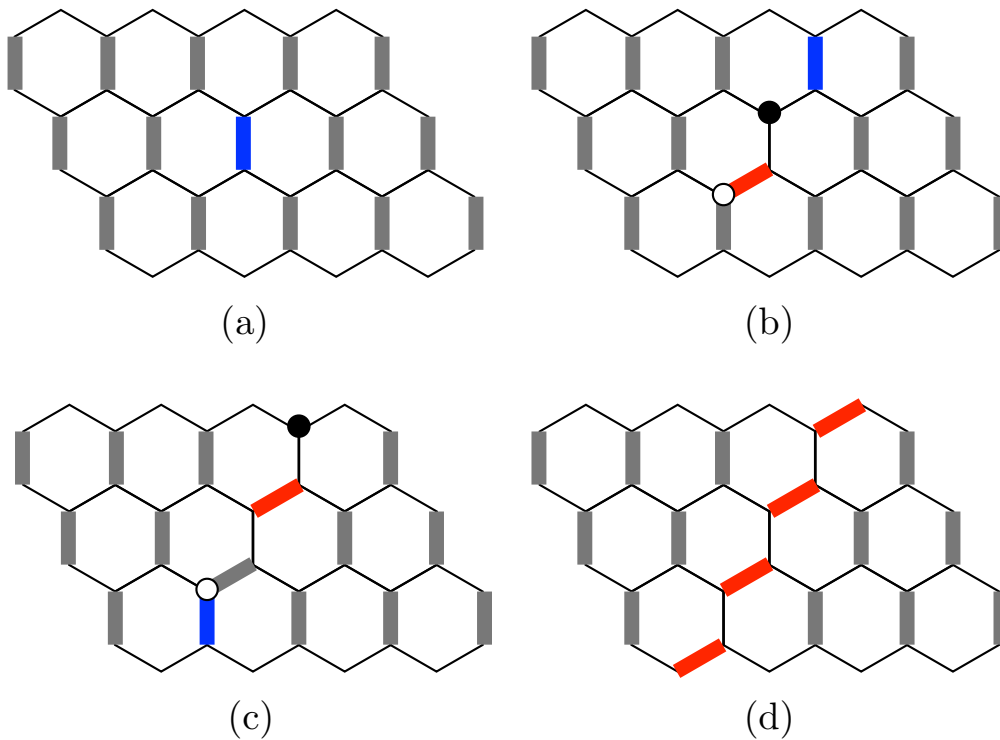
Figure III.4: **Excitations in the hexagonal dimer model.** (a) Ground state configuration. (b) Configuration after switching the blue dimer in (a) into the dimer shown in red. So doing, one creates a pair of monomers of opposite topological charge shown by white and black circles. (c) Configuration after switching the blue dimer in (b) into the dimer shown in red. The switching of the dimer induces the motion of the black monomer. (d) Configuration obtained by repetition of the same procedure. The pair of monomers finally disappear if one switches all the dimers along the string shown in red which ends at the boundaries of the lattice.

Note that this is not a usual phase transition as the continuous and first-order transitions described before. It takes the system from a critical phase with long range correlations into a frozen state. It is also very asymmetric since the free energy is constant in the ordered phase and a continuous function of the parameters in the quasi-ordered phase characterised by a diverging correlation length. These observations suggested Nagle to call it '*3/2-order transition*' [201]. From the low temperature side the thermodynamics are consistent with a first-order transition but, in the high-temperature side, there are large fluctuations at the vicinity of the transition proper of a continuous

phase transition with the associated critical exponent: $\alpha = 1/2$. Hence the name 3/2-order transition, as an 'average' between the first-order and second order like behaviour from one side to the oder of the transition. In 1973, Nagle identified the extended excitations of the dimer model with hydrocarbon chains present in biomembranes [201, 200]. The model predicts the qualitative behaviour of the phase transition occurring in lipid bilayers between a frozen *trans*-phase and a disordered *gauche*-phase. It has been shown that this unusual kind of transition can also occur in dimer models in $3D$ lattices [33]. Using transfer matrix techniques, a logarithmic divergence of the heat capacity ($\alpha = 0$) has been found when approaching the transition point from above.

The KDP model [243] is defined as the special case of the sixteen-vertex model introduced in the Introduction I for which $e = d = 0$ and $a \geq b = c$. This model exhibits a very asymmetric transition of the same kind. It is defined on a square lattice, in which the energy of a pair of ferromagnetic (or ferroelectric) vertices is set to zero and all other ones are equal and positive, i.e. $a = 1 > b = c = e^{-\beta\epsilon}$ as shown in Fig. III.5. The exact solution of the model [164, 25] shows that a transition takes place at $a = b + c$, i.e. $k_B T_c = \epsilon / \ln 2$. Below T_c the system is frozen in an ordered phase where all the vertices are of type a. The free energy is constant in this regime. Above T_c the free energy becomes a continuous function of the parameters and thermal fluctuations in the form of small loops of spins pointing along the loop are present. At T_c the free energy is singular with a critical exponent $\alpha = 1$. The first derivative of the free energy shows a step discontinuity at the transition. In the canonical classification this would correspond to a first-order phase transition. However, contrary to what happens in usual first-order transitions, critical exponents can be defined. Note that the transition temperature $k_B T_c = \epsilon / \ln 2$ can be obtained from the same arguments used for the dimer model. Indeed, this *'frozen-to-critical' transition* is of the same kind as the one discussed a few lines above: it is due to the presence of extended excitations in the form of *strings* of collinear arrows spanning the whole lattice (see Fig. III.5).

In order to further understand the equivalence between these two transitions and fix our terminology we should make a few remarks. An order parameter can be defined in the KDP model: the magnetisation M. It is defined as the average orientation of the arrows along the two directions of the square lattice. In the absence of an external field this order parameter exhibits a jump-discontinuity at $T_c = \epsilon / k_B \ln 2$: $M = 0$ at $T < T_c$ and $M = \pm 1$ at $T < T_c$. Because of its peculiarities, we will call it *KDP transition*. However, when an external field is included, the magnetisation becomes continuous [25, 266]. Wu showed that the six-vertex model in an infinite external field can be mapped onto the dimer problem on an hexagonal lattice studied by Kasteleyn [270]. Several authors, in particular in the field of frustrated magnetism, call this transition occurring in the six-vertex model in presence of a field *Kastelyn transition*, in honour of the work of Kasteleyn on the hexagonal dimer problem.

Neutron scattering experiments have found evidence for a Kasteleyn transition in Kagome ice [93]. This should not come as a surprise us since the Kagome Ice problem is equivalent to the dimer model in the hexagonal lattice. Kagome Ice is obtained in the laboratory by applying a [111] field to pyroclhore spin-ice materials. The Kasteleyn transition is induced by a field along to the Kagome planes.

Theoretical studies in the NN spin-ice model on the $3D$ pyrochlore lattice in a [100] field predict a Kasteleyn transition [130]. This is again expected since the NN spin-ice model is a six-vertex model on the diamond lattice. Experimental studies on spin-ice materials in a [100] field have been reported in [101, 95]. Below the freezing temperature, experimental samples are though to be out of equilibrium [101], avoiding a conclusive observation of the transition predicted theoretically [130].

A KDP transition is also expected to occur in spin ice model when an anisotropy favouring a
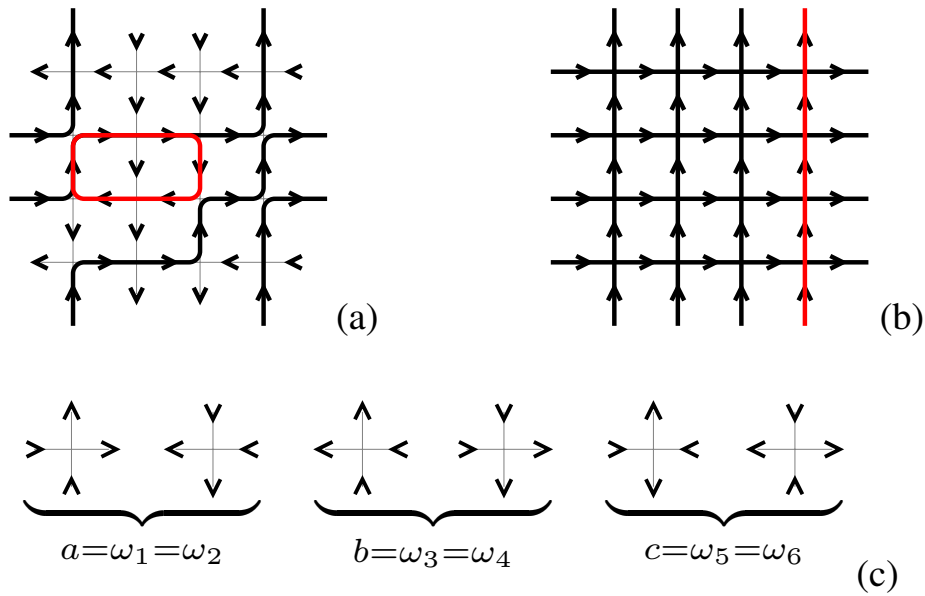
Figure III.5: **Excitations in the KDP model.** (a) A particular hight temperature configuration. A typical loop fluctuation is shown in red. (b) Low temperature configuration. The system is frozen into its ground state below T_c. A typical fluctuation in the form of an extended string is shown in red. (c) Six vertex configurations and their associated statistical weights a and $b = e^{-\beta\epsilon}$ where $\epsilon > 0$. The first two vertices are favoured.

pair of ferromagnetic vertices is introduced. This can be done in the laboratory by applying uni-axial pressure in a particular crystallographic direction [187]. In that way, bond distortion is introduced in the system which splits the degeneracy of the ice-ruled manifold. Jaubert et al. studied the effect of bond distortion on the NN spin-ice model on the pyroclhore lattice [131]. Using a mean field approach supported by Monte Carlo simulations and transfer matrix techniques, they argued that the special features of the KDP transition are due to the flatness of the probability distribution of the magnetisation at the transition. Hence, they claimed that the KDP transition corresponds to a *multi-critical point of infinite order*. Such a multi-critical point was previously studied by means of the Landau's mean field theory presented in section III.2.2 [28]. This theory predicts a jump discontinuity of the order parameter at the multi-critical point. As shown in Fig. III.2, the potential $\mathcal{F}(m)$, giving the probability of a configuration with magnetisation m, becomes flatter and flatter as p increases. The flatness of the Landau's potential makes the KDP transition radically different from the mean field picture of a first order phase transition with metastable states and hysteresis. Using the mean field potential in eq. (III.38), one finds the following associated critical exponents when approaching the critical temperature from above: $\beta = 0$, $\alpha = 1/2$, $\gamma = 1$ and $\nu = 1/2$.

The main property which explains the emergence of such unconventional collective behaviour in these systems is the presence of a hard constraint: the ice-rule for the KDP and spin-ice model, the 'tessellation' condition for dimers (i.e. there is no overlaps and no gaps in the dimer packing). In order to preserve the constraint, the only possible fluctuations in these systems are of the form of closed loops of dimers or spins. If we impose periodic boundary conditions, the hard constraint splits the phase space of the system into different *topological sectors*. These are characterised by the number of winding loops closing at the borders of the lattice thanks to PBC. In the condensed

matter literature, such a frozen phase due to the presence of a hard constraint is usually said to be *topologically ordered*. The intriguing effects arising from the imposition of a hard local constraint will be discussed in much more detail in the coming chapter.

III.3   Finite-size effects

The concept of phase transition only makes sense in the thermodynamic limit. This is a theoretical idealisation of real physical systems made by a finite number of elements. Although this number can be inconceivably large, a detailed analysis of the effects arising from the finiteness of the system should be done, in particular in view of the analysis of the data obtained by numerical simulations.

III.3.1   Around a second order phase transition

The collective behaviour in finite-size systems is smooth, no divergencies can take place since the partition function is a sum over a finite number of reals. The theory of critical phenomena is based on the scale invariance of the critical point. A finite system breaks the scale invariance and the length scale ξ can, at most, be of the order of the linear size of the system L. The divergencies associated with an infinite correlation length are then 'smoothed' by the bound imposed by L. Nevertheless, it is possible to define a transition temperature $T_c(L)$ for a finite system as the "rounded peak" corresponding to the divergence of some quantity in the thermodynamic limit (e.g. the second order moment of the probability distribution of the order parameter). Relevant finite size effects are expected to appear when $\xi \approx L$.

The renormalisation group approach to critical phenomena showed that the singular part of the free energy density is a generalised homogeneous function for p scaling variables $x_1...x_p$, i.e.

$$f_s(x_1, ..., x_p) = \lambda^{-n} f_s(\lambda^{a_1} x_1, ..., \lambda^{a_p} x_p), \ \ \forall \lambda \in \mathbb{R} \, . \tag{III.41}$$

When $L \lesssim \xi$ finite-size effects can be taken into account by including L^{-1} as an extra scaling field [4]. As a result

$$f_s(x_1, ..., x_p, L^{-1}) = \lambda^{-n} f_s(\lambda^{a_1} x_1, ..., \lambda^{a_p} x_p, \lambda L^{-1}), \ \ \forall \lambda \in \mathbb{R} \, . \tag{III.42}$$

Using this *finite size scaling hypothesis*, one can deduce the scaling form of the other thermodynamic quantities for a finite system size [98]. For a review see [15, 55].

Consider a second order phase transition described by an order parameter m. In order to illustrate these concepts let us consider again the Ising model d-dimensional lattice for which; $m = L^{-d} \langle \sum_{i=1}^{L^d} s_i \rangle$, where the brackets denote an ensemble average. When $\xi \approx L$ the system looks ordered. This defines a size dependent critical temperature $T_c(L)$, in general smaller than the infinite size prediction $T_c(\infty)$. Using the scaling relation eq. (III.12) one can write

$$T_c(L) - T_c(\infty) \propto \ L^{-1/\nu} \, . \tag{III.43}$$

The pseudo critical temperature can be located from the maximum (rounded peak) of the heat capacity C^{max} or susceptibility χ^{max}. From the scaling relation eq. (III.6) and (III.8) we find

$$C^{max} \sim (T_c(L) - T_c(\infty))^{-\alpha} \sim L^{\alpha/\nu} \, , \ \chi^{max} \sim (T_c(L) - T_c(\infty))^{-\gamma} \sim L^{\gamma/\nu} \, . \tag{III.44}$$

---

4. For an anisotropic system in two dimensions we must consider two correlation lengths $\xi_\perp$ and $\xi_\parallel$ which might diverge with different critical exponents.

The critical exponents can be determined using the following scaling relations:

$$C(t, L^{-1}) \sim L^{\frac{\alpha}{\nu}} \Phi_C(tL^{\frac{1}{\nu}}) \tag{III.45}$$

$$\chi(t, L^{-1}) \sim L^{\frac{\gamma}{\nu}} \Phi_\chi(tL^{\frac{1}{\nu}}) \tag{III.46}$$

$$m(t, L^{-1}) \sim L^{-\frac{\beta}{\nu}} \Phi_m(tL^{\frac{1}{\nu}}) \tag{III.47}$$

where the Φ_*'s are the scaling functions of the quantities indicated on the subscript. A useful quantity is the *Binder cumulant* [34]. It is the reduced forth order cumulant of the order parameter defined by

$$K_m = 1 - \frac{\langle m^4 \rangle}{3\langle m^2 \rangle^2} . \tag{III.48}$$

The finite size scaling analysis of this quantity gives:

$$K_m(t, L^{-1}) \sim \Phi_{K_m}(tL^{\frac{1}{\nu}}). \tag{III.49}$$

Therefore, it tends to three different fixed points: at $T = 0$, $T = \infty$ and $T = T_c$. It grows monotonically from $K(T \to \infty) = 0$ to $K(T = 0) = 2/3$ and gives a value K^*, independent of L, at the critical point. This allows for the location of the latter: the point where the Binder cumulants for different system sizes intersect gives an estimation of the critical point.

The arguments given above are not extremely precise since we are using the scaling forms obtained in the thermodynamic limit to study finite size effects. More precise arguments based on RG calculations in finite systems can be found in [55, 15].

III.3.2 Around a first order phase transition

The scaling arguments presented above are valid close to a critical point, where the correlation length diverges. This is no longer the case for a first order phase transition and a different finite-size scaling analysis is needed [221, 36, 66, 263].

In a second order phase transition, the shift of the transition temperature because of the finiteness of the system was characterised by the exponent $1/\nu$. Such exponent is not defined for a first order phase transition and the shift of the transition is only due to the volume of the system. For a first order phase transition one can write

$$T_c(L) - T_c(\infty) \propto L^{-d} \, , \quad C^{max} \sim L^d . \tag{III.50}$$

The reduced fourth order cumulant $K_m(t, L^{-1})$ shows a very different behaviour depending on the order of the transition [263]. Indeed, it develops a pronounced minimum at $t(L) \approx$ cte L^{-d}, close to the transition temperature and can take negative values. The basic assumption needed to deduce this results is that for a first-order phase transition one has a coexistence of ordered and disordered phases. A probability distribution for observing metastable states is constructed and used to compute thermodynamic quantities. Note that this theory has no reason to work out for a KDP transition.

III.4 Numerical methods

III.4.1 Monte Carlo dynamics

Monte Carlo methods stands for a class of numerical techniques used for solving physical problems. The goal of a Monte Carlo simulation in statistical mechanics can be: (i) the estimation

of the ensemble average of some thermodynamic observable at equilibrium; (ii) the estimation of time-dependent quantities and the study of the dynamics of the system under consideration. Both are related and do not need independent approaches. The microscopic dynamics are encoded in the updating rules used by Monte Carlo algorithm and equilibrium measurements can be done after the equilibration of the system. In this thesis Monte Carlo simulations have been used for both equilibrium and out-of -equilibrium studies of $2D$ spin-ice. There are many books which cover the applications of Monte Carlo methods to statistical mechanics and condensed matters problems. Here I briefly present the basis of the numerical methods used during the thesis and I refer the interested reader to [17, 151].

A Monte Carlo simulation of a lattice model must generate configurations accordingly to the Boltzmann distribution. From a state $\mu(0)$ of a $L \times L$ lattice system the agorithm generates via a Markov process a new state $\mu(1)$. The transition probability of this stochastic process is denoted $W(\mu(0) \rightarrow \mu(1))$. This procedure must guarantee that any state of the system can be generated using a finite number of steps. This is called the *ergodicity condition*. The stochastic process of generation of new states can be though as the microscopic evolution of the system. The probability $\mathcal{P}(\mu, t)$ of finding the system in the state $\mu(t)$ at time t is described by a master equation:

$$\frac{\partial \mathcal{P}(\mu, t)}{\partial t} = -\sum_{\nu} \left[\mathcal{P}(\mu, t)W(\mu \rightarrow \nu) - \mathcal{P}(\nu, t)W(\nu \rightarrow \mu) \right] . \qquad \text{(III.51)}$$

Suppose that this Markov process is able to reach an equilibrium state μ^e as $t \rightarrow \infty$. The dynamics are encoded in the *updating rules* used by the algorithm to get a new configuration $\mu(t+1)$ from a previous one $\mu(t)$. Different dynamics can be implemented in the algorithm depending on the physical situation one wants to simulate. All of them must ensure that, at equilibrium, states are generated accordingly to the Boltzmann distribution. A way to ensure that is to impose *detailed balance*

$$W(\mu \rightarrow \nu)e^{-\beta E(\mu)} = W(\nu \rightarrow \mu)e^{-\beta E(\nu)} . \qquad \text{(III.52)}$$

together with the ergodicity condition. Nevertheless, these two requirements do not determine completely the transition rates. A simple and widely used choice is given by the *Metropolis algorithm*:

$$W(\mu \rightarrow \nu) = g(\mu \rightarrow \nu)A(\mu \rightarrow \nu) \qquad \text{(III.53)}$$

where we have split the transition probabilities into an edge-selection probability

$$g(\mu \rightarrow \nu) = 1/L^2, \ \forall \nu \qquad \text{(III.54)}$$

and a flip-acceptance probability

$$A(\mu \rightarrow \nu) = \begin{cases} \exp\{-\beta(E(\nu) - E(\mu))\} & \text{if } E(\nu) - E(\mu) > 0 \\ 1 & \text{otherwise} \end{cases} . \qquad \text{(III.55)}$$

The transition probabilities defining the dynamics of the system can now be written as

$$W(\mu \rightarrow \nu) = \frac{1}{L^2}\min\left(1, e^{-\beta(E(\nu) - E(\mu))}\right) . \qquad \text{(III.56)}$$

The specification of the transition probabilities together with the updating rules used to generate new configurations define a Monte Carlo algorithm. During the simulations we update the time variable by one after we have performed L^2 times the two steps of the algorithm: (i) select a spin, (ii) flip it with the acceptance probability. This is called a Monte Carlo step and it is the unit of time in the simulations.

III.4.2 The Continuous-Time algorithm

For frustrated magnets showing a macroscopic degeneracy of the ground state - such as spin ice - the usual Metropolis algorithm, from now on called Fixed Step Monte Carlo algorithm (FSMC), is very inefficient. For systems at low temperature and, in general, displaying slow dynamics most of the updates proposed by the FSMC algorithm will be rejected. We have implemented an algorithm which overcomes this difficulty, the *Continuous Time Monte Carlo algorithm* (CTMC). In this section we present this technique for a general problem. The concrete implementation for the study of $2D$ spin ice can be found in the Appendix **??**.

The CTMC algorithm is also known with different names: Bortz-Kalos-Lebowitz [41], n-fold way or kinetic Monte Carlo. The basic aim of this algorithm is to get rid of the time wasted due to a large number of rejections when the physics of the problem imposes a very small acceptance ratio. It is extremely useful for the study of the long time behaviour of systems with complicated energy landscapes and a large number of metastable states. The main idea behind this method is to sample stochastically the time needed to update the system and then do it without rejections.

We can easily predict the time interval needed to update the system. Suppose that the system is at state μ at time t_0. The *exact* probability of leaving the state μ after Δt trials is

$$(W(\mu \rightarrow \mu))^{\Delta t} \left(1 - W(\mu \rightarrow \mu)\right) = (W(\mu \rightarrow \mu))^{\Delta t} - (W(\mu \rightarrow \mu))^{\Delta t + 1} .$$

In order to estimate for this quantity we have to generate a random number ξ uniformly distributed between 0 and 1. The latter corresponds to Δt trials if $0 < \xi < (W_{\mu\mu})^{\Delta t} - (W_{\mu\mu})^{\Delta t + 1}$ then $\Delta t + 1 < \frac{\ln \xi}{\ln W_{\mu\mu}} < \Delta t$. It follows that the number of steps needed to flip an arrow should be computed by

$$\Delta t = \text{Int} \left(\frac{\ln \xi}{\ln \left(1 - \sum_{\mu' \neq \mu} W(\mu \rightarrow \mu')\right)} \right) + 1 , \tag{III.57}$$

with the transition probabilities given by the Metropolis scheme:

$$W(\mu \rightarrow \mu') = \frac{1}{L^2} \min \left(1, e^{-\beta(E(\mu') - E(\mu))}\right) . \tag{III.58}$$

These transition probabilities are the same as for the FSMC algorithm, but we should notice that in this case the aim is to compute the time we have to wait before we do an update of the system. Using this time-step update, the output data of a CTMC calculation should be *identical* to the output of the usual FSMC. This has been checked in our simulations of $2D$ spin-ice (see Fig. III.7).

Equation (III.57) shows that we need to know the transition probabilities for all possible updates at each step. This is the main difficulty for the implementation of the CTMC algorithm since this number can grow exponentially with the system's size. However, for systems with only short range interactions one can only consider the neighbourhood of a site and the number of possible changes is fixed to n (hence the name n-fold way). There is then a finite number of such possible processes (and then a finite number of possible transition probabilities) independent of the system size.

For an Ising model on a square lattice with single-spin flip updates, all the possible changes one can generate in one step can be labelled by the change on the number of satisfied bonds $(n_{\mu'} - n_{\mu})$ before and after the spin flip. For this problem the CTMC algorithm is a 5-fold way since the change on the number of satisfied bonds can take five different values $n_{\mu'} - n_{\mu} = \pm 4, \pm 2, 0$ (see Fig. III.6). We then say that a spin has 5 energetic states.

Let us rewrite the transition probabilities W is the following enlightening form:

$$P_l = \frac{1}{L^2} \min \left(1, e^{-\beta \varepsilon_l}\right) \tag{III.59}$$

where ε_l is the energy difference after flipping an arrow in state l. In this form one observes taht the transition probabilities are completely determined by the state of a given site. One can compute Δt by counting the number of arrows occupying each one of the different possible states at each step:

$$\sum_{\mu' \neq \mu}^{2N} W(\mu \to \mu') = \sum_{l=1}^{5} g_l \, P_l \qquad \text{(III.60)}$$

where g_l is the number of spins in state l. One needs to keep record of the state of every spin on a list at each step. After each step the list must be updated.

$n_\mu = 0$ $n_{\mu'} = 4$ $n_\mu = 1$ $n_{\mu'} = 3$ $n_\mu = 2$ $n_{\mu'} = 2$
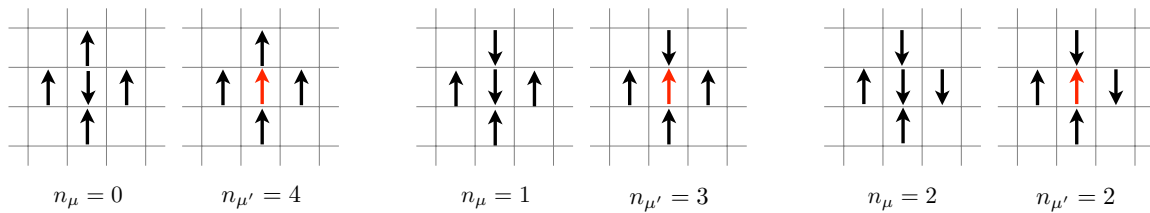
Figure III.6: Different possible states of a spin down in the $2D$ Ising model classified by the number of satisfied bonds n_μ. After flipping the central down spin, the number of satisfied bonds becomes $n_{\mu'}$. The difference $n_{\mu'} - n_\mu = l = 0, \pm 2, \pm 4$ determines the energetic state of the selected spin. By counting the number of spins g_l in the same state l one is able to compute needed to flip a spin.
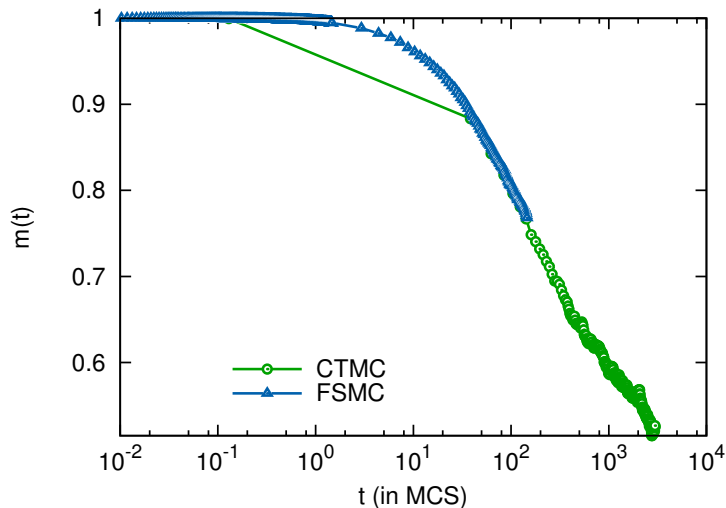
Figure III.7: Time evolution of the horizontal magnetisation in the sixteen-vertex model with: $L = 50$, $a = 2.4$, $b = c = 1$ and $d = e = 0.1$. The simulation starts from an ordered initial configuration where all the arrows point to the right. This data was obtained after averaging over 100 independent simulations. The results obtained with the FSMC and CTMC algorithm are in good agreement. The straight line in the CTMC plot is just due to the fact that we used linepoints and there is no data in between those points far away in time.

III.4.3 Equilibrium analysis of the simulation data

III.4.3.1 Equilibration

The computation of any thermodynamic average must be done only when the system is at equilibrium. Starting from an initial configuration one must run the simulation long enough, until the system has reached thermal equilibrium. This period is the *equilibration time* t_{eq}. It can depend on the initial configuration and it is difficult to predict in general. In order to check equilibration we proceed as follows:

(i) We compute the evolution of some quantity A from different initial conditions. Typically, for a ferromagnet we compute $\langle m(t) \rangle$ from a completely ordered FM and AF initial configurations. The brackets denote a statistical average performed over different independent realisations of the dynamics. In practice, one repeats the simulations for a different sequence of pseudo-random numbers. Usually, equilibrium is identified by a plateau in the evolution of this quantity (usually the energy). This emergence of a dynamical plateau in the simulated time window can be due to a metastable state and not the equilibrium one. This is the reason why we also introduce the next point.

(ii) We compute two-point correlations of the type $C(t, t_w) = \langle A(t)A(t_w) \rangle - \langle A(t) \rangle \langle A(t_w) \rangle$. At equilibrium, the system is time-translational invariant such that $C(t, t_w) = C^{eq}(t - t_w)$. Moreover, C must decay decay to zero for $t - t_w \approx t_{eq}$. For the models studied in this thesis the combination of these two measurements gives a criterium for the equilibration of our simulated samples.

III.4.3.2 Measurements

Once the equilibration has been checked, one can start doing thermal measurements. Independent equilibrium configurations can be generated in two ways:

(i) Let the system evolve from an initial configuration until equilibrium is reached. Repeat that for n different initial configuration uniformly distributed. The n configurations obtained are independent and thermal.

(ii) Let the system evolve from an equilibrium configuration. After a time period t_d the system has decorrelated from its initial configuration. This time is defined by the exponential decay of the equilibrium correlation function:

$$C^{eq}(t - t_{eq}) \propto \exp\left(-\frac{t - t_{eq}}{t_d} \right) \tag{III.61}$$

where $t > t_{eq}$. The time period t_d is the so-called *correlation time*. Then, by waiting periods of t_d one generates independent configurations from the initial equilibrium one. Let the system evolve from $t = 0$. Keep the configurations at times $t_n = t_{eq} + nt_d$. The n configurations obtained in this way are independent and thermally distributed. This second method is expected to be faster than (i) since, usually, $t_{eq} > t_d$.

Suppose we realise n independent measurements of some thermodynamic quantity A and denote $a_1, ..., a_n$ the values of such measurements. Then we estimate the thermal average $\langle A \rangle$ by

$$[A] = \frac{1}{n} \sum_{i=1}^{n} a_i . \tag{III.62}$$

This is what one measures in Monte Carlo simulations.

There are two sources of errors for such numerical measurements: i) *statistical* (from thermal fluctuations) and ii) *systematic* (from mistakes in the procedure we apply to compute the observables), just as for real experiments in a laboratory. Once we have checked the conditions needed to compute the observable we are interested in (e.g. equilibration), we can state that there are no systematic errors in our simulation data. Since we cannot get rid of statistical errors inherent to Monte Carlo techniques we must be able to carefully estimate them.

We denote by $A_1, ..., A_n$ different random realisations of the fluctuating quantity A. The statistical estimator of $\langle A \rangle$ is defined by

$$A^* = \frac{1}{n} \sum_{i=1}^{n} A_i \tag{III.63}$$

and is a random variable. This estimation is unbiased since

$$\langle A^* \rangle = \langle A \rangle \quad \text{and} \quad \sigma^2(A^*) = \frac{\sigma^2(A)}{n} \ . \tag{III.64}$$

A naive estimation of the dispersion $\sigma^2(A) = \langle (A - \langle A \rangle)^2 \rangle$ would be

$$[\sigma(A)] = \sqrt{\frac{1}{n} \sum_i (a_i - [A])^2} \ . \tag{III.65}$$

Unfortunately, this estimation is biased and causes the propagation of systematic errors. A faithful estimation of the standard deviation giving a measure of the statistical error on A is given by

$$\epsilon(A) = \sqrt{\frac{1}{n-1} \sum_i (a_i - [A])^2} \tag{III.66}$$

To perform an estimation of the deviation of another quantity $B = f(A_1, .., A_m)$, which is a function of a set of fluctuating quantities, we proceed as follows. The numerical estimator of $\langle B \rangle$ is

$$[B] = \frac{1}{n} \sum_{i=1}^{n} b_i \ . \tag{III.67}$$

In the limit of small deviations the dispersion of B can be approximated by

$$\sigma(B) \approx \sqrt{\sum_i^m \sigma^2(A_i) \left(\frac{\partial f(\vec{A})}{\partial A_i}_{|A_i = <A_i>} \right)^2} \ . \tag{III.68}$$

Then we estimate this quantity by replacing $\langle A_i \rangle$ and $\sigma^2(A_i)$ by our estimators.

III.4.3.3   Finite-size scaling analysis

Phase transitions can be studied by Monte Carlo simulations using the finite size scaling results presented in section III.3. In frustrated systems the phase diagrams can be very rich and the phase transitions taking place can, in principle, be of different kind. Our analysis must be able to distinguish between different types of phase transitions, determine the associated critical exponents and characterise the nature of the equilibrium configurations. One can proceed as follows:

1. Compute the Binder cumulant $K(t, L^{-1})$ for different system sizes L. If the transition is continuous the Binder cumulant must be monotonic from $K(T \gg 0, L^{-1}) = 0$ to $K(T = 0, L^{-1}) = 2/3$. At a critical point all the curves intersect. Hence, in a quasi-long range phase, all the data points for different system sizes collapse on top of each other. This makes the estimation of a KT transition point very difficult. If the transition is first order the transition temperature $T_c(L)$ is identified from the minimum of the K.

2. If the transition is continuous, use the scaling relation eq. III.49 to estimate the exponent ν. This is done by plotting K as a function of $t.L^{1/\nu}$ for different system sizes. Then we vary the value of $1/\nu$ until the data collapses into a single curve close to the transition.

3. Compute the maximum of the specific heat C^{max} for different sizes. If the transition is first order it scales as $C^{max} \sim L^d$. If instead it is continuous, it scales as $C^{max} \sim L^{\alpha/\nu}$. Using the estimation of the critical temperature and the exponent ν the exponent α can be estimated by data collapse. Check the consistency of this value of α with the value of ν previously determined by plotting $C.L^{-\alpha/\nu}$ as a function of $t.L^{1/\nu}$.

4. Compute the order parameter m and the susceptibility χ for different system sizes. If the transition is continuous the exponents β and γ can be estimated from $m(T_c(L)) \sim L^{-\beta/\nu}$ and $\chi^{max} \sim L^{\gamma/\nu}$.

5. Check the scaling laws eq. (III.13) and eq. (III.15).

In this form, finite-size scaling analysis is unable to distinguish between a continuous phase transitions for which $\xi \to \infty$ and a first order transition for which ξ is finite but larger than the maximum size of the system available in simulations. In order to give support to our results on $2D$ spin ice we also used a different numerical technique: the *Non-Equilibrium Relaxation Method* (NERM).

III.4.4   Non-equilibrium relaxation method

The numerical investigation of phase transitions usually exploits directly equilibrium results, by first sampling the canonical ensemble of a finite system and then performing a finite size analysis of the data. The NERM exploits the dynamical behaviour of the system to deduce equilibrium properties. This is done by letting the system relax towards equilibrium from a non-equilibrium initial condition. Using this method one avoids the difficulties raised by a correlation lenght $\xi > L$ but finite. A precise review on this method can be found in [211] and [3].

III.4.4.1   Short-time critical dynamics

Classical spin models do not have any intrinsic dynamics. To study the evolution of such a system we must begin by defining *a priori* updating rules. In the following we consider the relaxation of a spin model in contact with a thermal bath, exchanging energy with it. Therefore, the dynamical rules do not conserve energy and are stochastic. For this problem a natural choice is to introduce a local single-spin-flip kinetic rule - e.g. of the Monte Carlo type - without any conserved order parameter.

The choice of the microscopic dynamics is part of the modelling of the physical situation one is interested in. Depending on this choice, the system sets into different *dynamical universality classes* [117, 208]. The theory of *dynamical critical phenomena* extends the ideas of scaling and universality of equilibrium critical phenomena to the time-evolution properties of statistical models. In the vicinity of a critical point the correlation length diverges. Therefore, the system has to establish correlations between spins over an infinite range in order to reach equilibrium, a process which takes a diverging period of time τ. This is the so-called *critical slowing down*. The dynamical scaling hypothesis (which is less well founded that its equilibrium analog) asserts that the divergence of τ is characterised by a power law which defines the dynamical critical exponent z:

$$\tau \sim \xi^z \, . \tag{III.69}$$

Dynamical scaling extends the crucial notion of scale invariance in equilibrium critical phenomena for the time dependence of thermodynamic quantities. This exponent is strongly affected by the dynamical rules chosen in the simulations. During the evolution towards the critical point, the size

of the correlated regions given the time-dependent correlation length $\xi(t)$ grows accordingly to this exponent:

$$\xi(t) \sim t^{1/z} \, . \tag{III.70}$$

A field theoretic approach was proposed by Janssen et. al to describe the dynamical scaling behaviour of thermodynamic quantities evolving from an initial condition with a given magnetisation $m(0)$ and short range correlations [128]. By an RG analysis of a field theory with stochastic non-conserved order parameter dynamics (in the same universality class as the single-spin flip evolution in spin models), he showed that the evolution of the order parameter at the critical point is given by

$$m(t) \simeq t^{-\beta/(\nu z)} \, F(t^{x_0/z} m(0)) \tag{III.71}$$

with z the dynamic critical exponent, x_0 a new exponent which depends on the initial configuration and F a scaling function which verifies: $F(x) \simeq x$ for $x \ll 1$ and $F(x) \to$ ct for $x \to \infty$. In finite size simulations, this scaling form should be correct for 'short times'. By short times we mean here periods of time which are longer than some microscopic time t_μ but short enough to guarantee $\xi(t) \ll L$. This condition reduces finite size effects and avoids the need for the proper equilibration of the samples.

Suppose that one starts the evolution from a disordered initial state: $m(0) \ll 1$. Then we adjust the external parameters in order to be at a critical point (i.e. we perform a quench to the critical point). For times short enough such that $t^{x_0/z} m(0) \ll 1$ the magnetisation is given by

$$m(t) \simeq t^{-\beta/(\nu z)} t^{x_0/\nu} \simeq t^\theta \, , \quad t^{x_0/z} m(0) \ll 1 \tag{III.72}$$

where $\theta > 0$ is the so-called *initial flip* exponent. The order parameter initially grows. For longer times $t^{x_0/z} m(0) \gg 1$ the magnetisation decreases algebraically:

$$m(t) \simeq t^{-\beta/(\nu z)} \, , \quad t^{x_0/z} m(0) \gg 1 \, , \tag{III.73}$$

which allows for a determination of $\beta/(\nu z)$.

Suppose now that one starts the evolution from a completely ordered configuration: $m_0 = 1$. The time-evolution of m is given by [53]

$$m(t) \simeq t^{-\beta/(\nu z)} \, . \tag{III.74}$$

Together with the scaling eq. (III.73) one can extract important informations about the equilibrium properties of the system. For instance, the critical point. It can be determined by letting the system relax from an initial configuration (with $m(0) \ll 1$ or $m(0) = 1$) towards different points of the phase space. A critical point is characterised by a power law evolution of the order parameter, whereas it decays exponentially fast to its equilibrium value for a non-critical point. The departures from critical dynamics are very sensitive to small modifications of the parameters which allows for a precise location of the critical point.

The relaxation behaviour of the order parameter is also valuable for the study KT transitions [213]. The study of this transition by equilibrium measurements is hard because of the correlation length increases exponentially when approaching the transition and makes the equilibration times of the samples very long. In the XY model, the whole low temperature phase is critical. Therefore, for all $T \leq T_{KT}$ the relaxation of the order parameter from an ordered initial state must decay algebraically. From this simple observation one can deduce if a phase is critical or not and if a KT transition can occur. From the dynamical scaling of the relaxation time one can also determine the KT transition temperature precisely. I refer to [213, 211] for further details about relaxation studies for the KT transition.

III.4.4.2 NERM for a first-order phase transition

Finite-size scaling analysis of the simulation data is unable to distinguish between a second-order phase transition and a weak first order transition. By weak first order transition we mean here first order transitions with a finite but large, typically larger than the size of the system, correlation length. The NERM exploits the hysteresis phenomenon to determine the transition point and, more importantly to us, to give a criterium to distinguish between weak first order and second order transitions [2, 212].

Consider the relaxation of the system from a disordered (high temperature) initial configuration: $m(0) \ll 1$. By repeating the process at different temperatures, we get an estimation of the transition temperature T^* from power law time-dependence of m. The temperature T^* is a measure of the limit of metastability T_- of the ordered phase ($T^- < T_c$ as shown in Fig. III.1). At this point the disordered phase becomes stable and large (but finite) fluctuations are present. For a finite size system, it is equivalent to a critical point. One can repeat the same procedure from an ordered initial configuration: $m(0) = 1$ and get a different estimation of the transition temperature T^{**}. This value is a measure of the limit of metastability $T_+ > T_c$ of the disordered phase. This approach has been supported by numerical studies on exactly solvable models where the limit of metastability can be rigorously defined and computed [212, 168]. At a second order phase transition $T^* = T^{**} = T_c$.

IV

Hard constraints and $2D$ vertex models

If you are receptive and humble, mathematics will lead you by the hand.

Paul Dirac

Before Onsager's solution of the $2D$ Ising model in 1944 [210], the definition of a phase transition from fundamental statistical mechanics was a matter of debate. Mean field results and other approximations were already available but though to be too artificial to capture the real essence of phase transitions in real physical systems. The Ising model is probably the most simple model with a thermal phase transition and its precise study set the grounds of the theory of critical phenomena.

Twenty years later, the development of the renormalisation group (RG) theory clarified the concept of universality which theoretically explains the observation that, very different physical systems share the same critical exponents. In the context of 2D spin systems, models with different and unexpected universality classes were constructed. An example is the six-vertex model. The exact solution of particular cases of this model (ice, KDP and F model, see below) was accomplished by Lieb in 1967. He applied the Bethe *Ansatz* and exploited the formal equivalence between the six-vertex model and the XXZ spin chain solved a few months before by Yang and Yang [274].

The exact solution of the six-vertex model shows that the critical exponents depend on the precise values of the microscopic parameters. This model appeared then as a counterexample of the universality ideas coming from the RG theory. The theoretical physics community did not paid much attention to this results until the exact solution of the eight-vertex model by Baxter came out in 1971 [22]. The non-universality of the six-vertex model was though to result from the pathological definition of the model through '*hard constraints*' (here the ice rules). However this variation of critical exponents was confirmed by the exact solution of the less pathological eight-vertex model: its exponents also change continuously and lead to the six-vertex model ones by taking the appropriate limit. In order to do so, Baxter (and Yang [273]) introduced the Yang-

Baxter equation which, as we will discuss in this section was a capital contribution to the theory of *quantum integrability*.

In this chapter we review some exact results on constrained vertex models in order to discuss the role of a local constraint in the collective behaviour of the system. A detailed discussion on the equilibrium properties of the completely unconstrained sixteen-vertex models is let for the next chapter V.

IV.1   Exactly solvable lattice models

For sake of completeness, we include in this section we add some rapid comments on integrability issues for 'non-mathematical physicists'. A more precise exposition on this vast subject can be found in the references given in the text.

IV.1.1   The Yang-Baxter equation

Consider a statistical model on a square lattice [1]. A degree of freedom, an Ising spin for simplicity, is attached to each edge of the lattice. Let us focus on a vertex where two lines intersect as shown in Fig. IV.1. One associates to each line of the lattice a vector space $V_{h,v}$ indexed by h (as horizontal) and v (as vertical) (see Fig. IV.1).The Boltzmann weight of a configuration of four edges meeting at a vertex is encoded by a linear operator acting on the tensor product $V_h \bigotimes V_v$: the R-matrix. For Ising problems on a square lattice the $V_{h,v} \simeq \mathbb{C}^2$ and the R-matrix is a 4×4 matrix which gives the weight of the 2^4 possible configurations:

$$R_{h,v} = \begin{pmatrix} \langle + + |R| + + \rangle & \langle + + |R| + - \rangle & \langle + + |R| - + \rangle & \langle + + |R| - - \rangle \\ \langle + - |R| + + \rangle & \langle + - |R| + - \rangle & \langle + - |R| - + \rangle & \langle + - |R| - - \rangle \\ \langle - + |R| + + \rangle & \langle - + |R| + - \rangle & \langle - + |R| - + \rangle & \langle - + |R| - - \rangle \\ \langle - - |R| + + \rangle & \langle - - |R| + - \rangle & \langle - - |R| - + \rangle & \langle - - |R| - - \rangle \end{pmatrix} \qquad \text{(IV.1)}$$

$$w(i,j) = \quad \mu_i^j \xrightarrow{\quad h \quad} \mu_i^{j+1} \quad = \langle \alpha_i^j, \mu_i^j |R_{h,v}| \alpha_{i+1}^j, \mu_i^{j+1} \rangle$$
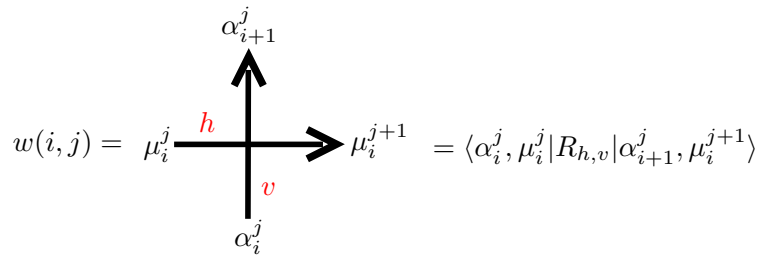
Figure IV.1: Graphical representation of the weight of a vertex with the edge variables α and μ. The arrows denote the abstract direction induced by the action of R (from bottom left to top right). The subscripts i denote a line of the lattice and the superscripts j a column.

The R-matrix is the central object to consider when one is interested in the integrability of the model. The model is said to be *integrable* provided its R-matrix satisfies:

1. The Yang-Baxter equation:

$$R_{12}R_{13}R_{23} = R_{23}R_{12}R_{13} \qquad \text{(IV.2)}$$

2. and the identity equation:

$$R_{12}R_{21} \propto 1_d. \qquad \text{(IV.3)}$$

---

1. Note that the following concepts can be extended to more general planar graphs with connectivity 4

These two equations are usually represented graphically as shown in Fig. IV.2.
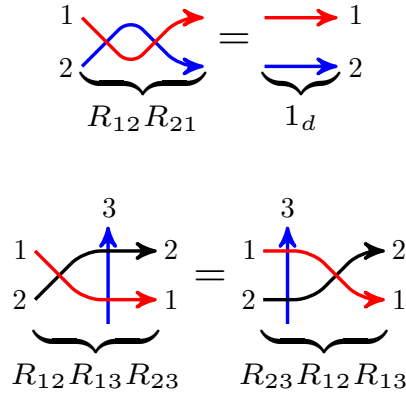
Figure IV.2: Digrammatic representation of the integrability conditions. Top: Identity equation. Bottom: Yang-Baxter equation.

IV.1.2 Classical and quantum integrability

In classical mechanics, a Hamiltonian system is said to be *integrable* if it satisfies *Liouville's theorem* [11, 12]. Consider a dynamical system with N degrees of freedom definig a $2N$-dimensional phase space Γ. Then, a system is Liouville's integrable if it has N functionally independent [2] integrals of motion $\{F_i\}_{i=1..N}$ in mutual involution, i.e.

$$\{H, F_i\} = 0 \, , \quad \{F_i, F_j\} = 0 \, , \quad \forall i, j = 1..N \ . \tag{IV.6}$$

So that the evolution of the system takes place on a compact and connected sub-manifold $M \subset \Gamma$ defined by some constant value of the integrals of motion. The solution of the equations of motion are periodic trajectories on M such that ergodicity is lost. Hence, integrable and non-integrable systems have very distinct dynamical properties.

One could be tempted to generalise this notion to quantum systems using the canonical quantisation prescription and replace Poisson brackets by commutators times $i/\hbar$. However, when trying to extend Liouville's theorem to hermitian operators acting on a Hilbert space, the notion of functional independence is lost. This definition of quantum integrability does not provide a correspondence between classical and quantum integrability [267]. At this day, there is still no unique and well accepted definition of quantum integrability. The correspondence between the non-ergodicity arising from classical integrability and the relaxation properties of quantum many-body systems is far from being clear and motivates a large number of current investigations (for a review see [217]). The relationship between the available definitions of quantum integrability and the out-of-equilibrium behaviour observed in quantum systems is still a matter debate. A recent

---

2. A set of N real functions of M variables

$$F_i(x_1, ...x_n) \, , \quad i = 1, ...M \tag{IV.4}$$

is functionally independent if and only if

$$\Psi[F_1, ...F_M] = 0 \Rightarrow \Psi = 0 \ . \tag{IV.5}$$

It is a generalisation of the notion of linear independence. Hence, analytic functions of the Hamiltonian H are trivial integrals of motion but do not fulfil Liouville's conditions. Note that this definition of independence cannot be extended to hermitian operators acting on a Hilbert space.

review on the different definitions of quantum integrability encountered in the literature can be found in [61].

Back to lattice models in classical statistical mechanics, the notion of integrability comes from the Yang-Baxter equation (IV.2) together with the identity relation eq.(IV.3). Let us explain quickly why. The operator R is assumed to depend on the difference of two *spectral parameters* λ and μ. These are related to the Boltzmann weights given by the Hamiltonian of the model via an appropriate parametrisation. The entries of the R-matrix, for instance $\langle + - |R| + - \rangle$, are replaced by some function of $\lambda - \mu$. The transfer matrix T can then be written as a product R-matrices along a line (see eq. (IV.17) for an explicit example). The R-matrix can be seen as the contribution of a vertex to the partition function which can be constructed by applying the R-operator at each vertex.

If the R-matrix of our lattice model verifies the integrability conditions eq. (IV.2) and (IV.3), then transfer matrices $T(\lambda)$ with different spectral parameters λ form an infinite set of commuting linear operators. All these operators can then be diagonalised simultaneously (for instance by using the Bethe *Ansatz*). Moreover, the transfer matrix of a $2D$ model describes the evolution of a $1D$ quantum system defined by the Hamiltonian:

$$H = -\frac{d}{d\lambda} \ln T(\lambda) \mid_{\lambda=0} \ . \tag{IV.7}$$

The commutativity of the transfer matrices allows to construct an infinite set of conserved quantities Q_i defined by

$$Q_i = -\frac{d^i}{d\lambda^i} \ln T(\lambda) \mid_{\lambda=0} \ , \tag{IV.8}$$

and verifying

$$[H, Q_i] = 0 \ , \quad [Q_i, Q_j] = 0 \ , \quad \forall i, j \in \mathbb{N} \ . \tag{IV.9}$$

We obtain in this way a quantum analog of Liouville's theorem eq. (IV.6): a $2D$ statistical lattice model verifying eq. (IV.2) and (IV.3) is said to be quantum integrable.

IV.2   Vertex models: general definition

In this Section we recall the definition and main equilibrium properties of bi-dimensional Ising-like vertex models defined on a square lattice. We focus on an $L \times L$ square lattice $\mathcal{V}$ with periodic boundary conditions. We label the coordinates of the lattice sites by (α, β). This lattice is bipartite, that is, it can be partitioned in two sub-lattices A and B of even $\alpha + \beta$ and odd $\alpha + \beta$ sites such that each edge connects a site in A to one in B. The degrees of freedom sit on the links, in other words, on sites of the 'medial' lattice $\hat{\mathcal{V}}$ that are placed on the midpoints of the bonds of the original lattice. The midpoints are hence labeled $(\alpha + 1/2, \beta)$ and $(\alpha, \beta + 1/2)$ [3]. We consider models in which the degrees of freedom are arrows aligned along the edges of the square lattice that can be naturally mapped onto Ising spins, say $S_{\alpha+1/2,\beta} = \pm 1$ (see Fig. IV.3). We choose a convention such that the positive value corresponds to an arrow pointing in the right or up direction, and conversely for negative spin: $S = 1$ if the arrow on the corresponding edge points along $\vec{u}_x$ or $\vec{u}_y$ and $S = -1$ otherwise. Then, instead of defining the system's Hamiltonian by an explicit interaction term between the Ising variables we assign a Boltzmann weight $\omega_k = \exp(-\beta\epsilon_k)$ to each of the $k = 1, \ldots, 2^4$ four-arrow configurations that may occur at vertex (α, β) (see Fig. V.1).

---

3. The lattice made by all the Ising variables is the medial graph of the original $L \times L$ square lattice where each site is occupied by a vertex.

The Hamiltonian of the general vertex model in the square lattice is then simply defined by the sum of the vertex energies

$$H = \sum_{(\alpha,\beta)} \epsilon_{(\alpha,\beta)} = \sum_{k=1}^{16} \epsilon_k n_k \qquad \text{(IV.10)}$$

where n_k is the number of vertices of type k.

A *charge* can be attributed to each single vertex configuration. Its definition is simply the number of in-coming minus the number of out-going arrows. We recall the definition of a charge given by

$$q = \frac{1}{2} \sum_{i \in v} \sigma_i \ \in \ \{0, \pm1, \pm2\}. \qquad \text{(IV.11)}$$

where $\sigma = \pm1$ if the arrow points into or out to the vertex v under consideration.
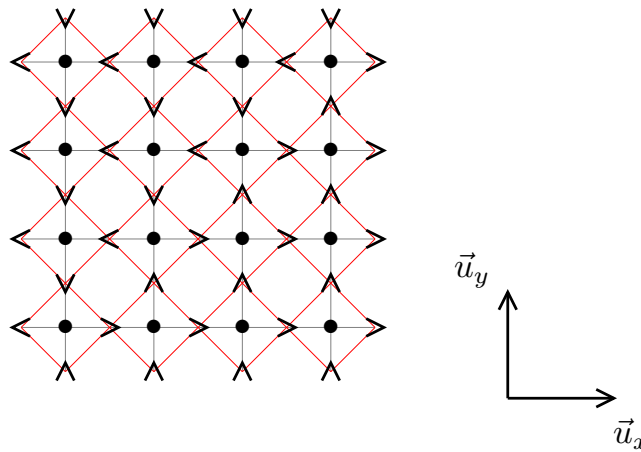

Figure IV.3: The square lattice of vertices $\mathcal{V}$ is represented in grey. Its medial lattice $\hat{\mathcal{V}}$ made by the centre of each edge occupied by an arrow is shown in red.
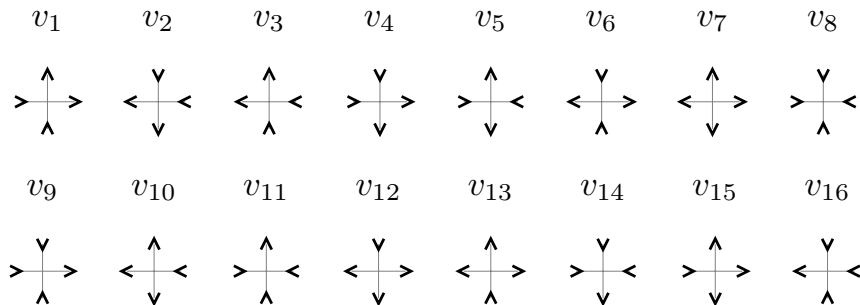

Figure IV.4: The sixteen vertex configurations of the square lattice.

IV.3   The six-vertex model

IV.3.1   Definition

In the six vertex model arrows or Ising spins sit on the edges of a (coordination four) square lattice and they are constrained to satisfy the two-in two-out ice rule [30, 215]. In consequence, each node on the lattice has four spins attached to it with two possible directions, in the form shown in Fig. IV.5. Accordingly to eq. (IV.11), the six-vertex model vertices have zero charge. (Note that the charge is not the sum of the spins attached to a vertex, such a *total spin* will be defined and used in sec. V.4.)
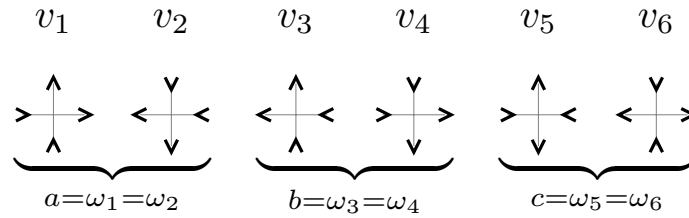
Figure IV.5: The six possible vertex configurations in the six vertex model with their associated weights.

Although in the initial modelling of ice all such vertices were equivalent, the model was generalised to describe ferroelectric systems by giving different statistical weights to different vertices: $\omega_k = \exp(-\beta \epsilon_k)$ with ϵ_k the energy of each of the $k = 1, \ldots, 6$ vertices. Spin reversal symmetry naturally imposes $\omega_1 = \omega_2 = a$ for the first pair of ferromagnetic vertices, $\omega_3 = \omega_4 = b$ for the second pair of ferromagnetic vertices, and $\omega_5 = \omega_6 = c$ for the anti-ferromagnetic ones, see Fig. IV.5. Note that since the vertices v_5 and v_6 act as sources and sinks of vertical and horizontal arrows, we must have the same number of them on each row and column if we impose periodic boundary conditions (PBC) and one has $\omega_5 = \omega_6 = c$ without symmetry assumptions. The conventional parameter names a, b, c have been introduced here. In the theoretical literature it is customary to parametrize the phase diagram and equilibrium properties in terms of a/c and b/c. This is the choice we also make here. Particular cases of the six-vertex model include:

- the *F model* of anti-ferroelectrics: the energy of the antiferromagnetic c-vertices is set to zero and all other ones are taken to be equal and positive, i.e. $c > a = b$ [231].
- the *KDP model* of ferroelectrics : the energy of a pair of ferromagnetic a- or b-vertices is set to zero and all other ones are equal and positive, e.g. $a > b = c$ [243].
- the *Ice model*: the energy of all vertices are equal, i.e. $a = b = c$ [165].

It is important to note, however, that in the context of experiments in artificial spin-ice type samples vertex energies are fixed and the control parameter is something used to prepare different configurations. Then, it is associated to a temperature. In [161] we used this alternative parametrisation and we compared the model predictions to experimental observations [206, 196]. We shall present these results in the next chapter.

IV.3.2   Transfer matrix formulation

The net arrow flux in the vertical (or horizontal) direction is conserved from row to row (respectively column) as a consequence of the ice-rules. From the flux conservation, the six-vertex model can be represented by non-crossing paths or strings going 'north-east' (NE). Edges with arrows pointing up or right are marked while edges with arrows down or left are unmarked, as

shown in Fig. IV.6 (this convention follows from the one we used in section IV.1 for the spectral parameters). One can interpret these paths as trajectories of particles where time evolution is along the vertical direction. There can be several arrangements of horizontal bonds in between to rows of vertical edges. As shown below, the row-to-row *transfer matrix* T is obtained after summing over all these possible arrangements of horizontal arrows. Then T encodes this 'vertical' time evolution. It is a linear operator acting on a row $|\phi_i\rangle$ (a 2^L dimensional vector) which generates the next one $|\phi_{i+1}\rangle$. With PBC, the initial and final state are identical, hence the partition function Z is a 'discrete path integral' along a closed loop:

$$Z = \sum_{|\phi_1\rangle} ... \sum_{|\phi_L\rangle} \langle\phi_1|T|\phi_{L-1}\rangle...\langle\phi_2|T|\phi_1\rangle = \mathrm{Tr}\, T^L \, , \qquad (\mathrm{IV.12})$$

which in the thermodynamic limit is given by the largest eigenvalue of T denoted λ_0.

The Because of the ice-rules, open paths are forbidden, hence the number of vertical 'red' edges is conserved from row-to-row. In the particle picture, it means that the transfer matrix must conserve the number of particles n. Thus T splits into $L + 1$ diagonal blocks: $T = \oplus_{n=0}^{L} T^{(n)}$. Each block $T^{(n)}$ is called a *topological sector* defined by n, the number of particles or strings in the system. A sector is left invariant by T. They are said to be *topologically protected* since no smooth deformation of the strings, hence no thermal fluctuation below the critical point, can change the number n. This number is a topological property of a given configuration which cannot be changed by updating a finite number of arrows (this point might become clearer after the discussion of the phase diagram). Then, in order to find the largest eigenvalue of T one can apply the Bethe *Ansatz* and solve the Bethe equations for each sector.

The 'coordinate'-Bethe *Ansatz* consist on trying a particular form for the eigenvector with largest eigenvalue of each block $T^{(n)}$. The so-called Bethe many-body wave function (this terminology comes from Bethe's work on the XXX quantum spin chain) is a completely anti-symmetrised product of one-body wave functions. Back to the six-vertex model, the eigenvalue problem writes:

$$\sum_{\mathbf{y}} T^{(n)}(\mathbf{x}, \mathbf{y})\phi(\mathbf{y}) = \lambda_n \phi(\mathbf{x}) \qquad (\mathrm{IV.13})$$

where $\mathbf{x} = (x_1, ..., x_n)$ gives the location of the coloured vertical bonds. The vector $\mathbf{x}$ specifies a configuration of the system after summation over the intermediate horizontal arrows. The Bethe *Ansatz* then tries the form:

$$\phi(\mathbf{x}) = \sum_{\{P\}} A_{p_1,...,p_n}\varphi(x_1)_{p_1}...\varphi(x_n)_{p_n} \qquad (\mathrm{IV.14})$$

where the sum runs over all the permutations $P = (p_1, ..., p_n)$, $A_{p_1,...,p_n}$ are constants (antisymmetric under permutation of the indices) and $\varphi(x)_i$ are solutions of eq. (IV.13) for the one particle sector $n = 1$. The calculations are long and carried on in detail in Baxter's book [25]. Most of the results presented in section IV.3.3 come from these calculations.

The reason why one can actually find the largest eigenvalue of T, i.e. solve the model, is because it is integrable. In order to show that, let us write the partition function of the six-vertex model as

$$Z = \sum_{l \in \mathcal{C}} \prod_{i=1}^{L} \prod_{j=1}^{L} w^l(i, j) \qquad (\mathrm{IV.15})$$

where $w^l(i, j)$ is the Boltzmann weight of the vertex at site (i, j) for a configuration $l \in \mathcal{C}$. For convenience, we denote by α the spin variables defined on the horizontal edges of the lattice and μ the vertical ones (see Fig. IV.1). The vertex weight is given by the R-matrix:

$$w^l(i, j) = \langle\alpha_i^j, \mu_i^j|R|\alpha_{i+1}^j, \mu_i^{j+1}\rangle \qquad (\mathrm{IV.16})$$
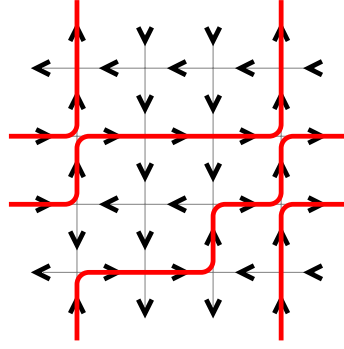
Figure IV.6: A particular configuration of the six-vertex model and its NE path representation shown in red lines. The number of strings in a row of vertical edges (here $n = 2$) is conserved.

where $\alpha_i^j = \pm 1$ denotes the spin linked to the vertex (i, j) from below and $\mu_i^j = \pm 1$ denotes the spin linked from the left (as shown in Fig. IV.1).

The transfer matrix can be constructed by adding vertex contributions and can hence be written as a product of R-matrices:

$$\langle \bar{\alpha}_i | T | \bar{\alpha}_{i+1} \rangle = \sum_{\mu_i^1 = \pm 1} \dots \sum_{\mu_i^L = \pm 1} \prod_j \langle \alpha_i^j, \mu_i^j | R | \alpha_{i+1}^j, \mu_i^{j+1} \rangle \qquad \text{(IV.17)}$$

The variable μ_i^1 appears in both extremities, so this sum is a trace over it represented in Fig. IV.7.

The R-matrix of the six vertex model is given by

$$R(u) = \begin{pmatrix} a(u) & 0 & 0 & 0 \\ 0 & b(u) & c(u) & 0 \\ 0 & c(u) & b(u) & 0 \\ 0 & 0 & 0 & a(u) \end{pmatrix} \qquad \text{(IV.18)}$$

where we have introduce the spectral parameter u [4]. This matrix verifies eq. (IV.2) and eq. (IV.3): the six-vertex model is quantum integrable, its transfer matrix T can be identified with the evolution operator of the XXZ quantum spin chain. We will go back to the equivalence between vertex models and quantum spin chains later on in section IV.4.4.

Figure IV.7: Graphical representation of the transfer matrix of the six-vertex model.

---

4. The dependence of R on the spectral parameters appears in the parametrisation of the weights. In the PM phase, it is convenient to parametrize the weights by:

$$a = \sin(\gamma - u) \,, \; b = \sin(u) \,, c = \sin \gamma \,, \quad \Delta = \cos \gamma \quad (0 < \gamma < \pi/2) \,. \qquad \text{(IV.19)}$$

IV.3.3   Equilibrium phase diagram

The free-energy density of the six vertex model with $a = b = c$ and periodic boundary conditions was computed by Lieb in the late 60s with the transfer matrix technique and the Bethe *Ansatz* to solve the eigenvalue problem [165]. The method was then extended to calculate the free-energy density of the the F model [163], KDP model [164], models with generic a, b, c values with periodic boundary conditions (PBC) [248], and the same general case with antisymmetric [?] and domain wall boundary conditions (DWBC) [146]. The effect of the boundary conditions is indeed very subtle in these systems as some thermodynamic properties depend upon them [145] contrary to what happens in conventional statistical physics models. An order parameter that allows one to characterise the different phases is the total *direct* and *staggered* magnetisation per spin

$$\langle M_\pm \rangle = \frac{1}{2}(\langle |m_\pm^x| \rangle + \langle |m_\pm^y| \rangle) \tag{IV.20}$$

with the horizontal and vertical fluctuating components given by

$$L^2 m_\pm^x = \sum_{(\alpha,\beta)\in A} S_{\alpha+1/2,\beta} \pm \sum_{(\alpha,\beta)\in B} S_{\alpha+1/2,\beta} \,, \tag{IV.21}$$

$$L^2 m_\pm^y = \sum_{(\alpha,\beta)\in A} S_{\alpha,\beta+1/2} \pm \sum_{(\alpha,\beta)\in B} S_{\alpha,\beta+1/2} \,. \tag{IV.22}$$

The angular brackets $\langle \ldots \rangle$ denote here and in the following the statistical average.

The equilibrium phases are classified by the anisotropy parameter

$$\Delta_6 = \frac{a^2 + b^2 - c^2}{2ab} \,, \tag{IV.23}$$

and they are the following.

a-Ferromagnetic (*a*-FM) *phase*: $\Delta_6 > 1$; i.e. $a > b + c$. Vertices v_1 and v_2 are favoured. The lowest energy state in the full FM phase is doubly degenerate: either all arrows point up and right (shown in Fig. [IV.8 (a)]) or down and left [i.e. $M_+ = 1$, with M_+ the magnetisation density defined in eq. (V.36)]. In this phase the system is frozen as the only possible excitations involve strings made by a number of degrees of freedom of the order of L. All over this phase the exact free energy per vertex is flat and given by [25]

$$f_{\text{FM}} = \epsilon_1 \,. \tag{IV.24}$$

At $a = b + c$ ($\Delta_6 = 1$) the system experiences a discontinuous phase transition between the frozen ferromagnet and a disordered (D) or spin liquid (SL) phase that we discuss below.

b-Ferromagnetic (*b*-FM) *phase*: $\Delta_6 > 1$; i.e. $b > a + c$. This phase is equivalent to the previous one by replacing a- by b-vertices. The free-energy is $f_{\text{FM}} = \epsilon_3$.

Spin liquid (SL) *phase*: $-1 < \Delta_6 < 1$; i.e. $a < b + c$, $b < a + c$ and $c < a + b$. In this phase the averaged magnetization is zero, $\langle M_\pm \rangle = 0$, and one could expect the system to be a conventional paramagnet. However, the ice constraints are stringent enough to prevent the full decorrelation of the spins all over the lattice, even at infinite temperature. The system is in a quasi long-range ordered phase with an infinite correlation length. At $c = a + b$ there is a Kosterlitz-Thouless phase transition between this critical phase and an anti-ferromagnetic phase with staggered order that is discussed below. The exact solution found by Baxter yields the free-energy density as a function of the parameters through a number of integral equations [25]. In the following section

we evaluate it numerically and we compare it to the outcome of the Bethe approximation. Close to the FM transition the singular part of the free-energy can be approximated by

$$f_{\text{FM}}^{(s)} \simeq \max(\epsilon_1, \epsilon_3) - \frac{1}{2}k_B T \left(\frac{b+c}{a} - 1\right) = \max(\epsilon_1, \epsilon_3) - \frac{1}{2}k_B T \, t^{2-\alpha} \,, \qquad (\text{IV.25})$$

with t the reduced distance to criticality, $t = (b+c)/a - 1$, and α an exponent that plays the rôle of the one of the heat-capacity and takes the value $\alpha = 1$ here. The first derivative of f_{SL} with respect to the distance from the transition t shows a step discontinuity at the SL-FM transition corresponding to a discontinuous phase transition but with a well defined set of critical exponents (see Fig. IV.1). Accordingly to the frozen-to-critical transition scenario discussed in section III.2.3.

Some special points in parameter space belonging to the SL phase deserve a few comments. Such as the ice point $a = b = c$ for which $\Delta_6 = 1/2$. At this special point the ground state is macroscopically degenerate giving rise to the residual entropy [165]

$$S/N = 3/2 \, \ln 4/3 \,. \qquad (\text{IV.26})$$

Another special set of points is defined by the *free-fermion* [5] condition $a^2 + b^2 = c^2$ ($\Delta_6 = 0$). If this relation between the parameters is verified, the integral equations simplify and the model can be solved using Pfaffians. It has been found that the correlations of the F model in the free fermion line decay as r^{-2} [20].

Antiferromagnetic (AF) *phase*: $\Delta_6 < -1$; i.e. $c > a + b$. Vertices v_5 and v_6 are favoured. The ground state is doubly degenerate, corresponding to the configurations $M_- = \pm 1$. The staggered order is not frozen, thermal excitations involving only a finite number of spins populate this phase. This is confirmed by the exact expression of the staggered magnetisation found by Baxter [20, 24]. The free energy has an essential singularity at the critical line (towards the SL phase)

$$f_{\text{AF}} \simeq e^{-\text{ct}/\sqrt{t}} \,, \qquad (\text{IV.27})$$

with ct a constant and $t = (a+b)/c - 1$ the distance to criticality, characteristic of an infinite order phase transition.

The transition lines are straight lines (given by $\Delta_6 = 1$ for the SL-FM and $\Delta_6 = -1$ for the SL-AF) and they are shown in Fig. IV.15 with solid (red) lines. The dashed line along the diagonal is the range of variation of the parameters in the F model. The horizontal dashed line is the one of the KDP model. The intersection of this two lines corresponds to the ice-model. Although the transitions are not of second order, critical exponents have been defined and are given in the first column of Table IV.1. The exponent α is taken from the expansion of the free-energy close to the transition, see eqs. (IV.25) and (IV.27). The ratios

$$\hat{\gamma} = \gamma/\nu \,, \quad \hat{\beta} = \beta/\nu \,, \quad \hat{\phi} = (2 - \alpha)/\nu \qquad (\text{IV.28})$$

follow from the use of the (divergent in the SL phase) correlation length ξ instead of t as the scaling variable [250] (see section III.1.4). As explained when we treat the eight-vertex model in section IV.4, these exponents generalise the concept of universality. Interestingly enough, the values of $\hat{\gamma}$, $\hat{\beta}$ and $\hat{\phi}$ are constant along the two transition lines and, moreover, they coincide with the ones of the 2D Ising model and the 2D XY model recalled in the last two columns of Table IV.1. They also satisfy the usual scaling relations. The exponents β, γ and ν are extrapolated from the eight-vertex model ones in the form explained in the next section.

---

5. As explained in more detail in section IV.4.4 that name comes from the mapping to the XXZ quantum spin chain. The fermionic representation of the XXZ model via the Jordan-Wigner transformation shows the equivalence with a free-fermion problem in 1D.
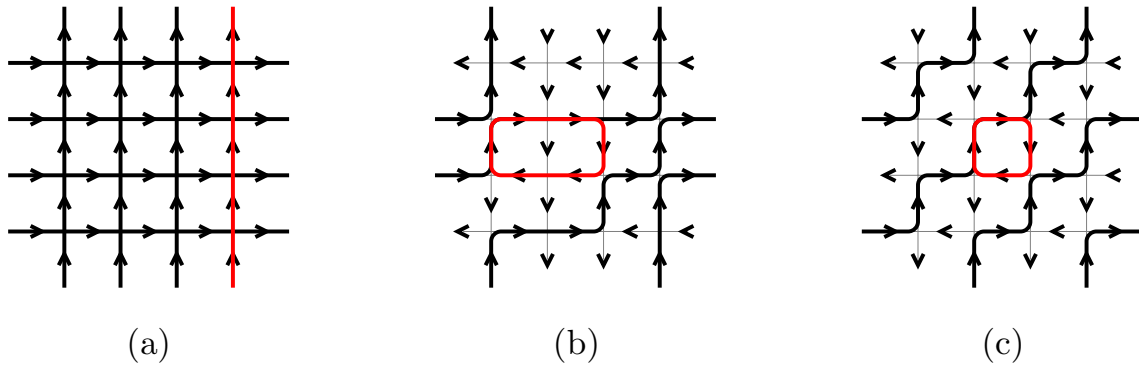
Figure IV.8: Equilibrium phases of the six-vertex model. The NE paths are represented by thick black lines. Typical fluctuations are shown by red lines. (a) a-FM ordered configurations. The only possible excitations of the system are extended strings spanning the whole lattice. (b) SL configuration. Excitations in the form of local loops are possible. (c) Saturated c-AF order. Elementary loops involving the four spins around a square plaquette are the lowest energy excitations populating the system in this phase.

IV.3.4 Height representation

In the study of crystal growth, solid-on-solid (SOS) models are theoretical simplifications introduced for the investigation of the *roughening transition* and the equilibrium shapes of interphases. In general, a SOS model is a constrained model for crystal growth where vacancies are forbidden. In the case of a body-centred cubic crystal (BC) , the SOS model can be mapped on to the six vertex model [26]. Since the equilibrium phase diagram of the latter is known exactly, this mapping allows for an exact description of the roughening transition.

The body-centred SOS model (BCSOS) is a constrained version of the BC Ising model with a nearest-neighbours (NN) coupling J_0 and next-to-nearest neighbours (NNN) coupling J_x, J_y and J_z along the three cartesian axes (shown in Fig. [IV.9 (b)]). We impose to all the spins in the bottom to be up (occupied sites represented in black in Fig. IV.9) and all the spins in the top to be down (vacancies represented in white in Fig. IV.9). The solid-on-solid constraint consists in fixing $J_0 \ll J_{x,y,z}$ and J_x, J_y, J_z constant. Therefore, a vacancy cannot be found below an occupied site. This constraint ensures the existence of a single domain wall or surface separating occupied sites from empty regions. One can specify in a unique way a configuration of the model by giving the shape of this domain wall. The coordinates $(x, y, h(x, y))$ of the occupied sites on the surface define a *height configuration* h describing a surface. The height difference between two nearest neighbour sites is constrained to be either 1 or -1 (in units of $l_0/2$, where l_0 is the lattice parameter). One can identify the configuration of four sites in the BCSOS with a vertex of the six-vertex model as shown in Fig. [IV.9 (d)]. This exact mapping is completed by giving the following relations:

$$\epsilon_1 = \epsilon_2 = J_y - J_x , \quad \epsilon_3 = \epsilon_4 = J_x - J_y , \quad \epsilon_5 = \epsilon_6 = -J_x - J_y . \qquad \text{(IV.29)}$$

Then both models share the same partition function.

The ice-rules make possible to represent the six-vertex model in the square lattice by a height function h. A height variable h_i is assigned to each site of the dual lattice (i.e. each square plaquette). One can construct a configuration of heights from a six-vertex model configuration in the following way. Fix some reference height, for instance $h = 0$ at the plaquette located in the

	SL-FM	SL-AF	$2D$ Ising	$2D$ XY
$\gamma/\nu = \hat{\gamma}$	7/4	7/4	7/4	7/4
$\beta/\nu = \hat{\beta}$	1/8	1/8	1/8	1/8
$(2-\alpha)/\nu = \hat{\phi}$	2	2	2	2
η	1/4	1/4	1/4	1/4
δ	15	15	15	15
α	1	∞	0	∞
β	1/16	∞	1/8	∞
γ	7/8	∞	7/4	∞
ν	1/2	∞	1	∞

Table IV.1: Critical exponents of the SL-FM and SL-AF transition lines of the six-vertex model compared to the ones of the $2D$ Ising model and the $2D$ XY model. The 'hat' exponents have been defined by using ξ as the parameter measuring the deviation from the critical point instead of t.

northwest corner of the lattice. The height is increased by one if, when traveling from the left to the right, or from the top to the bottom, we cross a spin pointing up or right. The height is decreased by one otherwise. This construction is illustrated in Fig. IV.10. Accordingly to these rules, one can associate to each vertex a unique (up to a constant) set of four integers as shown in Fig. IV.11. One can summarise these mapping by the equation:

$$h_{i+1} = h_i + \left(\vec{v}_{i,i+1} \times \vec{S}_{i,i+1} \right) \cdot \vec{u}_z \ . \tag{IV.30}$$

The vector $\vec{S}_{i,i+1}$ gives the direction of the arrow sitting on the edge between the two plaquettes i and $i+1$; $\vec{v}_{i,i+1}$ gives the direction followed during the construction of the heights. Since we are dealing with a square lattice : $(\vec{v}_{i,i+1} \times \vec{S}_{i,i+1}) \cdot \vec{u}_z = \pm 1$. It should be clear from this equation that one must assign arbitrarily the height h_0 of some plaquette before constructing h by recursion. Once this *gauge* h_0 has been fixed we can deduce from eq. (IV.30) the value of the height h_i at any site by recursion:

$$h_i = h_0 + \sum_{j=0 \ , \ j \in \mathcal{C}}^{i-1} \left(\vec{v}_{i,i+1} \times \vec{S}_{i,i+1} \right) \cdot \vec{u}_z \tag{IV.31}$$

where the sum is done all along an *arbitrary path* $\mathcal{C}$ from 0 to i. The height function is well defined since the value h_i is independent of the path chosen to compute it. Equivalently, the circulation of the height difference along any closed path denoted Γ is zero. We define the connection $\vec{A}_{i,i+1} = (h_{i+1} - h_i) \, \vec{v}_{i,i+1}$. Then, eq. (IV.31) is equivalent to

$$\sum_{j \in \Gamma} \vec{A}_{i,i+1} \cdot \vec{l}_{i,i+1} = 0 \quad \equiv \quad \oint_{\Gamma} \vec{A}.d\vec{l} = 0 \tag{IV.32}$$

where $\vec{l}_{i,i+1}$ is the displacement vector from site i to site $i+1$. From this equation if becomes clear that, when the gauge has been fixed, the uniqueness of the height function comes from the fact that there are no defects in the system.

From Fig. IV.11 we deduce that a flat a configuration of the BCSOS corresponds to an antiferromagnetic state in the six-vertex model. The *roughening transition* corresponds to the AF-SL transition of the F model. This transition is known to be of the KT type. From the Villain's representation of the XY model, we know that a duality transformation relates the discrete gaussian model, which is the simplest surface model, with the XY model [64]. From duality, the high
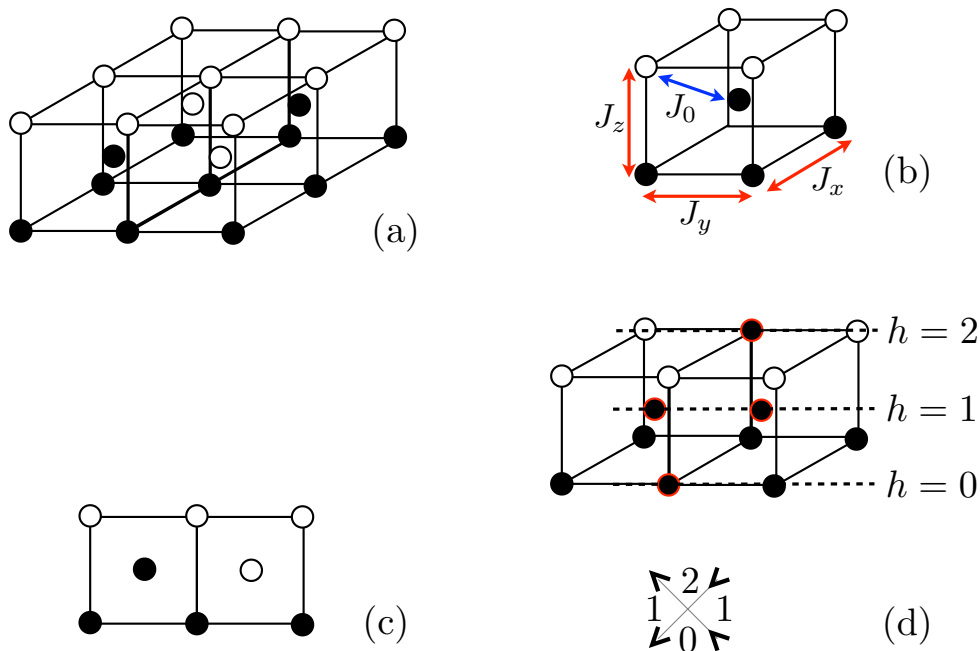
Figure IV.9: **Body-Centered Solid-On-Solid model (BCSOS).** (a) A particular configuration of the BCSOS for a small system made by four unit cells. Black and white dots represent occupied and empty sites respectively. (b) The interactions occuring in a unit cell. The NN interaction J_0 is represented in blue. The NNN ones in red. (c) The configuration in (a) observed along the x-axis. The height difference from site to site cannot be larger than a half of the lattice spacing. (d) The vertex configuration corresponding to the four occupied sites on the surface shown with a red ring.

temperature phase of the BCSOS model (rough) is mapped into the low temperature state of the F model (ordered AF), and the low temperature phase of the SOS model (flat) is mapped into the hight temperature phase of the F model, which is critical.

IV.3.5 Topological sectors and boundary conditions

In section IV.3.2 we introduced the concept of topological sector from the block diagonal decomposition of the transfer matrix. Then, in the discussion of the phase diagram we insist in the frozen-to-critical character of the FM transition due to the non-local nature of the excitations. In modern condensed matter terminology, the SL phase would be said to be a *topologically ordered phase*.

In the six-vertex model, strings fall into distinct homotopy classes, depending on whether or not they can be deformed into each other by smooth transformations (without intermediate intersections). The ice-rules divide the phase space into disconnected sectors characterised by the number of winding loops. Only transformations involving an extensive number of constituents of the system can make us visit all the configurations. If one only allows local updates can take the system from one state to another, ergodicity is broken [57]. This might be responsible of some kind of glassy dynamics. Recently, some authors have studied the slow dynamics due to this topological ergodicity breaking in hardly constrained models [65, 60, 63].

Consider the height representation of the six-vertex model on an $L \times L$ square lattice with PBC. At the boundaries the height function verifies: (i) $h(x, L) = h(x, 0) - n_r + (L^2 - n_r)$,
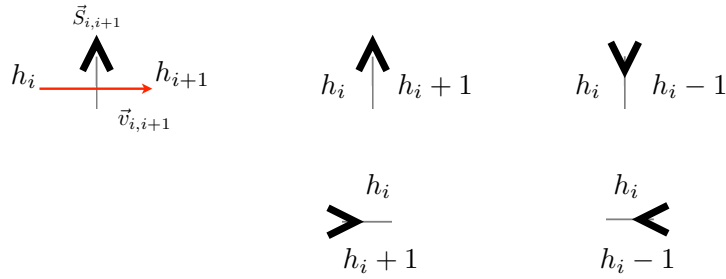
Figure IV.10: **Height representation of the six-vertex model.** The vector $\vec{v}_{i,i+1}$ is represented by an horizontal red arrow. It links two nearest neighbours of the dual lattice. The spin variable $\vec{S}_{i,i+1}$ equals $\pm\vec{u}_x$ if the black arrow points right or left and $\pm\vec{u}_y$ if it points up or down. The four possible height increments are shown.
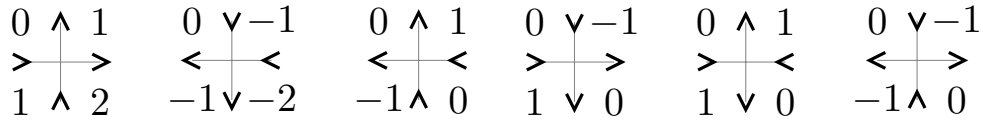
Figure IV.11: The six-vertices allowed by the ice-rules and the corresponding height configurations.

where n_r denotes the number of arrows pointing to the right one crosses when going from the bottom of the lattice towards the top; (ii) $h(L, y) = h(0, y) + n_u - (L^2 - n_u)$, where n_u denotes the number of arrows pointing up one crosses when going from the left of the lattice towards the right. The values of n_u and n_r define a topological sector. The connection with the definition given in section IV.3.2 is straightforward: n_u is equivalent to the number of marked lines (particles) in the NE path representation (see Fig. IV.6). By flipping local loops of arrows one can deform these paths and generate new configurations in the same sector. The difference between the height of the plaquettes in the horizontal and vertical boundaries is left identical. The value of the magnetisation in the horizontal and vertical direction is given by: $m_+^x = n_r - L^2$ and $m_+^y = n_u - L^2$. Hence, the magnetisation is left invariant under local transformations within a sector such that one can also characterise a sector by the value of the magnetisation.

In order to have winding loops and topological sectors one needs to 'close' the lattice from the boundaries, for instance using PBC. If we define the same model in a lattice with fixed boundary conditions string excitations of the FM phase do not belong anymore to a different homotopy class than the ones in the PM and AF phases and the system becomes 'ergodic'. Thus, we expect that different boundary conditions can notably affect the dynamical properties of the system. Dynamical properties will be discussed in chapter VI. The dependence of the phase space structure of the six-vertex model under different boundary conditions has been studied in [110].

The choice of the boundary conditions must satisfy the constraint. A particular choice of fixed boundary conditions which has attracted a great deal of attention is the so-called *Domain Wall Boundary conditions* (DWBC) [146]. The six-vertex model with DWBC can be exactly solved [145, 40], showing that the choice of the boundary conditions can affect the equilibrium

thermodynamic properties of the system as well. The DWBC consist on fixing all the arrows in boundary lines of the lattice to point into the bulk and all the arrows in the boundary columns to point out, as shown in Fig. IV.12. The phase diagram of the model is not altered by the boundary conditions. However, a complete order cannot be established with DWBC.

The six-vertex model with this particular choice of boundary conditions is closely related to important problems in combinatorics:

(i) There is a bijection between the six-vertex model with DWBC and *alternating sign matrices* (ASM). An ASM is a square lattice made of 0s, 1s and -1s such that the sum of each row and column is equal to 1 and the nonzero entries alternate sign in each row and column. The combinatorial problem of counting the number of such matrices of size n is equivalent to computing the partition function of the ice model ($\Delta_6 = 1/2$) with DWBC on a $n \times n$ lattice [152].

(ii) The six-vertex model with DWBC in the free-fermion point ($\Delta_6 = 0$) is equivalent to the *dimer model* in the Aztec diamond lattice [89, 140]. Reknown mathematicians (such as the 2006 Fields Medal, Andrei Okounkov) have been interested into this problem. They studied the the height function associated to this problem and found the *limit shape* separating different thermodynamic states. The emergence of an interface between a disordered and an ordered regions is the so-called *Arctic circle phenomenon*. In the six-vertex model at $\Delta_6 = 0$ the limit shape is a circle which delimits a FM region close to the boundaries and a SL region in the bulk. The SL region inside the circle is larger than the ordered phase. The ratio between the SL and FM phase is constant such that an extensive FM region is still present in the thermodynamic limit. This is shown in Fig. IV.12. Numerical simulations have given support for the existence of limit shapes away from the free-fermion point as well [253, 6].
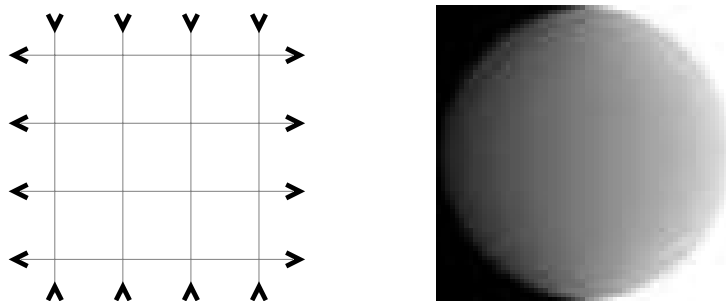
Figure IV.12: Left: Domain Wall Boundary Conditions in a 4×4 square lattice. Right: Numerical results for a 64×64 lattice from [253]. Greyscale plot of the horizontal local magnetisation (from -1 in black to $+1$ in white) for $a = b$ and $\Delta_6 = 0$. The grey disk is a SL region, clearly separated from FM regions of opposite magnetisation.

IV.4 The eight-vertex model

IV.4.1 Definition

The eight-vertex model is a generalisation of the six-vertex model introduced to remove its very unconventional properties due to the ice-rule constraint (frozen FM state, quasi long-range order at infinite temperature, etc.) [249, 92]. In this model the allowed local configurations are the ones with an even number of arrows pointing in or out of each vertex, adding the two vertices with weight d shown in Fig. IV.13 to the ones in Fig. IV.5. It was first solved by Baxter in the zero-field

case (i.e., with Z_2 symmetry) [22, 23].

$$v_1 \qquad v_2 \qquad v_3 \qquad v_4 \qquad v_5 \qquad v_6 \qquad v_7 \qquad v_8$$

$$\underbrace{}_{a=\omega_1=\omega_2} \quad \underbrace{}_{b=\omega_3=\omega_4} \quad \underbrace{}_{c=\omega_5=\omega_6} \quad \underbrace{}_{d=\omega_7=\omega_8}$$
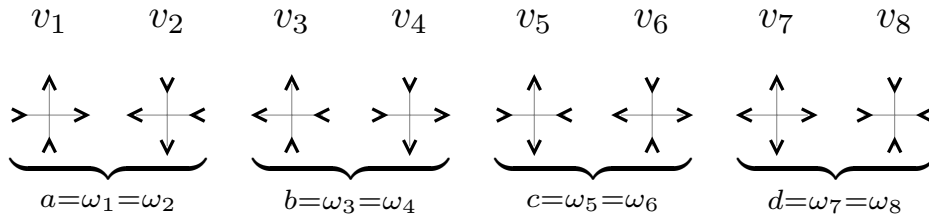
Figure IV.13: The eight vertex configurations with an even number of incoming and outgoing arrows.

Using the same NE convention as for the six-vertex model, the eight vertex model can be represented by non-intersecting loops as well. A typical configuration is shown in Fig. IV.14. The number of coloured links (bonds) incident at a vertex is always even, such that the NE paths form closed loops. Note however that the particle interpretation is no long valid in this case. The number of bonds is not conserved from row to row and the arrows along the loops do not define orientated paths. The solution of the eight-vertex model problem turns out to be much more involved than the six-vertex such that we refer the interested reader to Baxter's book for further details [25]. In the following we present some results of importance for the present work.
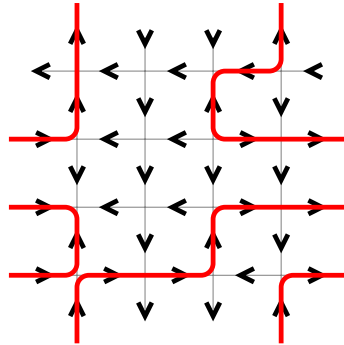
Figure IV.14: Path representation of the eight vertex model. The partition function of the eight-vertex model is equivalent to the weighted enumeration of closed polygons.

IV.4.2   Exact solution

The phase diagram of the eight-vertex model is characterized by the anisotropy parameter

$$\Delta_8 = \frac{a^2 + b^2 - c^2 - d^2}{2(ab + cd)} \tag{IV.33}$$

which becomes the six-vertex one when $d = 0$ (see eq.(IV.23)). This model sets into the following five phases depending on the weight of the vertices:

Ferromagnetic phase I (a-FM): $\Delta_8 > 1$ ($a > b + c + d$). This ordered phase is no longer frozen and $M_+ \leq 1$ is a continuous function of the parameters. Topological order is broken by the introduction of v_7 and v_8, i.e. by the relaxation of the ice-rules.
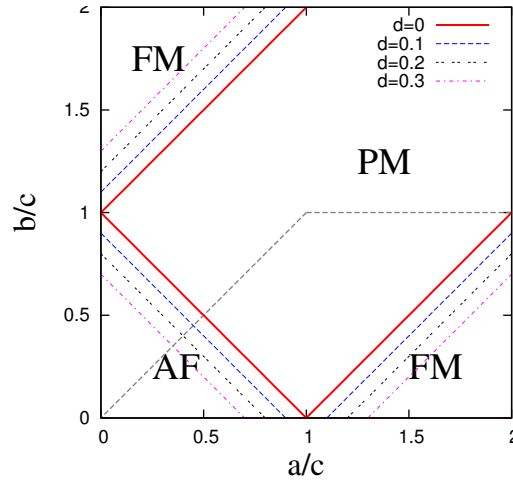
Figure IV.15: The phase diagram of the six- (red solid lines) and eight- (dashed lines) vertex models. In the case of the latter, the projection on the $d = 0$ plane is shown. Only for $d = 0$ the PM region becomes a SL phase.

Ferromagnetic phase II (b-FM): $\Delta_8 > 1$ ($b > a + c + d$). Fluctuations also exist in this ordered phase, equivalent to the previous one by replacing a-vertices by b-vertices; $M_+ \leq 1$.

Paramagnetic phase (PM): $-1 > \Delta_8 > 1$ [$a, b, c, d < (a + b + c + d)/2$]. As soon as $d > 0$ this phase is truly disordered, with a finite correlation length. The magnetisation vanishes $M_\pm = 0$.

Antiferromagnetic phase I (c-AF): $\Delta_8 < -1$ ($c > a + b + d$). The configurations are dominated by c-vertices with an alternating pattern of vertices of type 5 and 6 with defects; $M_- \leq 1$.

Antiferromagnetic phase II (d-AF): $\Delta_8 < -1$ ($d > a + b + c$). The configurations are dominated by d-vertices, with an alternating pattern of vertices 7 and 8 with defects. M_- is also different from zero in this phase; this order parameter does not allow one to distinguish this phase from the c-AF.

The transition lines are given by $\Delta_8 = 1$ for the PM-FM transitions and $\Delta_8 = -1$ for the PM-AF ones. The projection of the critical surfaces on the $d = 0$ plane yields straight lines translated by d/c with respect to the ones of the six-vertex model, in the direction of enlarging the PM phase, as shown with dashed lines in Fig. IV.15.

The effect of the d-vertices on the order of the different phase transitions is very important. As soon as one quits the $d = 0$ plane, the KT line between the c-AF and the SL phases becomes 'stronger' and the intersection between this and the $a = 0$ or $b = 0$ planes are of the KDP type (following our classification described in section III.2.3). On the contrary, the KDP transition lines between the FMs and SL phases become 'softer' when entering the $d > 0$ space and they become KT lines on the $a = 0$ and $b = 0$ planes. Finally, the separation between the d-AF and disordered phases is second order for a, b, $d > 0$ and it is of KT type on the $a = 0$ and $b = 0$ planes. As we will show in chapter V , this is consistent with our numerical results.

The critical exponents can be found from the analysis of the free-energy density close to the transition planes. Close to the $c = a + b + d$ surface the singular part of the free energy behaves as

$$f_s \sim |t|^{\pi/\mu} \ln |t| \quad \text{for} \quad \mu = \pi/n, \; n \in \mathbb{N} \,, \tag{IV.34}$$

$$f_s \sim |t|^{\pi/\mu} \qquad \text{otherwise} \tag{IV.35}$$

where

$$t = \frac{(a - a_c)(b - b_c)(c - c_c)(d - d_c)}{16abcd} \tag{IV.36}$$

is the deviation from the critical point and μ is a function of the vertex weights defined by [22]

$$\tan(\mu/2) = \sqrt{cd/ab} \,. \tag{IV.37}$$

The singular behaviour of all the other transitions occurring in the model can be deduced from this one. This can be done by using the symmetries of the model [25]:

$$Z_{8V}(a, b, c, d) = Z_{8V}(b, a, d, c) = Z_{8V}(b, a, c, d) = Z_{8V}(c, d, a, b) \,. \tag{IV.38}$$

Therefore, the critical exponents depend explicitly on the weights of the vertices via μ. They are given in the second column of Table IV.2.

On the $d \to 0$ plane of the phase diagram, where μ goes to 0, the AF-PM transition is *inifite order* and the six-vertex exponents given in the second column of Table IV.1 are recovered. The six-vertex model exponents associated with the FM-SL are also found by taking the limit $d \to 0$ when the parameter $\mu \to \pi$.

In the $b \to 0$ and $a \to 0$ manifolds, where μ goes to π, the AF-PM transition is *discontinuous*. This can be easily check from the critical exponents given in Table IV.2. For $\mu = 0$ we get "$\alpha = -\infty$" and $\alpha = 1$ for $\mu = \pi$, accordingly with the six-vertex model exponents. The critical exponents of the six- and eight vertex models are strongly dependent on the weight given to each vertex. This apparently violates the universality principle. In order to restore a 'kind of universality' Suzuki proposed in 1974 [250] to define new critical exponents using ξ as the scaling variable instead of t. Note that the same approach was used by Kosterlitz the same year for the XY model [148] (as mentioned in section III.1.4). Following this idea we define a new set of exponents $\hat{\gamma}$, $\hat{\alpha}$ and $\hat{\beta}$ by

$$\chi \sim \xi^{\hat{\gamma}}, \quad M \sim \xi^{-\hat{\beta}}, \quad C \sim \xi^{\hat{\alpha}} \,. \tag{IV.39}$$

Then $\hat{\beta} = \beta/\nu = 1/8$, independently of the details of the microscopic interactions. If one applies the scaling relations the other exponents η and δ are identical to the ones of the $2D$ Ising model and XY model:

$$\delta = 15, \quad \eta = \frac{1}{4} \,. \tag{IV.40}$$

Moreover, these new exponents verify the scaling relations. They are fixed by the value of the magnetic exponent δ and the dimension d of the model:

$$\hat{\gamma} = d \frac{\delta - 1}{\delta + 1}, \quad \hat{\beta} = \frac{d}{\delta + 1}, \quad \hat{\phi} = d, \quad \eta = 2 - d \frac{\delta - 1}{\delta + 1} \,. \tag{IV.41}$$

IV.4.3   Ising representation in the dual lattice

The eight-vertex model on a square lattice $\mathcal{V}$ is equivalent to an Ising model on its dual lattice $\mathcal{V}^*$ [133]. There is a one-to-one correspondence between a vertex configuration and a configuration of its four adjacent Ising spins as depicted in Fig. IV.16. An upward and rightward pointing arrow (a "+" spin located on an edge of $\mathcal{V}$) attached to a vertex corresponds to a pair of parallel Ising spins located at the center of the adjacent plaquettes (sites of $\mathcal{V}^*$). This representation is invariant by global spin reversal, meaning that there are $2^4/2 = 8$ different configurations as expected. In this way an Ising variable $\sigma_{ij} = \pm 1$ is attached to each site of $\mathcal{V}^*$. In order to complete the Ising representation of the vertex model one must establish the deduce the interactions between spins from the vertex weights. In the general eight-vertex model there are six interaction parameters:

	eight-vertex	$2D$ Ising	$2D$ XY
$\gamma/\nu = \hat{\gamma}$	7/4	7/4	7/4
$\beta/\nu = \hat{\beta}$	1/8	1/8	1/8
$(2-\alpha)/\nu = \hat{\phi}$	2	2	2
η	1/4	1/4	1/4
δ	15	15	15
α	$2 - \pi/\mu$	0	∞
β	$\pi/(16\mu)$	1/8	∞
γ	$7\pi/(8\mu)$	7/4	∞
ν	$\pi/(2\mu)$	1	∞

Table IV.2: Exact critical exponents of the six- and eight-vertex model with $\tan(\mu/2) = \sqrt{cd/ab}$. (The way in which the values for the six-vertex model are derived is explained in the text.) The critical exponents of $2D$ Ising model are recalled in the third column for comparison.

ω_1, ω_2, ω_3, ω_4, c and d. This is due to the fact that $v_{5,6,7,8}$ act as sources and sinks of arrows flux and must then be in equal number if one imposes PBC. Then, without loss of generality one can fix $\omega_5 = \omega_6 = c$ and $\omega_7 = \omega_8 = d$. The simplest Hamiltonian with interactions between the spins around a vertex (nearest and next-nearest neighbours spins), satifying the symmetry of the model and with the same number of parameters is

$$H = -J_0 - \sum_i \sum_j (J_1^x \sigma_{ij}\sigma_{i,j+1} + J_1^y \sigma_{ij}\sigma_{i+1,j}$$
$$+ J_2 \sigma_{i,j+1}\sigma_{i+1,j} + J_2' \sigma_{ij}\sigma_{i+1,j+1} + K\sigma_{ij}\sigma_{i,j+1}\sigma_{i+1,j}\sigma_{i+1,j+1}). \tag{IV.42}$$

This generalised Ising model includes two body and four body interactions without an external field. Anisotropic interactions between nearest neighbour spins are given by J_1^x and J_1^y, between next-nearest neighbour spins by J_2 and J_2' and the four spin interaction by K. The interactions between four spins surrounding a vertex are illustrated in Fig. IV.16. It is important to note here that the eight vertex model constraint $\alpha_{ij}\alpha_{i+1,j}\mu_{ij}\mu_{i,j+1} = 1$ is verified.
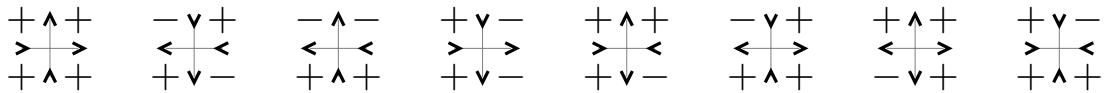
Figure IV.16: Equivalence between the eight-vertex configurations and the Ising spin arrangements in the dual lattice.

The correspondence between the coupling between spins and vertex weights is now straightforward. Consider each vertex configuration and compute the contribution of the Ising Hamiltonian. We obtain

$$\omega_1 = \exp[-\beta(J_0 + J_1^x + J_1^y + J_2 + J_2' + K)]$$
$$\omega_2 = \exp[-\beta(J_0 - J_1^x - J_1^y + J_2 + J_2' + K)]$$
$$\omega_3 = \exp[-\beta(J_0 + J_1^x - J_1^y - J_2 - J_2' + K)]$$
$$\omega_4 = \exp[-\beta(J_0 - J_1^x + J_1^y - J_2 + J_2' + K)]$$
$$\omega_5 = \omega_6 = c = \exp[-\beta(J_0 + J_2 - J_2' - K)]$$
$$\omega_7 = \omega_8 = d = \exp[-\beta(J_0 - J_2 + J_2' - K)]. \tag{IV.43}$$

The parameter J_0 is irrelevant for energetic considerations but must be added to the Hamiltonian IV.42 in order to have an invertible set of linear equations between the vertex energies and the interaction parameters. One can invert the linear set of equations obtained by taking the log of eq. IV.4.3 and write

$$
\begin{aligned}
J_0 &= -1/8(\epsilon_1 + \epsilon_2 + \epsilon_3 + \epsilon_4 + 2\epsilon_5 + 2\epsilon_7) \\
J_1^x &= 1/4(-\epsilon_1 + \epsilon_2 - \epsilon_3 + \epsilon_4) \\
J_1^y &= 1/4(-\epsilon_1 + \epsilon_2 + \epsilon_3 - \epsilon_4) \\
J_2 &= 1/8(-\epsilon_1 - \epsilon_2 + \epsilon_3 + \epsilon_4 - 2\epsilon_5 + 2\epsilon_7) \\
J_2' &= 1/8(-\epsilon_1 - \epsilon_2 + \epsilon_3 + \epsilon_4 + 2\epsilon_5 - 2\epsilon_7) \\
K &= 1/8(-\epsilon_1 - \epsilon_2 - \epsilon_3 - \epsilon_4 + 2\epsilon_5 + 2\epsilon_7).
\end{aligned}
\tag{IV.44}
$$

We can normalize the vertex energies such that $J_0 = 0$ and forget about the contribution coming from the constant term in eq. IV.4.3. The symmetric zero-field eight-vertex model $a = \omega_1 = \omega_2$, $b = \omega_3 = \omega_4$ corresponds to an Ising model with

$$
\begin{aligned}
J_1^x &= J_1^y = 0 \\
J_2 &= 1/4(-\epsilon_1 + \epsilon_3 - \epsilon_5 + \epsilon_7) \\
J_2' &= 1/4(-\epsilon_1 + \epsilon_3 + \epsilon_5 - \epsilon_7) \\
K &= 1/4(-\epsilon_1 - \epsilon_3 + \epsilon_5 + \epsilon_7).
\end{aligned}
\tag{IV.45}
$$

and equivalently

$$
\begin{aligned}
a &= \exp[-\beta(J_2 + J_2' + K)] \\
b &= \exp[-\beta(-J_2 - J_2' + K)] \\
c &= \exp[-\beta(J_2 - J_2' - K)] \\
d &= \exp[-\beta(-J_2 + J_2' - K)]
\end{aligned}
\tag{IV.46}
$$

The critical exponents are given by $\tan(\mu/2) = \sqrt{\frac{cd}{ab}} = e^{-2K}$. Therefore, the four-body interaction is responsible for the variation of critical exponents. The nearest-neighbour interactions vanish in the absence of an external field. The six-vertex model limit $d \to 0$ is not well defined in this representation since it corresponds to a non-trivial way of taking infinite interaction parameters. The eight-vertex model is equivalent to two interpenetrating Ising models coupled by the four spin interaction K. In the particular case $K = 0$ these two Ising models are independent and the thermodynamics of the eight-vertex problem become identical to the ones of the usual $2D$ Ising model. In particular, the free energy density of the eight vertex model is identical to the one computed by Onsager [6]:

$$
f_8 = f_{Ising}
\tag{IV.47}
$$

From eq. IV.45, the four spin interaction vanishes in the so-called *free fermion point*

$$
\epsilon_1 + \epsilon_3 = \epsilon_5 + \epsilon_7 \, .
\tag{IV.48}
$$

From this condition we get $J_2 = J_2'$ and

$$
a^2 + b^2 = c^2 + d^2 \, , \quad \Delta_8 = 0 \, .
\tag{IV.49}
$$

The free fermion condition was originally introduced to express the solvability of generalised Ising models [120, 92]. It is well known that the $2D$ Ising model solved by Onsager is equivalent to a
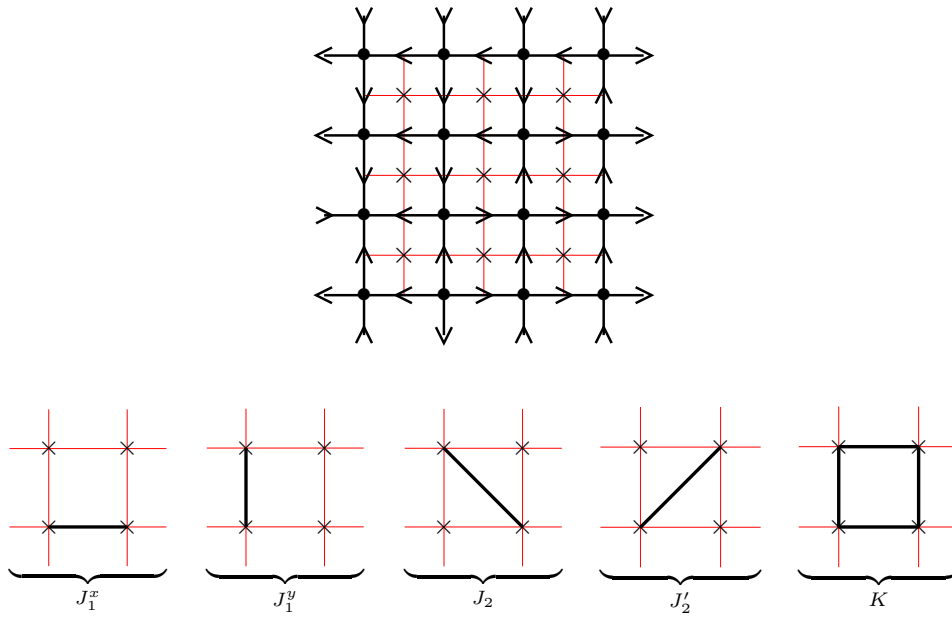
Figure IV.17: The eight vertex model square lattice shown in black with each vertex denoted by a dot and the corresponding sites of the dual lattice (in red) where the Ising spins are defined shown by crosses.

$1D$ chain of free fermions [235]. Similarly, the eight vertex model at the free fermion point turns out to be equivalent to a chain of free fermions, hence 'easily' solvable.

In view of the non-integrable sixteen-vertex problem, it is important to note here in what extent the equivalence with this Ising model is particular of the eight-vertex model. Let's define binary variables on the links of the original lattice $\mathcal{V}$. For all the vertices $w(i,j)$ we define two binary variables α_{ij} and $\alpha_{i+1,j}$ for vertical bonds and two for horizontal bonds denoted by $\mu_{i,j}$ and $\mu_{i,j+1}$. For the eight vertex model they are defined in the Ising representation by

$$\alpha_{ij} = \sigma_{ij}\sigma_{i,j+1}$$
$$\mu_{ij} = \sigma_{ij}\sigma_{i+1,j} \tag{IV.50}$$

This definition implies that, for all (i,j), the eight vertex model constraint is verified since

$$\alpha_{ij}\alpha_{i+1,j}\mu_{ij}\mu_{i,j+1} = 1 \tag{IV.51}$$

The Hamiltonian IV.42 can now be rewritten in terms of these new variables. We get

$$H = -\sum_{ij} \left(J_1^x \alpha_{ij} + J_1^y \mu_{ij} + J_2 \alpha_{ij}\mu_{ij} + J_2' \alpha_{i+1,j}\mu_{ij} + K\alpha_{ij}\alpha_{i+1,j} \right) \tag{IV.52}$$

This Ising representation of the model in the dual lattice can not be extended to the general sixteen-vertex problem. A different approach will be used in the next section.

As already mentioned, the exact solution of the eight-vertex model shows that the critical exponents are continuous functions of the interaction parameters. This contradicts *a priori* the

---

6. In the Ising case where $K = 0$ then $\mu = \pi/2$ and one finds the Ising exponents. For instance, $\beta = \pi/16\mu = 1/8$ when $\mu = \pi/2$.

universality hypothesis. The Ising model representation of the problem gives light into the source of this pathological behaviour. It was introduced by Kadanoff and Wegner to understand the origin of this apparent violation of universality. They argue that the four spin interaction gives rise to a marginal operator conjugate to K which gives K-dependent exponents [133].

IV.4.4 The Heisenberg XYZ spin chain

The transfer matrix of a classical two-dimensional statistical model can be thought of as an operator acting on the Hilbert space of a one-dimensional quantum many-body system. The partition function of the eight-vertex model in a square lattice $\mathcal{V} = L \times L$ can be written as

$$Z = \sum_{l \in \mathcal{C}} \prod_{i=0}^{L} \prod_{j=0}^{L} w^l(i,j) \tag{IV.53}$$

where $w^l(i,j)$ is the Boltzmann weight of the vertex at site (i,j) for a configuration $l \in \mathcal{C}$. The vertex weight can be re-written by introducing the R-matrix:

$$w^l(i,j) = \langle \alpha_i^j, \mu_i^j | R | \alpha_{i+1}^j, \mu_i^{j+1} \rangle \tag{IV.54}$$

where $\alpha_i^j = \pm 1$ denotes the spin linked to the vertex (i,j) from below and $\mu_i^j = \pm 1$ denotes the spin linked from the left. Here we use the same notations as in section IV.3.2. For the eight-vertex model the R-matrix is given by [7]

$$R = \begin{pmatrix} \omega_1 & 0 & 0 & \omega_7 \\ 0 & \omega_3 & \omega_6 & 0 \\ 0 & \omega_5 & \omega_4 & 0 \\ \omega_8 & 0 & 0 & \omega_2 \end{pmatrix} \tag{IV.55}$$

The partition function then reads

$$Z = \sum_{|\alpha\rangle} \sum_{|\mu\rangle} \prod_{(i,j) \in \mathcal{V}} \langle \alpha_i^j, \mu_i^j | R | \alpha_{i+1}^j, \mu_i^{j+1} \rangle = \sum_{|\alpha\rangle} \prod_{i} \langle \{\alpha_i\} | T | \{\alpha_{i+1}\} \rangle = \mathrm{Tr}\, T^L . \tag{IV.56}$$

The $2.2^L \times 2.2^L$ row-to-row transfer matrix T is given by

$$\langle \{\alpha_i\} | T | \{\alpha_{i+1}\} \rangle = \sum_{\mu_i^1 = \pm 1} \cdots \sum_{\mu_i^L = \pm 1} \prod_{j} \langle \alpha_i^j, \mu_i^j | R | \alpha_{i+1}^j, \mu_i^{j+1} \rangle . \tag{IV.57}$$

For convenience we note

$$T(i, i+1) = \sum_{\mu_i^1 = \pm 1} \cdots \sum_{\mu_i^L = \pm 1} \prod_{j} \langle \mu_i^j | R_i | \mu_i^{j+1} \rangle = \mathrm{Tr}_2\, (R_1.R_2...R_L) , \tag{IV.58}$$

where the trace is taken over the 2×2 matrix where each entry is an operator on a row of L spins. We defined the linear operator R_i acting on a row of horizontal edges such as

$$\langle \mu | R_i | \mu' \rangle = \langle \alpha_i, \mu | R | \alpha_{i+1}, \mu' \rangle \tag{IV.59}$$

which is the $2.2^L \times 2.2^L$ matrix:

$$R_i = \begin{pmatrix} \langle +, \mu | R | +, \mu' \rangle & \langle +, \mu | R | -, \mu' \rangle \\ \langle -, \mu | R | +, \mu' \rangle & \langle -, \mu | R | -, \mu' \rangle \end{pmatrix} . \tag{IV.60}$$

---

7. In the Z_2-symmetric case solved by Baxter: $\omega_1 = \omega_2 = a$, $\omega_3 = \omega_4 = b$, $\omega_5 = \omega_6 = c$ and $\omega_7 = \omega_8 = d$.

Each entry in this array corresponds to a $2^L \times 2^L$ matrix since each row $|\mu\rangle$ is a 2^L-dimensional vector. For the eight-vertex model one gets

$$R_i = \frac{1}{2} \begin{pmatrix} (\omega_1 + \omega_4)\mathbf{I} + (\omega_1 - \omega_4)\hat{\sigma}_i^z & 2(\omega_5\hat{\sigma}_i^+ + \omega_7\hat{\sigma}_i^-) \\ 2(\omega_6\hat{\sigma}_i^+ + \omega_8\hat{\sigma}_i^+) & (\omega_2 + \omega_3)\mathbf{I} - (\omega_2 - \omega_3)\hat{\sigma}_i^z \end{pmatrix} . \tag{IV.61}$$

The Pauli operators for the i-th spin on the chain $\hat{\sigma}_i = 1_2 \otimes ... \otimes \sigma_i \otimes ...1_2$ act on the Hilbert space of a quantum spin-$1/2$ chain of length L, where the σ_i are the usual 2×2 Pauli matrices. Let us focus on the symmetric model where

$$R_i = \frac{1}{2} \begin{pmatrix} (a + b)\mathbf{I} + (a - b)\hat{\sigma}_i^z & 2(c\hat{\sigma}_i^+ + d\hat{\sigma}_i^-) \\ 2(c\hat{\sigma}_i^- + d\hat{\sigma}_i^+) & (a + b)\mathbf{I} - (a - b)\hat{\sigma}_i^z \end{pmatrix} \tag{IV.62}$$

Now let us try to find a commuting Hamiltonian with only nearest neighbours interactions

$$H = \sum_{i=1}^{L} h_{i,i+1} \tag{IV.63}$$

where $h_{i,i+1}$ involves only variables on sites i and $i + 1$. We shall impose periodic boundary conditions (which will be shown to be necessary since the partition function is computed from a trace). We replace H by $H \otimes 1_2$, then the commutator $[T, H]$ can be written

$$[T, H] = \text{Tr}_2 \sum_i [R_1 R_2 ... R_i R_{i+1} .. R_L, h_{i,i+1}] \tag{IV.64}$$

$$= \text{Tr}_2 \sum_i \{R_1 .. R_{i-1}([R_i, h_{i,i+1}]R_{i+1} + R_i[R_{i+1}, h_{i,i+1}])R_{i+2} .. R_L\} \tag{IV.65}$$

Only two commutators should be calculated: $[R_i, h_{i,i+1}]$ and $[R_{i+1}, h_{i,i+1}]$. The convenient choice was found by Sutherland [249] and corresponds to the XYZ Heisenberg Hamiltonian

$$H = \sum_{i=1}^{L} \left(J^x \hat{\sigma}_i^x \hat{\sigma}_{i+1}^x + J^y \hat{\sigma}_i^y \hat{\sigma}_{i+1}^y + J^z \hat{\sigma}_i^z \hat{\sigma}_{i+1}^z \right) \tag{IV.66}$$

$$= (J^x + J^y) \sum_{i=1}^{L} \left(\hat{\sigma}_i^+ \hat{\sigma}_{i+1}^- + \hat{\sigma}_i^- \hat{\sigma}_{i+1}^+ + \Gamma \left[\hat{\sigma}_i^+ \hat{\sigma}_{i+1}^+ + \hat{\sigma}_i^- \hat{\sigma}_{i+1}^- \right] + \frac{\Delta}{2} \hat{\sigma}_i^z \hat{\sigma}_{i+1}^z \right) . \tag{IV.67}$$

The next step is to find J^x, J^y and J_z as functions of the vertex weights. This Hamiltonian commutes with T if

$$\Delta = \frac{2J^z}{J^x + J^z} = \frac{a^2 + b^2 - c^2 - d^2}{2(ab + cd)} , \quad \Gamma = \frac{J^x - J^y}{J^x + J^y} = cd. \tag{IV.68}$$

From this result we conclude that if we can find the spectrum of T then we can also find the quantum eigenstates and eigenvalues of H_{XYZ}. The largest eigenvalue of T, i.e. the thermal state, corresponds to the ground state of the quantum problem. The six-vertex model corresponds to the case $d = 0$. From the latter equation: $\Gamma = 0$ hence $J^x = J^y$. Note that non-global properties, such as two-point functions, cannot be computed from the eigenvector with the largest eigenvalue. Further refinements are needed for this purpose [147].

IV.5   The loop algorithm

Single-spin flip updates break the six- and eight- vertex model constraints and cannot be used to generate different configurations in these cases. Instead, as each spin configuration can be viewed as a non-intersecting (six vertex) or intersecting (eight vertex) loop configuration, stochastic non-local updates of the loops have been used to sample phase space [16, 253]. By imposing the correct probabilities all along the construction of non-local moves cluster algorithms can be designed [253, 90]. Non-trivial issues as the effect of boundary conditions have been explored in this way [253, 6].

Loop-algorithms, as usually presented in the context of Quantum Monte Carlo methods, exploit the world-line representation of the partition function of a given quantum lattice model [252]. As explained in section IV.4.4 the $2D$ six- and eight-vertex models are equivalent to the Heisenberg XXZ and XYZ quantum spin-1/2 chains, respectively [249, 251]. It is then not surprising to find the same kind of loop-algorithms in the vertex models literature. A configuration in terms of bosonic world lines of the quantum spin chain in imaginary time can be one-to-one mapped into a vertex configuration in the square lattice, such as the same loop algorithm samples equivalently the configurations of both models.

In this section we describe the loop algorithm broadly used to simulate constrained systems. The relationship between classical vertex models and quantum spin chains is also discussed from this point of view.

IV.5.1   Monte Carlo updates for the six- and eight-vertex models

In order so sample configurations in a constrained manifold, as the 2in-2out configurations of spin-ice, one has to think about updates which do not create defects. This is the purpose of the *loop algorithm*. In the six-vertex model, the divergence free condition is preserved by updating loops of arrows which point into the same direction along the loop [16]. The steps of this algorithm shown in Fig. IV.18 are:

- Choose a seed spin S_0 randomly among all the spins in the lattice. We denote by v_0 the vertex where it points to.
- Choose randomly a spin among the two outgoing ones attached to v_0.
- Continue this procedure keeping track of the cluster/path of spins we have chosen until the path encounters a vertex which already belongs to it, creating a closed *loop*.
- Reverse all the spins along the loop with a Metropolis rule.

The creation of loops can be done à *la* Kandel and Domany [134], i.e. impose detailed balance during the construction of the loop where the spins are successively flipped [91, 90]. The same ideas have also been applied to the eight vertex model [254]. One can interpret this process as the creation of two defects of charge $q = \pm 1$ moving from site to site until they recombine. Loops are the natural excitations in vertex models and can be though of as the creation and annihilation of two defects. This remark will be important when discussing dynamics.

The loop algorithm is used to sample the equilibrium configurations of hard constrained models in general. In these systems loops made by the relevant degrees of freedom in the system constitute the simplest possible updates. In colouring models [19, 21] loops are made by a sequence of two colours and they are updated by switching its colours. The 3-colouring model on the hexagonal lattice [19] has been studied by Monte Carlo simulations using loop updates [65, 60]. In this model, one can choose at random a site of colour A and a neighbour of colour B. Then construct a closed loop $ABABAB...BA$ for site to site. Then switch the colours $AB...BA \rightarrow BA..AB$ with a Metropolis rule. Similar updates have been used for the simulation of dimer models [4, 234], and spin ice [175].
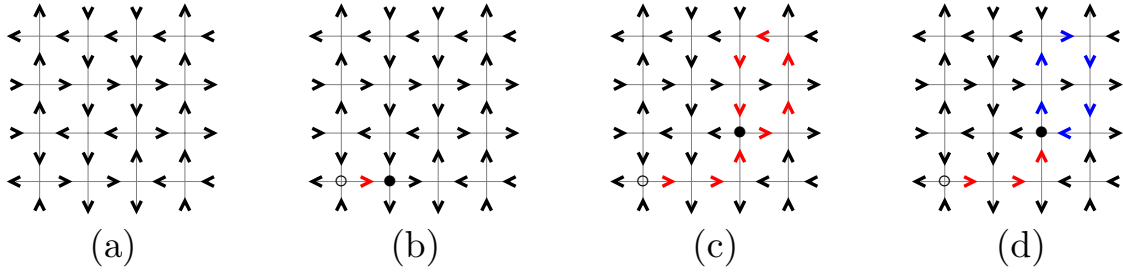
Figure IV.18: **Short Loop algorithm.** Starting from an ice-rule configuration (a) the algorithm constructs the path shown in red by adding spins one by one until it forms a closed loop (c). All the spins in the loop are flipped with probability $P \propto \min[1, e^{\beta \Delta E}]$ where ΔE is the energy difference between the configuration (d) and (a). Defects of opposite charge are shown by black and white circles.

IV.5.2 World-line representation of quantum spin-$1/2$ chains

In section IV.4.4 we showed the relationship between the six- and eight-vertex with the XXZ and XYZ quantum spin chains by inspection of the transfer matrix. Here we adopt a different route for the same scope. We start from the quantum Hamiltonian of the XXZ model and, by making use of the Suzuki-Trotter decomposition, we show the equivalence with the six-vertex problem [251].

The Hamiltonian of the XXZ spin half chain is

$$H^{XXZ} = \sum_{i=1}^{N} (J^x S_i^x S_{i+1}^x + J^x S_i^y S_{i+1}^y + J^z S_i^z S_{i+1}^z) = \sum_{i=1}^{N} h(i, i+1) \qquad \text{(IV.69)}$$

and we introduce the *anisotropy parameter* describing its phase diagram $\Delta_{XXZ} = J^z/J^x$. The partition function of the model can be sliced into M factors using the Suzuki-Trotter formula [251]:

$$Z_M = \text{Tr}\{[\exp(-\frac{\beta}{M} H_2) \exp(-\frac{\beta}{M} H_1)]^M\} \ , \qquad Z^{XXZ} = \lim_{M \to \infty} Z_M \ , \qquad \text{(IV.70)}$$

where we have split the Hamiltonian $H = H_2 + H_1$ into an odd $H_1 = \sum_{n=0} h(2n+1, 2n)$ and an even part $H_2 = \sum_{n=1} h(2n, 2n+1)$. By introducing the state of N spins $|\mathbf{S}_k\rangle_{k=1...M}$ for each one of the M factors one gets:

$$Z_M = \sum_{|\mathbf{S}_1\rangle} ... \sum_{|\mathbf{S}_M\rangle} \langle \mathbf{S}_1 | e^{-\Delta \tau H_2} | \mathbf{S}_M \rangle ... \langle \mathbf{S}_2 | e^{-\Delta \tau H_1} | \mathbf{S}_1 \rangle \qquad \text{(IV.71)}$$

where the index k is the 'imaginary time' coordinate in units of $\Delta \tau = \beta/M$. The partition function is the sum of the weight of each possible trajectory (the so-called *world lines*) obtained by application of the evolution operators $e^{-\Delta \tau H_1}$ and $e^{-\Delta \tau H_2}$. The representation of the partition function as a sum over path contributions is the discrete version of the path integral formulation of quantum mechanics. The fact that the world lines are closed is imposed by the PBC. The first step of the evolution is given by

$$\langle \mathbf{S}_2 | e^{-\Delta \tau H_1} | \mathbf{S}_1 \rangle = \prod_{i, \text{ odd}} \langle s(i, 2) s(i+1, 2) | \exp[-\Delta \tau h(i, i+1)] | s(i, 1) s(i+1, 1) \rangle \qquad \text{(IV.72)}$$

where $\{|s(i, k)\rangle\}$ are the eigenvectors of the spin operator S_i^z with eigenvalue $s(i, k) = \pm 1$ and i is an odd number. The quantum system has been mapped into a classical model defined by the
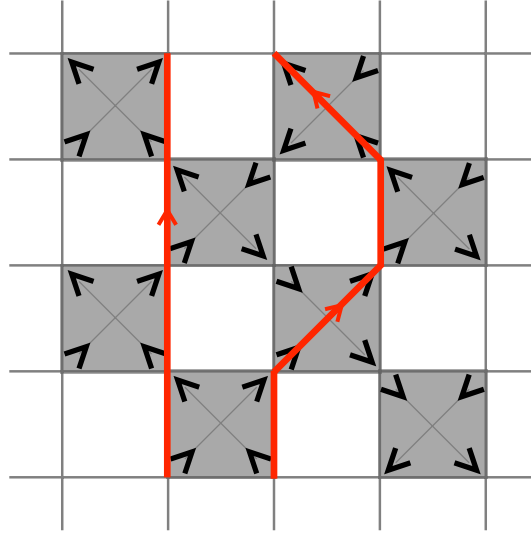
Figure IV.19: **World-line representation of the XXZ chain.** World-lines for the quantum spins are shown in red. The weights w in eq. (IV.73) which contribute to the partition function correspond to the dashed plaquettes shown in the picture. In the classical representation, each one of these grey plaquettes is a vertex verifying the ice-rule. Time evolution is represented by red arrows along the world lines.

spin variables $s(i, k)$ sitting on the site of a $N \times M$ lattice with coordinates (i, k). The lattice can be divided into two sub-lattices A and B. The partition function can then be written as a sum over configurations of this classical model as

$$Z_M = \sum_{\{s(i,k)\}} \prod_{(i,k) \in A} w(i, k) \tag{IV.73}$$

where $w(i, k)$ denotes the weight of a plaquette made by the four sites of coordinates $\{(i, k), (i + 1, k), (i + 1, k + 1), (i, k + 1)\}$. The product runs over the sites for which is $i + k$ even (i.e. the A sub-lattice). Only the shaded plaquettes shown in Fig. IV.19 contribute to the partition function with the weight $w(i, k)$. The latter is given by the elements of the 4×4 matrix:

$$w(i, k) = \langle s(i, k + 1)s(i + 1, k + 1)|e^{-\Delta \tau h(i, i+1)}|s(i, k)s(i + 1, k)\rangle , \tag{IV.74}$$

$$w(i, k) = \begin{pmatrix} e^{-\frac{\Delta\tau}{4}J^z} & 0 & 0 & 0 \\ 0 & e^{\frac{\Delta\tau}{4}J^z}\cosh(\frac{\Delta\tau}{2}|J^x|) & e^{\frac{\Delta\tau}{4}J^z}\sinh(\frac{\Delta\tau}{2}|J^x|) & 0 \\ 0 & e^{\frac{\Delta\tau}{4}J^z}\sinh(\frac{\Delta\tau}{2}|J^x|) & e^{\frac{\Delta\tau}{4}J^z}\cosh(\frac{\Delta\tau}{2}|J^x|) & 0 \\ 0 & 0 & 0 & e^{-\frac{\Delta\tau}{4}J^z} \end{pmatrix} . \tag{IV.75}$$

If one identifies the matrix elements above as following

$$\begin{aligned} \langle + + |e^{-\Delta\tau h(i, i+1)}| + +\rangle &= \langle - - |e^{-\Delta\tau h(i, i+1)}| - -\rangle &= \omega_1 = \omega_2 = a \\ \langle + - |e^{-\Delta\tau h(i, i+1)}| + -\rangle &= \langle - + |e^{-\Delta\tau h(i, i+1)}| - +\rangle &= \omega_3 = \omega_4 = b \\ \langle + - |e^{-\Delta\tau h(i, i+1)}| - +\rangle &= \langle - + |e^{-\Delta\tau h(i, i+1)}| + -\rangle &= \omega_5 = \omega_6 = c \end{aligned} \tag{IV.76}$$

the matrix eq. (IV.75) of the XXZ chain becomes *identical to the R-matrix of the six-vertex model* eq. (IV.18). The only six matrix elements which do not vanish conserve the magnetization in the z-direction. This conservation law is equivalent to the bond conservation in the NE path

representation of the six-vertex model, hence to the ice-rule. From eq. (IV.76), a, b and c depend on the couplings J^x, J^z and on $\Delta\tau$. In order to apply Suzuki-Trottrer theorem, one has to take the limit $\Delta\tau \to 0$ for all of this to make sense. One obtains the important result:

$$\lim_{\Delta\tau \to 0} \frac{a^2 + b^2 - c^2}{2ab} = \frac{J^z}{J^x} \,, \quad \Delta_6 = \Delta_{XXZ} \,. \tag{IV.77}$$
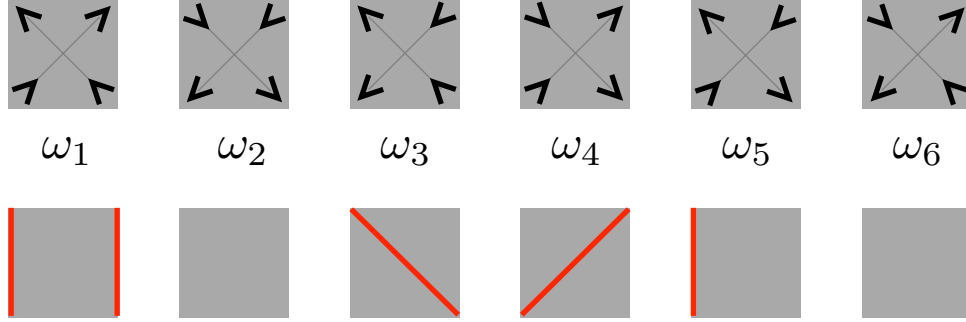

Figure IV.20: **Equivalence between the XXZ and the six-vertex model.** One-to-one correspondence between the six possible vertex configurations on a dashed plaquette and world-lines in the XXZ quantum chain.

The partition function of the XXZ and the six-vertex model are equal in the thermodynamic limit with PBC: $Z^{XXZ} = Z^{6V}$. The phase diagram is hence identical and characterised by the same anisotropy parameter. The correspondence between bosonic [8] world lines and vertex configurations is shown in Fig. IV.19 and Fig. IV.20. The quantum equivalent of the frozen FM phase in the KDP model is a gapped phase. The gap energy correspond to the energy associated with a string excitation.

In order to perform a Monte Carlo simulation of the XXZ chain one has to generate different world-lines configurations with the appropriate statistical weight. This can be done by deforming locally the world lines and updating the system accordingly to a Metropolis rule. An allowed deformation of a world line which preserves the conservation of the magnetisation along z can be generated by the loop algorithm described before. As shown in Fig. IV.21, a different configuration is generated by flipping all the arrows along a closed loop.

It is quite straightforward to generalise the mapping and show the equivalence between the XYZ and eight-vertex model. The Hamiltonian in this case is

$$H^{XYZ} = \sum_{i=1}^{N} (J^x S_i^x S_{i+1}^x + J^y S_i^y S_{i+1}^y + J^z S_i^z S_{i+1}^z) = \sum_{i=1}^{N} h(i, i+1) \tag{IV.78}$$

which gives the following plaquette weights:

$$\begin{aligned}
\langle ++|e^{-\Delta\tau h(i,i+1)}|++\rangle &= \langle --|e^{-\Delta\tau h(i,i+1)}|--\rangle &&= \omega_1 = \omega_2 = a \\
\langle +-|e^{-\Delta\tau h(i,i+1)}|+-\rangle &= \langle -+|e^{-\Delta\tau h(i,i+1)}|-+\rangle &&= \omega_3 = \omega_4 = b \\
\langle +-|e^{-\Delta\tau h(i,i+1)}|-+\rangle &= \langle -+|e^{-\Delta\tau h(i,i+1)}|+-\rangle &&= \omega_5 = \omega_6 = c \\
\langle ++|e^{-\Delta\tau h(i,i+1)}|--\rangle &= \langle --|e^{-\Delta\tau h(i,i+1)}|++\rangle &&= \omega_7 = \omega_8 = d
\end{aligned} \tag{IV.79}$$

verifying

$$\lim_{\Delta\tau \to 0} \frac{a^2 + b^2 - c^2 - d^2}{2(ab + cd)} = \frac{J^x + J^y}{2J^z} \,, \quad \Delta_8 = \Delta_{XYZ} \,. \tag{IV.80}$$

---

8. One can replace the operator S_i^z by a bosonic creator operator n_i. Since world lines do not cross the model turns out to describe hard core bosons in $1D$.
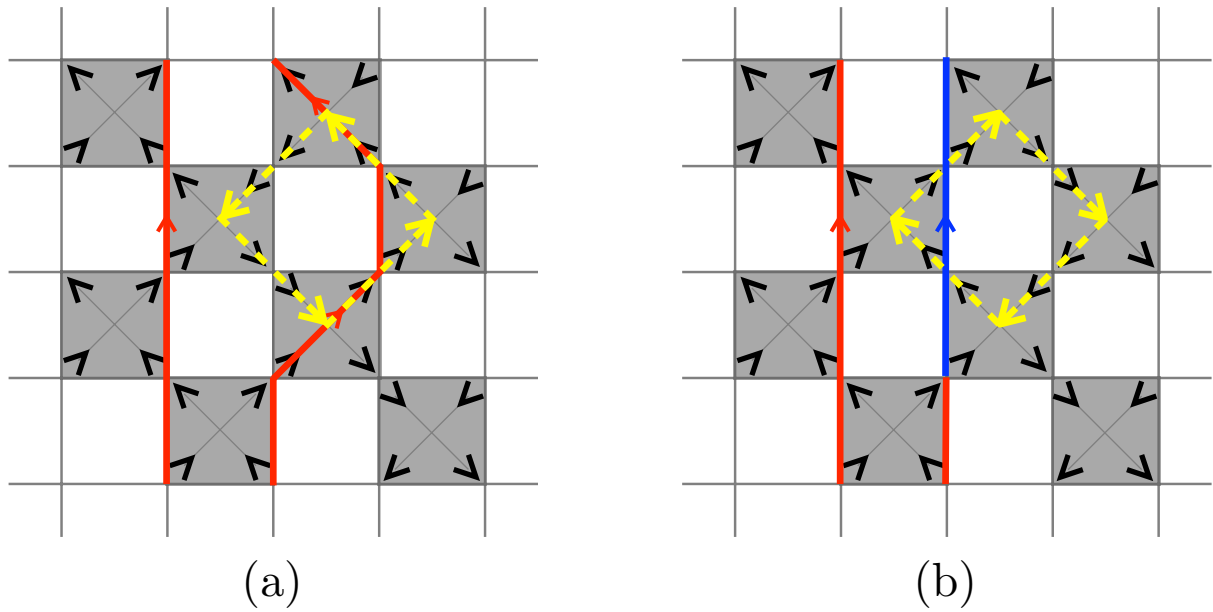
Figure IV.21: **Loop update in the XXZ model.** (a) Initial world line configuration. The yellow dotted lines denote a loop of arrows in the vertex representation. (b) Configuration obtained from (a) by switching all the arrows allong the yellow loop. The modification induced by this update in the world line configuration is shown in blue.

The inclusion of 4in and 4out vertex configurations does not break the 'closeness' of the world lines and the loop algorithm can be applied. The extra anisotropy $J^x = J^y$ introduces the possibility to world lines to go backwards as shown in Fig. IV.22. For the XYZ model there is no need to construct oriented loops since any closed loop update preserves the parity of the number of incoming and outgoing arrows at each vertex.
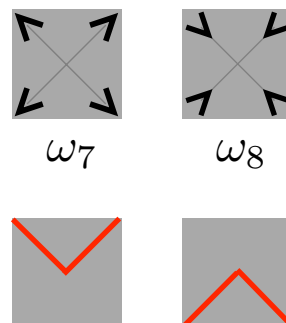
Figure IV.22: World line representation of the 4-in and 4-out plaquettes allowed in the XYZ model.

IV.6 General remarks about hardly constrained systems

IV.6.1 Emergent gauge structure and Coulomb phase

The definition of the height representation of the six-vertex model given in section IV.3.4 for a continuous formulation of the model. In the continuum the height configuration becomes a smooth function. One can introduce a coarse-grained field M defined by [278]

$$\vec{M}(x,y) = \left(-\frac{\partial}{\partial y} h(x,y), \frac{\partial}{\partial x} h(x,y) \right) . \tag{IV.81}$$

The coarse-grained field $\vec{M}(x,y)$ is the local average of the magnetisation around $\vec{r} = (x,y)$: $\vec{M}(\vec{r}) = \frac{1}{N_{\vec{r}}} \sum_{e \in \mathcal{D}_{\vec{r}}} \vec{S}_e$ where $\mathcal{D}_{\vec{r}}$ denotes a subdomain of the lattice around the point $\vec{r}$. The correlations of this are ruled by the divergence free constraint

$$\vec{\nabla} \cdot \vec{M}(x,y) = 0 , \quad \forall \, (x,y) \in \mathbb{R}^2 \tag{IV.82}$$

which is the continuum version of the ice-rules. In the absence of singularities, this constraint allows the existence of a 'scalar vector potential' h. This was already apparent from eq. (IV.81), which can be written symbolically as:

$$\vec{M}(x,y) \equiv \vec{\nabla} \times \vec{h}(x,y) , \quad \forall \, (x,y) \in \mathbb{R}^2 \tag{IV.83}$$

where $\vec{h}(x,y) = h(x,y)\vec{u_z}$. The ice-rules make rise quite naturally to a U(1) gauge structure. In the rough phase the effective action is supposed to be Gaussian:

$$S[h] = \frac{K}{2} \int \vec{M}^2 dx \, dy = \frac{K}{2} \int [\vec{\nabla} h]^2 dx \, dy . \tag{IV.84}$$

The probability distribution of a field configuration can be written as

$$\mathcal{P}[h] = \frac{1}{Z} e^{-\beta \frac{K}{2} \int \vec{M}^2 dx \, dy} \prod_{\vec{r}} \delta(\vec{\nabla}.\vec{M}) . \tag{IV.85}$$

By analogy with electrodynamics, the set of field configurations distributed accordingly with $\mathcal{P}$ is sometimes referred to as the *Coulomb phase* [115].

IV.6.2 Dipolar long range correlations

The computation of two-point correlation function in this theory only involves gaussian integrals and can be carried out analytically. In D-dimensions one gets the asymptotic correlations:

$$\left\langle M^{\mu}(\vec{r}) M^{\nu}(\vec{0}) \right\rangle = \frac{k_B T}{g} \left[\delta^d(\vec{r}) + \frac{1}{r^d} \left(\delta_{\mu\nu}^{-1} - d \frac{r^{\mu} r^{\nu}}{|\vec{r}|^2} \right) \right] . \tag{IV.86}$$

If we relax the divergence-free condition we get

$$\left\langle M^{\mu}(\vec{r}) M^{\nu}(\vec{0}) \right\rangle = \frac{k_B T}{g} \delta^{\mu\nu} \delta(\vec{r}) . \tag{IV.87}$$

It is explicit from this simple model that the constraint is responsible for the emergence of critical correlations. In $d = 2$ it gives:

$$\left\langle M^{\mu}(\vec{r}) M^{\nu}(\vec{0}) \right\rangle = \frac{k_B T}{g} \left(\delta^d(\vec{r}) + \frac{1}{r^2}(1 - 2\cos^2 \varphi) \right) \quad \text{for} \quad \mu = \nu \tag{IV.88}$$

$$\left\langle M^{\mu}(\vec{r}) M^{\nu}(\vec{0}) \right\rangle = \frac{k_B T}{g} \left(\delta^d(\vec{r}) - \frac{2 \sin \varphi \cos \varphi}{r^2} \right) \quad \text{for} \quad \mu \neq \nu . \tag{IV.89}$$

Many interesting aspects of the collective behaviour arising in the six-vertex model are due to the ice-rule constraint and can be also found in other constrained lattice models. A specially clear and unifying concept of constrained models is the existence of a height representation [114].The 4-state AF Potts model in the triangular lattice [195], the 3-colouring model on the hexagonal lattice [144] or the dimer model on the hexagonal lattice (which is equivalent to the ground state of the AF Ising in the triangular lattice) [38] allow for a height representation. The height function formulation is closely related to the Coulomb gas method [205], an efficient way to compute the critical exponents of constrained systems [39, 144].

IV.7 The sixteen-vertex model

IV.7.1 Definition

The most general model obtained by the relaxation of the ice-rules is the *sixteen-vertex model*, in which no restriction is imposed on the value of the binary variables attached on each edge of the lattice, and $2^4 = 16$ vertex configurations can occur. The three-in one-out and three-out one-in vertices that are added to the ones already discussed are shown in Fig. IV.23. In order to preserve the Z_2 symmetry, and with no external magnetic field applied that would break the rotation symmetry, all these 'defects' with charge 1 and -1 are given the same statistical weight that we call e. In the figure, vertices are ordered in pairs of spin-reversed couples (v_{10} is the spin reversed of v_9 and so on and so forth) and the difference with the following couples is a rotation by $\pi/2$ (v_{11} is equal to v_9 apart from a $\pi/2$-rotation and so on and so forth).
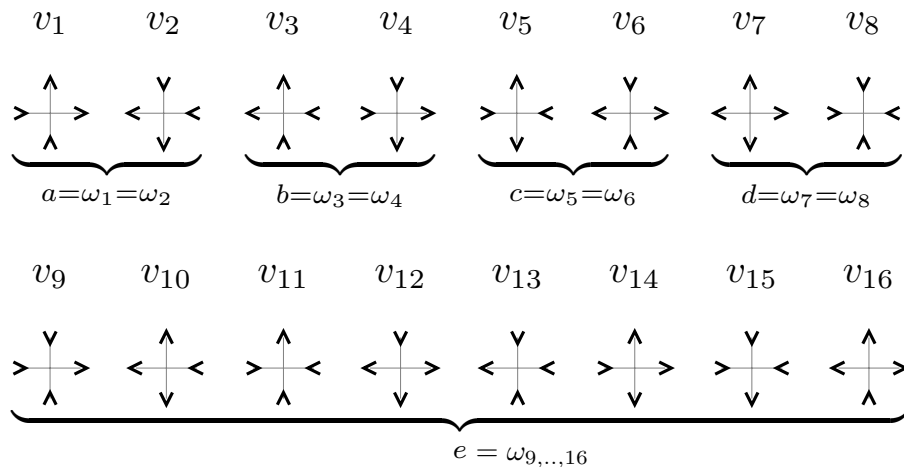
Figure IV.23: The sixteen configurations of the sixteen-vertex model. The eight three-in one-out (with charge $+1$) or three-out one-in (with charge -1) vertices are added. We give them equal weight e.

The new vertices naturally entail the existence of new phases. One can envisage the existence of a critical SL phase for $a = b = c = d = 0$ and $e > 0$ as this new eight-vertex model is equivalent to the dimer model solved by Kasteleyn. It is quite easy to see that e-AF stripe order is also possible. For instance, one can build an ordered configuration with alternating lines of v_9 and v_{10} vertices, or another one with alternating columns of v_{11} and v_{12} vertices. Phases of

this kind should appear if one favours one pair of spin-reversed related vertices by giving them a higher weight. The phase transitions to this phase are expected to be continuous since, for $a = b = c = d = 0$ and $\omega_{i>8} > 0$ local updates are in form of loops of spins around a plaquette are possible. The critical properties of such eight-vertex model are unknown.

IV.7.2 Ising representation in the medial lattice
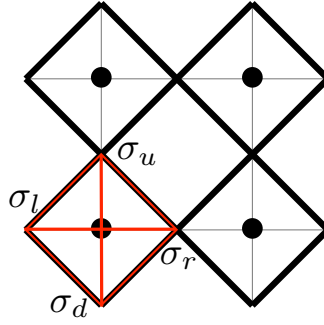
Figure IV.24: The four spin variables sitting on the sites of the medial lattice around a vertex. The red lines represent the interactions between them. This representation allows for a one-to-one map between a vertex configuration and an arrangement of four spins $\sigma_{r,u,l,d}$.

In this section we show the equivalence between the symmetric sixteen-vertex model with Z_2 symmetry and an Ising model with two-spin and four-spin interactions and without external field [166]. We consider the case where $a = \omega_1 = \omega_2$, $b = \omega_3 = \omega_4$, $c = \omega_5 = \omega_6$, $d = \omega_7 = \omega_8$ and $e = \omega_{i>8}$. A more general dicussion can be found in [166].

There is an obvious bijection between a vertex configurations on $\mathcal{V}$ and a four Ising spins configuration on $\mathcal{S}$: we assign a spin up(down) on $\mathcal{S}$ if the corresponding arrow on $\mathcal{V}$ points up (down) or right (left). The identification of the interactions between spins leading to the sixteen-vertex Hamiltonian defined above is much less obvious. One can identify the energy of each vertex to the energy with its four spins. The Hamiltonian for each square plaquette made of four spins surrounding a vertex reads

$$
\begin{aligned}
H_v = &-J_0 - J_1(\sigma_u\sigma_l + \sigma_r\sigma_d) - J_1'(\sigma_u\sigma_r + \sigma_l\sigma_d) \\
&- J_2(\sigma_u\sigma_d + \sigma_r\sigma_l) - K\sigma_u\sigma_d\sigma_r\sigma_l
\end{aligned} \tag{IV.90}
$$

where the subscripts u, d, l, r correspond to the four edges attached to a single vertex as illustrated in Fig. IV.24. The total lattice Hamiltonian H is then given by summing H_v all over the square lattice $\mathcal{V}$. The vertex energies can then be rewritten

$$
\begin{aligned}
\epsilon_1 = \epsilon_2 = \epsilon_a &= -J_0 - 2J_1 - 2J_1' - 2J_2 - K \\
\epsilon_3 = \epsilon_4 = \epsilon_b &= -J_0 + 2J_1 + 2J_1' - 2J_2 - K \\
\epsilon_5 = \epsilon_6 = \epsilon_c &= -J_0 - 2J_1 + 2J_1' + 2J_2 - K \\
\epsilon_7 = \epsilon_8 = \epsilon_d &= -J_0 + 2J_1 - 2J_1' + 2J_2 - K \\
\epsilon_9 = ... = \epsilon_{16} = \epsilon_d &= -J_0 + K
\end{aligned}
$$

$$\tag{IV.91}$$

The constant J_0 guarantees the set of linear equations can be inverted leading to

$$
\begin{aligned}
J_0 &= 1/16(-2\epsilon_a - 2\epsilon_b - 2\epsilon_c - 2\epsilon_d - 8\epsilon_e) \\
J_1 &= 1/16(-2\epsilon_a + 2\epsilon_b - 2\epsilon_c + 2\epsilon_d) \\
J_1' &= 1/16(-2\epsilon_a + 2\epsilon_b + 2\epsilon_c - 2\epsilon_d) \\
J_2 &= 1/16(-2\epsilon_a - 2\epsilon_b + 2\epsilon_c + 2\epsilon_d) \\
K &= 1/16(-2\epsilon_a - 2\epsilon_b - 2\epsilon_c - 2\epsilon_d + 8\epsilon_e).
\end{aligned}
\tag{IV.92}
$$

The eight-vertex model corresponds to the particular case $K = J_0$. The six-vertex model corresponds to an anisotropic Ising model with two body and four body interactions:

$$
\begin{aligned}
J_1 &= 1/8(-\epsilon_a + \epsilon_b - \epsilon_c) \\
J_1' &= 1/8(-\epsilon_a + \epsilon_b + \epsilon_c) \\
J_2 &= 1/16(-\epsilon_a - \epsilon_b + \epsilon_c) \\
K &= -1/8(\epsilon_a + \epsilon_b + \epsilon_c).
\end{aligned}
\tag{IV.93}
$$

This Ising model becomes isotropic when $\epsilon_c \to 0$ ($J_1 = J_1'$).

The model defined by the Hamiltonian IV.7.2 reduces to an Ising model with only two body exchange interactions if $K = 0$, i.e.

$$
4\epsilon_e = \epsilon_a + \epsilon_b + \epsilon_c + \epsilon_d \iff e^4 = abcd.
\tag{IV.94}
$$

When this condition is satisfied some equilibrium properties of the model can be computed. The coming section is devoted to them.

IV.7.3 Some exact results

The sixteen-vertex model loses the integrability properties. However, some exact results are available for a few special sets of parameters when the equivalent classical Ising model only has nearest and next-nearest neighbor two-body interactions, i.e. when $e^4 = abcd$ [166, 271].

In the c-AF sector this condition leads to the generalized F model defined by $c = 1$, $a = b < 1$, $d = a^u$ and $e = a^v$, with the constraint $4v = u + 2$. The model has been solved for the special cases:

(i) $v = 1$ and $u = 2$ (i.e. $e = a$ and $d = a^2$), the associated spin model simplifies into an antiferromagnetic Ising model with only nearest neighbor interactions. This model is known to exhibit a second-order phase transition at $\epsilon/k_B T_c = 2\ln(\sqrt{2} + 1)$ with a logarithmic divergence of the specific heat ($\alpha = 0$).

(ii) $v \to \infty$ and $u = 2$ (i.e. $e = 0$ and $d = a^2$) the system also exhibits a second-order phase transition in the same universality class as (i). Note that the exactly solved F model is recovered in the limit $v \to \infty$ and $u \to \infty$ ($d = e = 0$).

In the same way, in the a-FM sector this leads to the generalised KDP model [272] by setting $a = 1$, $b = c < 1$, $d = b^u$, $e = b^v$ and again $4v = u + 2$. For $v = 1$ and $u = 2$ (i.e. $e = a$ and $d = a^2$) the system exhibits a second-order phase transition with the same properties of its c-AF analog discussed above. For $v \to \infty$ and $u = 2$ (i.e. $e = 0$ and $d = a^2$) the system also exhibits a second-order phase transition in the same universality class as the previous case.

The equilibrium phases of $2D$ spin-ice

V.1 Parametrisation of the sixteen-vertex model

In this chapter, we consider the equilibrium properties of two different particular cases of the general sixteen-vertex model introduced in section IV.7. We shall fix these two different parametrisations before discussing their phase diagram. For clarity, let us recall the definition of the sixteen possible vertex configurations with their corresponding weight shown in Fig. V.1.

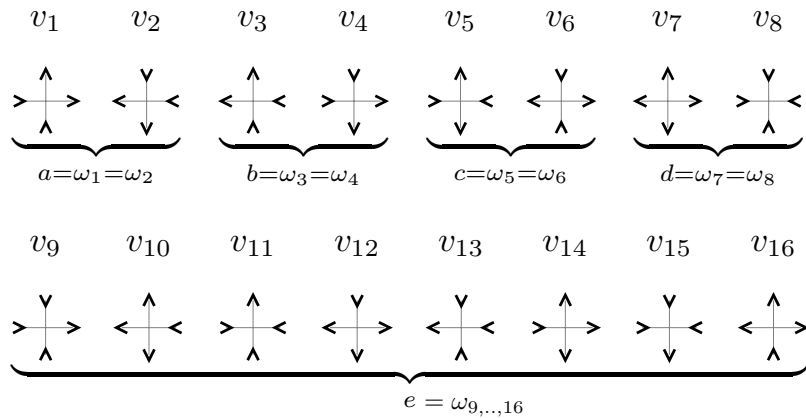Figure V.1: The sixteen vertices of the model with their Boltzmann weights $\omega_{i=1\ldots16}$.

V.1.1 The symmetric sixteen-vertex model

We define the *symmetric sixteen-vertex model* by setting

$$\begin{aligned}
\omega_1 = \omega_2 = a, \quad \omega_2 = \omega_4 = b, \quad \omega_5 = \omega_6 = c = 1 \\
\omega_7 = \omega_8 = d, \quad \omega_9 = \ldots = \omega_{16} = e \, .
\end{aligned} \tag{V.1}$$

The model is defined by four independent parameters a, b, d, e, and, for the sake of simplicity, we usually set $d = e$. In order to define a temperature from $\omega_i = e^{-\beta \epsilon_i}$ one has to fix three among the four before-mentioned parameters. Depending on the weight given to the vertices the model exhibits antiferromagnetic (AF) and ferromagnetic (FM) order. This parametrisation of the general sixteen-vertex model is an extension of the symmetric eight-vertex model where we give the same weight to all the *defects* breaking the parity constraint (i.e. with an odd number of incoming or outgoing arrows). The theoretical motivation to study this model is to try to extend the knowledge on integrable vertex models to non-integrable ones, and in particular, to understand the consequences of the 'integrability breaking' in the collective behaviour of vertex models. Although all the 3in-1out 1in-3out defects are equivalent, the model is very general.

The results obtained for this model and presented in section V.3 and section V.4.

V.1.2 The $2D$ spin-ice model

A particular choice of the vertex weights should be done in order to compare the predictions of the model with concrete experimental realisations. In $2D$ artificial spin-ice samples, one expects the interactions between the nano-islands to be dipolar. In order to fix the energy of the vertices some approximation has to be done. We adopt here the the values used by Nisoli et al. [206]. It uses of the 'dumbbell' picture where each dipole is considered as a pair of oppositely charged monopoles sitting on the vertices. Then, by considering only the Coulomb interactions among the monopoles around a vertex we find (after an appropriate normalisation of the energy units):

$$
\begin{aligned}
\epsilon_1 = \epsilon_2 = \epsilon_3 = \epsilon_4 = (\sqrt{2} - 1)/(\sqrt{2} - 1/2), &\quad a = b = \exp(-\beta \epsilon_1) \\
\epsilon_5 = \epsilon_6 = 0, &\quad c = 1 \\
\epsilon_7 = \epsilon_8 = 4\sqrt{2}/(2\sqrt{2} - 1), &\quad d = \exp(-\beta \epsilon_7) \\
\epsilon_9 = ... = \epsilon_{16} = 1, &\quad e = \exp(-\beta \epsilon_9)
\end{aligned}
\tag{V.2}
$$

This allows us to define the temperature of the system by, for instance, $k_B T = -\epsilon_1 / \ln(a)$. One could choose different vertex energies. Morgan and collaborators, use a point-dipole approach to set the energy of the vertices [196]. If one considers the dipole-dipole interaction between the four islands meeting at a vertex (and neglects the interaction with further neighbours) one gets: $\epsilon_5 = 0$, $\epsilon_9 = 1$, $\epsilon_1 \approx 0.69$ and $\epsilon_7 \approx 2.1$. One should check the relevance of these parameters by comparing the theoretical results obtained with the vertex model with numerical simulations of the dipolar model or experimental measurements.

The equilibrium properties of this model with the parameters in eq. (V.2) are presented in section V.5.

V.2 The cavity method

In chapter 4 we presented several exact results for $2D$ statistical models closely related to spin ice. There are however a very few interacting models which can be solved exactly and $2D$ spin ice in the presence of defects cannot be realistically modelled by an integrable theory. In $3D$ exact solutions are even rarer and approximate methods should be developed to tackle interacting systems in general. Depending on the features one is interested in and the model under investigation, different approaches are more suitable. Mean-field theory is the simplest approximation one can do to get some insight into the collective behaviour of a system. It is often used as a preliminarily study when trying to understand a complicated problem with many interacting degrees of freedom. After a short presentation of the standard mean field approximation an improvement over this method is presented: the *cavity method*. It is a more sophisticated mean-field method based

on the Bethe-Peierls approximation introduced in 1935 [32]. The name 'cavity method' comes from the extension of the method to the study of spin glasses [183, 184] and has become since then a standard method in disordered systems. Other contexts in which the Bethe-Peierls (BP) approximation has been used the name given to this approach differs, but all of them are based upon the same basic assumptions.

The BP approximation and its generalisations have been used in a broad class of different situations. The bond percolation model can be exactly solved in the Bethe lattice [245, 67]. The computation of the percolation threshold using the BP approximation is due to the early work by Flory in 1941 [99]. He identified the *gelation* problem of polymer physics with the percolating transition. The Bethe lattice approach turns out to be accurate since polymers tend to avoid the presence of loops. Since then this method has been used in several works on polymer physics [109]. Different problems where the BP approximation has shown to be very fruitful include Anderson's localisation [1, 282, 142], Ising models with multi-spin interactions [194, 52], sandpiles [83], quantum many-body systems [237], computer science problems [275] and, more importantly to us, frustrated magnets [68, 193] and, in particular, spin ice [276, 130]. Further comments about these works and the extensions made to study geometrically frustrated lattice models will be given at the end of this section. Then, we adapt the Bethe-Peierls approximation (or cavity method) in order to investigate the whole phase diagram of generic vertex models.

V.2.1   A prelude: Mean field approximation

There are many formulations of mean-field theory. The one presented here is a molecular field approximation and it is based on the same grounds as the original formulation of Bragg and Williams in 1934 [42]. This choice has been done in order to make a clear connection with the cavity method and its improvements over this standard mean-field approach.

In any interacting statistical model each degree of freedom interacts with its neighbours up to some range and, eventually, with an external field. For pedagogical reasons, we consider the textbook example, the Ising model defined by N interacting spins accordingly to the Hamiltonian

$$H(\{\sigma\}) = -J \sum_{\langle i,j \rangle} \sigma_i \sigma_j \ , \tag{V.3}$$

where the sum runs over all the links of a lattice of coordination number c (the number of links per vertex). In a mean field model the interaction of a given spin with its surrounding its replaced by an average over all the spins in the system which create an effective molecular field acting on it. To illustrate the nature of the approximation we focus upon a single spin located on site i. The local Hamiltonian for this spin is

$$H_i = -\sigma_i \left(J \sum_{j=1}^{c} \sigma_j \right) \tag{V.4}$$

where we sum only over the c nearest-neighbours of i. The mean field approximation assumes that one can replace the fluctuating variable in this sum by an homogeneous mean value which will be determined self-consistently: $\sum_{j=1}^{c} \sigma_j \approx c\langle \sigma \rangle$. The neighbouring spins are replaced by an effective *molecular field*:

$$h_{eff} = cJ\langle \sigma \rangle \ . \tag{V.5}$$

The goal of a mean field calculation is to compute this effective field induced by the presence of the sourrounding spins. This approximation decouples the spins and the approximated Hamiltonian reduces to the one of a single body problem, i.e.

$$H_{MF} = -h_{eff} \sum_{i} \sigma_i \ . \tag{V.6}$$

Using this approximation, the free energy can be written explicitly as a function of the magnetisation $m = \langle \sigma \rangle$ [1]:

$$\beta F_{MF}[m] = -J\frac{cN}{2}m^2 + \frac{1+m}{2}\ln\left(\frac{1+m}{2}\right) + \frac{1-m}{2}\ln\left(\frac{1-m}{2}\right) \tag{V.8}$$

From eq. (V.5), the mean field felt by a spin is completely determined by the magnetisation, leading to the *self-consistent* equation

$$m = \tanh\left(cKm\right) \tag{V.9}$$

where $K = \beta J$. The self-consistent equation can be solved graphically. The approximation neglects the presence of spatial correlations between neighbours [2]. After rescaling the coupling constant by the number of spins, it can be easily shown that mean field theory is equivalent to an 'infinite dimension' approximation (since all the vertices of the lattice are coupled equally [3]). It is then equivalent to do a mean field calculation and an exact calculation on a fully connected graph where the vertices are occupied by the interacting degrees of freedom (see Fig. V.2). There is no notion of distance in the theory and the exponents associated with the spatial structure of the system, i.e. ν and η, are not well defined (see Chapter 3). One would then expect that the mean field approximation becomes accurate in the limit of c very large.

Using this approximation one can compute the thermodynamic quantities of the system and the associated critical exponents. We briefly present here the main results in zero field $h = 0$ which will be compared with the more elaborate method we develop in the coming section. The stable solutions of the self-consistent equation (V.9) is

$$m(T) = \begin{cases} 0, & \text{for } \beta Jc \leq 1 \\ \pm m_0(T), & \text{for } \beta Jc > 1 \end{cases} . \tag{V.13}$$

Therefore, $\beta Jc = 1$ gives the critical temperature T_c of the model. The solutions $m_0(t) \neq 0$ give the spontaneous magnetisation of the system characterising the ordered phase. The thermodynamic quantities show a different qualitative behaviour if $T > T_c$ or $T < T_c$. The main results

---

1. The expansion of F_{MF} for small m gives the Landau free energy and shows the connection between Landau's theory and the standard mean field approach on a lattice model. For small m one can write

$$F_{MF}[m] = \text{ct} + \frac{1}{2}a(J)(T - T_c)m^2 + bm^4 + O(m^6) \tag{V.7}$$

where a and b are positive real number. In Landau's theory its is constructed *a priori* by symmetry requirements.

2. This can be shown explicitly by rewriting

$$\sigma_i\sigma_j = m^2 + m(\sigma_i - m) + m(\sigma_j - m) + (\sigma_i - m)(\sigma_j - m) \tag{V.10}$$

which gives the mean-field Hamiltonian (V.6) up to a constant if we neglect the last term $(\sigma_i - m)(\sigma_j - m)$, i.e. the spatial correlations.

3. The dimensionality of a lattice can be defined as the following. Consider a site i and count the number of sites attached to it at a given 'distance' r. By distance between two sites i and j we mean here the minimal number of edges that one must visit in order to get from i to j. For a D-dimensional lattice and r large, the number of sites attached to i scales as r^d. More formally, the number of sites at distance r from a given site is given by

$$C_r = \sum_{n=0}^{r} g_n \tag{V.11}$$

where g_n is the number of n-th nearest neighbours of a site. The dimension of the lattice is then given by

$$d = \lim_{r \to \infty} \frac{\ln C_r}{\ln r} \text{ , i.e. } C_{r \to \infty} \sim r^d. \tag{V.12}$$
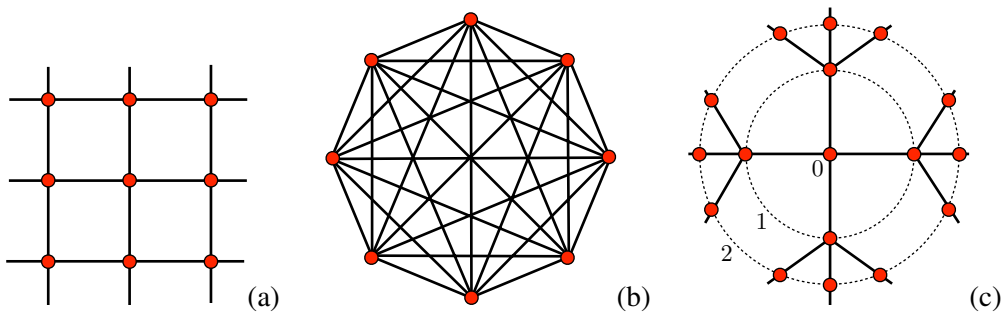
Figure V.2: (a) Original square lattice. (b) **Fully connected lattice**, i.e. mean field approximation of (a). (c) **Cayley tree** of connectivity $c = 4$ and $L = 2$ shells, i.e. Bethe-Peierls approximation of (a).

are summarised in Table V.1 where we have introduced the deviation from the critical temperature $t = 1 - T_c/T$. The free energy and the magnetic susceptibility are continuous at the transition point, the heat capacity has a jump discontinuity.

	$T > T_c$	$T < T_c$	$T \sim T_c$
$m(T)$	0	$\pm m_0(t)$	$\sqrt{3t} \sim |t|^\beta, \beta = 1/2$
$\beta f(T)$	$-\ln 2$	$-\frac{1}{2}\ln\left(\frac{4}{1-m_0^2}\right) + \frac{m_0^2}{2}(1 - \beta Jc)$	$-\ln 2 + \frac{3}{4}t^2 \sim |t|^{2-\alpha}, \alpha = 0$
$\chi(T)$	$(cJt)^{-1}$	$\frac{1-m_0^2}{cJ(t+m_0^2)}$	$\sim |t|^{-\gamma}, \gamma = 1$

Table V.1: Thermodynamic quantities and critical behaviour of the Ising mean field theory. The deviation from the critical point $t = 1 - T_c/T$ has been introduced.

This set of critical exponents defines the mean field Ising universality class. All approximation methods dealing with infinite dimensional models neglecting spatial correlations fall into this class. Indeed, there are several ways to implement such an approximation and most of them are so important in their respective fields of application that they even have their own name: saddle-point approximation, Bogoliubov approximation, Bragg-Williams approximation, Flory approximation, etc. All of them can predict correct qualitative behaviour except near the critical point.

V.2.2   The Bethe-Peirls approximation

The Bethe-Peierls approximation consists in assuming that in the absence of a given site, the remaining neighbouring sites are uncorrelated [86]. Like the mean-field model, it approximates the model by defining the interacting variables in an infinite dimensional lattice better suited for exact calculations, the *Bethe lattice* [25]. The main improvement over the mean field approximation is that, in the Bethe-Peierls approach (BP), correlations between nearest-neighbours are taken into account and the connectivity of the original model is preserved. It takes into account the interactions of the neighbours of a given site with the other spins of the lattice by a 'mean molecular field'. Loops of links connecting spins are absent, and hence long-range correlations are not taken into account. The BP approximation will hence be accurate for any interacting graph where loops are irrelevant. An important example is given by regular random graphs for which

loops do not affect the thermodynamic behaviour of the problem. Random graphs include loops of typical length $\sim \ln N$ and hence are locally equivalent to a Bethe lattice at the thermodynamic limit, for which the BP method is exact.

The Bethe lattice is a connected graph with no loops, where each site is connected to c nearest neighbours. It can be constructed recursively in the following way: start from a central point, or seed, i_0 and attach c links connecting i_0 with its c neighbours. The set of these c points is called the *first shell* $n = 1$ denoted ∂i_0. From now on we should use ∂i to denote the set of vertices adjacent to the vertex i. The next shell $n = 2$ is constructed by attaching $(c - 1)$ vertices to each vertex of the previous shell in order to preserve the connectivity c of the graph. The shell $n+1 > 2$ is constructed by adding $(c - 1)$ vertices to each vertex in shell n. The shells $0, 1, 2$ of the graph constructed in such a way with $c = 4$ are shown in Fig. [V.2 (c)]. There are $N_n = c(c - 1)^{n-1}$ sites in shell n and therefore the total number in the graph is

$$N = \sum_{n=1}^{L} N_n = \frac{c\left((c-1)^L - 1\right)}{c - 2} \tag{V.14}$$

The L-th shell corresponds to the boundary of the graph. In this form, the finite graph we have constructed is a *Cayley tree*. The Bethe lattice is a Cayley tree which ignores the boundary sites and considers only properties of sites 'deep' in the bulk in the thermodynamic limit. Typically, one focuses on the central site. Then, by assuming translational invariance, the results obtained for the central site can be extended to the full Bethe lattice.

In order to illustrate the Bethe-Peierls approach let us consider the Ising model on a Bethe lattice of coordination number c in the absence of any external field. The probability of a given configuration of spins, denoted $\{\sigma\} = (\sigma_0, ..., \sigma_{N-1})$, is given by

$$\mathbf{P}(\{\sigma\}) = \frac{1}{Z} \exp\left(K \sum_{\langle i,j \rangle} \sigma_i \sigma_j\right), \qquad Z = \sum_{\{\sigma\}} \exp\left(K \sum_{\langle i,j \rangle} \sigma_i \sigma_j\right) \tag{V.15}$$

where the sum is over all the edges of the Bethe lattice and $K = \beta J$. It is useful to define the *marginal probability* of a spin σ_0 by

$$p(\sigma_0) = \sum_{\{\sigma\}\backslash\sigma_0} \mathbf{P}(\{\sigma\}), \tag{V.16}$$

where $\{\sigma\}\backslash\sigma_0$ denotes the configurations for which the spin σ_0 has been removed. The sum above runs over all the spins but σ_0. We will also use the standard notation $\partial i\backslash j$ for the sites in the neighbourhood of i different from j. Equation (V.16) can be written in terms of the c neighbours of the central spin $\{\sigma_i\}_{i\in\partial 0}$ as

$$p(\sigma_0) = \frac{1}{z_0} \sum_{\{\sigma_i\}_{i\in\partial 0}} p_c(\sigma_0|\sigma_1, ..., \sigma_c) \prod_{j\in\partial 0} \exp(K\sigma_0\sigma_j) \tag{V.17}$$

where $p_c(\sigma_0|\sigma_1, ..., \sigma_c)$ is the joint probability of $\{\sigma_i\}_{i\in\partial 0}$ in the absence of σ_0 and z_0 a normalisation factor. The Bethe-Peierls approximation assumes the statistical independence of each neighbour of σ_0 in its absence, i.e

$$p(\sigma_0) \stackrel{BP}{=} \frac{1}{z_0} \sum_{\{\sigma_j\}_{j\in\partial 0}} p_c(\sigma_0|\sigma_1)...p_c(\sigma_0|\sigma_c) \prod_{j\in\partial 0}^{c} \exp(K\sigma_0\sigma_j) . \tag{V.18}$$

If we remove the central spin σ_0 in the 0-th shell the lattice splits into c disconnected rooted trees (see Fig. V.3). Therefore, it is equivalent to do a Bethe-Peierls approximation of a model on a
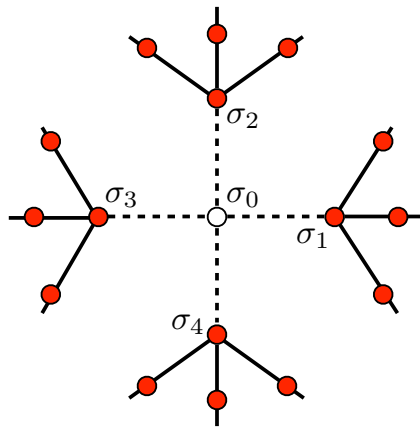
Figure V.3: **Cayley tree** with $c = 4$ and $L = 2$. When the central site 0 is removed (in white), the graph splits into c disconnected rooted sub-trees.

finite dimensional lattice and solve it on a Bethe lattice. In a similar way that it is equivalent to apply a mean field approximation to a finite dimensional problem and to solve it exactly on a fully connected graph.

The fundamental quantity to compute self-consistently in this approach is the "cavity" probability $p_c(\sigma_0|\sigma_j)$. We assume translational invariance in the bulk of the lattice: then we define the *cavity probabilities* $\mu(\sigma_j) \equiv p_c(\sigma_0|\sigma_j) = p_c(\sigma_i|\sigma_j)$, i.e. the marginal probability of σ_j in the modified lattice where one of its neighbours $i \in \partial j$ has been removed. Note that there is no more a central site when imposing translational invariance and the same reasoning applies to any site in the bulk of the lattice. Equation (V.18) can be rewritten as

$$p(\sigma_i) = \frac{1}{z_s} \prod_{j \in \partial i}^{c} \sum_{\{\sigma_j\}} \mu(\sigma_j) \exp(K\sigma_i\sigma_j) \tag{V.19}$$

with the normalisation factor:

$$z_s = \sum_{\sigma_i} \left(\prod_{j \in \partial i}^{c} \sum_{\{\sigma_j\}} \mu(\sigma_j) \exp(K\sigma_i\sigma_j) \right) \tag{V.20}$$

which can be though of as the partial partition function of a site.

In order to establish the self-consistent equation let us consider the cavity probability $\mu(\sigma_j)$ and take advantage of the natural recursive structure of the tree. When a neighbouring spin σ_i has been removed, $j \in \partial i$ has $c-1$ neighbours: $\{\sigma_k\}_{k \in \{\partial j \setminus i\}}$. The *self-consistent* equation for the cavity probabilities μ then is

$$\mu(\sigma_j) = \frac{1}{z_c} \prod_{k \in \{\partial j \setminus i\}}^{c-1} \sum_{\{\sigma_k\}} \mu(\sigma_k) \exp(K\sigma_j\sigma_k) \tag{V.21}$$

where z_c is the normalisation factor:

$$z_c = \sum_{\sigma_j} \left(\prod_{k \in \{\partial j \setminus i\}}^{c-1} \sum_{\{\sigma_k\}} \mu(\sigma_k) \exp(K\sigma_j\sigma_k) \right) . \tag{V.22}$$

In the thermodynamic limit all the sites are assumed to be equivalent and one can then write the self-consistent equation in the following compact form

$$\mu(\sigma) = \frac{1}{z_c} \left[\sum_{\{\sigma'\}} \mu(\sigma') \exp(K\sigma\sigma') \right]^{c-1} , \qquad z_c = \sum_{\sigma} \left(\sum_{\sigma'} \mu(\sigma') \exp(K\sigma\sigma') \right)^{c-1} . \quad \text{(V.23)}$$

In order to obtain thermodynamic quantities from this equation it is useful to parametrize μ by a 'cavity field' h_c and the marginal probability p by an effective field h_{eff}:

$$\mu(\sigma) = \frac{\exp(\beta h_c \sigma)}{2\cosh(\beta h_c)} , \qquad p(\sigma) = \frac{\exp(\beta h_{eff}\sigma)}{2\cosh(\beta h_{eff})} . \quad \text{(V.24)}$$

Then, using eqs. (V.23) and (V.19) one can write a self-consistent equations for the fields [4]

$$h_c = \frac{c-1}{2\beta} \ln \left[\frac{\cosh(\beta h_c + K)}{\cosh(\beta h_c - K)} \right] = \frac{c-1}{\beta} \text{arctanh}[\tanh(K)\tanh(\beta h_c)] , \quad \text{(V.25)}$$

$$h_{eff} = \frac{c}{2\beta} \ln \left[\frac{\cosh(\beta h_{eff} + K)}{\cosh(\beta h_{eff} - K)} \right] = \frac{c}{\beta} \text{arctanh}[\tanh(K)\tanh(\beta h_{eff})] . \quad \text{(V.26)}$$

These equations can be solved graphically. The slope of the right-hand-side of eq. (V.26) at $h_{eff} = 0$ is $s = (c-1)\tanh(K)$. For $s \leq 1$, the only solution is $h_{eff} = 0$. If $s > 1$ there are three solutions: $h_{eff} = 0$, $\pm h_0(T) \neq 0$. The critical point is then determined by

$$(c-1)\tanh(\beta_c J) = 1 . \quad \text{(V.27)}$$

After solving the self-consistent equation the thermodynamic quantities can be computed. The magnetisation is given by

$$m = \sum_{\sigma} \sigma p(\sigma) = \tanh(\beta h_{eff}) , \quad \text{(V.28)}$$

the partition function by

$$Z = \left(\frac{z_s}{z_l^{c/2}} \right)^N , \qquad z_l = \sum_{\sigma} \sum_{\sigma'} \mu(\sigma)\mu(\sigma') \exp(K\sigma\sigma') = \frac{z_s}{z_c} , \quad \text{(V.29)}$$

and the *Bethe free-energy* by

$$F/N = f_s - \frac{c}{2} f_l , \quad f_s = -k_B T \ln z_s , \quad f_l = -k_B T \ln z_l . \quad \text{(V.30)}$$

The Bethe free-energy is written as the sum over site and link contributions. Note that eq. (V.28) is identical to the mean field result eq. (V.9) for $h_{eff} = cJm$.

In the square lattice, the BP approximation gives a critical temperature $k_B T_c/J \approx 2.885$ which is much closer to the exact value $k_B T_c/J = \text{arcsinh}(1)/2 \approx 2.269$ [210] than the mean field prediction $k_B T_c/J = 4$. Note that, for the Ising chain ($c = 2$) the BP calculation is exact (since a one dimensional lattice is a Cayley tree) whereas the mean field approximation fails to describe its qualitative behaviour.

The BP approximation is of the mean field kind since correlations beyond nearest neighbours are neglected. It is an infinite dimensional approach, and hence it belongs to the mean field universality class: the critical exponents have the same values as those of the mean field model (see Table V.1). However, the description of the qualitative behaviour away from the critical point is

---

4. Using the relation: $\text{arctanh}(x) = \frac{1}{2} \ln \left[\frac{1+x}{1-x} \right]$.
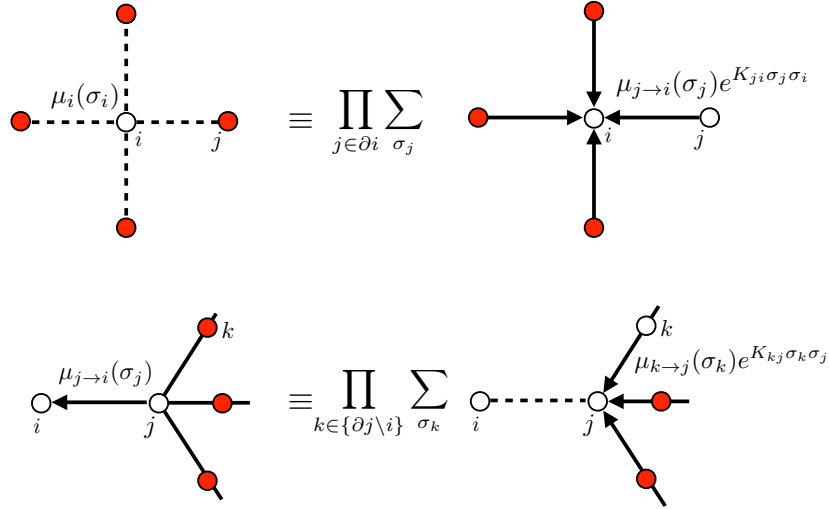
Figure V.4: Schematic representations of the BP recursion relations eq. (V.31) and (V.32).

improved compared to the mean field approach: for instance, the critical temperature is closer to the exact one, the heat capacity does not vanish for $T > T_c$.

In the simple example of the Ising model on a Bethe lattice all the sites were equivalent (homogeneous model). The Bethe-Peierls approximation presented above can be extended to the study of non-homogeneous systems on a general graph $\mathcal{G}$ where all the sites are not equivalent and the interactions between sites $\{J_{ij}\}$ can depend on the link.

Then, the marginal probability $p(\sigma)$ eq. (V.19) depends on the site which has been removed. We denote the marginal probability of the modified system where the site i has been removed by $\mu_i(\sigma_i)$. The BP approximation consist in assuming that $\mathcal{G}$ is locally a tree. Then, using new notations which make appear explicitly the inhomogeneity between different sites, eq. (V.19) and eq. (V.21) become

$$\mu_i(\sigma_i) = \frac{1}{z_i} \prod_{j \in \partial i}^{c} \sum_{\{\sigma_j\}} \mu_{j \to i}(\sigma_j) \exp(K_{ij} \sigma_i \sigma_j) \tag{V.31}$$

$$\mu_{j \to i}(\sigma_j) = \frac{1}{z_{j \to i}} \prod_{k \in \{\partial j \setminus i\}}^{c-1} \sum_{\{\sigma_k\}} \mu_{k \to j}(\sigma_k) \exp(K_{kj} \sigma_k \sigma_j) \tag{V.32}$$

respectively, where $K_{ij} = \beta J_{ij}$. A diagrammatic representation of these recursion relations is shown in Fig. V.4.

From what we presented in the previous section it is straightforward to find the self-consistent equation

$$h_{j \to i}(\sigma_j) = \frac{1}{\beta} \sum_{k \in \partial j \setminus i} \operatorname{arctanh}[\tanh(K_{kj}) \tanh(\beta h_{k \to j})] \tag{V.33}$$

for the cavity fields defined by

$$\mu_{j \to i}(\sigma_j) = \frac{\exp(\beta h_{j \to i} \sigma_j)}{2 \cosh(\beta h_{j \to i})} . \tag{V.34}$$

In this form, the cavity method can be applied to very general models by choosing the appropriate
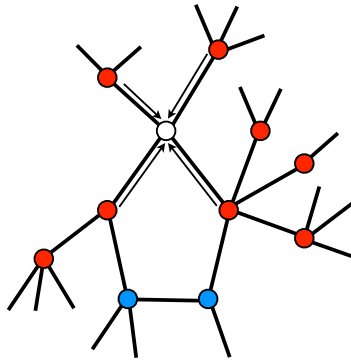
Figure V.5: Representation of the messages arriving at the site shown in white of a generic network. The BP approximation on a generic graph consist in neglecting the correlations due to the link between the nodes marked in blue.

lattice structure and interacting Hamiltonian. On a generic graph with loops the existence of solutions of the recursion equations (V.31, V.32) is far from being obvious. The cavity variables $\mu_{j \to i}(\sigma_j)$ can be though of as 'messages' between the nodes of a network (Fig. V.5). The problem of finding a fixed point of the recursion relations is equivalent to an inference problem: find the optimal solution considering all the statistical dependencies between the nodes of the network. This technique was introduced in artificial intelligence by Pearl [216] where it is known under the name of 'Belief Propagation'. Modern techniques of statistical mechanics, and disordered systems in particular, have been largely applied to optimisation problems in the last decades. Indeed, several important satisfiability problems can be reformulated in terms of spin models. The quest of a solution of a logical problem subject to some constraints turns out to be equivalent to finding the ground state of a spin glass Hamiltonian. For a review on the subject I refer the interested reader to [275, 192, 182].

The BP approach presented above considers exactly the pair interactions in an elementary 'cluster' made by a site and its c links. The Bethe lattice is then constructed by recursion from this cluster. There have been many attempts to improve this approximation (see [86] for a review on the subject). An important one is due to Kikuchi and is usually referred to as *cluster variation method*. In this approximation a finite number of different kinds of clusters of are systematically constructed and taken into account in the computation of thermodynamic quantities. It contains the mean-filed and BP approximations as special cases.

In order to describe four-spin interactions (as occurs in vertex models) one should replace edges linking two sites by a plaquette made by four sites as shown in Fig. V.6. Connecting such structures results on a *Cactus tree* (sometimes called *Husimi tree*)[5]. A variational reformulation of the BP approximation on cactus trees has also been introduced [220]. The lattice shown in Fig. [V.6 (c)] can be constructed easily by replacing each site of Bethe lattice with coordination number $c = 4$ by a square plaquette made of four spins (each one sitting on the vertices of the squares). It has been shown that approximate Ising models with multi-spin interactions by a cactus graph predicts the correct qualitative behaviour where a direct mean field approximations fails [194]. These lattices present a recursive structure and recursion relations can be established in the same way as in a Bethe lattice. The only difference between a calculation on a Bethe lattice and on a cactus is the number of terms in the recursion relations: it grows exponentially with the size

---

5. In graph theory, a cactus is a connected graph in which any two loops have, at most, one site in common. Every edge in such a graph belongs to at most one loop. In the following we will discuss 'regular' cacti for which all the loops are identical
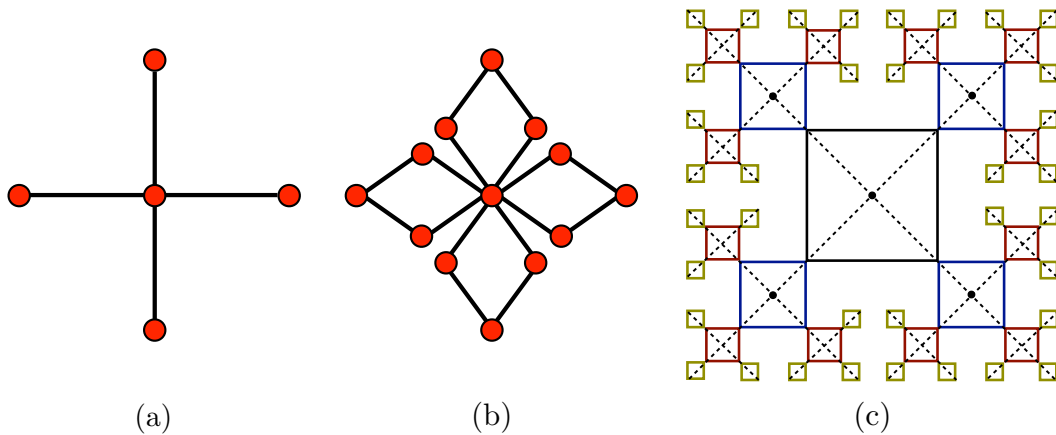
Figure V.6: (a) The elementary unit of the Bethe lattice. (b) Minimal elementary unit taking which takes into account four-spin interactions. (c) Cactus tree with $c = 4$ and $L = 3$. A Cayley tree with $c = 4$ and $L = 3$ is shown in dotted lines.

of an elementary plaquette. Hence, a balance between accuracy and computational complexity should be found.

In order to apply the BP approximation to a geometrically frustrated system, the introduction of cactus trees is needed. As pointed out in chapter II, the central object one must keep is the elementary local frustrated loop with a negative loop product as defined by eq. (II.6) . The sites of a Bethe lattice can be replaced by the relevant frustrated unit. This approximation has been applied to spin liquids [68], the AF Ising model on the triangular lattice [193] and the nearest-neighbours spin-ice model on the pyrochlore lattice [276, 130]. Although the critical properties of the physical system are lost, by defining the appropriate cactus tree, this method predicts a qualitatively correct phase diagram for these systems. In section V.4 we apply the BP approximation to the six-, eight- and sixteen-vertex models. When defining vertex models on a Bethe lattice of vertices, we reproduce the results of [276, 130]. We go further by defining an 'orientated' tree which allows for the investigation of all kind of possible orders occurring in the system (in particular the AF ones which were not studied in [276, 130]). We improve these results by defining the model on a cactus made by plaquettes of four vertices. This allows us to include the relevant low energy excitations of spin-ice.

V.3 Numerical simulations of the sixteen-vertex model

The $2D$ sixteen-vertex model is isomorphic to the Ising model on the checkerboard lattice with many-body interactions [166]. While this model is integrable for a special set of parameters for which the equivalent Ising model has two-body interactions only, none of these special cases corresponds to our choice of parameters. We used two numerical methods to explore the equilibrium properties of the generic model; the Continuous time Monte Carlo (CTMC) method that that we briefly explain in Sec. III.4.2 and in App. A and the Non-equilibrium relaxation method (NERM) that we equally explained in Sec. III.4.4.

V.3.1 Methods

V.3.1.1 Monte-Carlo algorithm

The numerical analysis of the equilibrium properties of $2D$ vertex models has been restricted, so far, to the study of the six and eight vertex cases. As explained in section IV.5.1, these models are simulated using non-local loop updates [16, 253]. By imposing the correct probabilities all along the construction of non-local moves cluster algorithms can be designed [253, 90]. Non-trivial issues as the effect of boundary conditions have been explored in this way [253, 6].

The loop algorithms could be modified to include three-in – one-out and one-in – three-out defects for the study of spin-ice systems [175, 130]. However, the simultaneous inclusion of four-in and four-out defects makes this algorithm inefficient compared to a Monte Carlo algorithm with local updates. For this reason, we will use local moves in our numerical studies, implemented by the Continuous-Time Monte Carlo algorithm (CTMC).

V.3.1.2 Non-equilibrium relaxation method

The fact that dynamic scaling applies during relaxation at a critical point [128] suggested to use short-time dynamic measurements to extract equilibrium critical quantities with numerical methods [129, 3]. Magnetized, $M_\pm^0 \equiv M_\pm(t = 0) = \pm 1$, and non-magnetized, $M_\pm^0 = 0$, configurations can be used as starting conditions and the critical relaxation

$$M_\pm(t) \simeq t^{-\beta/(\nu z)}\, F(t^{x_0/z} M_\pm^0) \qquad (V.35)$$

with z the dynamic critical exponent, and $F(x) \simeq x$ for $x \ll 1$ and $F(x) \to$ ct for $x \to \infty$, can be used to extract either the critical parameters or the critical exponents. This expression is expected to hold for $t^{1/z} \ll L$ and $t^{1/z} \ll \xi_{eq}$ with ξ_{eq} the equilibrium correlation length.

V.3.1.3 Observables

We used the following strategy to study the different phase transitions. We recall for clarity the definitions introduced in section V.1. We chose the relevant order parameter, $\langle M_+ \rangle$ or $\langle M_- \rangle$, to study FM or AF phases. These are the total *direct* and *staggered* magnetisation per spin

$$\langle M_\pm \rangle = \frac{1}{2}(\langle |m_\pm^x| \rangle + \langle |m_\pm^y| \rangle) \qquad (V.36)$$

with the horizontal and vertical fluctuating components given by

$$L^2 m_\pm^x = \sum_{(m,n)\in A_1} S_{m+1/2,n} \pm \sum_{(m,n)\in A_2} S_{m+1/2,n}\,, \qquad (V.37)$$

$$L^2 m_\pm^y = \sum_{(m,n)\in A_1} S_{m,n+1/2} \pm \sum_{(m,n)\in A_2} S_{m,n+1/2}\,. \qquad (V.38)$$

The angular brackets $\langle \ldots \rangle$ denote here and in the following the statistical average. The notations follow the ones already introduced in section V.1. The indices (m, n) are the coordinates of each vertex and $((2m + 1)/2), n)$ and $(m, (2n + 1)/2)$ locate the mid-points of the right- and up-pointing bonds. In the expressions for m we divided the lattice into two sub-lattices A and B such that $m + n$ is even and odd, respectively. The $\pm$ signs allow one to distinguish between FM and AF order.

From the scaling analysis of the corresponding fourth-order reduced Binder's cumulant

$$K_{M_\pm} = 1 - \frac{\langle M_\pm^4 \rangle}{3\langle M_\pm^2 \rangle^2} \simeq \Phi_K(t L^{1/\nu}) \qquad (V.39)$$

with t the distance to the critical point, we extracted ν. From the maximum of the magnetic susceptibility

$$\chi_\pm = L^2 \left[\langle M_\pm^2 \rangle - \langle M_\pm \rangle^2 \right] \simeq L^{\gamma/\nu} \Phi_\chi(tL^{1/\nu}) \tag{V.40}$$

we extracted γ/ν, then γ as ν was already known. From the maximum of the specific heat

$$C_E = L^{-2} \left[\langle E^2 \rangle - \langle E \rangle^2 \right] \simeq L^{\alpha/\nu} \Phi_C(tL^{1/\nu}) \tag{V.41}$$

we extracted α/ν, therefore α. Here, $E = \sum_k n_k \epsilon_k$ with n_k the number of vertices of type k and ϵ_k their energy. The direct measurement of β is difficult, we thus deduced it from the scaling relation $\beta = \frac{1}{2}(2 - \alpha - \gamma)$. Finally, we checked hyper-scaling, i.e. whether $d\nu = 2 - \alpha$ is satisfied by the exponent values obtained, that we summarize in Table V.2 for the SL/PM-FM transition and two choices of parameters.

V.3.1.4 Equilibration
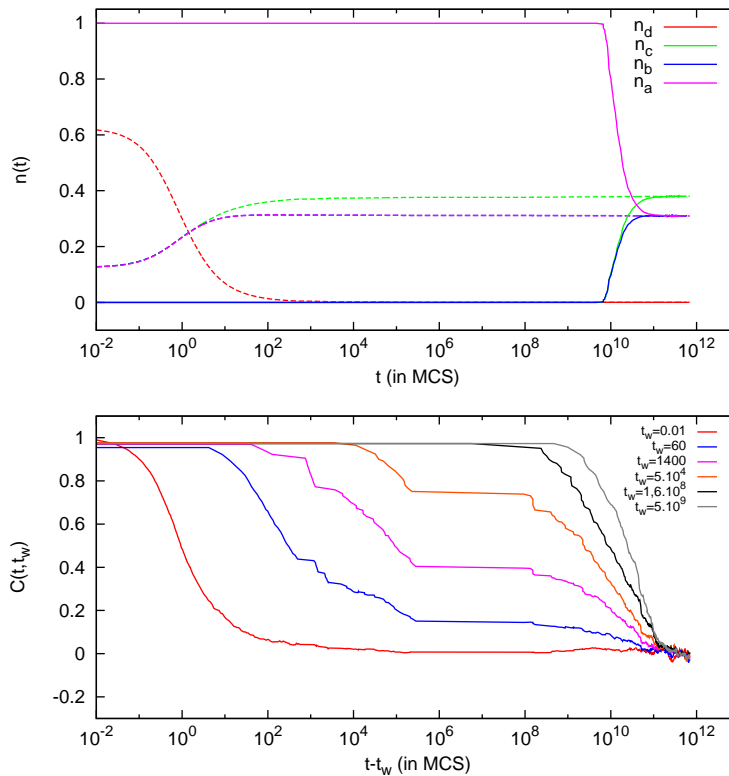
Figure V.7: Test of the equilibration of $L = 100$ samples for $a = b = 1$ and $d = e = 10^{-7}$. The data shown has been averaged over 300 independent runs. Top: Evolution of the density of vertices $n_{a,b,c,d}$ from a completely magnetised initial configuration with $n_a = 1$ (plain lines) and from a random initial configuration (dotted lines). Bottom: Two-time self correlation function of the system at different times (shown in the key) from a random initial configuration (i.e. $a = b = c = d = e = 1$). The correlations are not time translational invariant until later times $t \gtrsim 10^{12}$ MCs.

In order to estimate the thermal average of some thermodynamic quantity we must ensure the equilibration of the samples before performing any measurement. This is done by verifying that (i) the density of vertices stabilises at long times at the same value starting the evolution from very different (uncorrelated) initial configurations; (ii) the spatially local two-time correlation function is time translational invariant. This test is shown in Fig. V.7 for a special set of parameters.

V.3.2 Phase transitions and critical singularities

In this subsection we present a selected set of results from our simulations by describing the kind of phases and critical properties found. All our results are for a square lattice with linear size L and periodic boundary conditions.

V.3.2.1 The PM-FM transition

In order to diminish the number of parameters in the problem we studied the PM-FM transition for the special choice $d = e$.

As the direct magnetization density $\langle M_+ \rangle$ defined in eqs. (V.36)-(V.38) is the order parameter for the PM-FM transition in the six vertex model, we study this quantity to investigate the fate of the FM phase in the sixteen vertex model. In Fig. V.8 (a) we show $\langle M_+ \rangle$ for $b = 0.5$ and two values of d as a function of a, $L = 10, \ldots, 40$ and we averaged over $10^3 - 10^4$ samples. The variation of the magnetization as a function of a shows a sharp jump at $a = 1.5$ for $b = 0.5$ and $d = 0$, as one would expected for a first order phase transition. For $d > 0$ the curve takes a sigmoid form that gets wider (less step-like) for increasing d. The intersection point appears at larger values of a for larger values of d. These features suggest that the transition to the FM phase is continuous, occurs at larger values of a, and that there are fluctuations in the ordered state. The crossing of K_{M_+} at height $1/3$ (dotted horizontal line) for several values of L shown in Fig. V.8 (b) determines the transition point $a_c(b, d)$. Consistently with a second-order phase transition, K_{M_+} remains positive for all L.
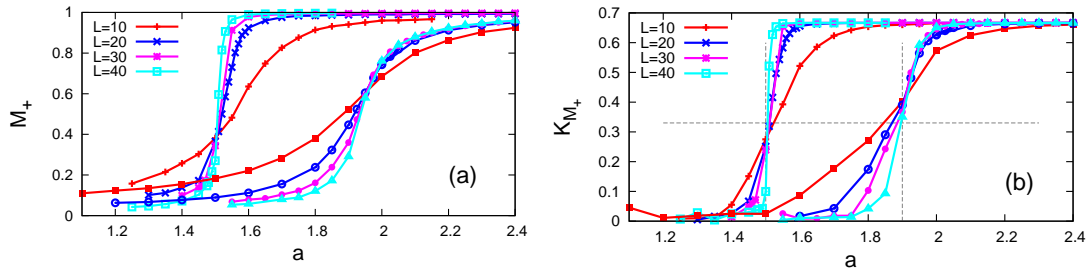
Figure V.8: Study of the FM transition. (a) Magnetization per spin $\langle M_+ \rangle$ and (b) magnetization cumulant K_{M_+} as a function of a for $b = 0.5$, $d = 10^{-5}$ (the group of curves on the left) and $d = 0.1$ (the ones on the right), and several L given in the key. The crossing points of K_{M_+} determine $a_c(b, d)$. The vertical dotted (black) lines are the critical values predicted by $|\Delta_{16}| = 1$. The horizontal dotted level is $1/3$.

In Fig. V.9 we show $\langle M_+ \rangle$ as a function of a for $b = 0.5$ and three values of the parameter $d = e$ (all normalised by c). The data for the $2D$ model (shown with coloured points) demonstrate that the presence of defects tends to disorder the system and, therefore, the extent of the PM phase is enlarged for increasing values of $d = e$. Moreover, the variation of the curves gets smoother for increasing values of $d = e$ suggesting that the transitions are of second order (instead of first order) with defects. The data displayed with black points for the same parameters are the result of the

analysis of the model defined on a tree and we postpone its discussion to Sec. V.4. The numerical results suggest that the equilibrium phases of the sixteen vertex model could be characterised by a generalisation of the anisotropy parameter of the eight-vertex model:

$$\Delta_{16} = \frac{a^2 + b^2 - c^2 - (d + 3e)^2}{2[ab + c(d + 3e)]} \ . \tag{V.42}$$

In the same way as in the integrable cases, the proposal is that the PM phase corresponds to the region of the parameters' space where $|\Delta_{16}| < 1$, the FM phases corresponds to $\Delta_{16} > 1$ (and the AF ones to $\Delta_{16} < -1$). It follows that the projection of the FM-transition hyper-planes onto the $(a/c, b/c)$ plane should be parallel to the ones of the six and eight vertex models and given by $a_c = b + c + d + 3e$ (or equivalently $b_c = a + c + d + 3e$). As shown in Fig. V.9, the numerical results are close to this assumption but they do not justify it completely either (We will compare the trend of the transition lines with $d = e$ as obtained with the cavity method in Sec. V.4.). As we will explain in detail in the following section, our BP treatment for the model defined on a tree of single vertices predicts a similar shift of the transition lines given by $a_c = b + c + d + 2e$. The parameter capturing all transition lines is, within this analytic approach,

$$\Delta_{16}^{sv} = \frac{a^2 + b^2 - c^2 - d^2 + 2(a + b - c - d)e}{2(cd + ab + e(a + b + c + d + 2e))} \tag{V.43}$$

(see section V.4 for the technical details). For the more sophisticated tree made of 'plaquette' units the transition lines are not parallel to the ones of the six- and eight-vertex models and an analytic form of the anisotropy parameter, Δ_{16}^{pl}, has not been found. However, the transition lines can be computed numerically and their evaluation leads to the phase diagram depicted in Fig. V.22.
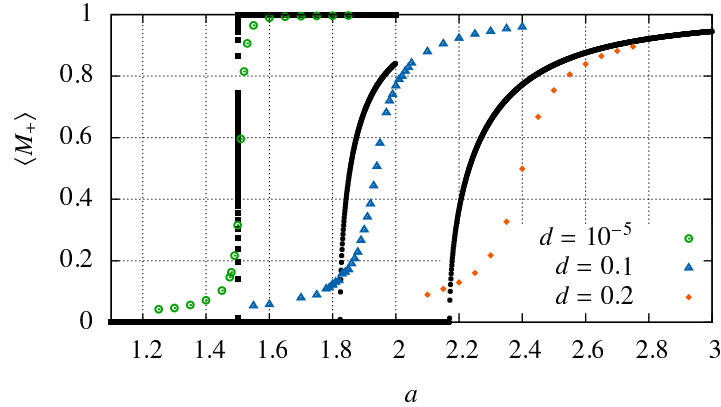
Figure V.9: Equilibrium magnetisation density, $\langle M_+ \rangle$, of the sixteen vertex model with $d = e$ taking three values given in the key and $b = 0.5$ as a function of a (parameters normalised by c). The coloured data points are the result of the numerical simulations of the $2D$ model for $L = 40$ while the black dots have been obtained with the analytic solution of the model defined on the tree, as explained in Sec. V.4.

Further evidence for the transition becoming second order comes from the analysis of the fourth-order cumulant defined in eq. (V.39). In Fig. V.10 we display raw data for $d = e = 10^{-5}$ (a) and scaled data for $d = e = 0.1$ (b) as a function of $t = (a - a_c)/a_c$. In both cases $b = 0.5$ and, as above, we normalise all parameters by c. From the analysis of the scaling properties we extract $a_c = 1.5$ for $d = e = 10^{-5}$ and $a_c = 1.93$ for $d = e = 0.1$. Sets of data for linear system

sizes $L = 10,\ 20,\ 30,\ 40,\ 50$ are scaled quite satisfactorily by using $1/\nu = 1.65 \pm 0.05$ for the small d and $1/\nu = 1 \pm 0.1$ for the large value of d.
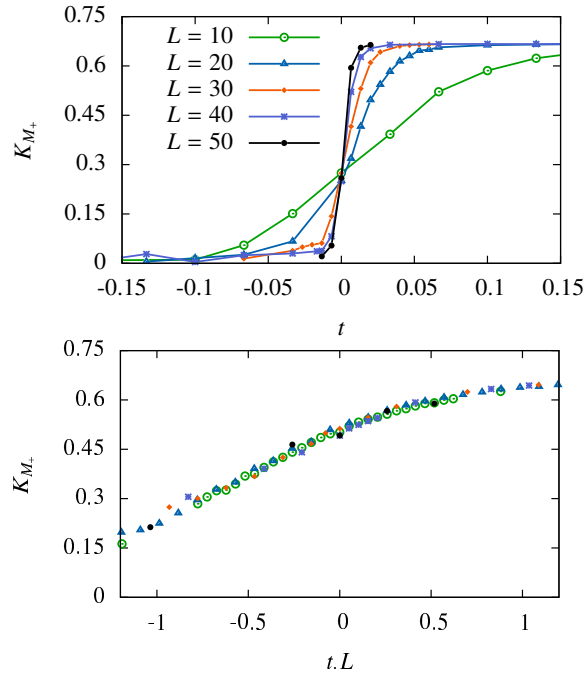
Figure V.10: Analysis of the Binder fourth-order cumulant defined in eq. (V.39) across the FM-PM transition in the sixteen vertex model. (a) Raw data for $d = e = 10^{-5}$. (b) Scaling plot for $d = e = 0.1$. One extracts $1/\nu = 1.65 \pm 0.05$ in case (a) and $1/\nu = 1 \pm 0.1$ in case (b) from this analysis.

In order to complete the analysis of this transition we studied the magnetic susceptibility (V.40) associated to the direct magnetization M_+ and its finite size scaling. Figure V.11 displays χ_+ for $b = 0.5$, $d = e = 10^{-5}$ (a) and $d = e = 0.1$ (b), and five linear sizes, $L = 10,\ 20,\ 30,\ 40,\ 50$. The data collapse is very accurate and it allows us to extract the exponent $\gamma/\nu \simeq 1.75 \pm 0.02$ in both cases. The study of the maximum of χ_+ displayed in the insets confirms this estimate for γ/ν. We repeated this analysis for other values of $d = e$ and we found that in all cases critical scaling is rather well obeyed and, interestingly enough, γ/ν is, within numerical accuracy, independent of $d = e$. This is similar to what happens in the eight-vertex model since, as shown in Table IV.2, this ratio is independent of the parameters.

The ratio α/ν is obtained from the finite size analysis of the specific heat (not shown) that is consistent with $C^{max} \simeq L^{\alpha/\nu}$ (instead of L^D for a first order phase transition). We found $\alpha/\nu \simeq 1.30 \pm 0.06$ for these values of b and $d = e = 10^{-5}$ and a logarithmic divergence of the heat capacity, i.e. $\alpha/\nu \approx 0$ for $d = e = 0.1$ (cf. Table V.2), although this is difficult to assert numerically.

The numerical exponents at the second order phase transition with $d = e$ and both different from zero are compared to the ones of the six vertex model and the $2D$ Ising model in Table V.2. It is interesting to note that for very small value of $d = e$ the exponents are rather close to the ones of the six-vertex model while for large value of $d = e$ they approach the ones of the $2D$ Ising model. The numerical critical exponents we obtained depend on the parameter $d = e$, as suggested from the theory of the eight vertex model. As shown in Table V.2, the ratios of critical exponents $\hat{\gamma}$, $\hat{\beta}$ and $\hat{\phi}$ do not depend on the choice of the external parameters. As one could expect, the values we obtained for these generalized critical exponents are equal to the ones of the eight

vertex model and the $2D$ Ising model, since these two latter models are special cases of the sixteen vertex model.

The NERM yields values of the critical a that are in agreement (within numerical accuracy) with the ones found with the conventional analysis. We do not show this analysis here.
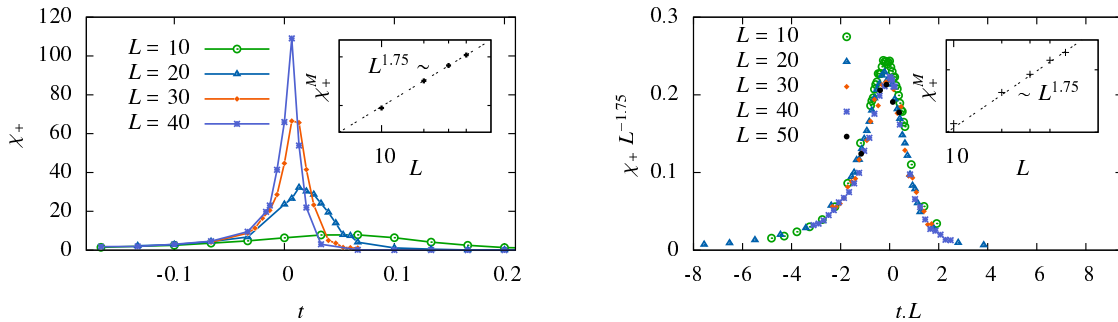

Figure V.11: The magnetic susceptibility across the PM-FM transition for $b = 0.5$, $d = e = 10^{-5}$ (a) and $d = e = 0.1$ (b). Where t is the distance to the critical point measured as $t = (a - a_c)/a_c$ with $a_c = 1.5$ (a) and $a_c = 1.93$ (b). From the finite size scaling of the maximum shown in the insets one extracts $\gamma/\nu \simeq 1.75 \pm 0.02$ in both cases.

	six-vertex	MC ($d = e = 10^{-5}$)	MC ($d = e = 0.1$)	$2D$ Ising
$\gamma/\nu = \hat{\gamma}$	7/4	1.75 ± 0.02	1.75 ± 0.02	7/4
$\beta/\nu = \hat{\beta}$	1/8	0.125 ± 0.05	≈ 0.125	1/8
$(2 - \alpha)/\nu = \hat{\phi}$	2	2.00 ± 0.15	≈ 2	2
α	1	0.84 ± 0.23	≈ 0	0
β	1/16	0.050 ± 0.014	≈ 0.125	1/8
γ	7/8	1.06 ± 0.03	1.75 ± 0.18	7/4
ν	1/2	0.60 ± 0.02	1.0 ± 0.1	1
$2\nu = 2 - \alpha$?	yes	yes	yes	yes

Table V.2: Numerical values of the critical exponents at the FM-PM transition in the sixteen vertex model as compared to the ones in the six vertex model (first column) and $2d$ Ising model (fourth column). The parameter μ, $\tan(\mu/2) = \sqrt{cd/ab}$, has been chosen to take the same value in the two MC columns, $\mu = \pi$. We did not include error bars for $\hat{\beta}$, $\hat{\phi}$, α and β in the column corresponding to $d = e = 0.1$ as our determination of α is not precise enough to distinguish between $\alpha = 0$ (the value used to extract the remaining exponents) and a very small but non-vanishing value.

V.3.2.2   The PM-AF transition

We now focus on the transition between the c-AF and PM phases. For the six-vertex model this is a KT transition while for the eight-vertex model it is of second order as soon as $d > 0$. In this case we chose to work with $d = 10^{-5} \neq e = 10^{-3}$ and with $d = e = 10^{-5}$. We present data obtained with the NERM.

Figure V.12 shows the relaxation of the staggered averaged magnetisation at $b = c = 1$ and different values of a given in the caption. The power-law relaxation, typical of the critical point, is
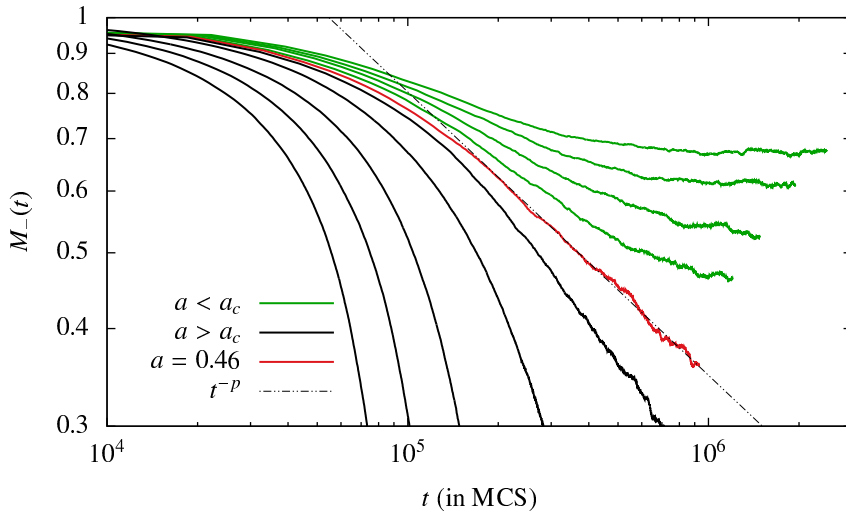
Figure V.12: Non-equilibrium relaxation of the staggered magnetization from a fully ordered initial condition $M_-^0 = 1$ at different values of $a = b$, for $c = 1$, $e = 10^{-3}$ and $d = 10^{-5}$. After a short transient the relaxation at the critical point follows a power law t^{-p} with $p = \beta/(\nu z)$. We identify such critical relaxation at $a_c = 0.46 \pm 0.01$. A precise estimation of the exponent z its harder and the NERM has only been used here to estimate the transition point.

clearly identifiable from the figure. We extract a critical weight $a_c = 0.46 \pm 0.01$ for the c-AF-PM phase transition. Moreover, the data allow us to prove that the PM phase is not of SL-type as soon as a finite density of defects is allowed. Indeed, the relaxation of M_- does not follow a power law within this phase; instead, for $a > a_c$ the decay is exponential. Although the determination of a_c is rather clear in this way, it is very hard to determine the value of the exponent p, and hence of z, with good precision as p is extremely sensitive to the choice of a_c.

The standard analysis of the c-AF-PM transition is not as clean as for the FM-PM one. Figure V.13 (b) shows the scaling plot of the Binder cumulant of the staggered magnetisation for $b = 0.5$ and, in this case, $d = e = 10^{-5}$. From it one extracts $1/\nu = 0.4 \pm 0.05$. The susceptibility fluctuates too much to draw certain conclusions about the exponent γ. The analysis of the specific heat (not shown) suggests a logarithmic divergence $\alpha \approx 0$. The dependence of the critical line on the parameters is reasonably well described by Δ_{16}.

Both e and d vertices make the disordered phase be a conventional PM, and the transitions be second order. Although d does not break integrability while e does their effect, in these respects, are the same. The variation of the critical exponents in the eight-vertex model is known but in the sixteen-vertex case it is not. Unfortunately, it is very hard to get such a precise measurement of the observables close to the critical lines to conclude about the exponents in the sixteen-vertex case. Possibly, a renormalization group approach would be useful in this respect.

V.4 Vertex models on a tree

In this Section we study the properties of the six-, eight- and sixteen-vertex models defined on the Bethe lattice by using the cavity method. Aiming at capturing the properties of the two-dimensional squared lattice problem we will first consider a standard Bethe lattice of uniform connectivity $c = 4$, and then, we will improve such approximation by taking into account small loops by applying the same method to plaquettes of 2×2 vertices connected in a tree-like way.
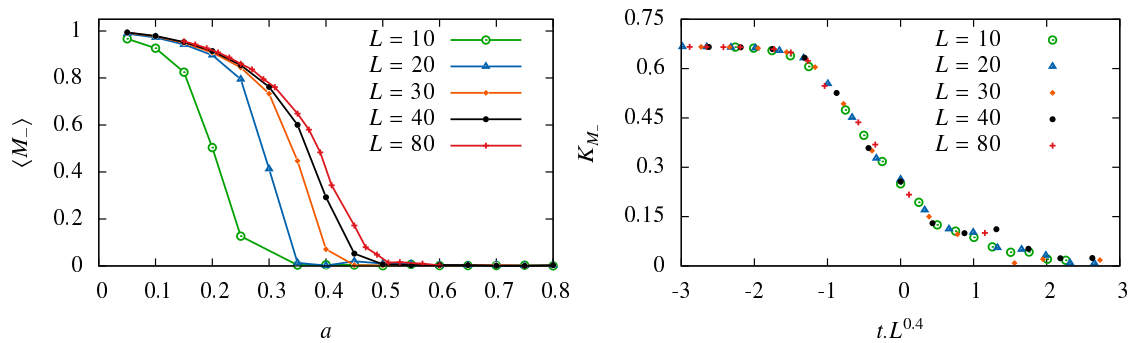
Figure V.13: Study of the c-AF-PM transition for $b = 0.5$ and $d = e = 10^{-5}$. (a) The averaged staggered magnetization as a function of a for several system sizes given in the key. (b) Scaling plots across the c-AF-PM transition of the Binder cumulant of the staggered magnetization. t is the distance from the critical point $t = (a - a_c)/a_c$ with $a_c = 0.5$. The best scaling of data is obtained for $1/\nu = 0.4 \pm 0.05$.

As shown in the following, such approach, compared to the exact and the numerical results in two dimensions turns out to be remarkably good.

In the following we specialise our discussion to the analysis of the six-, eight- and sixteen-vertex models on a tree made of simple vertices or four site plaquettes. The definition of the vertices requires the selection of a particular orientation of the edges adjacent to a given site. We will define "horizontal" and "vertical" edges, each one with two possible orientations. This procedure allows us to associate a statistical weight to each vertex configuration, even in such non-Euclidean geometry. In the recurrence equations this partition will translate into four species of rooted trees, depending on the position (left, right, down or up) of the missing neighbour.

V.4.1 The oriented tree of vertices

We focus on a regular tree with no loops and fixed connectivity $c = 4$ for all the sites (vertices) in the *bulk*, thus conserving the local connectivity of the square lattice geometry. The sites on the boundary, also called the leaves, have only one neighbour.

The evaluation of the physical quantities using this geometry is based on the determination of the properties of the site at the *root* of the rooted tree. As discussed in section V.2.2 a rooted tree is a tree in which all the sites have the same connectivity $c = k + 1$ apart from the root (and the leaves) which has only k neighbours. The Bethe lattice (or Cayley tree) is obtained by connecting $k + 1$ rooted trees with a central site.

In the models we are interested in, each site is a vertex and its coordination, which is fixed, is the number of vertices connected to it. In order to distinguish one vertex from another one, and later identify all possible ordered phases, we define the analogue of the two orthogonal directions of the Euclidean squared lattice. Given that the connectivity of the graph is equal to four, each vertex has four terminals that we call "up" (u), "down" (d), "left" (l) and "right" (r). So far, the vertices were labeled by their positions. Here, for the sake of clarity, we label them with a single latin index, say i, j, k. Vertices are connected through edges $\langle i^d j^u \rangle$ and $\langle i^l k^r \rangle$ that link respectively the "down" extremity of a vertex i with the "up" terminal of a neighboring vertex j, or the "left" end of i with the "right" end of its neighbor k. The symbols $\langle i^d j^u \rangle$ and $\langle i^l k^r \rangle$ denote undirected edges, so that $\langle i^d j^u \rangle = \langle j^u i^d \rangle$ and $\langle i^l k^r \rangle = \langle k^r i^l \rangle$. In this way, one creates a bipartition of the edges into "horizontal" (left-right $\langle i^l k^r \rangle$) and "vertical" (up-down $\langle i^d j^u \rangle$) edges. This notation gives a notion of which vertex is above (i) and which one is below (j) and similarly

for the horizontal direction.

Each edge is occupied by an arrow shared by two vertices. An arrow defined on the $\langle i^l k^r \rangle$ edge is the left arrow for the i vertex and the right arrow for the neighboring k vertex. A similar distinction holds for the vertical $\langle i^d j^u \rangle$ edges. Each arrow, as any binary variable, can be identified with a spin degree of freedom, taking values in $\{-1, 1\}$. In this construction there are two kinds of spins, those living on horizontal edges, $s_{\langle i^l k^r \rangle}$, and those sitting on vertical edges, $s_{\langle i^d j^u \rangle}$. We choose a convention such that $s_{\langle j^u i^d \rangle} = +1$ if the arrow points up and -1 otherwise. Similarly, $s_{\langle k^r i^l \rangle} = +1$ if the arrow points right and -1 otherwise, for the horizontal arrows (see Fig. V.14) This is the analog of the convention used for the spin sign assignment used in the $2D$ model. Clearly, these definitions are not unique and one may introduce other ones if found more convenient.
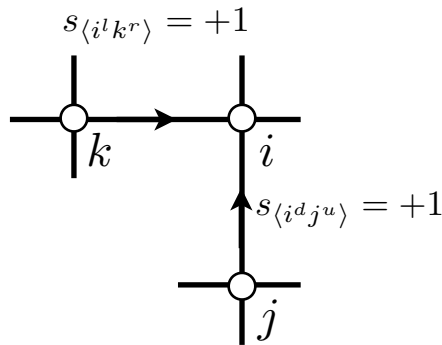
Figure V.14: Two spins living on a horizontal and a vertical edge taking both value $+1$.

The local arrow configuration defines the state of the selected vertex. With the spin definition given above, we can assign a total spin S_i to each vertex i, and define it as the sum of the spins attached to it, $S_i \equiv \sum_{j \in \partial i} s_{\langle ij \rangle}$. With this assignment, the spin associated to each type of vertices is $S_i = \pm 4$ if the vertex is of type a, $S_i = 0$ if it is a b one, $S_i = 0$ if the vertex is of kind c, $S_i = 0$ for a d vertex, and $S_i = \pm 2$ for the e ones.
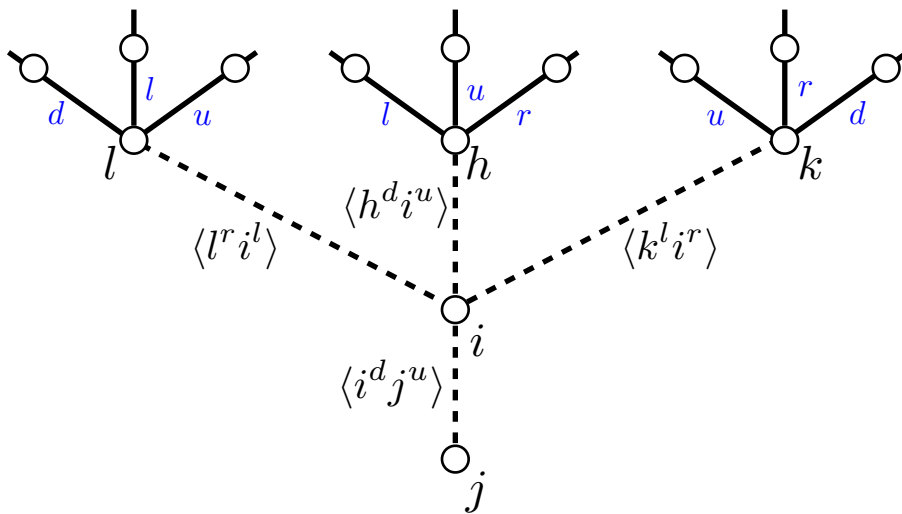
Figure V.15: Construction of an "up rooted tree" from the merging of a left, up, right and down rooted tree.

Consider now a site (vertex) i at the root of a rooted tree. There are four possible distinct kinds of rooted trees depending on whether the missing vertex j that should be attached to the root be the one on its left, right, up or down direction. By analogy with the two dimensional case, one could interpret these rooted trees as the result of the integration of a transfer matrix approach applied in four possible directions. This can be emphasised by taking into account the particular direction of the missing edge at the root that we will indicate as follows: $i^p \to j^q$, with $p, q \in \{u, d, l, r\}$. For instance, an "up rooted tree" is the one where the root i lacks the connection to the up terminal of the vertex j, i.e. the link $i^d \to j^u$ is absent. As shown in Fig. V.15, such a rooted tree is obtained by merging a left, an up and a right rooted tree (with root vertices l, h and k respectively) with the addition of a new vertex i through the links $l^r \to i^l$, $h^d \to i^u$, $k^l \to i^r$ (pictorially the transfer matrix is moving "down"). Similarly a "left rooted tree" is obtained by merging a down, a left and an up rooted tree, and so on. The Bethe lattice is finally recovered by joining an up, a left, a down and a right rooted tree with the insertion of the new vertex. Equivalently, given a tree, one creates rooted (cavity) trees removing an edge.

V.4.2   The tree of plaquettes

As we will show, the results obtained by using the tree constructed above turn out to be remarkably accurate in the reproduction of the $2D$ phase diagram that, in many respects, is also exact. In order to further improve the comparison with the finite dimensional case we used a similar Bethe lattice made of "plaquettes" (see Fig. V.16). This means that the basic unit is not a single vertex but a square of 2×2 vertices and that the tree is constructed by connecting one of these plaquettes to other four ones, without forming loops of plaquettes. As we will see, in some cases, the presence of local loops of spins within the plaquette can result in qualitative different results, that go in the direction of the $2D$ behavior.

In the following we will refer to the first simpler geometry as the "single vertex problem" and to the second one as the "plaquette model".

V.4.2.1   Discussion

A mean-field approximation to the pyrochlore spin-ice system, leading to the same tree-like structure that we use here, was used in [276] and [130]. In these papers no distinction between the orientation (up, down, left, right) of the edges was made. The approach was apt to deal with the SL and FM phases only [130]. Our approach keeps track of four different directions and allows us to simultaneously study all possible phases, including the AF ones. Within such an approach it is also quite straightforward to remove the degeneracy of the vertices by introducing external fields or other perturbations.

A tree *without loops* yields a very good approximation to the transition towards the frozen FM phase (KDP problem) in pyrochlore spin-ice [276, 130]. This is due to the absence of fluctuations in the frozen FM phase. Such an approximation is not, however, precise enough to describe the unfrozen staggered AF order, since this phase is populated by loop fluctuations at finite temperature. By building the tree with elementary loops we captured some of these fluctuations.

V.4.3   The six and eight-vertex model on a tree of vertices

In this Subsection we study the six- and the eight-vertex models on a tree of vertices. We present the self-consistency equations for the marginal probabilities, their fixed points and stability analysis, the free-energy of the different phases and the ensuing phase diagram.
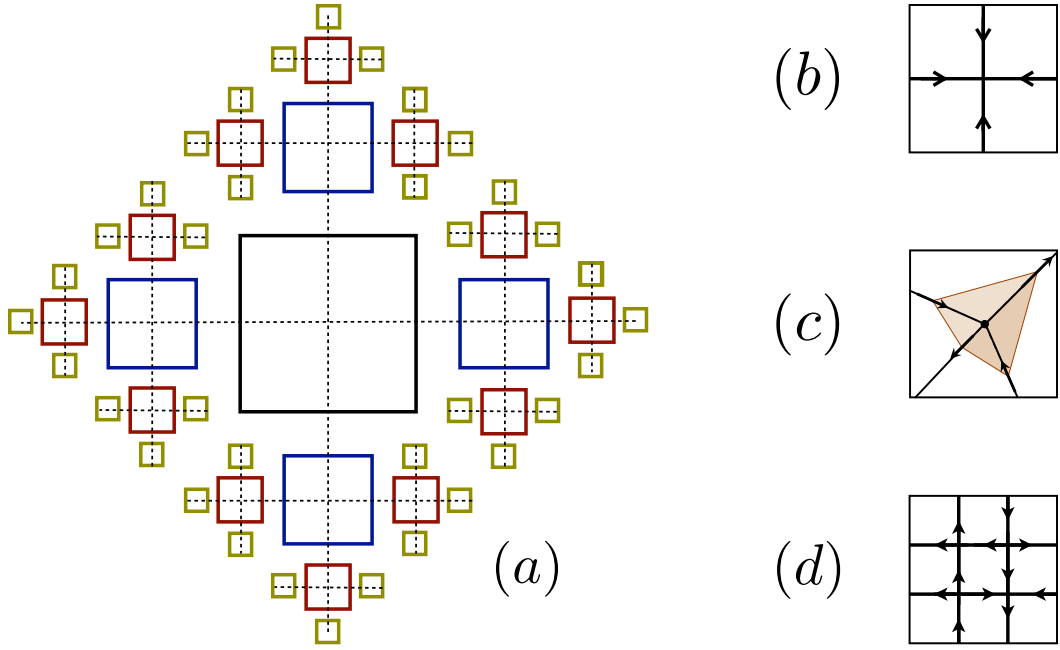
Figure V.16: The main panel shows how to construct a Bethe lattice of individual units that can be chosen at wish. In the right panel we show four different choices of such units. The image in (b) represents a single vertex that once inserted in (a) builds the simplest Bethe lattice of vertices, discussed in the text. The tetrahedron in (c) can be equally thought of as a planar vertex, as the one in Fig. (b). We discuss such representation in section V.4.2.1. Finally panel (d) shows a plaquette of four vertices that is the unit also considered in the text.

V.4.3.1   Recursion equations

We call $\psi_\zeta^{i^\alpha \to j^\beta}$, with $\alpha, \beta \in \{u, d, l, r\}$, the probability that the root vertex i – in a rooted tree where $\langle i^\alpha j^\beta \rangle$ is the missing edge – be of type $\zeta \in \chi_v^8 = \{v_1, \ldots, v_8\}$. Such probabilities must satisfy the normalization condition

$$\sum_{\zeta \in \chi_v^8} \psi_\zeta^{i^\alpha \to j^\beta} = 1 , \qquad \forall \, \langle i^\alpha j^\beta \rangle . \tag{V.44}$$

In the recurrence procedure we will only be concerned with the state of the arrow on the missing edge. Therefore, by considering a root vertex i with a missing edge $i^\alpha \to j^\beta$, we define $\psi_i^\beta \equiv \psi^{i^\alpha \to j^\beta}(+1)$ as being the probability that the arrow that lies on the missing edge $\langle i^\alpha j^\beta \rangle$ takes the value $s_{\langle i^\alpha j^\beta \rangle} = +1$. Then,

$$\begin{aligned}
\psi_i^u &= \psi_{v_1}^{i^d \to j^u} + \psi_{v_3}^{i^d \to j^u} + \psi_{v_6}^{i^d \to j^u} + \psi_{v_8}^{i^d \to j^u} , \\
\psi_i^d &= \psi_{v_1}^{i^u \to j^d} + \psi_{v_3}^{i^u \to j^d} + \psi_{v_5}^{i^u \to j^d} + \psi_{v_7}^{i^u \to j^d} , \\
\psi_i^l &= \psi_{v_1}^{i^r \to j^l} + \psi_{v_4}^{i^r \to j^l} + \psi_{v_6}^{i^r \to j^l} + \psi_{v_7}^{i^r \to j^l} , \\
\psi_i^r &= \psi_{v_1}^{i^l \to j^r} + \psi_{v_4}^{i^l \to j^r} + \psi_{v_5}^{i^l \to j^r} + \psi_{v_8}^{i^l \to j^r} ,
\end{aligned} \tag{V.45}$$

and

$$\psi^{i^\alpha \to j^\beta}(-1) = 1 - \psi^{i^\alpha \to j^\beta}(+) = 1 - \psi_i^\beta . \tag{V.46}$$

Note that other parameterizations are possible for these probabilities. For instance, one could

use an effective field acting on the spin $s_{\langle i^\alpha j^\beta \rangle}$, *i.e.* $\psi_i^\beta = e^{h_i^\beta}/(e^{h_i^\beta} + e^{-h_i^\beta})$, and the recurrent equations would be equivalently written for the fields h_i^β.

The operation of merging rooted trees allows us to define the set of probabilities associated to the new root in terms of those belonging to the previous generation. In the bulk of the tree one does not expect such quantities to depend on the precise site. Then, the explicit reference to the particular vertex i in eq. (V.45) can be dropped, and four equations for the cavity probabilities are obtained.

In the BP approximation, the strategy is to write down the self-consistent equations due to the site independence of the behaviour in the bulk. Then, one should find the solutions, i.e. fixed points of these equations. Assuming the statistical weights to be symmetric under the arrow reversal and defined as in Fig. V.1, the *self-consistent equations* read:

$$
\psi^u = \hat{\Psi}^u[a,b,c,d,\psi^u,\psi^d,\psi^l,\psi^r] = g^u(a,b,c,d,\psi^u,\psi^d,\psi^l,\psi^r)/z^u
$$

$$
= \frac{1}{z^u}\left[a\psi^l\psi^u\psi^r + b(1-\psi^l)\psi^u(1-\psi^r) + c(1-\psi^u)(1-\psi^l)\psi^r + d\psi^l(1-\psi^u)(1-\psi^r) \right]
$$

$$
\psi^l = \hat{\Psi}^l[a,b,c,d,\psi^u,\psi^d,\psi^l,\psi^r] = g^l(a,b,c,d,\psi^u,\psi^d,\psi^l,\psi^r)/z^l
$$

$$
= \frac{1}{z^l}\left[a\psi^d\psi^l\psi^u + b(1-\psi^d)\psi^l(1-\psi^u) + c\psi^d(1-\psi^l)(1-\psi^u) + d(1-\psi^d)(1-\psi^l)\psi^u \right]
$$

$$
\psi^d = \hat{\Psi}^d[a,b,c,d,\psi^u,\psi^d,\psi^l,\psi^r] = g^d(a,b,c,d,\psi^u,\psi^d,\psi^l,\psi^r)/z^d
$$

$$
= \frac{1}{z^d}\left[a\psi^r\psi^d\psi^l + b(1-\psi^r)\psi^d(1-\psi^l) + c(1-\psi^r)(1-\psi^d)\psi^l + d\psi^r(1-\psi^d)(1-\psi^l) \right]
$$

$$
\psi^r = \hat{\Psi}^r[a,b,c,d,\psi^u,\psi^d,\psi^l,\psi^r] = g^r(a,b,c,d,\psi^u,\psi^d,\psi^l,\psi^r)/z^r
$$

$$
= \frac{1}{z^r}\left[a\psi^u\psi^r\psi^d + b(1-\psi^u)\psi^r(1-\psi^d) + c\psi^u(1-\psi^r)(1-\psi^d) + d(1-\psi^u)(1-\psi^r)\psi^d \right]
$$

$$
\text{(V.47)}
$$

where z^i are normalisation constants which guarantee that ψ^i is the probability that a spin takes the value $(+1)$:

$$
z_\alpha = g^\alpha(a,b,c,d,\psi^u,\psi^d,\psi^l,\psi^r) + g^\alpha(a,b,c,d,1-\psi^u,1-\psi^d,1-\psi^l,1-\psi^r) . \quad \text{(V.48)}
$$

The first term in this sum stems from the un-normalized contribution of a spin $(+1)$ while the second term is for a spin (-1), see eq. (V.46).

V.4.3.2   Order parameters

According to the definitions in eq. (V.36), we characterize the phases by direct and staggered magnetizations. In particular, we define the following order parameters, each one associated with

a particular ordered phase and all of them vanishing in the PM state: [6]

$$m_{a\text{-FM}} = \frac{a}{Z_v}[\psi^l\psi^u\psi^r\psi^d - (1-\psi^u)(1-\psi^l)(1-\psi^r)(1-\psi^d)] \,,$$

$$m_{b\text{-FM}} = \frac{b}{Z_v}[(1-\psi^l)\psi^u(1-\psi^r)\psi^d - \psi^l(1-\psi^u)\psi^r(1-\psi^d)] \,,$$

$$m_{c\text{-AF}} = \frac{c}{Z_v}[\psi^u\psi^l(1-\psi^r)(1-\psi^d) - (1-\psi^u)(1-\psi^l)\psi^r\psi^d] \,,$$

$$m_{d\text{-AF}} = \frac{d}{Z_v}[(1-\psi^l)\psi^u\psi^r(1-\psi^d) - \psi^l(1-\psi^u)(1-\psi^r)\psi^d] \,,$$

(V.49)

where Z_v is the contribution of a vertex to the partition function defined in eq. (V.53).

V.4.3.3 Fixed points and free energy

In order to allow for a fixed point solution associated to c-AF and d-AF order we study eqs. (V.47) on a bipartite graph. We partition the graph into two distinct subsets of vertices A_1 and A_2, such that each vertex belonging to A_1 is only connected to vertices belonging to A_2 and vice-versa. This amounts to doubling the fields degrees of freedom $\{\psi_1^\alpha, \psi_2^\alpha\}$, one for the sub-lattice A_1 and the other one for the sub-lattice A_2, and to solve the following set of coupled equations:

$$\psi_1^\alpha = \hat{\Psi}^\alpha[a, b, c, d, \psi_2^u, \psi_2^d, \psi_2^l, \psi_2^r] \,,$$ (V.50)

$$\psi_2^\alpha = \hat{\Psi}^\alpha[a, b, c, d, \psi_1^u, \psi_1^d, \psi_1^l, \psi_1^r] \,,$$ (V.51)

with $\alpha = u, d, r, l$. The FM and PM phases are characterized by $\psi_1^\alpha = \psi_2^\alpha$, while the AF phases by $\psi_1^\alpha = 1 - \psi_2^\alpha$.

Considering the solution associated to A_1 only, the fixed points are

$$\boldsymbol{\psi}_{\text{PM}} = (\psi^u = \tfrac{1}{2}, \psi^l = \tfrac{1}{2}, \psi^r = \tfrac{1}{2}, \psi^d = \tfrac{1}{2}) \,,$$

$$\boldsymbol{\psi}_{a\text{-FM}} = (\psi^u = 1, \psi^l = 1, \psi^r = 1, \psi^d = 1) \,,$$

$$\boldsymbol{\psi}_{b\text{-FM}} = (\psi^u = 1, \psi^l = 0, \psi^r = 0, \psi^d = 1) \,,$$

(V.52)

$$\boldsymbol{\psi}_{c\text{-AF}} = (\psi^u = 1, \psi^l = 1, \psi^r = 0, \psi^d = 0) \,,$$

$$\boldsymbol{\psi}_{d\text{-AF}} = (\psi^u = 1, \psi^l = 0, \psi^r = 1, \psi^d = 0) \,,$$

as can be checked by inserting these values into eqs. (V.47) and (V.50). The overall arrow reversal symmetry allows for the solution $\boldsymbol{\psi}' = 1 - \boldsymbol{\psi}$, which for the AF phase is nothing but the exchange of ψ_1^α with ψ_2^α. Note that these solutions exist for any value of the vertex weights a, b, c and d. Their stability, however, that will be discussed in more detail in Sec. V.4.3.4, changes with the parameters. The numerical iteration of the same set of equations, confirms that these are indeed the only attractive solutions of the system for different regimes of parameters.

In order to calculate the free-energy, it is useful to consider the contributions to the partition function coming from a vertex, an horizontal edge and a vertical edge. These quantities are defined

---

6. Note that this is an extension of the definition given in eq. (V.36) needed in order to make the difference between FM orders dominated by a or b vertices, as well as AF orders dominated by c or d.

as follows:

$$
\begin{aligned}
Z_v[\psi^l, \psi^r, \psi^u, \psi^d] &= a\left[\psi^l\psi^u\psi^r\psi^d + (1-\psi^u)(1-\psi^l)(1-\psi^r)(1-\psi^d)\right] \\
&\quad + b\left[(1-\psi^l)\psi^u(1-\psi^r)\psi^d + \psi^l(1-\psi^u)\psi^r(1-\psi^d)\right] \\
&\quad + c\left[(1-\psi^u)(1-\psi^l)\psi^r\psi^d + \psi^u\psi^l(1-\psi^r)(1-\psi^d)\right] \\
&\quad + d\left[\psi^l(1-\psi^u)(1-\psi^r)\psi^d + (1-\psi^l)\psi^u\psi^r(1-\psi^d)\right]
\end{aligned}
\tag{V.53}
$$

and

$$
Z_{\langle lr\rangle}[\psi_i^l, \psi_j^r] = \psi_i^l\psi_j^r + (1-\psi_i^l)(1-\psi_j^r) \, ,
\tag{V.54}
$$

$$
Z_{\langle ud\rangle}[\psi_i^u, \psi_j^d] = \psi_i^u\psi_j^d + (1-\psi_i^u)(1-\psi_j^d) \, .
\tag{V.55}
$$

The first term Z_v represents the shift in the partition function brought in by the introduction of a new vertex which is connected with four rooted trees. The other terms $Z_{\langle lr\rangle}$ and $Z_{\langle ud\rangle}$ represent the shift in the partition function induced by the connection of two rooted trees (respectively one left and one right or one up and one down) through a link. In terms of these quantities one can compute the intensive free-energy (where here and in the following we normalize by the number of vertices) which characterizes the bulk properties of the tree in the thermodynamic limit:

$$
\begin{aligned}
\beta f[a, b, c, d, \boldsymbol{\psi}_1, \boldsymbol{\psi}_2] = -\frac{1}{2}\Big(& \ln Z_v[\boldsymbol{\psi}_1] + \ln Z_v[\boldsymbol{\psi}_2] + \\
& - \ln Z_{\langle lr\rangle}[\psi_1^l, \psi_2^r] - \ln Z_{\langle lr\rangle}[\psi_2^l, \psi_1^r] - \ln Z_{\langle ud\rangle}[\psi_1^u, \psi_2^d] - \ln Z_{\langle ud\rangle}[\psi_2^u, \psi_1^d] \Big) \, .
\end{aligned}
\tag{V.56}
$$

The free-energy (V.56) evaluated at the fixed points (V.52) reads as follows:

$$
\begin{aligned}
\beta f_{\mathrm{PM}} &= \beta f[a, b, c, d, \boldsymbol{\psi}_{\mathrm{PM}}] = -\ln\left(\frac{a+b+c+d}{2}\right) \, , \\
\beta f_{a\text{-FM}} &= \beta f[a, b, c, d, \boldsymbol{\psi}_{a\text{-FM}}] = -\ln a \, , \\
\beta f_{b\text{-FM}} &= \beta f[a, b, c, d, \boldsymbol{\psi}_{b\text{-FM}}] = -\ln b \, , \\
\beta f_{c\text{-AF}} &= \beta f[a, b, c, d, \boldsymbol{\psi}_{c\text{-AF}}] = -\ln c \, , \\
\beta f_{d\text{-AF}} &= \beta f[a, b, c, d, \boldsymbol{\psi}_{d\text{-AF}}] = -\ln d \, .
\end{aligned}
\tag{V.57}
$$

By comparing these free-energy densities and by equating the ones of the different phases one readily determines the critical hyper-planes in the four dimensional phase diagram. For instance, from the condition $f_{\mathrm{PM}} = f_{a-\mathrm{FM}}$ one finds $a_c = b + c + d$. Following this procedure one finds that the critical planes have exactly the same parameter dependencies as in the six-vertex model defined on the square lattice. The BP approximation yields, then, the exact topology of the phase diagram.

The order parameters (V.49) are easily evaluated at the fixed points (V.52). The PM solution ψ_{PM} yields vanishing magnetizations for all the order parameters. On the contrary, any ordered solution $\psi_{fp=*}$ gives a saturated value of the associated magnetization $m_{fp=*} = 1$ and zero for the other components $m_{fp\neq*} = 0$.

V.4.3.4   Stability analysis

The stability of the fixed points is determined by the eigenvalues of the Jacobian matrix,

$$M \equiv \frac{d\hat{\Psi}^\alpha}{d\psi^\beta}\Big|_{\psi^{\mathbf{fp}}} , \tag{V.58}$$

that describes the derivative of the vector function $\hat{\mathbf{\Psi}} = (\hat{\Psi}^u, \hat{\Psi}^r, \hat{\Psi}^l, \hat{\Psi}^d)$ defined in (V.47) with respect to the fields $\{\psi^\alpha\}$, evaluated at the fixed point, $\psi^{\mathbf{fp}}$, in question. The eigenvectors are parametrized as $(\delta\psi^u, \delta\psi^r, \delta\psi^l, \delta\psi^d)$. The solution examined becomes unstable as soon as one of the eigenvalues reaches one, $|E_{max}| = 1$.

Indeed, one easily proves that the criterium $|E_{max}| < 1$ is the correct one to identify the phase transitions associated to a diverging susceptibility χ. The susceptibility is given by

$$\chi = \frac{1}{N}\frac{\mathrm{d}\sum_{\langle ij\rangle}\langle s_{\langle ij\rangle}\rangle}{\mathrm{d}h} = \frac{1}{N}\sum_{\langle ij\rangle,\langle kl\rangle}\langle s_{\langle ij\rangle}s_{\langle kl\rangle}\rangle_c \propto \sum_{\alpha,\beta=\langle ud\rangle,\langle lr\rangle}\sum_{r=1}^\infty\sum_{\mathcal{P}(r)}\langle s_0^\alpha s_r^\beta\rangle_c \tag{V.59}$$

where in the last equality we used the homogeneity of the solution. The symbol $\mathcal{P}(r)$ indicates that the sum runs over all the paths that connect a given spin on an edge of type α, supposed to be the centre (site denoted by 0) of the tree, to all the remaining spins that live on edges of type β and are located at a distance r from 0 (in terms of the number of edges that make the path). As the tree has no loops, such paths are uniquely defined. The above formula can be simplified by using the fluctuation-dissipation relation

$$\langle s_0^\alpha s_r^\beta\rangle_c = \frac{\mathrm{d}\langle s_r^\beta\rangle}{\mathrm{d}h_0^\alpha} , \tag{V.60}$$

where h_0^α is a field conjugated to s_0^α. The above expression can be evaluated by using the chain rule

$$\frac{\mathrm{d}\langle s_r^\beta\rangle}{\mathrm{d}h_0^\alpha} = \frac{\mathrm{d}\hat{\Psi}^{\gamma_1}}{\mathrm{d}\psi_0^\alpha}\prod_{i=2}^{r-1}\frac{\mathrm{d}\hat{\Psi}^{\gamma_i}}{\mathrm{d}\psi^{\gamma_{i-1}}}\frac{\mathrm{d}\langle s_r^\beta\rangle}{\mathrm{d}\psi^{\gamma_{r-1}}} \tag{V.61}$$

where the particular values taken by $\{\gamma_i\} \in \{u, d, l, r\}$ depend on the path followed. Each derivative is finally evaluated in the PM solution. Then, defining the vectors $|v_\alpha\rangle$ such that $v_\alpha^\beta = \frac{\mathrm{d}\hat{\Psi}^\beta}{\mathrm{d}\psi^\alpha}$ and $|w_\alpha\rangle$ such that $w_\alpha^\beta = \frac{\mathrm{d}\hat{\Psi}^\alpha}{\mathrm{d}\psi^\beta}$ one obtains

$$\begin{aligned}
\chi &= \sum_{\alpha,\beta=\langle ud\rangle,\langle lr\rangle}\sum_{r=1}^\infty\sum_{\mathcal{P}(r)}\langle s_0^\alpha s_r^\beta\rangle_c \\
&= \sum_{\alpha,\beta=\langle ud\rangle,\langle lr\rangle}\sum_{r=1}^\infty\sum_{\mathcal{P}(r)}\frac{\mathrm{d}\hat{\Psi}^{\gamma_1}}{\mathrm{d}\psi_0^\alpha}\prod_{i=2}^{r-1}\frac{\mathrm{d}\hat{\Psi}^{\gamma_i}}{\mathrm{d}\psi^{\gamma_{i-1}}}\frac{\mathrm{d}\langle s_r^\beta\rangle}{\mathrm{d}\psi^{\gamma_{r-1}}} \\
&\propto \sum_{\alpha,\beta=\langle ud\rangle,\langle lr\rangle}\sum_{r=1}^\infty\langle v_\alpha|M^{r-2}|w_\beta\rangle \simeq \sum_{r=1}^\infty\mathrm{Tr}M^r.
\end{aligned} \tag{V.62}$$

As long as the absolute values of the eigenvalues remain smaller than one, *i.e.* $|E_{max}| < 1$, the series converges yielding a finite susceptibility.

Let us focus on the stability of the PM phase ψ_{PM}, *i.e.* $\psi^l = \psi^r = \psi^d = \psi^u = \frac{1}{2}$. The matrix M evaluated in the PM solution is

$$M_{\psi_{\text{PM}}} = \begin{bmatrix} \dfrac{a+b-c-d}{a+b+c+d} & \dfrac{a-b+c-d}{a+b+c+d} & \dfrac{-a+b+c-d}{a+b+c+d} & 0 \\[3mm] \dfrac{a-b+c-d}{a+b+c+d} & \dfrac{a+b-c-d}{a+b+c+d} & 0 & \dfrac{-a+b+c-d}{a+b+c+d} \\[3mm] \dfrac{-a+b+c-d}{a+b+c+d} & 0 & \dfrac{a+b-c-d}{a+b+c+d} & \dfrac{a-b+c-d}{a+b+c+d} \\[3mm] 0 & \dfrac{-a+b+c-d}{a+b+c+d} & \dfrac{a-b+c-d}{a+b+c+d} & \dfrac{a+b-c-d}{a+b+c+d} \end{bmatrix}. \quad \text{(V.63)}$$

Its eigenvalues are

$$E_1^{\text{PM}} = \frac{3a-b-c-d}{a+b+c+d}\,, \qquad E_2^{\text{PM}} = \frac{-a+3b-c-d}{a+b+c+d}\,,$$
$$E_3^{\text{PM}} = \frac{a+b-3c+d}{a+b+c+d}\,, \qquad E_4^{\text{PM}} = \frac{a+b+c-3d}{a+b+c+d}\,. \quad \text{(V.64)}$$

In the basis $(\delta\psi^u, \delta\psi^r, \delta\psi^l, \delta\psi^d)$ the corresponding eigenvectors can be written: $v_1 = (1,1,1,1)$, $v_2 = (1,-1,-1,1)$, $v_3 = (-1,1,-1,1)$ and $v_4 = (-1,-1,1,1)$. In general, the eigenvalue E_1^{PM} regulates the instability towards the a-FM, E_2^{PM} towards the b-FM, E_3^{PM} towards the c-AF, and E_4^{PM} towards the d-AF.

One reckons that the stability of PM solution can be stated in terms of the condition

$$\left| \frac{(1 + E_3^{\text{PM}})(1 + E_4^{\text{PM}}) - (1 - E_1^{\text{PM}})(1 - E_2^{\text{PM}})}{(1 + E_3^{\text{PM}})(1 + E_4^{\text{PM}}) + (1 - E_1^{\text{PM}})(1 - E_2^{\text{PM}})} \right| < 1, \quad \text{(V.65)}$$

which in terms of a, b, c, d reads

$$\left| \frac{a^2 + b^2 - c^2 - d^2}{2(ab + cd)} \right| = |\Delta_8| < 1\,. \quad \text{(V.66)}$$

Therefore, the stability analysis of the PM phase also yields the same location of the phase boundaries as in the exact solution on the $2D$ square lattice [see eq. (IV.33) and Fig. IV.15].

A similar analysis can be carried out to evaluate the stability of the FM and AF phases. One has to evaluate the matrix (V.58) in the ordered solutions. Considering the fixed point $\psi_{a\text{-FM}}$ as an example, one obtains the four eigenvalues:

$$E_1^{a\text{-FM}} = \frac{b+c+d}{a}\,, \qquad E_2^{a\text{-FM}} = \frac{b-c-d}{a}\,,$$
$$E_3^{a\text{-FM}} = \frac{b-c+d}{a}\,, \qquad E_4^{a\text{-FM}} = \frac{b+c-d}{a}\,, \quad \text{(V.67)}$$

and the corresponding eigenvectors are the same (in the same order) that we have already discussed for the PM solution. From eq. (V.67), one sees that $E_1^{a\text{-FM}} = 1$ as soon as $a = b + c + d$, *i.e.* when $\Delta_8 = 1$, while for larger values of a the a-FM fixed point is stable. Moreover, the solution may develop multiple instabilities when some vertices are missing. Analogous results hold for the other ordered phases.

Finally, let us remark that the model also has discontinuous transition points separating ordered phases, for instance the a-FM and the c-AF at $a = c$ and $b = d = 0$, the b-FM and the c-AF at $b = c$ and $a = d = 0$, the c-AF and the d-AF at $c = d$ and $a = b = 0$, etc.

V.4.3.5   The six-vertex model: phase diagram

For the six-vertex model we found four different fixed points. These characterise the possible equilibrium phases: (i) a-FM phase, (ii) b-FM phase, (iii) c-AF phase, (iv) a, b, c-PM phase (we want to distinguish the PM phase found with this method that differs from the actual SL phase in $D = 2$ in ways that we will describe below). The transition lines were found in two equivalent ways. On the one hand, we compared the free energies of the PM and ordered phases as given in eqs. (V.56). On the other hand, we analyzed when one of the eigenvalues of the stability matrix reaches one signaling the instability of the considered phase. We found that, as in the $2D$ model, the phase transitions are controlled by the anisotropy parameter Δ_6 defined in eq. (IV.23), with the transition lines determined by $|\Delta_6| = 1$.

Some remarks are in order here:

(i) For $d = 0$, the eigenvalue $E_4 = 1, \forall\, a, b, c$. The PM phase in the six-vertex model is therefore in the limit of stability. This is reminiscent of the critical properties of the spin-liquid phase in $D = 2$.

(ii) Similarly, for $a = 0$ the eigenvalue $E_1 = -1 \,\forall\, b, c, d$.

(iii) The same holds for the other vertices: for $b = 0$ then $E_2 = -1, \forall\, a, c, d$; for $c = 0$ then $E_3 = 1, \forall\, a, b, d$.

These remarks are in agreement with the exact solution of the eight vertex model: as soon as one among the four vertex weights is zero, the system is critical.

The transition between the paramagnetic and the ordered solutions (both FM and AF) is discontinuous. This can be seen at the level of the fixed point ψ^α or by the inspection of the singularity in the free energy. Still, it is characterized by the absence of metastability and hysteresis and a diverging susceptibility. The transitions between the PM and the ordered solutions are all discontinuous: the (possibly staggered) magnetization jumps from zero to one. This can also be seen from the inspection of the singularity in the free-energy. Still, the transitions are characterised by the absence of metastability and hysteresis, and they have a diverging susceptibility. In fact, approaching the transition line from the two sides, both the paramagnetic and the ferromagnetic solutions become unstable. This kind of transition corresponds to the 'frozen-to-critical' KDP transition discussed in section III.2.3 and IV.3.3. Note that if one focuses on the transition point, plugs into the equations the critical value $a = a_c = b + c$, and assumes the homogeneity of the solution $\psi^\alpha = \psi \,\forall \alpha$, the remaining equation has the trivial form $\psi = \psi$. This means that all the values of ψ are valid. One can actually see that, the free energy for the same critical value of $a = a_c$, does not depend on ψ and thus it is uniformly minimised by all values of the magnetisation. The PM-AF transition shares the same properties of the KDP transitions towards the FM phases.

At the spin ice point $a = b = c$ the entropy is $S^{sv}/N = -\beta f_{sv} = \ln 3/2 \simeq 0.405$, *i.e.* the Pauling result (see Fig. V.21).

V.4.3.6   The eight-vertex model: phase diagram

The addition of d vertices does not change the properties of the a-FM, b-FM and c-AF transitions. As a function of d there is a second AF transition, denoted d-AF, towards a phase with staggered order of 4in and 4out vertices. This transition is also discontinuous and towards a completely frozen phase. Moreover, as for the six-vertex model both the FM and the PM solutions become unstable on the transition planes. When all the statistical weights are different from zero

the four eigenvalues of the stability matrix within the PM phase are smaller than one. The transition lines are altogether characterized by the condition $|\Delta_8| = 1$, as for the $2D$ model.

V.4.3.7 Summary

In short, the location of the transition lines of the $2D$ six- and eight-vertex models are reproduced exactly by the tree of single vertices. However, the critical properties on the tree are different from the ones of the $2D$ model. The absence of loops 'freezes' the ordered phases and makes all transitions discontinuous, with $m_{\mathrm{PM}} = 0$ and $m = 1$ on the ordered side. While this holds for the PM-FM transition in $2D$ it does not for the PM-AF on the same finite dimensional lattice.

V.4.4 The six- and eight-vertex model on a tree of plaquettes

In this Subsection we study the six- and eight-vertex models on a tree of plaquettes. The calculations proceed along the same lines as the ones for the single vertex tree. They become, though, rather involved as the number of configurations allowed on a plaquette is quite large.

V.4.4.1 Recursion equations

Each rooted tree of plaquettes has two missing edges, which means that one has to write appropriate self-consistent equations for the joint probability of the two arrows lying on those edges. The analogue of ψ^α, which in the previous section described the marginal probability of the arrow to point up or right, depending on whether it is a vertical or an horizontal edge, now becomes a probability vector with four components. The marginal probability to find a pair of arrows with values $++, -+, +-, --$ will be denoted by $\boldsymbol{\psi}^\alpha = \{\psi^\alpha_{++}, \psi^\alpha_{-+}, \psi^\alpha_{+-}, \psi^\alpha_{--}, \}$. The superscript $\alpha = u, d, l, r$ denotes, just as before, whether the pair of arrows are on the missing edges of an up, down, left, right rooted tree. This is illustrated in Fig. V.17. In this definition the spins take positive values if the arrows point from down to up or from left to right, as before. Moreover, we assume that the first symbol indicates the state of the arrow that is on the left, for the vertical edges, and on the top, for the horizontal ones. Consequently, the second symbol refers to the value taken by the spin sitting on the right or the bottom edge, for vertical and horizontal edges, respectively.

In order to allow all possible ordered phases we preserve the distinction between the different direction u, r, l and d, which amounts to study a set of 4×4 self consistent equations. Let us write the vertex weights as follows

$$w_{s_1,s_2,s_3,s_4}(a,b,c,d) = \frac{1}{4}\Big[a'(1+s_1s_2s_3s_4)+b'(s_1s_3+s_2s_4)+c'(s_1s_4+s_2s_3)+d'(s_1s_2+s_3s_4)\Big]$$
(V.68)

where $s_1, \ldots, s_4$ are taken as in Fig. V.18, and

$$
\begin{aligned}
a' &= \frac{1}{2}(a+b+c+d)\,, & b' &= \frac{1}{2}(a+b-c-d)\,, \\
c' &= \frac{1}{2}(a-b+c-d)\,, & d' &= \frac{1}{2}(a-b-c+d)\,.
\end{aligned}
$$
(V.69)
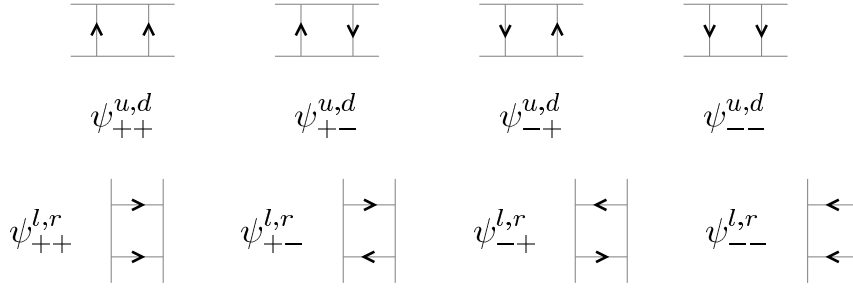
Figure V.17: Definitions of $\{\psi^\alpha_{++}, \psi^\alpha_{-+}, \psi^\alpha_{+-}, \psi^\alpha_{--}\}_{\alpha=u,l,r,d}$ used in the recurrent equations for the plaquette model. Left: $\psi^{u,d}$ where the first index $\pm$ denotes the value of the spin on the left and second index denotes the spin on the right. Right: $\psi^{l,d}$ where the first index $\pm$ denotes the value of the spin on the top and second index denotes the spin on the bottom.
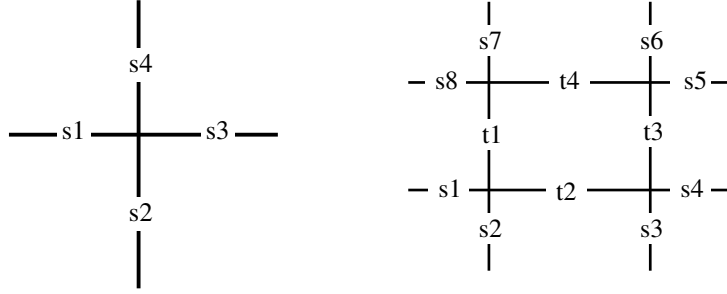
Figure V.18: Left panel: representation of the variables $\{s_i\}$ used in the definition of the vertex weight eq. (V.68). Right panel: numbering assigned to the spin/arrow variables in eqs. (V.73) and (V.75). We denote by $\boldsymbol{S_P} = \{s_1, s_2, s_3, s_4, s_5, s_6, s_7, s_8, t_1, t_2, t_4\}$ the set of spin variables on a plaquette.

Similarly, we introduce a new parameterization of the probability vector,

$$
\begin{aligned}
\psi^\alpha_{s_1 s_2} &= \frac{1}{2}\Big[(1+s_1 s_2)\frac{\psi^\alpha_{++} + \psi^\alpha_{--}}{2} + (s_1 + s_2)\frac{\psi^\alpha_{++} - \psi^\alpha_{--}}{2} + \\
&\quad + (1 - s_1 s_2)\frac{\psi^\alpha_{+-} + \psi^\alpha_{-+}}{2} + (s_1 - s_2)\frac{\psi^\alpha_{+-} - \psi^\alpha_{-+}}{2}\Big] \quad\quad\quad \text{(V.70)}\\
&= \frac{1}{4}\Big[1 + s_1 s_2\, s^\alpha + (s_1 + s_2)\, p^\alpha + (s_1 - s_2)\, q^\alpha\Big],
\end{aligned}
$$

where we introduced the set of variables

$$
\phi^\alpha = (p^\alpha, s^\alpha, q^\alpha) \equiv (\psi^\alpha_{++} - \psi^\alpha_{--}, \psi^\alpha_{++} + \psi^\alpha_{--} - \psi^\alpha_{-+} - \psi^\alpha_{+-}, \psi^\alpha_{+-} - \psi^\alpha_{-+}), \quad\quad \text{(V.71)}
$$

which exploits the fact that, due to the normalisation conditions, for each direction only three variables have to be determined. For the sake of completeness we also report the inverse mapping:

$$
\begin{aligned}
\psi^\alpha_{++} &= \frac{1}{4}(1 + s^\alpha + 2p^\alpha), & \psi^\alpha_{+-} &= \frac{1}{4}(1 - s^\alpha + 2q^\alpha), \\
\psi^\alpha_{-+} &= \frac{1}{4}(1 - s^\alpha - 2q^\alpha), & \psi^\alpha_{--} &= \frac{1}{4}(1 + s^\alpha - 2p^\alpha).
\end{aligned}
\quad\quad \text{(V.72)}
$$

The self-consistent equations for the probability vector describing up, left, right and down rooted trees now read

$$\psi^u_{s_2 s_3} = \hat{\Psi}^u_{s_2 s_3}[a, b, c, d, \boldsymbol{\psi}^u, \boldsymbol{\psi}^l, \boldsymbol{\psi}^r, \boldsymbol{\psi}^d]$$

$$\propto \sum_{\boldsymbol{S_P} \backslash \{s_2, s_3\}} w_{s_1, s_2, t_2, t_1} w_{t_1, s_3, s_4, t_3} w_{t_4, t_3, s_5, s_6} w_{s_8, t_1, t_4, s_7} \psi^l_{s_8 s_1} \psi^u_{s_7 s_6} \psi^r_{s_5 s_4} \, ,$$

$$\psi^l_{s_5 s_4} = \hat{\Psi}^l_{s_5 s_4}[a, b, c, d, \boldsymbol{\psi}^u, \boldsymbol{\psi}^l, \boldsymbol{\psi}^r, \boldsymbol{\psi}^d]$$

$$\propto \sum_{\boldsymbol{S_P} \backslash \{s_5, s_4\}} w_{s_1, s_2, t_2, t_1} w_{t_1, s_3, s_4, t_3} w_{t_4, t_3, s_5, s_6} w_{s_8, t_1, t_4, s_7} \psi^d_{s_2 s_3} \psi^l_{s_8 s_1} \psi^u_{s_7 s_6} \, ,$$

(V.73)

$$\psi^d_{s_7 s_6} = \hat{\Psi}^d_{s_7 s_6}[a, b, c, d, \boldsymbol{\psi}^u, \boldsymbol{\psi}^l, \boldsymbol{\psi}^r, \boldsymbol{\psi}^d]$$

$$\propto \sum_{\boldsymbol{S_P} \backslash \{s_6, s_7\}} w_{s_1, s_2, t_2, t_1} w_{t_1, s_3, s_4, t_3} w_{t_4, t_3, s_5, s_6} w_{s_8, t_1, t_4, s_7} \psi^l_{s_8 s_1} \psi^d_{s_2 s_3} \psi^r_{s_5 s_4} \, ,$$

$$\psi^r_{s_8 s_1} = \hat{\Psi}^r_{s_8 s_1}[a, b, c, d, \boldsymbol{\psi}^u, \boldsymbol{\psi}^l, \boldsymbol{\psi}^r, \boldsymbol{\psi}^d]$$

$$\propto \sum_{\boldsymbol{S_P} \backslash \{s_8, s_1\}} w_{s_1, s_2, t_2, t_1} w_{t_1, s_3, s_4, t_3} w_{t_4, t_3, s_5, s_6} w_{s_8, t_1, t_4, s_7} \psi^u_{s_7 s_6} \psi^r_{s_5 s_4} \psi^d_{s_2 s_3} \, ,$$

and the normalization constant is given by $z^\alpha = \sum_{s_i, s_j} \psi^\alpha_{s_i s_j}$.

We found more convenient to focus on the variables $\boldsymbol{\phi}^\alpha = (\phi^\alpha_1, \phi^\alpha_2, \phi^\alpha_3) = (p^\alpha, s^\alpha, q^\alpha)$ for which one can readily derive a set of self-consistent equations from eqs. (V.73),

$$p^\alpha = \hat{\Phi}^\alpha_1[a, b, c, d, \boldsymbol{\phi}^u, \boldsymbol{\phi}^l, \boldsymbol{\phi}^r, \boldsymbol{\phi}^d] \equiv \hat{\Psi}^\alpha_{++} - \hat{\Psi}^\alpha_{--} \, ,$$
$$s^\alpha = \hat{\Phi}^\alpha_2[a, b, c, d, \boldsymbol{\phi}^u, \boldsymbol{\phi}^l, \boldsymbol{\phi}^r, \boldsymbol{\phi}^d] \equiv \hat{\Psi}^\alpha_{++} + \hat{\Psi}^\alpha_{--} - \hat{\Psi}^\alpha_{-+} - \hat{\Psi}^\alpha_{+-} \, , \qquad \text{(V.74)}$$
$$q^\alpha = \hat{\Phi}^\alpha_3[a, b, c, d, \boldsymbol{\phi}^u, \boldsymbol{\phi}^l, \boldsymbol{\phi}^r, \boldsymbol{\phi}^d] \equiv \hat{\Psi}^\alpha_{-+} - \hat{\Psi}^\alpha_{+-} \, ,$$

with $\alpha = u, l, r, d$. The argument of the functions in the rightest hand side is given in terms of the transformations (V.72). In the PM phase there is no symmetry breaking and $p^\alpha = q^\alpha = 0$. The ordered phases and the corresponding phase transitions are characterized by the spontaneous symmetry breaking associated to FM, $p^\alpha \neq 0$, or AF, $q^\alpha \neq 0$, order.

V.4.4.2 The free energy

The free-energy per vertex can be generically written as:

$$\beta f[a, b, c, d, \boldsymbol{\psi}^u, \boldsymbol{\psi}^l, \boldsymbol{\psi}^r, \boldsymbol{\psi}^d] = \frac{1}{4} \left\{ \ln \left[\sum_{s_1, s_2} \psi^d_{s_1 s_2} \psi^u_{s_1 s_2} \right] + \ln \left[\sum_{s_1, s_2} \psi^l_{s_1 s_2} \psi^r_{s_1 s_2} \right] \right.$$

$$\left. - \ln \left[\sum_{\boldsymbol{S_P}} w_{s_1, s_2, t_2, t_1} w_{t_1, s_3, s_4, t_3} w_{t_4, t_3, s_5, s_6} w_{s_8, t_1, t_4, s_7} \psi^l_{s_8 s_1} \psi^u_{s_7 s_6} \psi^r_{s_5 s_4} \psi^d_{s_2 s_3} \right] \right\}$$

(V.75)

where one can rewrite ψ in terms in ϕ.

V.4.4.3 Stability analysis

Similarly to what was done for the model on the tree of vertices, we investigate the stability of the solutions by studying the stability matrix

$$M_{i,j}^{\alpha,\beta} = \frac{\mathrm{d}\hat{\Phi}_i^\alpha}{\mathrm{d}\phi_j^\beta}\bigg|_{\hat{\phi}^{\mathbf{fp}}}\,, \qquad \alpha,\beta = u,l,d,r\,, \qquad i,j = 1,2,3\,. \tag{V.76}$$

This is a 12x12 matrix. The location of the parameter values where the PM solution becomes unstable is the same as the ones for which the free-energies of the different phases coincide. We parametrize the 12 component eigenvectors as

$$\delta\varphi_P = (\delta p^u, \delta s^u, \delta q^u; \delta p^d, \delta s^d, \delta q^d; \delta p^l, \delta s^l, \delta q^l; \delta p^r, \delta s^r, \delta q^r)\,. \tag{V.77}$$

V.4.4.4 Fixed points

Let us discuss each fixed-point solution – phase – separately.

The paramagnetic phase. The PM fixed point is of the form $\phi_{\mathrm{PM}} \equiv \phi_{\mathrm{PM}}^u = \phi_{\mathrm{PM}}^l = \phi_{\mathrm{PM}}^r = \phi_{\mathrm{PM}}^d = (p_{\mathrm{PM}} = 0, s_{\mathrm{PM}}, q_{\mathrm{PM}} = 0)$ with s_{PM} determined by eq. (V.74). We introduce the quantities

$$x = \frac{a-b}{a+b+c+d}\,, \qquad y = \frac{c-d}{a+b+c+d}\,, \qquad z = \frac{a+b-c-d}{a+b+c+d}\,, \tag{V.78}$$

and these equations can be easily inverted as

$$\frac{a}{a+b+c+d} = \frac{1}{4}(1+z+2x)\,, \qquad \frac{b}{a+b+c+d} = \frac{1}{4}(1+z-2x)\,,$$
$$\frac{c}{a+b+c+d} = \frac{1}{4}(1-z+2y)\,, \qquad \frac{d}{a+b+c+d} = \frac{1}{4}(1-z-2y)\,, \tag{V.79}$$

thus expressing the vertex weights as linear functions of x, y and z up to an irrelevant factor $(a+b+c+d)^{-1}$.

The self-consistent equation for s_{PM} now takes the form

$$(a+b+c+d)^4(x^2-y^2)(1+z^2)\Big[1+2\frac{\Upsilon+1}{\Upsilon-1}s_{\mathrm{PM}} - 2\frac{\Upsilon+1}{\Upsilon-1}s_{\mathrm{PM}}^3 - s_{\mathrm{PM}}^4\Big] = 0\,, \tag{V.80}$$

with

$$\Upsilon(a,b,c,d) = \frac{4x^2+z^2-1}{4y^2+z^2-1} = \frac{(a+b)(c+d)-(a-b)^2}{(a+b)(c+d)-(c-d)^2}\,. \tag{V.81}$$

Apart from the trivial solutions $s_{\mathrm{PM}} = 1, -1$, the PM solution is given by

$$s_{\mathrm{PM}} = \frac{1-\sqrt{\Upsilon}}{1+\sqrt{\Upsilon}}\,. \tag{V.82}$$

Equation (V.82) suggests that the PM solution depends upon a single parameter Υ such that it remains unchanged if the vertex weights a, b, c, d are modified in such a way to preserve the value of Υ. Note that the limit of infinite temperature for the eight-vertex model, *i.e.* $a = b = c = d$, corresponds to $s_{\mathrm{PM}} = 0$ which implies $\psi_{++}^\alpha = \psi_{--}^\alpha = \psi_{+-}^\alpha = \psi_{-+}^\alpha = 1/4$, $\forall\alpha \in \{u,l,r,d\}$. We anticipate that this result is also obtained for the sixteen-vertex model. On the contrary, the limit of infinite temperature for the six-vertex model $a = b = c$ and $d = 0$ (or, more generally, when one out of the four vertices is absent) corresponds to a non-trivial solution $s_{\mathrm{PM}} \neq 0$ which implies $\psi_{++}^\alpha = \psi_{--}^\alpha \neq \psi_{+-}^\alpha = \psi_{-+}^\alpha$.

By inserting the PM solution in the free-energy density (V.75) one obtains

$$
\beta\, f_{\mathrm{PM}}(a,b,c,d) \;=\; -\ln\left(\frac{a+b+c+d}{2}\right)
$$

$$
-\frac{1}{4}\ln\left[1+\frac{(x^2-y^2)^2(-3+2x^2+2y^2-z^2)}{(-1+2x^2+2y^2+z^2)}\right], \qquad (\text{V.83})
$$

where x, y and z are given in terms of the vertex weights in eq. (V.78). This function is clearly invariant under the exchange of a with b, and c with d, together with the simultaneous exchange of the weights of the FM vertices with the AF ones.

Ferromagnetic phases. In order to study the ordered phases we introduce the following functions of four variables:

$$
\nu(\{w_m\}) = \frac{w_1^2 - w_2^2 - (w_3+w_4)^2}{w_1^2 - w_2^2 - (w_3-w_4)^2}\,, \qquad (\text{V.84})
$$

$$
\Sigma(\{w_m\}) = \frac{1}{4}\ln\left[\frac{w_1^2 - w_2^2 - w_3^2 - w_4^2}{2w_3^2 w_4^2(w_1^2+w_2^2) + (w_1^4 + w_3^2 w_4^2)(w_1^2 - w_2^2 - w_3^2 - w_4^2)}\right], (\text{V.85})
$$

with $\{w_m\} = w_1,\, w_2,\, w_3,\, w_4$ and

$$
\mu(\{w_m\}) = \frac{(w_1^2 - w_2^2 - (w_3-w_4)^2)(w_1^2 - w_2^2 - (w_3+w_4)^2)}{(w_1^2 - w_2^2 - w_3^2 - w_4^2)\sqrt{(w_1^2 - w_2^2 - w_3^2 - w_4^2)^2 - 4w_3^2 w_4^2}}
$$

$$
\times \frac{(2w_3^2 w_4^2 + w_1^2(w_1^2 - w_2^2 - w_3^2 - w_4^2))w_1^2}{(w_1^2(w_1^2(w_1^2 - w_2^2 - w_3^2 - w_4^2) + 2w_3^2 w_4^2) - w_3^2 w_4^2(-w_1^2 - w_2^2 + w_3^2 + w_4^2))}\,. \qquad (\text{V.86})
$$

Note that ν, Σ and μ are symmetric under the exchange of w_3 and w_4. In the following we will describe only one solution among the two possible ones allowed by symmetry.

The a-FM is homogeneous along all the directions and it is given by

$$
\phi_{a\text{-FM}}^{\alpha} = \phi_{a\text{-FM}} = \left(p_{a\text{-FM}} = \sqrt{\nu(a,b;c,d)},\, s_{a\text{-FM}} = 1,\, q_{a\text{-FM}} = 0\right), \qquad (\text{V.87})
$$

$\forall\,\alpha = u,l,r,d$. It implies $\psi_{+-} = \psi_{-+} = 0$ and spontaneous symmetry breaking since $\psi_{++} \neq \psi_{--}$. The associated free-energy and magnetization read

$$
\beta\, f_{a\text{-FM}}(a,b,c,d) = \Sigma(a,b;c,d)\,,
$$

$$
m_{a\text{-FM}}(a,b,c,d) = \mu(a,b;c,d)\,. \qquad (\text{V.88})
$$

The extension of these results to the other phases is rather straightforward. The b-FM is characterized by the same functions, with the exchange of b and a. One finds $\phi_{b\text{-FM}}^{l,r} = \left(p_{b\text{-FM}} = -\sqrt{\nu(b,a;c,d)},\, s_{b\text{-FM}} = 1,\, q_{b\text{-FM}} = 0\right)$ for the horizontal edges while the positive sign remains on the vertical ones.

Antiferromagnetic phases. AF order can also be characterized by the functions ν, Σ and μ defined in eqs. (V.84), (V.85) and (V.86). In particular, for the c-AF phase,

$$
\phi_{c\text{-AF}}^{\alpha} = \phi_{c\text{-AF}} = \left(p_{c\text{-AF}} = 0,\, s_{c\text{-AF}} = -1,\, q_{c\text{-AF}} = \sqrt{\nu(c,d;a,b)}\right). \qquad (\text{V.89})
$$

This implies $\psi_{++} = \psi_{--} = 0$ and a staggered order with $\psi_{+-} \neq \psi_{-+}$. The free-energy and staggered magnetization read

$$
\beta\, f_{c\text{-AF}}(a,b,c,d) = \Sigma(c,d;a,b)\,,
$$

$$
m_{c\text{-AF}}(a,b,c,d) = \mu(c,d;a,b)\,. \qquad (\text{V.90})
$$

The solution dominated by d vertices is of the same form as the one above, with the exchange of c and d, and $q_{d\text{-AF}}^{l,r} = -q_{c\text{-AF}}^{l,r}$ meaning that the c-AF and d-AF solutions only differ by a sign along the horizontal edges. This is expected since a d vertex can be obtained from a c one by reversing its horizontal arrows.

V.4.4.5   The six-vertex model: phase diagram

The solution (V.82) evaluated at $d = 0$ describes the PM phase of the six-vertex model. The fixed point is characterized by a value of s_{PM} in the interval $-1 \leq s_{\text{PM}} \leq 0$. As for the model on the tree of vertices, as soon as one of the vertex weights is set to zero, the stability matrix (V.76) has an eigenvalue with absolute value equal to one. This calculation allows us to show explicitly how the introduction of a hard constraint radically affects the collective behavior of the system: it turns the conventional PM phase into a disordered one with a soft mode. The normalized eigenvector associated to this mode is of the form

$$\delta\varphi_{\text{PM}} = (1/2, 0, 0; -1/2, 0, 0; -1/2, 0, 0; 1/2, 0, 0) . \tag{V.91}$$

The PM-FM transitions are of the same type as the ones found in the single vertex problem. From eqs. (V.87) and (V.88) evaluated at the limiting case $d = 0$ one finds a discontinuous transition towards a frozen phase with $p_{a\text{-FM}} = 1$, *i.e.* $\psi_{++} = 1$, at $a_c = b + c$ (or $b_c = a + c$) where $s_{\text{PM}} = 0 \ \forall b, \ c$, as can be read from eq. (V.82). The free-energy density in the frozen phase, $f_{a\text{-FM}} = -\ln a$, and the magnetization, $m_{a\text{-FM}} = 1$, are identical to the exact results on the square lattice. At the transition, $\beta f_{\text{PM}}(a_c, b, c) = \beta f_{a\text{-FM}}(a_c, b, c) = -\ln a_c$.

On the transition lines both the PM and FM solutions become unstable. One can check that fixing $a = b + c$ (or equivalently $b = a + c$) and looking for a solution of the type $\phi_{a-\text{FM}}^c = (p_{a-\text{FM}}^c, s_{a-\text{FM}}^c, q_{a-\text{FM}}^c = 0)$ the two equations for $p_{a-\text{FM}}^c$ and $s_{a-\text{FM}}^c$ become dependent and simultaneously satisfied by the condition $(p_{a-\text{FM}}^c)^2 - s_{a-\text{FM}}^c = 0$, that describes an entire line of fixed points joining the FM solution ($p_{a-\text{FM}} = 1, s_{a-\text{FM}} = 1$) to the PM one ($p_{\text{PM}} = 0, s_{\text{PM}} = 0$).

The PM-AF transition for the Bethe lattice of plaquettes is still placed at $c_c = a + b$ but it is qualitative different from the one on the single vertex tree. The small loops of four spins allow for fluctuations in the AF phase and the transition becomes a continuous one with a singularity of the second derivative of the free-energy. On this line the PM solution reaches the critical value $s_{\text{PM}} = -1$. Beyond this line the PM solution becomes imaginary. The magnetization, $m_{c\text{-AF}}$, is given by

$$m_{c\text{-AF}}(c; a, b) = \frac{\sqrt{2}(a+b)^3[(a+b)^2 + ab]}{\sqrt{ab}[(a+b)^4 + ab((a+b)^2 + ab)]} \sqrt{\frac{c - c_c}{c_c}} + \mathcal{O}\left[\left(\frac{c - c_c}{c_c}\right)^{3/2}\right] \tag{V.92}$$

close to the transition line, which gives the mean-field exponent $\beta = 1/2$ (see Fig. V.20).

In Fig. V.21 we report the comparison between the free-energy for the single vertex (f_{sv}), the plaquette (f_{pl}) and the $2D$ (f_{2D}) [25] models. In the left panel we show the free-energy in the PM and FM phases, as a function of a/c moving along the line $a\, b = c^2$. The right panel of Fig. V.21 shows the free-energy in the PM and AF phases as a function of a/c, moving along the line $a = b$. The figure clearly shows that the discontinuity of f_{sv} at the transition is smoothed out by the inclusion of small loop fluctuations.

On the spin-ice point $a = b = c$ the entropy per vertex of the six-vertex model on a tree of plaquettes is

$$S_{pl}/N = -\beta f_{pl} = -\frac{1}{4} \ln \frac{3}{16} \simeq 0.418 . \tag{V.93}$$

This result goes in the direction of the one obtained by Lieb for the $2D$ model $S_{2D} = (3/2) \ln(4/3) \simeq 0.4315$ (see Fig. V.21).

As it can be seen from Fig. V.21 the free-energy of the frozen FM phases is the same for the square lattice model, the tree of single vertices and the tree of plaquettes. Instead, in the PM and AF phases $f_{2D} < f_{pl} < f_{sv}$.
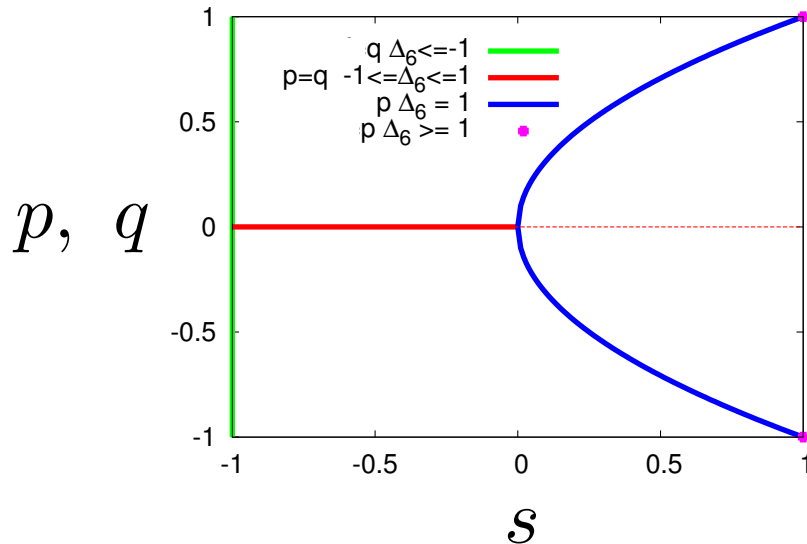

Figure V.19: Schematic picture of the solutions of the six-vertex model with the plaquette. As far as $-1 \leq \Delta_6 \leq 1$ the solution is $(p = 0, -1 \leq s \leq 0, q = 0)$; at the critical value $a = b + c$, *i.e.* $\Delta_6 = 1$, a line of fixed points $(p = \sqrt{s}, 0 \leq s \leq 1, q = 0)$ is found and for larger values of a, $\Delta_6 \geq 1$, the solution is frozen in the value $(p = 1, s = 1, q = 0)$. The AF transition occurs at $\Delta_6 = -1$, where $s = -1$ and for $c > a + b$ the value of s remains frozen at $s = -1$ while $q > 0$. In the figure, in the symmetry broken phases, we report both solutions related by arrow reversal.

The properties discussed insofar are a general consequence of the form of the functions in eqs. (V.84), (V.85) and (V.86), independently of the precise specification of their arguments. Similar conclusions are drawn when any of the four types of vertices is missing. Note that for $w_1 > w_2, w_3$ and $w_4 = 0$ one recovers:

$$\nu(w_1, w_2; w_3, 0) = \nu(w_1, w_2; 0, w_4) = 1 \, ,$$
$$\Sigma(w_1, w_2; w_3, 0) = \Sigma(w_1, w_2; 0, w_4) = -\ln w_1 \, ,$$
$$\mu(w_1, w_2; w_3, 0) = 1 \, ,$$

while for $w_2 = 0$ and $w_1 > w_3, w_4 \neq 0$ they all take a non trivial value. This means that when one of the weights of the AF vertices (c or d) vanishes the FM phases are frozen (since $\mu = 1$ and $\Sigma \equiv$ cte). The same holds for the AF order in absence of one of the FM vertices [see eq. (V.88)].

V.4.4.6   The eight-vertex model: phase diagram

Quite a different behavior emerges in the more general eight-vertex model when one considers the plaquette model instead of the tree of single vertices. While with the single vertex tree the addition of vertices of type d does not change the discontinuous frozen-to-critical nature of the transitions, with the plaquette one sees that they actually do.

When $a, b, c, d \neq 0$ the free-energy at the transition planes shows a singularity in its first derivatives suggesting a *first-order phase transition*. Indeed, one can check that

$$f_P(w_2 + w_3 + w_4, w_2; w_3, w_4) = \Sigma(w_2 + w_3 + w_4, w_2; w_3, w_4) \, , \qquad \text{(V.94)}$$
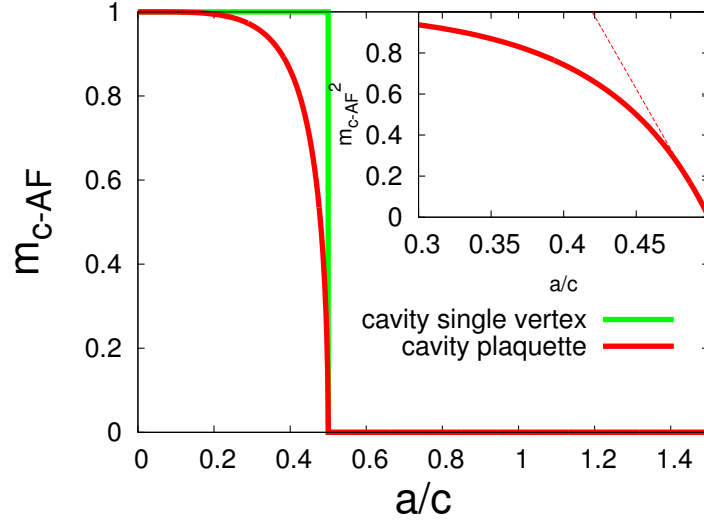
Figure V.20: Staggered magnetization in the six-vertex model as a function of a/c along the line $b = a$. The red curve shows the result on the tree of plaquettes, *i.e.* a continuous transition, while the green step shows the results obtained with the tree of single vertices, *i.e.* the transition towards a completely ordered phase. The inset shows the mean-field exponent $m_{a\text{-FM}}^2 \simeq [(a - a_c)/c]$.

where w_3 and w_4 are the statistical weights of FM or AF vertices if the transition under consideration is a PM-FM or a PM-AF one. Consequently, the magnetization at the transition shows a finite jump towards a *non-frozen ordered phase*.

Let us now focus on the a-FM-PM transition and look closely at the equations at the transition where $a = b + c + d$. In particular, if we try a solution of the type $\phi_{c\,F1} = (p_c^{a\text{-FM}}, s_c^{a\text{-FM}}, q_c^{a\text{-FM}} = 0)$, it turns out that the system is once again undetermined. The equations for $p_c^{a\text{-FM}}$ and $s_c^{a\text{-FM}}$ become dependent. The relation between $p_c^{a\text{-FM}}$ and $s_c^{a\text{-FM}}$ defines a line of fixed points joining $\phi_P[b + c + d, b, c, d]$ and $\phi_{a\text{-FM}}[b + c + d, b, c, d]$. The dependence between $p_c^{a\text{-FM}}$ and $s_c^{a\text{-FM}}$ is implicitely given by:

$$\gamma(p_{a\text{-FM}}^c, s_{a\text{-FM}}^c) = 4 \left[\frac{(c + d)b}{2cd} + 1 \right] (p_{a\text{-FM}}^c)^2 - 4 \frac{(c + d)b}{2cd} s_{a\text{-FM}}^c + (1 - s_{a\text{-FM}}^c)^2 = 0 \ . \quad \text{(V.95)}$$

One can actually check that the soft modes of the matrix $M_{ij}^{\alpha,\beta}$ at $a = a_c$ are defined by the tangent to the curve defined in eq. (V.95). The eigenvector with maximal eigenvalue (equal to 1) evaluated in the PM solution is of the form

$$\delta\varphi_{\text{PM}}^{\alpha\,c} = (\delta s^\alpha = 0, \delta p^\alpha = \delta p_{\text{PM}}^{\alpha\,c}, \delta q^\alpha = 0) \ . \quad \text{(V.96)}$$

The eigenvector associated to the unstable FM mode is

$$\delta\varphi_{a\text{-FM}}^{\alpha\,c} = (\delta s^\alpha = \delta s_{a\text{-FM}}^{\alpha\,c}, \delta p^\alpha = \delta p_{a\text{-FM}}^{\alpha\,c}, \delta q^\alpha = 0) \ . \quad \text{(V.97)}$$

Then, one can verify that for both solutions (and in general for the points along the line)

$$\delta s_{\text{PM}}^{\alpha\,\alpha}/\delta p_{\text{PM}}^c = -\gamma_p/\gamma_s\big|_{\phi=\phi_{\text{PM}}} = 0 \ , \quad \text{(V.98)}$$

$$\delta s_{a\text{-FM}}^c/\delta p_{a\text{-FM}}^c = -\gamma_p/\gamma_s\big|_{\phi=\phi_{a\text{-FM}}} = 2\sqrt{2cd + b(c + d)}/\sqrt{b(c + d)} \ , \quad \text{(V.99)}$$
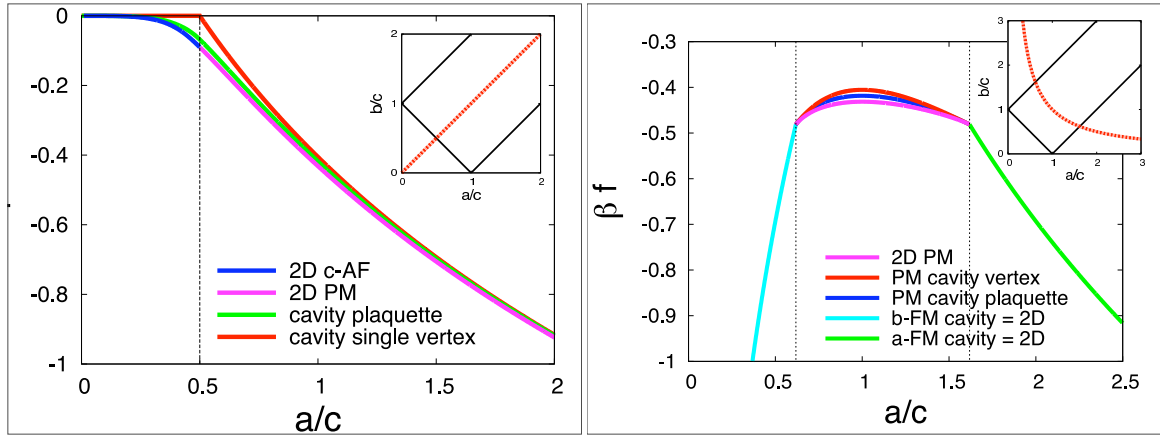
Figure V.21: The variation of the free-energy density of the six-vertex model along two paths in the phase diagram indicated in the insets, $a/c = b/c$ and $a\,b = c^2$. Left panel: free-energy of the PM phase for $0.6 \lesssim a/c \lesssim 1.6$ for the Bethe lattice of single vertices (red curve), of plaquettes (blue curve) and in the two dimensional model (pink line). Outside from this region, in the FM phases, all the calculations lead to the same free-energy (green and light blue lines). Right panel: free-energy in the PM phase ($a/c > 1/2$) and AF phase ($a/c < 1/2$) obtained from the Bethe lattice of single vertices (red curve), of plaquettes (green curve) and the exact results on the two dimensional model (pink and blue line).

where γ_s and γ_p stand for the partial derivatives of the function γ defined in eq. (V.95) with respect to s or p.

Similar considerations also hold for the other transitions occurring in the model. For instance, at the transition point towards the c-AF phase, $c_c = a + b + d$, on can identify a line of fixed points of the form $\phi_c^{c\text{-AF}} = (p_c^{c\text{-AF}} = 0, s_c^{c\text{-AF}}, q_c^{c\text{-AF}})$, where $s_c^{c\text{-AF}}$ and $q_c^{c\text{-AF}}$ lie on the curve:

$$4\Big[1 + \frac{d(a+b)}{2ab}\Big](q_c^{c\text{-AF}})^2 + 4\frac{d(a+b)}{2ab} s_c^{c\text{-AF}} + (1 + s_c^{c\text{-AF}})^2 = 0 \qquad (V.100)$$

which connects the antiferromagnetic solution to the paramagnetic one.

Let us also note another important property of the solutions. To this purpose we consider eqs. (V.69) as a transformation $\aleph$ of the weights:

$$(a', b', c', d') = \aleph(a, b, c, d) \,. \qquad (V.101)$$

This transformation is an involution: $\aleph\left[\aleph(a, b, c, d)\right] = (a, b, c, d)$. We may then express a, b, c, d in terms of a', b', c', d' in exactly the same way.

One can note that $\Upsilon[a', b', c', d'] = \nu[a, b, c, d]$ or, similarly, $\Upsilon[a, b, c, d] = \nu[a', b', c', d']$. Moreover, $f_{\text{PM}}[a', b', c', d'] = f_{a\text{-FM}}[a, b, c, d]$. Then, one can map one solution into the other,

$$
\begin{aligned}
s_{\text{PM}}[a, b, c, d] &= \frac{\psi_{--}^{\text{PM}}[a, b, c, d] - \psi_{+-}^{\text{PM}}[a, b, c, d]}{\psi_{++}^{\text{PM}}[a, b, c, d] + \psi_{+-}^{\text{PM}}[a, b, c, d]} \\[6pt]
&= \frac{s_{a\text{-FM}} - p_{a\text{-FM}}[a', b', c', d']}{1 + p_{a\text{-FM}}[a', b', c', d']} \\[6pt]
&= \frac{\psi_{--}^{a\text{-FM}}[a', b', c', d'] - \psi_{+-}^{a\text{-FM}}[a', b', c', d']}{\psi_{++}^{a\text{-FM}}[a', b', c', d'] + \psi_{+-}^{a\text{-FM}}[a', b', c', d']} \,,
\end{aligned}
\qquad (V.102)
$$

and viceversa. The transition can be recognized as the fixed point of the transformation (V.69) which is consistent with the transition in $2D$ at $a_c = b + c + d$. Thanks to the mapping (V.102)

the infinite temperature solution $\phi_{\text{PM}}[a, a, a, a]$ can be mapped into the completely ordered state $\phi_{a\text{-FM}}[a', 0, 0, 0]$. At the transition point though, $\phi_{\text{PM}}[b + c + d, b, c, d] \neq \phi_{a\text{-FM}}[b + c + d, b, c, d]$, but the line described by eq. (V.95) preserves some continuity between the two solutions. The same duality holds for the solution found for the single vertex Bethe lattice where the free-energy of the PM phase can be mapped into the free-energy of the completely frozen FM solution under the mapping $\aleph$ in eq. (V.69).

For the disordered points lying on the surfaces $a + d = c + b$ or $a + c = d + b$ in the PM phase we have $s_{\text{PM}} = 0$. The free-energy at these points computed with the single vertex tree (V.108) is the same as for the plaquette model and coincides exactly with the exact result of the $2D$ model [25]. This can be understood thanks to the transformation $\aleph$: it maps these PM regimes into the frozen FM phase of the six-vertex model and since loops in this phase are irrelevant, the free-energy on the Bethe lattice is the same as in $2D$.

V.4.5 The sixteen-vertex model on a tree of single vertices

We now attack the truly novel model including charge ± 2 defects, see Fig. IV.23. We use the same method tested above for the better-known six- and eight-vertex models.

V.4.5.1 Recursion relations and fixed points

We call $\psi_\zeta^{i^\alpha \to j^\beta}$ the probability for the root vertex i in a rooted tree with missing edge $\langle i^\alpha j^\beta \rangle$ be of type ζ with $\zeta \in \chi_v^{16}\{v_1, v_2, ..., v_{16}\}$. As in the analysis of the six- and eight-vertex models we introduce the cavity probabilities $\psi_i^\beta \equiv \psi_\zeta^{i^\alpha \to j^\beta}(+1)$ to find a positive spin on the missing edge of the rooted tree; these satisfy

$$\psi_i^u = \psi_{v_1}^{i^d \to j^u} + \psi_{v_3}^{i^d \to j^u} + \psi_{v_6}^{i^d \to j^u} + \psi_{v_8}^{i^d \to j^u} + \psi_{v_9}^{i^d \to j^u} + \psi_{v_{11}}^{i^d \to j^u} + \psi_{v_{13}}^{i^d \to j^u} + \psi_{v_{16}}^{i^d \to j^u} \, ,$$

$$\psi_i^d = \psi_{v_1}^{i^u \to j^d} + \psi_{v_3}^{i^u \to j^d} + \psi_{v_5}^{i^u \to j^d} + \psi_{v_7}^{i^u \to j^d} + \psi_{v_{10}}^{i^u \to j^d} + \psi_{v_{11}}^{i^u \to j^d} + \psi_{v_{14}}^{i^u \to j^d} + \psi_{v_{16}}^{i^u \to j^d} \, ,$$

$$\text{(V.103)}$$

$$\psi_i^l = \psi_{v_1}^{i^r \to j^l} + \psi_{v_4}^{i^r \to j^l} + \psi_{v_6}^{i^r \to j^l} + \psi_{v_7}^{i^r \to j^l} + \psi_{v_9}^{i^r \to j^l} + \psi_{v_{12}}^{i^r \to j^l} + \psi_{v_{14}}^{i^r \to j^l} + \psi_{v_{16}}^{i^r \to j^l} \, ,$$

$$\psi_i^r = \psi_{v_1}^{i^l \to j^r} + \psi_{v_4}^{i^l \to j^r} + \psi_{v_5}^{i^l \to j^r} + \psi_{v_8}^{i^l \to j^r} + \psi_{v_9}^{i^l \to j^r} + \psi_{v_{11}}^{i^l \to j^r} + \psi_{v_{14}}^{i^l \to j^r} + \psi_{v_{15}}^{i^l \to j^r} \, .$$

Along the same reasoning outlined in Sec. V.4.3, we derive the self-consistent equations:

$$\psi^u = \hat{\Psi}^u[a,b,c,d,e,\psi^u,\psi^d,\psi^l,\psi^r]$$

$$= \frac{1}{z^u}\Big[a\,\psi^l\psi^u\psi^r + b(1-\psi^l)\psi^u(1-\psi^r) + c(1-\psi^u)(1-\psi^l)\psi^r + d\psi^l(1-\psi^u)(1-\psi^r)$$

$$+e\Big(\psi^l(1-\psi^u)\psi^r + \psi^l\psi^u(1-\psi^r) + (1-\psi^l)\psi^u\psi^r + (1-\psi^l)(1-\psi^u)(1-\psi^r)\Big)\Big]$$

$$\psi^l = \hat{\Psi}^l[a,b,c,d,e,\psi^u,\psi^d,\psi^l,\psi^r]$$

$$= \frac{1}{z^l}\Big[a\psi^d\psi^l\psi^u + b(1-\psi^d)\psi^l(1-\psi^u) + c\psi^d(1-\psi^l)(1-\psi^u) + d(1-\psi^d)(1-\psi^l)\psi^u$$

$$+e\Big(\psi^d\psi^l(1-\psi^u) + \psi^d(1-\psi^l)\psi^u + +(1-\psi^d)\psi^l\psi^u + (1-\psi^d)(1-\psi^l)(1-\psi^u)\Big)\Big]$$

$$\psi^d = \hat{\Psi}^d[a,b,c,d,e,\psi^u,\psi^d,\psi^l,\psi^r]$$

$$= \frac{1}{z^d}\Big[a\psi^r\psi^d\psi^l + b(1-\psi^r)\psi^d(1-\psi^l) + c(1-\psi^r)(1-\psi^d)\psi^l + d\psi^r(1-\psi^d)(1-\psi^l)$$

$$+e\Big((1-\psi^r)\psi^d\psi^l + \psi^r(1-\psi^d)\psi^l + \psi^r\psi^d(1-\psi^l) + (1-\psi^r)(1-\psi^d)(1-\psi^l)\Big)\Big]$$

$$\psi^r = \hat{\Psi}^u[a,b,c,d,e,\psi^u,\psi^d,\psi^l,\psi^r]$$

$$= \frac{1}{z^r}\Big[a\psi^u\psi^r\psi^d + b(1-\psi^u)\psi^r(1-\psi^d) + c\psi^u(1-\psi^r)(1-\psi^d) + d(1-\psi^u)(1-\psi^r)\psi^d$$

$$+e\Big(\psi^u(1-\psi^r)\psi^d + \psi^u(1-\psi^r)\psi^d + \psi^u(1-\psi^r)\psi^d + (1-\psi^u)(1-\psi^r)(1-\psi^d)\Big)\Big]$$

$$(V.104)$$

where z^α are normalization constants [taking different values from the ones defined in eq. (V.47) as they now take into account the contributions from $e \neq 0$]. In order to obtain AF solutions, these equations must be studied on bipartite graphs as in eq. (V.50).

We consider here the case in which the vertices $v_9,\dots,v_{16}$ have the same weight e and arrow reversal symmetry applies to the other vertices as well. The fixed points of eqs. (V.104) on A_1 are

$$\psi^u_{PM} = \psi^l_{PM} = \psi^r_{PM} = \psi^d_{PM} = \frac{1}{2}\,,$$
$$\psi^u_{a\text{-FM}} = \psi^l_{a\text{-FM}} = \psi^r_{a\text{-FM}} = \psi^d_{a\text{-FM}} = h_+(a,b,c,d,e)\,,$$
$$\psi^u_{b\text{-FM}} = \psi^d_{b\text{-FM}} = h_+(b,a,c,d,e)\,, \qquad \psi^l_{b\text{-FM}} = \psi^r_{b\text{-FM}} = h_-(b,a,c,d,e)\,, \quad (V.105)$$
$$\psi^u_{c\text{-AF}} = \psi^l_{c\text{-AF}} = h_+(c,b,a,d,e)\,, \qquad \psi^r_{c\text{-AF}} = \psi^d_{c\text{-AF}} = h_-(c,b,a,d,e)\,,$$
$$\psi^u_{d\text{-AF}} = \psi^r_{d\text{-AF}} = h_+(d,b,c,a,e)\,, \qquad \psi^d_{d\text{-AF}} = \psi^l_{d\text{-AF}} = h_-(d,b,c,a,e)\,,$$

with

$$h_\pm(w_1,w_2,w_3,w_4,w_5) = \frac{1}{2} \pm \frac{w_1 - w_2 - w_3 - w_4 - 2w_5}{2\sqrt{(w_1-w_2-w_3-w_4)^2 - 4w_5^2}}\,.$$

V.4.5.2   Free-energy, stability and order parameters

The vertex partition function is now

$$
\begin{aligned}
Z_v[\psi^l, \psi^r, \psi^u, \psi^d] = {} & a\left[\psi^l\psi^u\psi^r\psi^d + (1-\psi^u)(1-\psi^l)(1-\psi^r)(1-\psi^d)\right] \\
& + b\left[(1-\psi^l)\psi^u(1-\psi^r)\psi^d + \psi^l(1-\psi^u)\psi^r(1-\psi^d)\right] \\
& + c\left[\psi^l(1-\psi^u)(1-\psi^r)\psi^d + (1-\psi^l)\psi^u\psi^r(1-\psi^d)\right] \\
& + d\left[(1-\psi^u)(1-\psi^l)\psi^r\psi^d + \psi^u\psi^l(1-\psi^r)(1-\psi^d)\right] \\
& + e\left[\psi^l(1-\psi^u)\psi^r\psi^d + (1-\psi^l)\psi^u(1-\psi^r)(1-\psi^d)\right. \\
& \qquad + \psi^l\psi^u(1-\psi^r)\psi^d + (1-\psi^l)(1-\psi^u)\psi^r(1-\psi^d) \\
& \qquad + (1-\psi^l)\psi^u\psi^r\psi^d + \psi^l(1-\psi^u)(1-\psi^r)(1-\psi^d) \\
& \qquad \left. + (1-\psi^l)(1-\psi^u)(1-\psi^r)\psi^d + \psi^l\psi^u\psi^r(1-\psi^d)\right],
\end{aligned}
\tag{V.106}
$$

which in the limit $e \to 0$ gives back eq. (V.53). The free-energy reads

$$
\begin{aligned}
\beta f[a, b, c, d, e, \boldsymbol{\psi}_1, \boldsymbol{\psi}_2] = {} & -\frac{1}{2}\Big(\ln Z_v[\boldsymbol{\psi}_1] + \ln Z_v[\boldsymbol{\psi}_2] + \\
& - \ln Z_{\langle lr\rangle}[\psi_1^l, \psi_2^r] - \ln Z_{\langle lr\rangle}[\psi_2^l, \psi_1^r] - \ln Z_{\langle ud\rangle}[\psi_1^u, \psi_2^d] - \ln Z_{\langle ud\rangle}[\psi_2^u, \psi_1^d] \Big),
\end{aligned}
\tag{V.107}
$$

where $Z_{\langle lr\rangle}$ and $Z_{\langle ud\rangle}$ are defined in eqs. (V.54) and (V.55), respectively. Once evaluated in the solutions outlined above the free energies of the different phases are:

$$
\begin{aligned}
\beta f_{\text{PM}} &= \beta f[a, b, c, d, e, \boldsymbol{\psi}_{\text{PM}}] = -\ln\left[\frac{a+b+c+d+4e}{2}\right], \\
\beta f_{a\text{-FM}} &= \beta f[a, b, c, d, e, \boldsymbol{\psi}_{a\text{-FM}}] = -\ln\left[a - \frac{2e^2}{-a+b+c+d}\right], \\
\beta f_{b\text{-FM}} &= \beta f[a, b, c, d, e, \boldsymbol{\psi}_{b\text{-FM}}] = -\ln\left[b - \frac{2e^2}{a-b+c+d}\right], \\
\beta f_{c\text{-AF}} &= \beta f[a, b, c, d, e, \boldsymbol{\psi}_{c\text{-AF}}] = -\ln\left[c - \frac{2e^2}{a-c+b+d}\right], \\
\beta f_{d\text{-AF}} &= \beta f[a, b, c, d, e, \boldsymbol{\psi}_{d\text{-AF}}] = -\ln\left[d - \frac{2e^2}{a-d+b+c}\right].
\end{aligned}
\tag{V.108}
$$

The order parameters are defined as in Sec. V.4.3.2 where the normalization is now the one defined in eq. (V.106). The PM solution $\boldsymbol{\psi}_{\text{PM}}$ is the same as for the eight-vertex model and yields vanishing magnetization for all the order parameters. Differently from the six- and the eight-vertex model, where the ordered parameters jump discontinuously to one at the phase transition on the tree of single vertices, when $e \neq 0$ any ordered FM or AF solution is associated to a continuously growing magnetization. Considering the a-FM phase transition and plugging $\boldsymbol{\psi}_{a\text{-FM}}$ into (V.49) one obtains:

$$
m_{a\text{-FM}} = \frac{a\sqrt{(-a+b+c+d)^2 - 4e^2}}{a^2 - a(b+c+d) + 2e^2} .
\tag{V.109}
$$

The expansion close to the critical point $a_c = b + c + d + 2e$ yields the expected mean-field exponent $\beta = 1/2$:

$$m_{a\text{-FM}} = \frac{b + c + d + 2e}{\sqrt{e}(b + c + d + 3e)}\sqrt{a - a_c} + +\mathcal{O}\left[(a - a_c)^{3/2}\right] . \tag{V.110}$$

In the limit $e \to 0$ one recovers from eq. (V.109) the saturated value, $m_{a\text{-FM}} = 1$, characteristic of the frozen ordered phase in the eight-vertex model. Consistently, the same limit in (V.110) shows a divergence of the coefficient of the singular term $\sqrt{a - a_c}$. Analogous results hold for the other phase transitions and the corresponding order parameters; these results can be obtained by simply exchanging the parameter a and the opportune vertex weight in eqs. (V.109) and (V.110).

We study the stability properties of the PM phase by analyzing the eigenvalues of the stability matrix introduced in eq. (V.63), now in the case $e \geq 0$. The eigenvalues associated to the PM solution ψ_{PM} are

$$E_1^{\text{PM}} = \frac{3a - b - c - d}{a + b + c + d + 4e} , \qquad E_2^{\text{PM}} = \frac{-a + 3b - c - d}{a + b + c + d + 4e} ,$$
$$E_3^{\text{PM}} = \frac{a + b - 3c + d}{a + b + c + d + 4e} , \qquad E_4^{\text{PM}} = \frac{a + b + c - 3d}{a + b + c + d + 4e} , \tag{V.111}$$

with the same eigenvectors as in Sec. V.4.3. Overall the stability is controlled by the condition:

$$\left|\frac{(1 + E_3^{\text{PM}})(1 + E_4^{\text{PM}}) - (1 - E_1^{\text{PM}})(1 - E_2^{\text{PM}})}{(1 + E_3^{\text{PM}})(1 + E_4^{\text{PM}}) + (1 - E_1^{\text{PM}})(1 - E_2^{\text{PM}})}\right| = |\Delta_{16}^{sv}| < 1 \tag{V.112}$$

with

$$\Delta_{16}^{sv} = \frac{a^2 + b^2 - c^2 - d^2 + 2(a + b - c - d)e}{2[cd + ab + e(a + b + c + d + 2e)]} . \tag{V.113}$$

This *generalised anisotropy parameter* implies that, in the presence of a non-vanishing vertex weight e, all the transition lines are shifted by $2e$ with respect to the value obtained for the eight-vertex model. This should be compared to the conjectured value for the $2D$ model, Δ_{16} given in eq. (V.42), and with the numerical results also in $2D$. The BP approach on the tree of vertices gives the expected qualitative behavior, meaning an increase of the PM phase with increasing e. However, the conjectured Δ_{16} given in eq. (V.42) is closer to the numerics (not surprisingly, as its functional form was guessed from the analysis of the numerical results). Unfortunately, we do not have an exact result in $2D$ to compare with and conclude about the expression, or even the existence, of such Δ_{16} parameter.

V.4.6 The sixteen-vertex model on the tree of plaquettes

The previous procedure can be extended straightforwardly to the case of the sixteen vertex model on the plaquette if one includes in the statistical weights a non vanishing e. With the definition,

$$w_{s_1,s_2,s_3,s_4}(a, b, c, d, e) = \frac{1}{4}\Big[a'(1 + s_1 s_2 s_3 s_4) + b'(s_1 s_3 + s_2 s_4) + c'(s_1 s_4 + s_2 s_3)$$
$$+ d'(s_1 s_2 + s_3 s_4)\Big] + \frac{e}{2}(1 - s_1 s_2 s_3 s_4) , \tag{V.114}$$

and a', b', c' and d' given in eq. (V.68), the equations (V.73), (V.74) and (V.75) apply to the sixteen-vertex model as well. Obviously, the calculations become more involved.

The PM solution is of the type $\phi_{\text{PM}} \equiv \phi^u_{\text{PM}} = \phi^l_{\text{PM}} = \phi^r_{\text{PM}} = \phi^d_{\text{PM}} = (p_{\text{PM}} = 0, s_{\text{PM}}, q_{\text{PM}} = 0)$ and s_{PM} is the solution to the equation:

$$(a + b + c + d)^4 (x^2 - y^2)\Big[u_4\, s^4_{\text{PM}} + u_3\, s^3_{\text{PM}} + u_2\, s^2_{\text{PM}} + u_1\, s_{\text{PM}} + u_0\Big] = 0 \qquad \text{(V.115)}$$

with

$$u_0(x, y, z, t) = (1 + t)^2 + z^2\ ,$$

$$u_1(x, y, z, t) = -\frac{(1 + t)^4 + z^4 - 2(1 + z^2 - t^2)(x^2 + y^2)}{x^2 - y^2}\ ,$$

$$u_2(x, y, z, t) = -12t\ , \qquad\qquad\qquad\qquad\qquad\qquad \text{(V.116)}$$

$$u_3(x, y, z, t) = \frac{(1 - t)^4 + z^4 - 2(1 + z^2 - t^2)(x^2 + y^2)}{x^2 - y^2} = -u_1(x, y, z, -t)\ ,$$

$$u_4(x, y, z, t) = -((1 - t)^2 + z^2) = -u_0(x, y, z, -t)\ .$$

The variables x, y and z were already defined in eq. (V.78) and $t = 4e/(a+b+c+d)$. This equation reduces to the eight-vertex model equation on the tree of plaquettes, eq. (V.80), when $t = 0$. Note that the presence of a non-zero value of t implies a much more complicated dependence on the parameters. We do not solve this equation explicitly, however one can show that, as for the eight vertex model, the limit of infinite temperature $a = b = c = d = e$ corresponds to the trivial solution $s_{\text{PM}} = 0$.

V.4.7   The sixteen-vertex model: phase diagram

The phase diagram obtained with the Bethe lattice made of single vertices in qualitative agreement with the results obtained with the MC simulations on the $2D$ squared lattice. All the transition lines are smooth in the sense that they become continuous when all possible vertices are present.

The results on the tree of vertices predict a uniform shift of the critical lines, with respect to the eight-vertex model, by $2e$ [compare eq. (V.111) together with the criticality condition $|E_\alpha| = 1$]. This implies, for instance, that the critical value for the a-FM transition occurs at $a^{sv}_c = b + c + d + 2e$. This is not exactly the case for the $2D$ squared lattice. While for small values of d and e, one numerically finds $a^{2D}_c \simeq b + c + d + 3e$ (the results reported in [160], for large values of these parameters we see a deviation from the linear behaviour. We do not have an analytic expression for the transition surfaces for the tree of plaquettes. However, from the numerical evaluation of the MC data, one concludes that for the FM transition $a^{sv}_c < a^{pl}_c < a^{2D}_c$ (where the superscript sv, pl and $2D$ stands for single vertex, plaquette and $2D$ model). Similar results hold for the other transitions.

In Fig. V.22 we report the phase diagram of the sixteen-vertex model on the plane of parameters $(a/c, b/c)$, for two fixed values of $d/c = e/c$. We show the projection of the transition surfaces obtained with Monte Carlo simulations on the $2D$ square lattice (black points), the tree of plaquettes (orange and red dotted lines) and the transition lines obtained according to the proposed value in eq. (V.42) (plain lines), together with the exact phase diagram at $d = e = 0$. The data for the model on the tree of plaquettes has been obtained by analysing the magnetisation, see Fig. V.9.

V.4.8   Summary and conclusions

In summary, we computed the equilibrium phases of the six-, eight- and sixteen-vertex model defined on tree-like lattices. The nature of the phase transitions depend upon the elementary unit
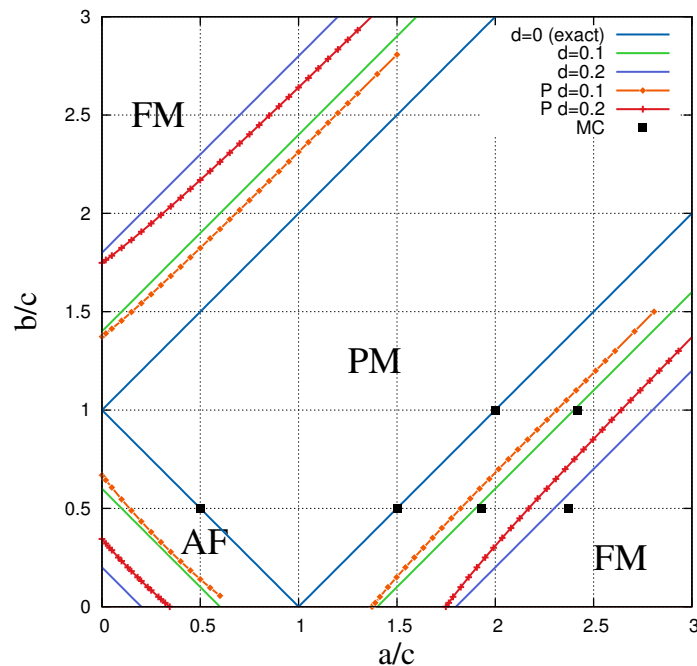
Figure V.22: **Phase diagram of the sixteen-vertex model.** The figure shows the projection of the transition surfaces on to the plane of parameters $(a/c, b/c)$, for two fixed values of $d/c = e/c = 0.1$ and $d/c = e/c = 0.2$. Orange and red dotted lines represent the results obtained with the cavity method for the tree of plaquettes. Green and violet plain lines shows the proposed behaviour of the transition lines as predicted by eq. (V.42) for the two dimensional model. Black dots indicate the transition point obtained with Monte Carlo simulations for the model defined on the squared lattice. Blue solid lines represent the exact phase diagram in the limiting case $d = e = 0$ (six-vertex model).

used for the construction of the tree. In Table. V.3 we review the nature of the phase transitions obtained for the six- and eight-vertex model . Note that the location of the transition points we obtained corresponds exactly with the solution of the $2D$ model. However, the critical exponents of the finite dimensional model cannot be reproduced by this approach.

Table V.4 is a survey of the critical behavior of the sixteen-vertex model on the tree of single vertices, on the tree of plaquettes and on the $2D$ square lattice (numerical MC data).

In the bidimensional six-vertex model the disordered phase is critical (a SL), the FMs are frozen and the AF has fluctuations. In the tree of single vertices the PM phase (that we call sPM in the table) is similar to a critical phase in the sense that one of the eigenvectors of the stability matrix is identical to one, although the model being defined on a tree, cannot have a power-law dependence of the correlation functions as in a truly critical phase. The FMs and AF phases are frozen. In the tree of plaquettes the soft nature of the PM phase is maintained, the FM phases remain frozen but the AF phase admits fluctuations.

In the $2D$ eight-vertex model the disordered phase is no longer critical and the FM and AF phases have fluctuations, with continuous transitions between all these. In the trees of single vertices and plaquettes the PM phase is a conventional one. As for the FM and AF phases, they are frozen on the tree of single vertices but have fluctuations on the tree of plaquettes. The transitions are frozen-to-PM in the first case and discontinuous in the latter.

The use of a tree of plaquettes allows us to introduce fluctuations in the ordered phases that

	6V single vertices	8V single vertices	6V plaquettes	8V plaquettes
PM-FMs	Frozen-to-sPM	Frozen-to-PM	Frozen-to-sPM	Discont-to-PM
PM-AFs	Frozen-to-sPM	Frozen-to-PM	Cont.-to-sPM	Discont.-to-PM

Table V.3: Transitions in the six- and eight-vertex models on tree-like lattices. We call sPM the paramagnetic phase with a maximal eigenvalue identical to one, which is a remembrance of the critical nature of this phase in $2D$. The comparison to the $2D$ behavior is encoded in the color rule: the text is colored in blue when we find agreement between the $2D$ model and the BP approximation (accepting to take the sPM phase as the equivalent on the tree of the critical phase in $2D$); contrarily, we use red when the model on the tree does not behave as the $2D$ one. We recall that in $2D$ the PM-AFs transitions in the six-vertex model are of Kosterlitz-Thouless type while the order-disorder transitions in the eight-vertex model are continuous. We stress that the plaquette-tree model constitutes an important improvement over the single vertex approach as it captures the fluctuating character of the ordered phases.

make the transitions softer.

In the finite dimensional problem the SL-FM transition becomes second order as soon as $d > 0$ or $e > 0$. The critical exponents depend upon the parameters but we cannot assert their concrete dependence as this is rather hard to obtain numerically.

	16V single vertices	16V plaquette	16V $2D$
PM-FMs	Continuous	Continuous	Continuous
PM-AFs	Continuous	Continuous	Continuous

Table V.4: Transitions found in the sixteen-vertex model on a tree of single vertices and plaquettes (cavity method), and the $2D$ square lattice (MC simulations).

V.5 Application to artificial spin ice: the $2D$ spin-ice model

In this section we demonstrate that a simplified version of the more realistic dipolar spin-ice model in $2D$, the sixteen-vertex model, or $2D$ *spin-ice model* as defined in section V.1.2, is an accurate model for the equilibrium behaviour of artificial spin-ice samples. Concretely, we use numerical simulations and we apply the computations presented below in the Bethe lattice made of plaquettes that yields a remarkably accurate approximation to the equilibrium properties of the square lattice $2D$ model and real samples as well.

V.5.1 Equilibrium phases and critical properties

We studied the $2D$ model with the CTMC algorithm with single-spin updates. The usual finite-size scaling analysis faces serious difficulties close to the SL phase since for a small weight of defects one cannot easily tell the difference between a critical phase with $\xi_{eq} \to \infty$ and a disordered phase with $L < \xi_{eq} < \infty$. The non-equilibrium relaxation method (NERM) distinguishes these cases by investigating how the system relaxes to its equilibrium state from a completely ordered configuration $M_-(0) = 1$. At a critical point the staggered magnetisation follows a power law $M_-(t) \sim t^{-\beta/(\nu z_c)}$ where β and ν are the equilibrium critical exponents associated to the

order parameter and the correlation length and z_c is the dynamical exponent. Instead, away from criticality $M_-(t)$ decays exponentially. At short times the dynamic correlation length $\xi(t) \ll L$ avoiding the difficulty raised by $\xi_{eq} \gtrsim L$. This allows one to extract the critical temperature and critical exponents of from the dynamic results.
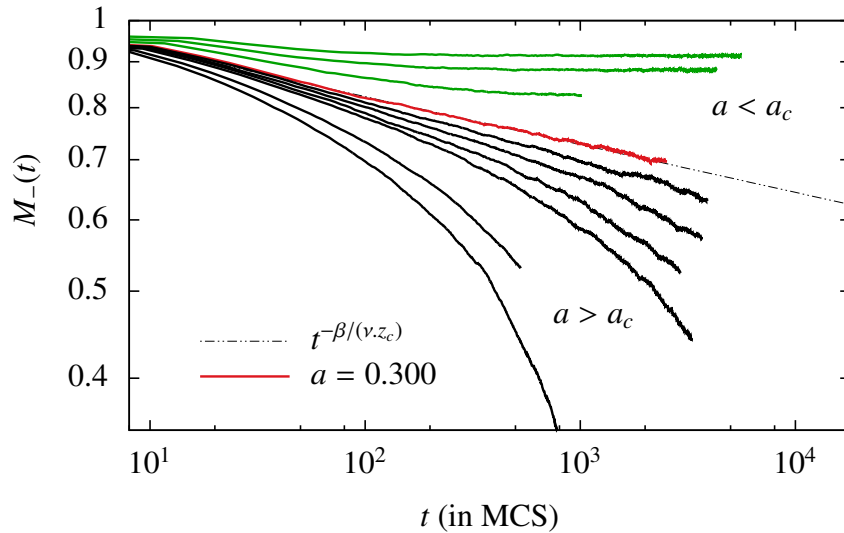

Figure V.23: The relaxation of the staggered magnetization from $M_-(0) = 1$ at different inverse temperatures parametrized as $a = e^{-\epsilon_1 \beta}$ with $a = 0.27, 0.28, 0.29, 0.30, 0.302, 0.304, 0.306, 0.308, 0.315, 0.32$. The dashed line is the best fit obtained with a power law decay. It gives a critical value $a_c = 0.300 \pm 0.002$ with an exponent $\beta/(\nu z_c) = 0.053 \pm 0.01$.

A single critical power-law decay of $M_-(t)$ at $\beta_c = 2.65 \pm 0.017$ can be easily identified from Fig. V.23, showing that the SL phase is broken at finite temperature by the presence of defects. A generalised set of critical exponents, independent of the choice of parameters, have been defined in the eight-vertex model [25]. Among them $\hat{\beta} = \beta/\nu = 1/8$. Our analytic and numeric results suggest that the sixteen-vertex model is in the same generalised universality class with $\hat{\beta} = 1/8$ as well [100]. Fixing this value for the ratio of equilibrium exponents the NERM yields $z_c = 2.35 \pm 0.40$ although a more accurate computation of $\hat{\beta}$ would be needed to give further support to this result.
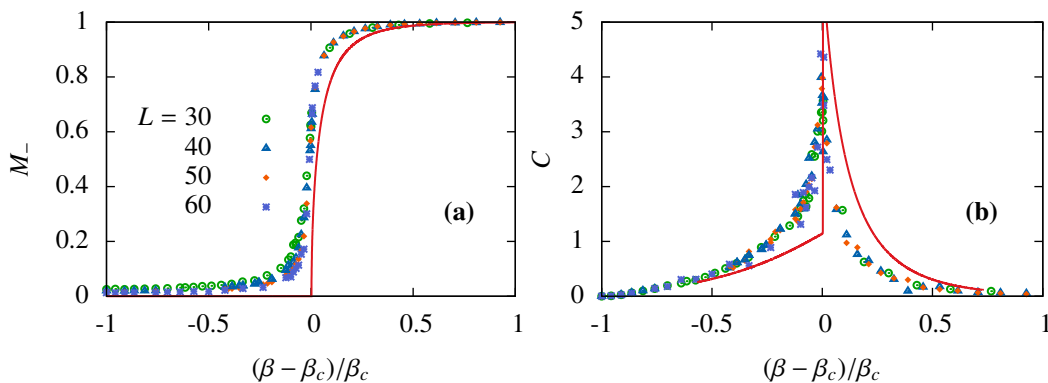

Figure V.24: Staggered magnetisation M_- (a) and specific heat C (b) as a function of the distance to the critical inverse temperature β_c for system sizes $L = 30, 40, 50, 60$. The (red) solid lines are the results of the analytic calculation on the tree of plaquettes.
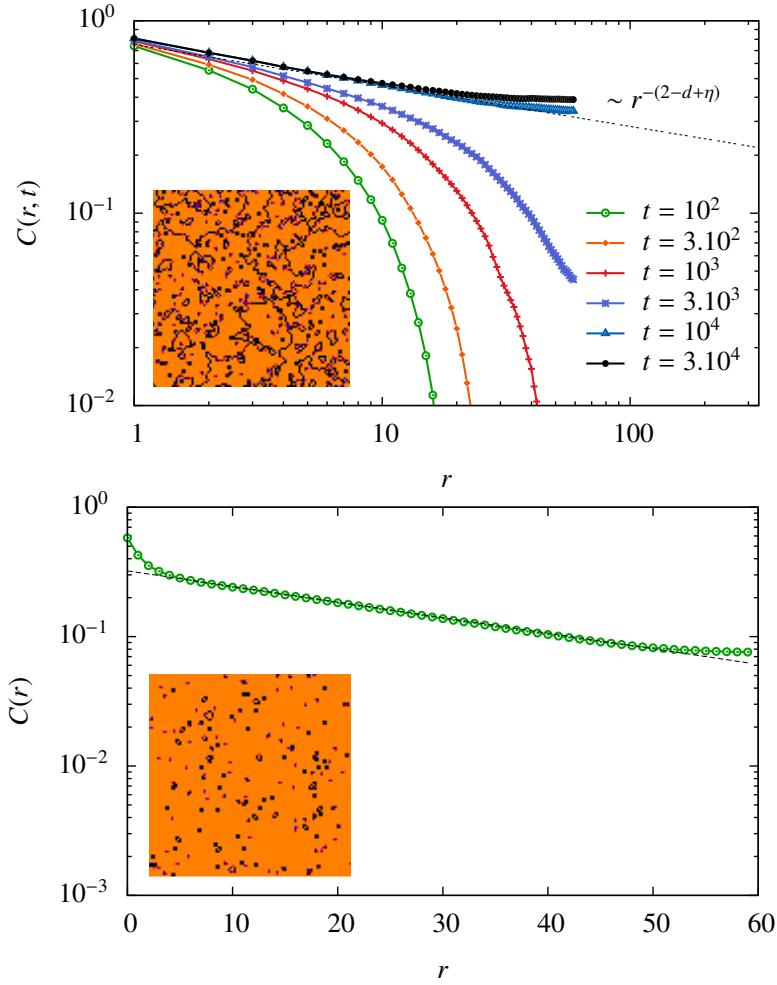
Figure V.25: The space-time $C(r,t)$ and equilibrium $C(r) = \lim_{t\to\infty} C(r,t)$ correlation function close to the phase transition (top panel, $\beta = 2.65$) and in the ordered phase (bottom panel, $\beta = 3$). The colored lines-points in the top panel are dynamic data after a quench from $T \to \infty$. The equilibrium critical correlation function (black dots) is confronted to an algebraic decay $\sim r^{-0.22}$ (dotted line); note that $\eta = 1/4$ for the Ising model. The insets show two typical configurations in these conditions. Orange regions are c-AF ordered, black dots correspond to FM vertices (a and b), red and blue dots correspond to oppositely charged defects of type e; d vertices are absent. Connected correlations in the ordered regime agree with an exponential decay $\sim \exp(-r/\xi)$ with $\xi = 36$.

In Fig. V.24 we display equilibrium CTMC data for M_- (a) and the heat capacity $C = L^{-2}(\langle E^2 \rangle - \langle E \rangle^2)$ (b) as a function of the distance to the critical inverse temperature, $(\beta - \beta_c)/\beta_c$. These results are in agreement with the NERM analysis and confirm the second order phase transition at $\beta_c \approx 2.65$. Figure V.24 also displays the analytic results for M_- and C (solid red lines). The theory predicts a second-order phase transition with a systematic shift of the critical point by around 5% towards higher temperature.

Figure V.25 (a) displays the space-dependence of the correlation function defined as

$$C(r,t) = \frac{1}{(2L)^2} \langle \sum_{i,j} S_{i,j}(t) S_{i+r,j+r}(t) \rangle \qquad (V.117)$$

for different times after a quench from $\beta \to 0$ to $\beta_c = 2.65$ (in log-log scale). The indices (i,j)

denote a site of the $2L \times 2L$ square lattice made by all the arrows. $S_{i,j} = +1$ if the arrow points right or up and $S_{i,j} = -1$ otherwise. With these definitions, r is given in units of $a_0/\sqrt{2}$. The dynamic curves approach, for increasing times, the asymptotic equilibrium law that close to the transition is a power-law with an exponential cut-off. The figure also shows, in an insert, a typical configuration (see the caption for the vertex color code). In the bottom panel we present the equilibrium $C(r) = \lim_{t \to \infty} C(r,t)$ in the c-AF phase (linear scale) and an ordered configuration in the insert. The equilibrium correlations decay exponentially to a non-zero asymptotic value $c_0 \approx 0.42$. The approach to such configurations is fast if the initial state is a completely ordered $T = 0$ ground state but it is very slow and occurs *via* the coarsening process if the initial condition is a disordered one [160, 50]. Dynamical issues like coarsening will be discussed in the next chapter.

Putting together the results of extensive NERM and CTMC numerical simulations for a large range of parameters we obtained the phase diagram shown in Fig. V.26.
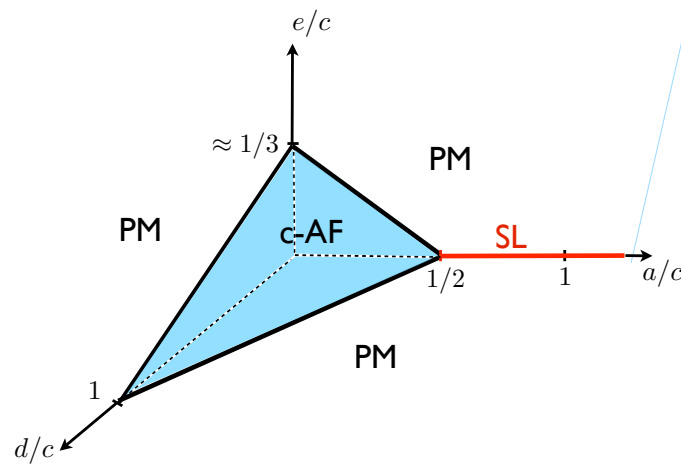

Figure V.26: $3D$ projection of the phase diagram of $2D$ spin ice on the square lattice for $a = b$. The thick (red) line indicates the SL phase ending at the KT transition point ($d = e = 0$ and $a/c = b/c = 1/2$). The c-AF phase is indicated by the (blue) tetrahedron. In the rest of the phase diagram and for $d \lesssim 2a + 3e + c$ (otherwise a d-AF phase would be found) one finds a PM.

V.5.2 Experimental density of defects

In Fig. V.27 we plot the vertex population of each vertex type as a function of the canonical inverse temperature $\beta = -\ln a/\epsilon_1$. The results of our MC simulations (colored lines-points) and BP calculation (solid black lines) are confronted to experimental data from the British collaboration (data points) [197]. In this experiment, spin configurations are visualized at the end of a sample preparation process in which the thickness of the magnetic islands grow by deposition. The Ising spins flip by thermal fluctuations during the growth process. However, as the time scales for these moves increase with the growing size of the islands, once a certain thickness is reached the flipping times become too large and the spins *freeze*. Using ideas pioneered by Edwards in the context of granular matter [88], the assumption that with this procedure one samples configurations from an effective equilibrium ensemble at an *effective temperature* β_E is hence made. Moreover, taking the vertices as being independent (mean-field approximation) one concludes $\langle n_i \rangle = \exp\left(-\beta_E \epsilon_i\right)/Z$, where Z is the normalization constant, and β_E is extracted from the data for $\langle n_i \rangle$. This is the way in which the data-points have been drawn [196].

Our model reproduces quantitatively the experimental data at temperatures far enough from

the critical point. We argue that at temperatures close to T_c the annealing time leading to the frozen configuration is not long enough to sample the equilibrium distribution because of critical slowing down. It would be interesting to explore the connection between the experimental cooling procedure and a cooling rate in the numerical simulations. Evidence for critical slowing down in this system was already given in Fig. V.25 (a) where the spatial correlation at different times after a quench from $T \to \infty$ to T close T_c are shown.
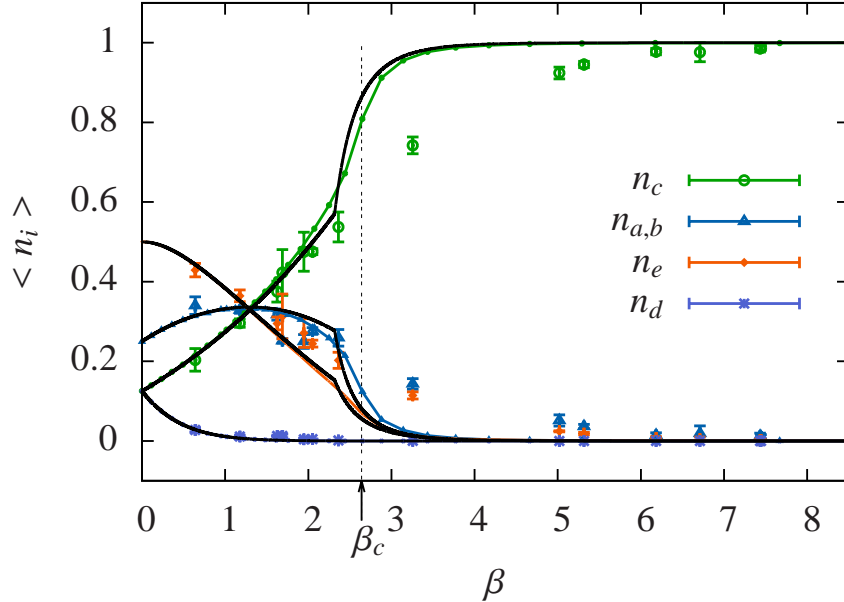

Figure V.27: Averaged density of vertices as a function of inverse temperature. The points are data from the experiment in [197, 196] and β is estimated as explained in the text. The solid colored lines are the fits to the CTMC data. The solid black lines are the BP analytic results. The vertical dotted line indicates the critical inverse temperature.

V.6 Extension of mappings for constrained models to the generic case

Most of the contents of this section is still work in progress. The included here in order to give possible further directions in the investigation of generic lattice models. In particular, we stress how to extend the known mappings to surface growth models and quantum spin chains for constrained models when we include thermally activated defects such as monopoles in spin-ice.

V.6.1 Height representation, monopoles and dislocations

The sixteen-vertex model cannot be represented faithfully by a height configuration because of the presence of defects. This can be understood from eq. (IV.32). A defect in the six-vertex model is characterised by

$$\sum_{j \in \Gamma} \vec{A}_{i,i+1} \cdot \vec{l}_{i,i+1} = 2q \quad \equiv \quad \oint_{\Gamma} \vec{A}.d\vec{l} = 2q \tag{V.118}$$

where Γ is a closed path around a vertex and q is its charge. Note that, in the continuum formulation, this equation is identical to the definition of a vortex in the XY model (see eq. (III.20)). The height configuration is not uniquely defined in the presence of defects. Just as for the XY model

in the presence of vortices, or for the electromagnetic field in the presence of magnetic monopoles, the function h is *multivalued*. This is illustrated in Fig. V.28: along any closed loop sourrounding a defect the height field goes from some value $h(x, y)$ to a different one $h(x, y) + 2q$. The shift between these two values of the height at the same plaquette is given by the charge of the defect. In order to fix its value one must choose arbitrarily a branch cut starting at a defect site and going to infinity or ending at a different defect of opposite charge. Then, one can construct a height configuration by recursion from a vertex configuration using eq. (IV.31) for any path $\mathcal{C}$ which does not go through the branch cut. This was already discussed in section III.1.4 and III.1.5: one needs to fix a branch cut for each topological defect in order to define the value of θ, **u** or **A**.
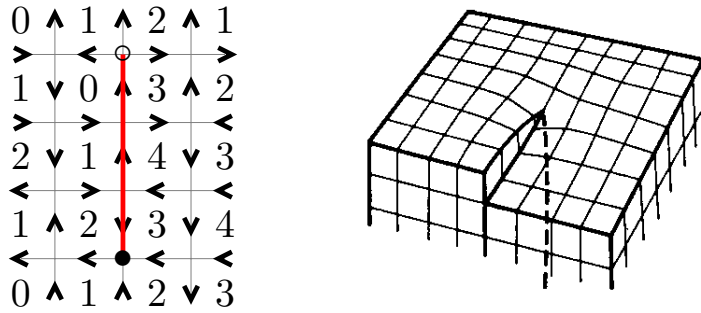

Figure V.28: Height configuration presence of two defects linked by a branch cut shown in red. Right: A screw dislocation in the crystal surface of Burgers vector $\mathbf{b} = (0, 0, -l_0)$ (picture extracted from [157]).

As shown in Fig. V.28, branch cuts associated to defects in the vertex model correspond to *screw dislocations* in the SOS representation. The height function of the vertex model can describe the surface of a crystal. Screw dislocations are characterised by a Burgers vector **b** orthogonal to the surface: $\mathbf{b} = (0, 0, b)$. Consider a positively charged defect as the one showed by a white circle in Fig V.28. After going around it in the trigonometric direction, the height experiences a brutal 'climb' which is equal to two times the height difference between NN in the BC lattice, i.e. a lattice spacing l_0 (see section IV.3.4 for the notations). Instead, for a negative charge, the height experiences a brutal fall of the same magnitude. The Burgers vector is then $\mathbf{b} = (0, 0, q)l_0$ pointing into or out to the bulk of the crystal.

In the following, we extend the arguments used by Blöte and Nightingale to study the AF Ising model on the triangular lattice [39] to the six-vertex model with defects (sixteen-vertex model). For the Gaussian SOS model, the asymptotic correlation function of two height variables at a distance r is given by (see eq. III.22): $g(r) = \langle (h(0,0) - h(x,y))^2 \rangle \sim \ln r$. The long-wave length behaviour of the system is then described by an effective Coulomb gas model:

$$S[\rho] = \int \int d\vec{r} d\vec{r}' \rho(\vec{r}) g(|\vec{r} - \vec{r}'|) \rho(\vec{r}') + \beta E_c \int d\vec{r} \rho^2(\vec{r}) \tag{V.119}$$

where ρ is the charge density and $E_c \approx \epsilon_e$ is the energy of creation of a defect. From these arguments, one would expect defects to interact via a $2D$ Coulomb potential. This potential is different form the $1/r$ form expected from dipolar interactions in $2D$ spin-ice samples [264, 190, 189].

V.6.2   Mapping into a quantum spin chain

The contents of this subsection are a prelude of the unfinished work we are doing in close collaboration with Laura Foini. We are trying to generalise the known mappings between quantum

spin chains and constrained vertex models (six- and eight-vertex models) to the unconstrained case. This is an old problem pointed out by Lieb and Wu more than thirty years ago [166]:

> Find a non-trivial linear Hamiltonian that commutes with the transfer matrix for the sixteen vertex problem.
>
> *E. Lieb and F. Wu* , in Phase transitions and critical phenomena Vol. 1 *[166]*

In previous sections we presented two different approaches to show the relationship between a classical lattice model and a quantum spin chain. The first one, described in section IV.4.4, is based on the computation of commutators between the R-matrices of the classical model and the local quantum Hamiltonian acting on two sites of the chain. Then, one has to prove that the commutator $[H, T]$ vanish when the interaction parameters of both models verify some equations. The second one, described in section IV.5.2, makes use of the Suzuki-Trotter decomposition to write the partition function of the quantum model as a path integral (a sum for lattice models). Then these paths are identified with configurations of a classical statistical model in the 'limit of continuous imaginary time' $\Delta\tau \to 0$. Both methods need a good 'guess' of the quantum Hamiltonian in order to prove its equivalence with a classical model. In the following I motivate our 'guess' and discuss the difficulties encountered to prove (if true!) its equivalence with the sixteen-vertex model.

The $R-$matrix for the sixteen-vertex model is

$$R = \begin{pmatrix} \omega_1 & \omega_{11} & \omega_9 & \omega_7 \\ \omega_{14} & \omega_3 & \omega_6 & \omega_{15} \\ \omega_{16} & \omega_5 & \omega_4 & \omega_{13} \\ \omega_8 & \omega_{10} & \omega_{12} & \omega_2 \end{pmatrix} . \tag{V.120}$$

and the transfer matrix $T = \text{Tr}_2(\prod_i R_i)$ where R_i reads

$$R_i = \begin{pmatrix} R_i^{11} & R_i^{12} \\ R_i^{21} & R_i^{22} \end{pmatrix} . \tag{V.121}$$

First of all we should find a representation of the transfer matrix in terms of Pauli matrices. This has been done in [166]:

$$\begin{array}{ll} R_i^{11} = & \frac{1}{2}(\omega_1 + \omega_4) + \frac{1}{2}(\omega_1 - \omega_4)\hat{\sigma}_i^z + \omega_{16}\hat{\sigma}_i^+ + \omega_9\hat{\sigma}_i^- \\ R_i^{12} = & \frac{1}{2}(\omega_{11} + \omega_{13}) + \frac{1}{2}(\omega_{11} - \omega_{13})\hat{\sigma}_i^z + \omega_5\hat{\sigma}_i^+ + \omega_7\hat{\sigma}_i^- \\ R_i^{21} = & \frac{1}{2}(\omega_{14} + \omega_{12}) + \frac{1}{2}(\omega_{14} - \omega_{12})\hat{\sigma}_i^z + \omega_8\hat{\sigma}_i^+ + \omega_6\hat{\sigma}_i^- \\ R_i^{22} = & \frac{1}{2}(\omega_3 + \omega_2) + \frac{1}{2}(\omega_3 - \omega_2)\hat{\sigma}_i^z + \omega_{10}\hat{\sigma}_i^+ + \omega_{15}\hat{\sigma}_i^- \end{array}, \tag{V.122}$$

where

$$\hat{\sigma}_i = 1_2 \otimes ... \otimes \sigma_i \otimes ...1_2 \tag{V.123}$$

are $L \times L$ matrices and σ_i the usual 2×2 Pauli matrices. In our case, we keep only five parameters a, b, c, d, e and we get

$$\begin{array}{ll} R_i^{11} = & \frac{1}{2}(a + b) + \frac{1}{2}(a - b)\hat{\sigma}_i^z + e\hat{\sigma}_i^x \\ R_i^{12} = & e + c\hat{\sigma}_i^+ + d\hat{\sigma}_i^- \\ R_i^{21} = & e + d\hat{\sigma}_i^+ + c\hat{\sigma}_i^- \\ R_i^{22} = & \frac{1}{2}(a + b) + \frac{1}{2}(b - a)\hat{\sigma}_i^z + e\hat{\sigma}_i^x \end{array} . \tag{V.124}$$

We rewrite the transfer matrix the symmetric sixteen-vertex model as

$$T = \text{Tr}_2 \prod_i^L \begin{pmatrix} a\, \hat{\sigma}_i^+ \hat{\sigma}_i^- + b\, \hat{\sigma}_i^- \hat{\sigma}_i^+ + e(\hat{\sigma}_i^+ + \hat{\sigma}_i^-) & e\,\text{I} + c\hat{\sigma}_i^+ + d\hat{\sigma}_i^- \\ e\,\text{I} + c\hat{\sigma}_i^- + d\hat{\sigma}_i^+ & b\, \hat{\sigma}_i^+ \hat{\sigma}_i^- + a\, \hat{\sigma}_i^- \hat{\sigma}_i^+ + e(\hat{\sigma}_i^+ + \hat{\sigma}_i^-)\,. \end{pmatrix} \tag{V.125}$$

The XYZ Hamiltonian eq. (IV.66) conserves parity such that terms of type

$$\langle + + |\exp[-\Delta\tau h(i, i+1)]| + -\rangle = e = 0 \tag{V.126}$$

in the Suzuki-Trotter decomposition vanish. In the sixteen-vertex problems one has to include these terms to fill the sixteen entries of the R-matrix. The quantum Hamiltonian must allow such terms, and, for simplicity, give them equal weight. The simplest Hamiltonian verifying this is the one of the XYZ chain in a transverse field:

$$h_{i,i+1} = J^x \hat{\sigma}_i^x \hat{\sigma}_{i+1}^x + J^y \hat{\sigma}_i^y \hat{\sigma}_{i+1}^y + J^z \hat{\sigma}_i^z \hat{\sigma}_{i+1}^z + h\hat{\sigma}_i^x \,. \tag{V.127}$$

This Hamiltonian gives non-parity conserving defects with weight

$$\langle + + |e^{-\Delta\tau h(i,i+1)}| + -\rangle = \left[h - e^{\frac{\Delta\tau}{2}\sqrt{(J^y - J^z)^2 + 16h^2}} \right] \frac{e^{-\frac{\Delta\tau}{4}(J^x + \sqrt{(J^y - J^z)^2 + 16h^2})}}{\sqrt{(J^y - J^z)^2 + 16h^2}} \tag{V.128}$$

$$= \langle + + |e^{-\Delta\tau h(i,i+1)}| - +\rangle = .. = \langle + - |e^{-\Delta\tau h(i,i+1)}| + +\rangle = e \,. \tag{V.129}$$

In our model, all these weights are equal to the weight of single charged defects, e. Complicated expressions of this kind relate the parameters of the classical model: a, b, c, d, e, with the ones of the quantum chain: J^x, J^y, J^z, h, $\Delta\tau$. Some function of a, b, c, d, e (as the parameters Δ and Γ for the eight-vertex model) should be found in such a way that, after taking the limit $\Delta\tau$, we find a well defined function of J^x, J^y, J^z, h. In section IV.4.4, we found how to relate the parameters of the classical model with the ones of the quantum chain for the eight-vertex model via the parameters Δ and Γ. The extension of this mapping would allows us to map the phase diagram of the sixteen-vertex model with the phase diagram of the quantum problem.

In order to rigorously prove the mapping, we have to compute $C_i = [R_i R_{i+1}, h_{i,i+1}]$ for all i and several system sizes L. Our goal is now to find J^x, J^y, J^z and h as functions of a, b, c, d and e. Then following Sutherland's ideas [249] we compute these commutators for $L = 2, 3, ...$ and try to find a relation between the parameters which do not depend on L. For small values of L, the commutators do not give us any useful equation. The calculations become rapidly too complicated for larger values of L and we did not converge to any concluding result proving the mapping.

Dynamics in $2D$ spin-ice

VI.1 Stochastic models

VI.1.1 Microscopic dynamics

From a fundamental point of view, the evolution of any system, both classical or quantum, is generated by its Hamiltonian. The Poisson brackets between a quantity A and the Hamiltonian H (or the commutators for a quantum system) give the time-evolution of A. For a macroscopic system a different approach has to be taken since the number of coupled differential equations to solve make the problem forbiddingly complex. One usually deals with *macroscopic* variables, constructed by averaging over microscopic constituents which evolve in 'microscopic' time scales t_μ. For instance, in hydrodynamics one describes the flow of a fluid by a density field instead by looking at the precise location and momentum of each particle. By doing so, one ends up with a theory for the study of the evolution of the system at large time scales $t_M \gg t_\mu$.

We are interested here in systems in contact with a thermal bath. The latter is made by a large number of degrees of freedom interacting with the system and providing thermal agitation. The microscopic state of the bath is unknown but we assume that it is in a thermal state (by definition a thermal bath is ergodic). Thus, the evolution of a system with Hamiltonian H coupled to a thermal bath is modelled by a *stochastic process*.

Consider the probability $P_\mu(t)$ to find the system on a state μ at time t. It is then assumed that the evolution of the system is a Markov process described by a *master equation*:

$$\frac{d}{dt}P_\mu(t) = \sum_{\sigma \neq \mu} \left[P_\sigma(t)W_{\sigma\mu} - P_\mu(t)W_{\mu\sigma} \right] \tag{VI.1}$$

where $W_{\sigma\mu}$ is the transition rate from state σ to state μ. In classical statistical lattice models, even though the Hamiltonian has been defined, one must equip the model with updating rules encoded in the transition rates. A kinetic model is defined by both its Hamiltonian and the dynamical

protocol chosen. As already mentioned when presenting Monte Carlo methods, a way to reach thermal equilibrium at long times is to have a dynamical process that satisfies detailed balance:

$$\frac{W_{\sigma\mu}}{W_{\mu\sigma}} = \exp\left(-\beta(E_\mu - E_\sigma)\right) \tag{VI.2}$$

where E_μ denotes the energy of state μ and β the inverse temperature of the bath. Then a choice must be done for the dynamical rules depending on the physical situation one plans to model. In the following we make use of single spin-flip *Monte Carlo dynamics* (see section III.4.1).

VI.1.2 Dynamical universality

At a first sight, the choice of the dynamical rules can seem quite arbitrary. However, the *dynamical universality hypothesis* claims that different updating protocols which share some common features display the same universal properties. A dynamical universality class is defined by: (i) the dimension of the order parameter; (ii) the dimension of the system; (iii) the symmetries of the model; (iv) the range of the interactions; (v) the conservation laws. Note that (i), (ii), (iii), (iv) define a universality class in equilibrium critical phenomena. The relevant characteristic of a dynamical process is the existence of *conserved quantities* which constraint the updates of the system. An extension of the effective Ginzburg-Landau-Wilson (GLW) field theory has been used for the study of dynamical collective phenomena. The classification of models in different dynamical universality classes follows from Hohenberg and Halperin's classical review article [117].

For concreteness, we focus on Z_2 symmetric problems with a scalar order parameter ϕ and described by the effective Hamiltonian:

$$H[\phi] = \int d\mathbf{x} \left[\frac{1}{2}(\nabla\phi(\mathbf{x}))^2 + \frac{1}{2}r\,\phi(\mathbf{x})^2 + \frac{1}{4}u\,\phi(\mathbf{x})^4\right] \tag{VI.3}$$

We shall only discuss here two classes of universality commonly encountered in the context of Ising-like problems:

(i) *Non-conserved order parameter (NCOP)* or *Model A* [117]: There is no conserved quantity during the evolution. In Ising spin systems, the system can be updated by single spin-flips. Two important examples are Monte Carlo dynamics [17] and Glauber dynamics [106]. These models are well suited to study of the evolution of a ferromagnet. A phenomenological GLW-like theory can be constructed from the assumption that, for NCOP dynamics, the evolution of the scalar order parameter ϕ is ruled by the minimisation the Hamiltonian in eq. (VI.3). The order parameters 'flows' towards the minimum of energy. This is encoded in the so-called *time-dependent Ginzburg-Landau equation*:

$$\frac{\partial}{\partial t}\phi(\mathbf{x}, t) = -\frac{\delta}{\delta\phi}H[\phi] + \eta(\mathbf{x}, t) \tag{VI.4}$$

where η is a stochastic function which models the presence of a thermal bath. The latter equation is a field-theoretic version of a Langevin equation where the Hamiltonian plays the role of the potential acting on a Brownian particle.

(ii) *Conserved order parameter (COP)* or *Model B* [117]: As the name suggests, the order parameter (the magnetisation) of the model must be conserved during the evolution. The system can be updated by flipping pairs of anti-parallel spins. This is known as Kawasaki dynamics and can also be implemented in a Monte Carlo scheme [17]. This kinetic model mimics the flow of particles in a lattice-gas. From the mapping between the Ising model and a lattice-gas, the conservation of the magnetisation is equivalent to the conservation of particles. A phenomenological evolution

equation can also be established in this case. Since the flux of ϕ must be conserved its evolution follows a continuity equation, also called *Cahn-Hilliard equation*:

$$\frac{\partial}{\partial t}\phi(\mathbf{x}, t) = -\vec{\nabla} \cdot \vec{J} + \eta(\mathbf{x}, t) \tag{VI.5}$$

where the current $\vec{J}$ is given by the gradient of the energy variation $-\vec{\nabla}\frac{\delta H}{\delta \phi}$.

The dynamical exponents associated to the same model described by H with NCOP and COP are different. The collective dynamical behaviour is independent of the choice of the updating rules, as soon as they belong to the same class.

VI.2   Dynamics through a phase transition

Consider a system in contact with a thermal bath. At equilibrium, the thermal state of the system is characterised by the external parameters of the bath, like the temperature or the external magnetic field. One can set the system in an out-of-equilibrium situation by suddenly changing this parameters. An infinitely rapid variation of the parameters is called a *quench*. By this simple protocol the system is forced to evolve in an out-of-equilibrium manner towards the equilibrium state characterised by the new external parameters. In particular, we are interested in quenches which make the system evolve through phase transitions.

VI.2.1   Coarsening

For concreteness we focus on Ising-like problems with Z_2 symmetry displaying a second order phase transition at some critical temperature T_c. Consider that the system is initially is its disordered phase ($T \ll T_c$) and then quenched into an ordered phase ($T > T_c$).

The system will then try to order in time. This will be done by growing locally regions of parallel spins. However, the symmetry is not breaking during the dynamics and there is no reason why the system should choose a positive or a negative magnetised equilibrium state. The tendency to order locally cannot be satisfied by the global constraints imposed by the symmetry of the problem. Regions where the order parameter take one among the two possible values grow in time. The competition between them leads to very *slow dynamics* and the time needed in order to reach equilibrium t_{eq} diverges in the thermodynamic limit. This slow dynamical process due to the symmetry between different phases is known as *coarsening* or *phase ordering dynamics* [49, 76].

Note that coarsening is a very usual situation in a large class of systems. Volcanic rocks, like granite, made by different materials, have grains of different size depending on the cooling conditions of the lava. Different cooling procedures such as quenches or annealing are commonly used in material science to change the properties of metallic alloys. Coarsening has been studied in a large diversity of systems as binary liquid mixtures [241], soap froths [257], superconductors [222], etc.

Consider the infinite temperature state of the $2D$ Ising model on an $L \times L$ square lattice as an initial configuration. After the quench into its FM phase, the interactions will tend to order the spins locally by aligning nearest-neighbours. This will grow domains of spins pointing 'up' and 'down' as shown in Fig. VI.1. By symmetry, the number of spins up and down should be equal. In order to equilibrate one should correlate all the spins in the system, i.e. grow a domain of the size of the system. Similarly to what happens at the vicinity of a critical point, the equilibration of the system needs periods of time of the order of L^{z_d}. This protocol provides a simple way to prepare out-of-equilibrium states since, for large enough systems the equilibration time is very large. Note
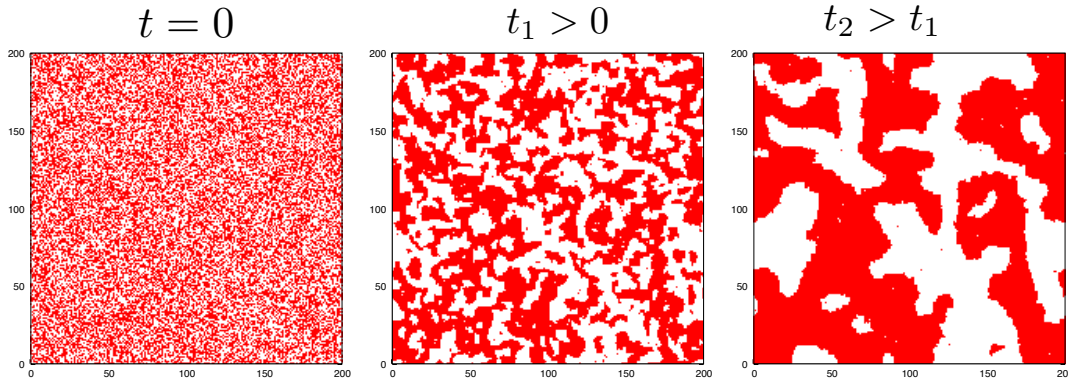
Figure VI.1: Snapshots of the $2D$ Ising model after a quench from infinite temperature to a subcritical temperature. Spins up and down are represented by red and white dots. Red and white regions grow in time.

that this exponent z_d is *a priori* different from the dynamical critical exponent z associated with the divergence of the correlation time at a critical point.

VI.2.2 Dynamical scaling hypothesis

The relaxation of a system after a quench from a disordered configuration into an ordered phase exhibits the growth of ordered regions characterised by a typical *growing length R*. The *dynamical scaling hypothesis* asserts that, after some transient time, the domain pattern remains statistically identical during the time evolution. In the time regime where dynamical scaling applies (from now on called the *coarsening regime*) all the length scales become time-independent when properly rescaled by $R(t)$, the unique relevant length scale in the system. This looks similar to Widom's scaling hypothesis for equilibrium critical phenomena: the key notion of scale invariance is extended to time evolution.

In view of our work on $2D$ spin-ice, we focus our discussion on NCOP dynamics of the Monte Carlo type. A quantitative understanding of coarsening dynamics starts by the computation of time-dependent observables such as the time dependent magnetisation

$$M(t) = \frac{1}{L^2} \sum_{i=1}^{L^2} S_i(t) \tag{VI.6}$$

and the *two-point self correlation functions*

$$C(t, t_w) = \frac{1}{L^2} \sum_{i=1}^{L^2} \langle S_i(t) S_i(t_w) \rangle , \quad t > t_w \tag{VI.7}$$

$$G(r, t) = \frac{1}{L^2} \sum_{i=1}^{L^2} \langle S_i(t) S_j(t) \rangle \tag{VI.8}$$

where the brackets denote an average over independent realisations of the dynamics [1], $S_i(t)$ is the value of the spin on site i at time t and r is the distance between sites i and j. From these quantities one can get an estimation of the equilibration time t_{eq}. Dynamical scaling states that, after a long

---

1. In practice, it corresponds to running independent simulations using different random number generators.

enough period of time such that $R(t) \gg \xi$ (where ξ is the equilibrium correlation length), $r \gg \xi$ and $r/R(t) < \infty$:

$$C(t, t_w) \simeq M_{eq}^2 \, F_C \left(\frac{R(t)}{R(t_w)} \right), \qquad \text{(VI.9)}$$

$$G(r, t) \simeq M_{eq}^2 \, F_G \left(\frac{r}{R(t)} \right). \qquad \text{(VI.10)}$$

Note that dynamical scaling has not been proved in general. In static critical phenomena, scaling is justified from scale invariance and the RG theory. However, the application of standard RG methods is much more subtle for phase ordering dynamics because of their non-perturbative character [49]. An RG theory providing a justification of the dynamic scaling hypothesis is still lacking. It is usually assumed, and proved in a few cases (see below), that R grows as a power law of time

$$R(t) \simeq \lambda \, t^{1/z_d} \qquad \text{(VI.11)}$$

where z_d is the dynamical exponent defined by $t_{eq} \sim L^{z_d}$ and λ is a non-universal factor which depends on temperature. Since this length scale is macroscopic in the coarsening regime, one expects that the exponent z_d will be independent of the microscopic specificities of the model and defines a dynamical universality class. As we discussed in the previous section, for NCOP dynamics we expect to get a single value $z_d = 1/2$ for a class of different systems.

Dynamical scaling and the power law growth of R are strongly supported by many numerical simulations and a fewer analytical treatments. The more relevant examples for our purposes are:

(i) *Exact*. In $1D$ systems exact solutions are available [48]. In the kinetic Ising chain with Glauber dynamics domains grow as $t^{1/2}$ and dynamical scaling is obeyed.

(ii) *Mean field*. In the $O(N)$ model evolving accordingly to the time-dependent Ginzburg Landau equation (VI.4), exact calculations can be done in the large N limit [74]. The typical size of the domains also grows as $t^{1/2}$.

(iii) *Allen-Cahn equation*. In the thermodynamic limit, equilibrium is never reached. Instead, there is a coexistence of ordered regions of order parameter $\phi = \pm 1$ separated by *domain walls*. These are *topological defects* which carry an excess of energy. The relaxation of the system proceeds through the annihilation of topological defects. A domain wall can be described by a unit vector $\vec{n}$ orthogonal to the surface of the wall and pointing in the direction of increasing ϕ (in the field-theory formulation). At zero temperature, and close to a domain wall, the NCOP evolution equation (VI.4) takes the form

$$\vec{v} = \frac{\partial \vec{n}}{\partial t} = -[\vec{\nabla} \cdot \vec{n}]\vec{n} \qquad \text{(VI.12)}$$

where $\vec{n}$ is a unit vector normal to the domain wall and $\vec{v}$ is the wall velocity. This is the so-called Allen-Cahn equation [5]. For systems like the $2D$ Ising model with well defined walls carrying a surface tension, the coarsening dynamics proceed through the minimisation of its local curvature, hence called *curvature driven* coarsening. This tends to create smooth surfaces between ordered regions (as shown in Fig VI.1).

Consider a spherical domain in a d-dimensional space. Its curvature is $(d-1)/R$ such that the Allen-Cahn equation becomes: $\dot{R}(t) = (1-d)/R$ which implies that the spherical domain decreases with the same $t^{1/2}$ power law.

(iv) *Scaling arguments*. Inspired by the latter result for a single spherical domain one estimates

that the evolution of the growing length for NCOP dynamics follows the differential equation:

$$\frac{dR(t)}{dt}\tau(R,T) = \frac{1}{R} \qquad\qquad (VI.13)$$

where τ is the characteristic time to flip a spin in the domain wall. Depending on the behaviour of $\tau(R,T)$ the growing length can follow different laws [155, 238]. One recovers the $t^{1/2}$ growth for systems which do not involve energy barriers scaling with R during the coarsening, i.e. τ is a positive constant. For systems which need to overcome energy barriers growing with the size of the domain the situation is more involved. For instance, in models with competing interactions such as the Ising model with nearest-neighbour (NN) ferromagnetic interactions and next-to-nearest (NNN) antiferromagnetic ones J_1 and J_2 respectively. For this model in three dimensions, the energy barrier to remove an edge of spins in the domain wall is $\Delta E(L) = 4(L+1)J_2$. By an Arrhenius argument one can estimate the time needed to overcome this barrier by $\tau \sim \exp(\beta\Delta E(L))$. This simple argument gives a logarithmic growth $R(t) \sim \ln t$ which has been supported by numerical simulations [238] The same arguments based on an spherical domain can be applied to COP dynamics and give a $R(t) \sim t^{1/3}$ growth [121], in agreement with numerical simulations and RG calculations.

(v) *Geometrical properties.* The distribution of hull-enclosed areas of $2D$ Ising-like models with curvature driven dynamics can be computed analytically. Thus providing a strong argument supporting dynamical scaling [239, 10].

VI.2.3 Topological defects

The reader has probably remarked that the central object in the previous discussion were the domain walls. Their motion characterises completely the coarsening regime. Domain walls are the simplest example of topologically stable structures (topological defects). Local fluctuations cannot destroy them, their stability is responsible for slow dynamics.

Topological defects can be spatially extended, such as domain walls, or localised, such as vortices in the $2D$ XY model. In general, extended topological defects arise when $n < d$, where n is the dimension of the order parameter. Even for localised defects, one usually associates a length scale to topological defects such as a typical vortex anti-vortex distance. Coarsening proceeds by shrinking (i.e. annihilating) topological defects. The decay of topological defects after cooling a macroscopic system across a phase transition is also of great importance for cosmology [261].

In the spin-ice model, one expects two kind of topological defects: (i) domain walls between different ordered regions; (ii) defects in the form of charged vertices (monopoles). At high temperature monopoles proliferate. After a quench into an ordered phase they are going to move and annihilate. At the same time, ordered regions will grow. The evolution of extended defects (domain walls) proceed through the reduction of the area of individual domains via, for instance, curvature driven dynamics (e.g. $R \sim t^{-1/2}$). A different mechanism should take place in order to annihilate localised defects (vortices in the XY model, monopoles in spin-ice). Two defects of opposite vorticity/charge should meet in the appropriate way to annihilate. It means that, in spin-ice, two monopoles sitting in neighbouring sites can annihilate only if they share a spin that, if flipped, recovers the ice-rules. Note that the orientation between localised defects in the $2D$ XY model does not play any role in the annihilation rate of vortices. The interplay between these to processes (domain growth and 'directional' annihilation of defects) has to be analysed in detail in order to understand spin-ice dynamics. In the following pages we tackle this problem using Monte Carlo simulations.

VI.3   Model and methods

Here we address the dynamics of $2D$ spin-ice models with only short-range interactions, i.e. a vertex model. For the sake of simplicity we focus on thermal quenches in the $2D$ square lattice spin ice model built as a stochastic extension of the six-vertex model. We consider an $L \times L$ square lattice $\mathcal{V}$ with unit spacing and periodic boundary conditions (PBC). The model has been already defined on section IV.7. For clarity, let us recall some notations. We assign a Boltzmann weight $\omega_k \propto e^{-\beta \epsilon_k}$ to each of the $k = 1, \ldots, 2^4$ four-arrow vertex configurations. The energy is $H = \sum_{k=1}^{16} \epsilon_k n_k$, where n_k is the number of vertices of type k. We set $\omega_1 = \omega_2 = a$, $\omega_3 = \omega_4 = b$, $\omega_5 = \omega_6 = c$ for the ice-rule vertices and $\omega_7 = \omega_8 = d$, $\omega_9 = ... = \omega_{16} = e$ for the 2-fold and 1-fold defects, respectively, ensuring invariance under reversal of all arrows (see Fig. VI.2). Henceforth we measure the weights in units of c.
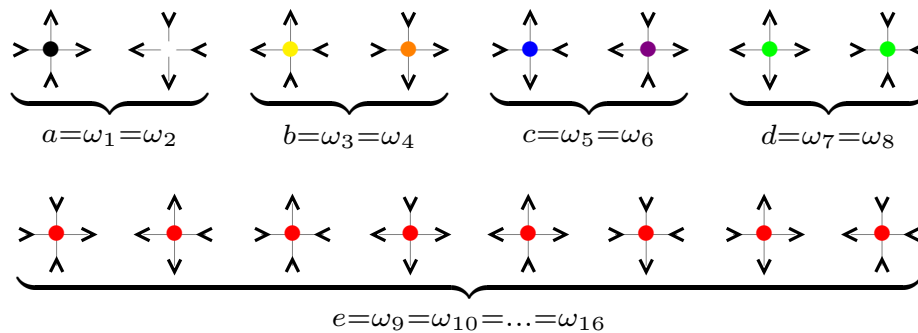

Figure VI.2: The sixteen vertex configurations on the $2D$ square lattice and their weights. The first six vertices verify the ice-rule. The next pair completes the eight-vertex model and have charge $q = \pm 2$. The last eight vertices have charge $q = \pm 1$. This color code is used in Fig. VI.12.

VI.3.1   Updating rules

We use a rejection-free continuous-time Monte Carlo (MC) algorithm, with local spin-flip updates and non-conserved order parameter as described in section III.4.2. The details of the algorithm are given in appendix A. This allows for thermally-activated creation of defects. The longest time reached with this method, once translated in terms of usual MC sweeps, is of the order of 10^{25} MCs, a scale that is unreachable with usual Metropolis algorithms. This allows us to analyse different dynamic regimes.

In spin-ice materials, and in artificial $2D$ realisations in particular, the dynamics are expected to be of the single spin-flip kind without any conserved quantity. The motion of the defects can be visualised by microscopy in ASI samples [153, 178] and agree with this picture. Moreover, our dynamics are ergodic for both fixed and periodic boundary conditions. One could think about a dynamical rule which preserves the ice rules and do not create defects, i.e. a dynamical six-vertex model. With PBC one needs to introduce loop updates of any size and winding number in order to sample the whole phase space. Such a dynamics has been studied in the 3-colouring model on the hexagonal lattice and leads to glassy behaviour [65]. Another possible local dynamics which preserve the ice rules would be to update the system by small loops made by four spins around a square plaquette. These dynamics are not ergodic for PBC but they are, for instance, for the six-vertex model with DWBC (defined in Fig. IV.12). For the spin-ice problem, these two possible dynamical models seems quite artificial and do not allows us to study defects' motion in the way that it is observed to occur in the laboratory.

A completely disordered initial condition is fixed by placing arrows at random at each edge of the square lattice $\mathcal{V}$. If we impose PBC it follows that the number of positive and negative charges is identical. The system remains globally neutral during the evolution, since the system is updated by single spin flips which cannot create any excess of charge.

VI.3.2   Observables

We now turn to the dissipative stochastic dynamics of an equilibrium initial configuration at $a = b = d = 1$ (i.e. $T \to \infty$) after a quench to sets of parameters in the (i) disordered, (ii) FM, and (iii) AF phases. In case (i) the system should equilibrate easily but the question remains as to whether it gets blocked in metastable states with a large density of defects. In cases (ii) and (iii) the interactions between the spins, mediated by the choice of vertex weights, should create ordered domains, FM or AF. The quantitative characterisation of growth in the ordering processes is given by two possibly different growing lengths extracted from correlation functions along orthogonal directions $\parallel$ and $\perp$ that we identify.

The relaxation dynamics of clean lattice systems are usually studied in terms of time-dependent macroscopic observables averaged over different realisations of the dynamics (denoted by $\langle ... \rangle$). In particular, we compute the following quantities:

(i) The *density of vertices* of each type:

$$\langle n_a(t) \rangle = \langle n_1(t) + n_2(t) \rangle \, , \ \ \langle n_b(t) \rangle = \langle n_3(t) + n_4(t) \rangle \, , \ \ \langle n_c(t) \rangle = \langle n_5(t) + n_6(t) \rangle, \quad \text{(VI.14)}$$

$$\langle n_d(t) \rangle = \langle n_7(t) + n_8(t) \rangle \, , \ \ \langle n_e(t) \rangle = \langle \sum_{k=9}^{16} n_k(t) \rangle. \quad \text{(VI.15)}$$

(ii) The *two-times self-correlation function* defined by:

$$C(t, t_w) = \frac{1}{2L^2} \sum_{(i,j) \in \hat{\mathcal{V}}} \langle S_{(i,j)}(t) S_{(i,j)}(t_w) \rangle \quad \text{(VI.16)}$$

with $t > t_w$. The indices (i,j) denote the coordinates of a spin in the medial lattice $\hat{\mathcal{V}}$ (i.e. the vertices of the square lattice shown in red in Fig. VI.3).

(iii) The *space-time correlation functions*. The definition of the relevant correlation functions between different points in the lattice is not straightforward when we introduce some anisotropy in the model (for example by choosing $a > b$). For convenience, we define a set of correlation functions between spins in different orientations: along the Cartesian axis $\vec{u}_x$ and $\vec{u}_y$ and along the $\pi/4$-rotated axis $\vec{u}_\parallel$ and $\vec{u}_\perp$ (see Fig. VI.3). The space-time self correlation functions along the $\vec{u}_\parallel$ and $\vec{u}_\perp$ are defined by

$$G^{\parallel}(r = n, t) = \frac{1}{L^2} \sum_{(i,j) \in \hat{\mathcal{V}}} \langle S_{(i,j)} S_{(i,j+n)} \rangle \quad \text{(VI.17)}$$

$$G^{\perp}(r = n, t) = \frac{1}{L^2} \sum_{(i,j) \in \hat{\mathcal{V}}} \langle S_{(i,j)} S_{(i+n,j)} \rangle \quad \text{(VI.18)}$$

and along the $\vec{u}_x$ and $\vec{u}_y$ axis by

$$G^x(r = \sqrt{2}n, t) = \frac{1}{L^2} \sum_{(i,j) \in \hat{\mathcal{V}}} \langle S_{(i,j)} S_{(i+n,j+n)} \rangle \quad \text{(VI.19)}$$

$$G^y(r = \sqrt{2}n, t) = \frac{1}{L^2} \sum_{(i,j) \in \hat{\mathcal{V}}} \langle S_{(i,j)} S_{(i-n,j+n)} \rangle \tag{VI.20}$$

where $n \in \mathbb{N}$.

(iv) The *growing lengths* $L^{\parallel,\perp}(t)$ along $\vec{u}_\parallel$ and $\vec{u}_\perp$. They are extracted numerically from the decay of the space-time correlations by:

$$G^{\parallel,\perp} \left[L^{\parallel,\perp}(t), t \right] = 0.3 . \tag{VI.21}$$

More refined analysis of $G^{\parallel,\perp}$ lead to equivalent results for $L^{\parallel,\perp}(t)$ within our numerical precision.
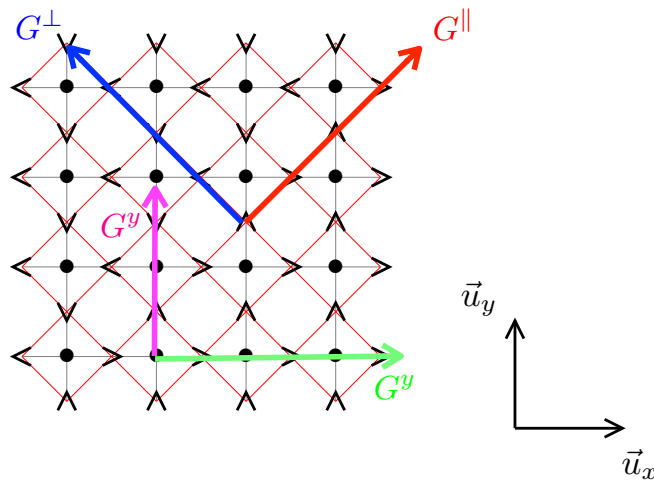

Figure VI.3: Correlations between spins along different directions. The lattice $\mathcal{V}$ made of L^2 vertices is shown in grey. Its medial lattice $\hat{\mathcal{V}}$ made of $2L^2$ spins is shown in red.

VI.4   Quench into the PM phase

In the following, we study the evolution of the model after a quench from a random initial condition ($a = b = c = d = e = 1$) into a different PM state, typically close to the SL critical phase ($a = b = c = 1$ and $d, e \ll 1$). In the initial configurations defects are common. We are interested here in the mechanisms leading to their annihilation.

VI.4.1   Dynamical arrest

For the sake of simplicity, let us set $d = e$. Figure VI.4 displays the time-dependent density of defects, $n_d(t)$, defined as the number of vertices of type 7-16 divided by L^2, after an infinitely rapid quench to $a = b = 1$ and $d = 10^{-8}, \ldots, 10^{-1}$ of samples with linear size $L = 50$ (a) and $L = 100$ (b). These data have been averaged over 10^3 runs.

For large d (black dark curves) $n_d(t)$ quickly saturates to its equilibrium value. Numerical estimates of the equilibrium density of defects, n_d^{eq}, for $d = 10^{-1}$, 10^{-2}, 10^{-3} are shown with dotted black lines. As expected n_d^{eq} is an intensive quantity that increases with d. It does not depend upon the system size for $L \geq 50$ and $d > 10^{-3}$.

For small d ($\lesssim 10^{-4}$) the systems do not reach equilibrium within the simulated time-window. After a first decay, $n_d(t)$ gets frozen at approximately constant values before relaxing, in a much

longer time-scale, to a configuration in which only two defects are present in our small samples. Note that in order to distinguish the $d-$dependent equilibrium values for these very small ds one would need to equilibrate much larger samples. Unfortunately, the special purpose loop algorithm devised for the 6 vertex model does not apply to our generalized case. For our working sizes we see asymptotes taking the value $2/L^2$ on average.
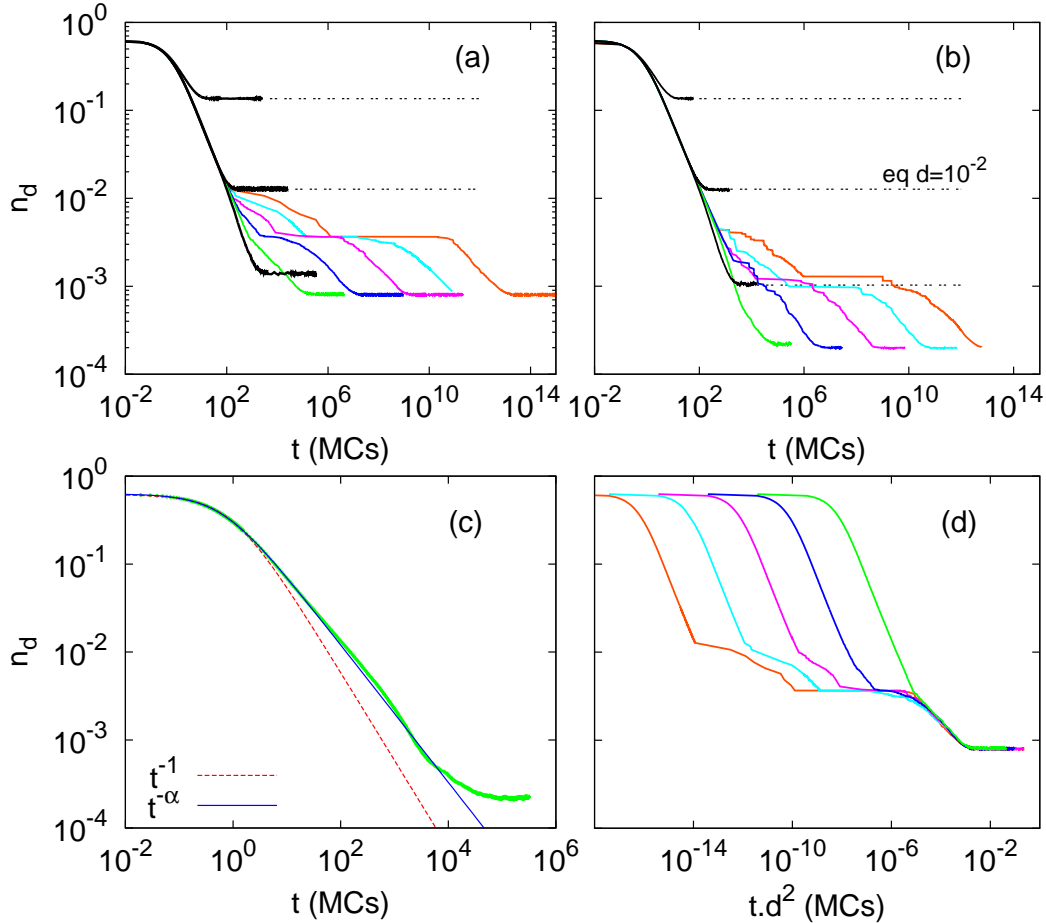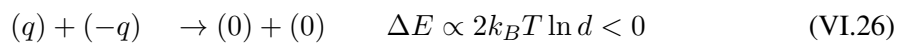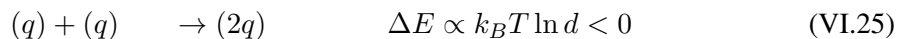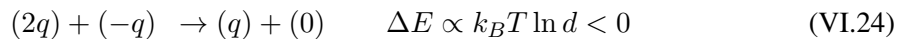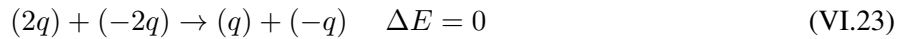

Figure VI.4: Time-dependent density of defects, $n_d(t)$, after a quench from $T \to \infty$ to $a = b = 1$ and $d = 10^{-1}, 10^{-2}, \dots, 10^{-8}$. (a) $L = 50$ and (b) $L = 100$. The black curves are for $d = 10^{-1}, 10^{-2}, 10^{-3}$. The grey (color) curves are for smaller values of d decreasing from left to right. (c) Short time behaviour in the case $d = 10^{-4}$ and $L = 100$ confronted to the decay $\rho_0/(1 + \Omega t)$ (dashed curve) [59] and the fit $\rho_0/(1 + \Omega t)^\alpha$ with $\alpha = 0.78$ (blue plain curve). (d) Test of scaling with td^2 for systems with $L = 50$.

The initial decay of n_d is fitted by a power-law decay

$$n(t) = \frac{\rho_0}{(1 + \Omega t)^\alpha} \tag{VI.22}$$

with $\alpha \simeq 0.78$ over three orders of magnitude in t and n_d, as shown in panel (c) in Fig. VI.4. The power-law is shown with a solid blue line in the figure together with the data for $d = 10^{-4}$ and $L = 100$. This law is different from the simple t^{-1} decay found with a mean-field approximation to a diffusion-reaction model shown with a dashed red line in the same figure [59]. The exponent α depends on the parameters of the system in a non trivial way that we shall discuss in later in sections VI.4.2 and VI.5.1. Finite size effects will also be discussed in the next subsection.

The decay is next arrested at a metastable density of defects $n_d^{pl} \approx 10/L^2$. The plateau lasts longer for smaller d and its height is roughly independent of d. This feature is reminiscent of what was found numerically in dipolar spin-ice although contrary to the modelling in [59] our model does not have long-range interactions. At the entrance to the plateau the system has between 3 and 4 times more defects of type 7-8 than those of type 9-16 which are only 2 or 3. Therefore, in the final decay from the plateau to the asymptotic value $n_d \approx 2/L^2$ the remaining doubly charged defects have to disappear. This may be due to two kinds of processes. In terms of a reaction-diffusion model the relevant processes taking place with their energetic gain/cost are:

$$(2q) + (-2q) \rightarrow (q) + (-q) \quad \Delta E = 0 \tag{VI.23}$$

$$(2q) + (-q) \;\; \rightarrow (q) + (0) \quad \Delta E \propto k_B T \ln d < 0 \tag{VI.24}$$

$$(q) + (q) \qquad \rightarrow (2q) \qquad \Delta E \propto k_B T \ln d < 0 \tag{VI.25}$$

$$(q) + (-q) \;\; \rightarrow (0) + (0) \quad \Delta E \propto 2k_B T \ln d < 0 \tag{VI.26}$$

In the first case, two defects of type 7 and 8 meet to produce two singly (and oppositely) charged defects with no energetic gain. The total density of defects remains constant after this reaction. An example of the second case is a reaction in which a defect of type 7 (charge $q = 2$) meets one of type 14 (charge $q = -1$) to produce a defect of type 10 (charge $q = 1$) and a spin-ice vertex with no charge. This corresponds to an energetic gain ΔE. Note that the number of single charged defects has not been modified in this process but the number of doubly charged defects diminished and so did the total number of defects. In both cases the remaining defects need to diffuse, a process with no energetic cost, to find a partner and annihilate. From inspection of the individual runs and the densities of single and doubly charged defects we see that the second process is favoured, as also suggested by the energetic gain.

The time regime where the density of defects finally leaves the plateau and reaches its equilibrium value, is characterised by a scaling of the dynamic curves with the scaling variable td^2 [56] as shown in Fig. [VI.4 (d)] for the $L = 50$ data. This scaling strongly suggests that the relevant time scale in the system is the typical time needed to create a pair of single defects. From an ice-rule state, the energy change associated with the reaction : $(0) + (0) \rightarrow (q) + (-q)$ is $\Delta E \propto -k_B T \ln d^2$. Then, by a simple Arrhenius argument, the typical time to overcome this barrier is $\propto \exp(\beta \Delta E)$ giving the before mentioned time scaling $\tau \propto d^{-2}$.

VI.4.2   Time evolution for $d < e$

In real spin-ice realisations, both in $2D$ and $3D$, the energy associated to doubly charged defects d is larger than the one of single charged defects e. One should then study in detail the effect of $d < e$ in the time evolution of the model.

At a first sight, one could think that the emergence of the dynamical plateau in the density of defects discussed in the previous section, is due to the presence of doubly charged defects d. The reaction in eq. (VI.25) is accompanied by an energy gain when $d = e$, meaning that the creation of doubly charged vertices are favoured dynamically. Then, d-vertices get stuck, since any update of one of its legs will break the vertex into two single charged defects accordingly to $(2q) \rightarrow (q) + (q)$, at an energy cost $\Delta E \propto -k_B T \ln d > 0$.

When $d < e$ the situation changes and the annihilation of double defects can be favoured. The

energy difference associated with the previous reactions is:

$$(2q) + (-2q) \rightarrow (q) + (-q) \quad \Delta E \propto -2k_BT \ln(e/d) \quad \text{(VI.27)}$$
$$(2q) + (-q) \rightarrow (q) + (0) \quad \Delta E \propto k_BT \ln d < 0 \quad \text{(VI.28)}$$
$$(q) + (q) \rightarrow (2q) \quad \Delta E \propto k_BT \ln(e^2/d) \quad \text{(VI.29)}$$
$$(q) + (-q) \rightarrow (0) + (0) \quad \Delta E \propto 2k_BT \ln e < 0. \quad \text{(VI.30)}$$

One should differentiate three cases:

(i) $d = e$: All the defects have the same weight. The decay of d-defects into two e-defects following the reaction $(2q) \rightarrow (q) + (q)$ is done by at an energy cost $\Delta E \propto -k_BT \ln d > 0$.

(ii) $d < e$, $d > e^2$: Single charged defects e are slightly more favourable than d-defects. However, the decay of d-defects into two e-defects still needs to overcome an energy barrier $\Delta E \propto -k_BT \ln(e^2/d) > 0$.

(iii) $d < e^2$: Doubly charged defects are very unfavourable. The decay of d-defects now takes places spontaneously since leads to an energy gain $\Delta E \propto -k_BT \ln(e^2/d) < 0$.

We now investigate the dynamical consequences of choosing different weights for the two kind of defects. In particular the fate of the dynamical plateau when doubly charged defects are rapidly suppressed.

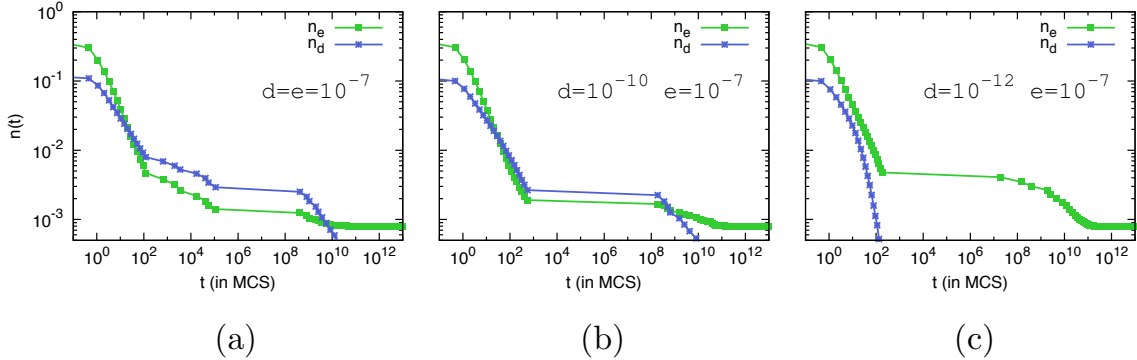(a)   (b)   (c)

Figure VI.5: Decay of the density of vertices for $a = b = c = 1$ and $L = 50$ averaged over 500 realisations. The weights of the defects are indicated on the figure and for all of them $e^2 < d$ which favours the creation of doubly charged defects. (a) $e = d$ and $\ln(e^2/d)/\ln(10) = -7$. (b) $e > d$ and $\ln(e^2/d)/\ln(10) = -4$. (c) $e > d$ and $\ln(e^2/d)/\ln(10) = -2$.

As shown in Fig. VI.5, the decay of n_e freezes at a metastable density for $d < e$ verifying $d > e^2$. For large enough values of d $\left(\ln(d/e^2)/\ln(10) \gtrsim 2\right)$ the density of e-vertices n_e is smaller than n_d in the plateau regime. For $\ln(d/e^2)/\ln(10) \lesssim 2$ d-vertices rapidly disappear and n_e remains larger than n_d for all times. After a rapid decay, n_e gets frozen into a metastable state for long periods of time before it finally reaches its equilibrium value. Hence, one can conclude that the presence of d-defects in the system is not responsible for the emergence of the dynamical plateau.

The evolution of the defect's density for $d = e^2$ is shown in Fig. VI.6. The density of e-defects remains larger than n_d during the whole evolution for the three sets of parameters. Similarly to what was observed for $e = d$, the system gets blocked into a metastable plateau only for small enough values of $e \lesssim 10^{-4}$, and the existence of this arrested dynamical regime is not due to the presence of d-vertices. The evolution of n_e and n_d for $d < e^2$ shown in Fig. VI.7 supports

Figure VI.6: Time evolution of the density of defects n_e and n_d for $a = b = c = 1$ and $L = 50$ averaged over 500 realisations. The weights of the defects are indicated on the figure and verify $e^2 = d$.

this observation. Although n_d rapidly vanishes, n_e exhibits a dynamical arrest at a constant value which, in principle, can depend on the weight of the vertices in a complicated manner.
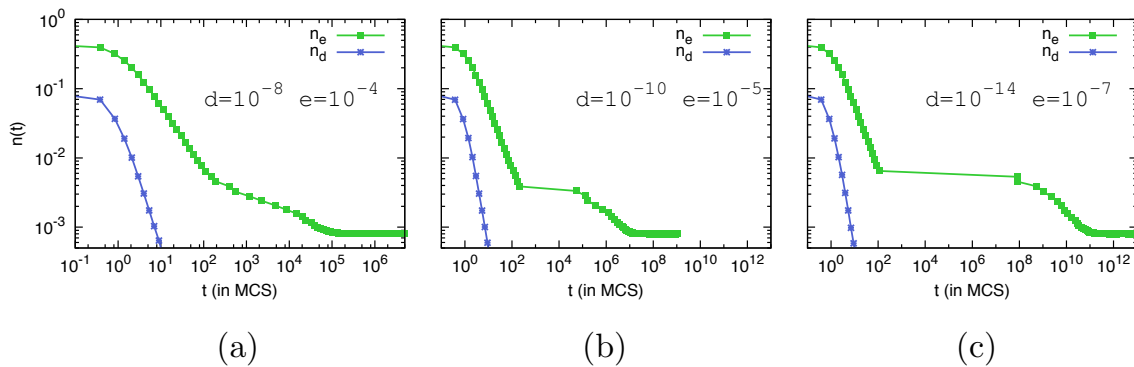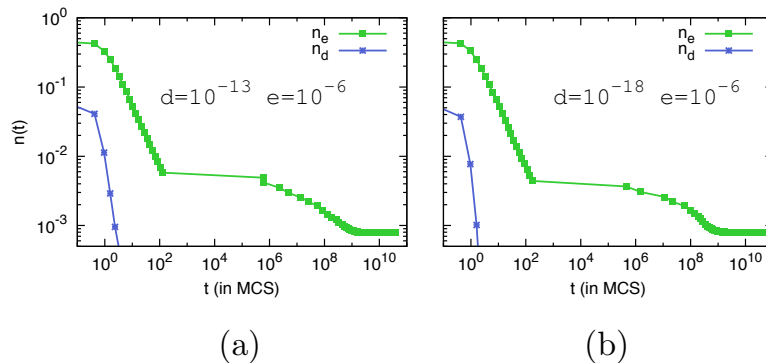

Figure VI.7: Time evolution of the density of defects n_e and n_d for $a = b = c = 1$ and $L = 50$ averaged over 500 realisations. The weights of the defects are indicated on the figure and verify $e^2 > d$.

In order to understand the emergence of the frozen regime we repeated the numerical experiment with fixed boundary conditions (FBC): the state of each spin on the boundary is kept fixed from the initial configuration during the simulation. One has to be careful when choosing the boundary conditions and make sure that these do not induce a polarisation of the sample. Indeed, polarised boundary conditions such as the DWBC can have dynamical consequences such as the drift of magnetic monopoles. These effects should be studied independently.

In the initial high temperature state, defects of any kind populate the system. After the quench, the relaxation proceeds through the annihilation of oppositely charged defects. In order to do so, defects have to meet in the appropriate manner, meaning that the reversal of the spin shared by both of them restores the ice rule. In the reaction-diffusion language this corresponds to the process $(q) + (-q) \rightarrow (0) + (0)$. Two defects of opposite charge ± 1 can also meet in the 'wrong' way and create a pair of doubly charged defects accordingly to: $(q) + (-q) \rightarrow (2q) + (-2q)$ by a single spin-flip. Starting from a completely ordered FM configuration, one can create a pair of defects by flipping a string of spins. The string can wind around the lattice by PBC. Then, in order to annihilate these pair of defects one must flip back all the spins in the string. One can think about this kind of extended structures to be responsible of the slowing down of the dynamics. If so, the evolution of the system with FBC, where winding strings are absent, should not present a

dynamical plateau. As shown in Fig. [VI.8 (a)] this is not the case: a metastable plateau in the evolution of the density of defects appears with FBC as well. This is due to the fact that, in the presence of more than a single pair of defects, there is always a way to annihilate all the defects without going through the boundaries of the lattice. In this sense, the dynamics do not feel the nature of the boundary conditions.

It is interesting to remark here the presence of a 'bump' in the evolution of the density of defects in the time regime in between the rapid annihilation and the plateau (see Fig. VI.8 (a)]). This seems to be a particularity of $e = d$ together with PBC. In all our simulations we observed that the bump desappears as soon as one among these two conditions is not fulfilled. This behaviour is not well understood yet.
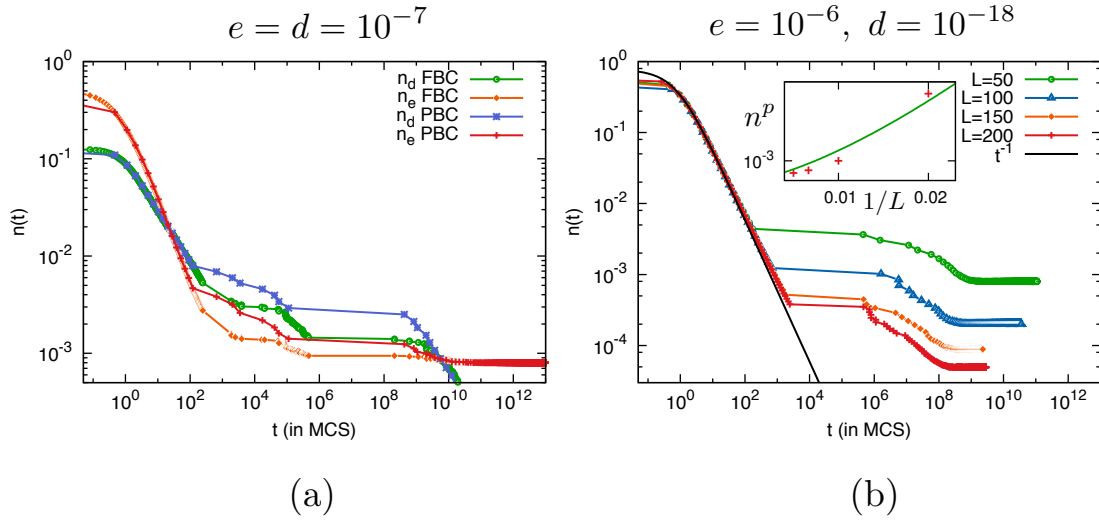

Figure VI.8: (a) Time evolution of the density of defects for different boundary conditions: periodic boundary conditions (PBC) and fixed boundary conditions (FBC). The data plotted were obtained from CTMC simulations by averaging over 500 realisations of the dynamics with $L = 50$, $a = b = c = 1$ and $d = e = 10^{-7}$. (b) Plateau for different system sizes with PBC at $d = 10^{-18}$, $e = 10^{-6}$, $a = b = c = 1$. For $L = 100, 150$, and 200 the data have been obtained after averaging over 300 runs, and over 1000 runs for $L = 50$. The decay of n is confronted to $\rho_0/(1 + \Omega t)$ (black line). The inset shows the height of the plateau n^p as a function of the inverse linear size $1/L$. The dots obtained for $L = 50, 100, 150, 200$ are confronted to an algebraic decay $(1/L)^\kappa$ with $\kappa = 1.4$.

As already mentioned in the previous section, the metastable density of defects for $d = e$ is $n_d \approx 10/L^2$, which vanishes at the thermodynamic limit. One should then ask wether the observed metastable density is a finite size effect or not. In order to ask this question we simulated systems of different sizes under the same conditions. The results obtained are shown in Fig. [VI.8 (b)]. The height of the plateau n^p and the time spend by the system in this regime decreases with the size of the system, as shown in the inset Fig. [VI.8 (b)]. The data can be roughly fitted by a power-law decay $n^p = L^{-\kappa}$. This suggests that the dynamical arrest observed in the simulations is a finite size effect which do not last in the thermodynamic limit. The evaluation of the plateau height is subject to strong fluctuations in such a way that the exponent $\kappa = 1.4$ has to be taken as a 'guide to the eye' rather than a precise measure. In order to get more precise estimation of the size dependence of the defects' density in the plateau, one should simulate larger systems. Our analysis gives, however, a strong indication that the plateau is due to the finiteness of the samples.

The evolution of n_e shown in Fig. [VI.8 (b)] has been fitted by a diffusive decay $\rho_0/(1 + \Omega t)$. Interestingly, when $d < e^2$ the decay of the defects' density agrees with the diffusive picture proposed in [59] for $3D$ spin ice. The presence of d-defects modifies this behaviour and makes the decay slower (see Fig. [VI.4 (c)]). The density of defects scales asymptotically as $n_e \sim t^{-1}$ and gives rise to a typical growing length

$$R(t) \simeq \frac{1}{\sqrt{n_e(t)}} \sim t^{1/2} \, . \tag{VI.31}$$

A few comments about this growing length should be done here. In the $2D$ XY model, a growth $R(t) \sim (t/\ln t)^{1/2}$, has been found. Scaling arguments given by Yurke et. al [279] for the $2D$ XY model, show that logarithmic corrections should be included in order to take into account the presence of vortices. The $t^{1/2}$ part of the growth law comes from the soft domain walls which evolve by curvature driven dynamics. The $\ln$ corrections come from the presence of vortices, which slows down the dynamics. Here we do not expect the presence of extended defects, however a $t^{1/2}$ growth arises. If we omit the logarithmic correction due to vortices of the XY model we get the scaling $n(t) \sim t^{-1}$ and $R(t) \sim t^{1/2}$.

VI.4.3 Ageing

In Fig. VI.9 we show the decay of the two-time correlation function C as a function of the time difference $t - t_w$ for different values of t_w shown in the key. One can distinguish different dynamical regimes from these curves. For short times, as long as neighbouring monopoles annihilate in a few MCS the correlations are time translational invariant (as in equilibrium) and close to one. At later times time-translational invariance is lost and the system exhibits *ageing*. The longer the waiting-time t_w is, the slower the decay to the correlations will be. The behaviour of C for $e < 10^{-4}$ characterises the metastable state. As shown in Fig. [VI.9 (b)], for waiting times t_w shorter than the time associated with the dynamical arrest, the correlations seem to indicate that the system is at equilibrium after $t \approx 10^7$ MCS. One has to wait until $\approx 10^{12}$ MCs to reach the equilibrium state. For larger times, the correlations develop a plateau reminiscent of the metastable density of defects, meaning that the system is not in thermal equilibrium at 10^7 MCS. The system do not evolve during a period of time in between $\approx 10^7$ and 10^9. As argued before, this might be due to finite size simulations.

VI.5 Quench into the a-FM phase

Now we turn on the ordering dynamics following a quench from a random initial condition into the FM phase dominated by a-vertices (i.e. $a \gtrsim b + 1 + d + 3e$).

VI.5.1 Decay of topological defects

In this section, we pursue a similar analysis for the relaxation towards the FM phase: we study the decay of the defects' density for different values of the external parameters. In Fig. VI.10 we show the evolution of the density of defects $n(t) = n_e(t) + n_d(t)$ after a quench to $a = 5$, $b = 1$, $d = e^2$ and different values of e for two different system's sizes $L = 50$ (a) and $L = 100$ (b). The data shown has been averaged over 10^3 independent realisations of the dynamics.

For small enough e ($e \lesssim 10^{-3}$) the system gets frozen into a dynamical plateau. Similarly to what was discussed in the section above, the time period the system spends in this plateau is
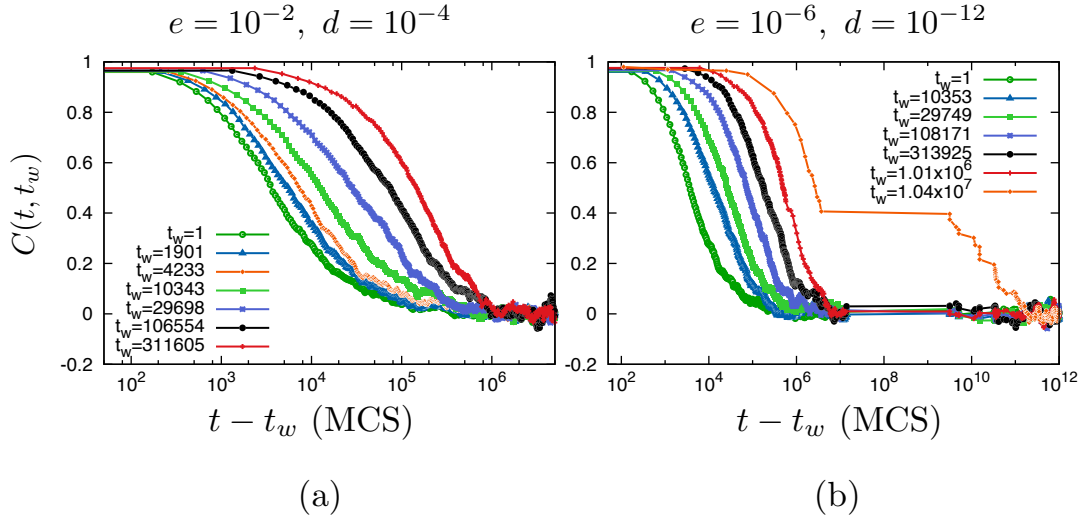
Figure VI.9: Two-time self correlation function C after a quench from a random initial configuration for a system $L = 50$ and averaged over 500 realisations for $a = b = c = 1$ and (a) $d = 10^{-4}$, $e = 10^{-2}$; (b) $d = 10^{-12}$, $e = 10^{-6}$.

longer for smaller e. The evolution is dramatically slowed down at a metastable density of defects $n^{pl} \approx 44/L^2$ for $L = 50$ and $n^{pl} \approx 88/L^2$ for $L = 100$. The height of the plateau seems to decrease with the size of the systems as $\sim 1/L$, slower than the $\sim 1/L^2$ behaviour found in the PM case. In order to conclude about the size dependence of the plateau height one should run simulations for larger sizes, which, unfortunately, we cannot reach in a reasonable time with our simulations.

The decay of n_e has also been fitted by the power law decay eq. (VI.22) with $\alpha \simeq 0.59$ over the whole time regime before the systems reaches the plateau density (as shown in Fig. [VI.10 (c)]). This power law is compared with the t^{-1} power-law already discussed. The decay of n becomes slower than the diffusive law in the FM phase. Note that this power-law decay does not depend on the size of the system as already suggested by the data shown in Fig. [VI.8 (b)].

The ordering process following a quench into the FM phase is characterised by a time scale $\tau \propto e^{-2}$ in the regime where the n leaves the plateau. As shown in Fig. [VI.10 (d)] for $L = 50$ all the curves collapse into a single curve when rescaling the time variable by τ. Therefore, the typical time associated with the creation of a pair of defects is the relevant time scale in the long time regime.

The evolution of the density of defects n following a quench into different points of the FM phase is shown in Fig. VI.11 for $L = 50$ (a) and $L = 100$ samples. During a short time regime ($t \lesssim 10$ MCs) the density of defects decays independently of a. For later times, the decay of n depends on the value of a. In particular, the expected power-law decay $n(t) \sim t^{-\alpha}$ becomes slower for larger values of a. Therefore, the exponent α depends on the weights of the vertices and decreases when increasing a. The metastable density of defects increases with a and depends on the system size. This study should be completed by a more detailed discussion on finite-size effects.

VI.5.2 Anisotropic domain growth

We choose $a = 5$, $b = 1$ and $d = e = 10^{-5}$, favouring vertices with weight a. In Fig. VI.12 we present the density of vertices, $n_\kappa(t)$, with $\kappa = a, b, c, d$, in a log-linear scale. The evolution is illustrated with three configurations at instants shown with vertical arrows. Domains grow
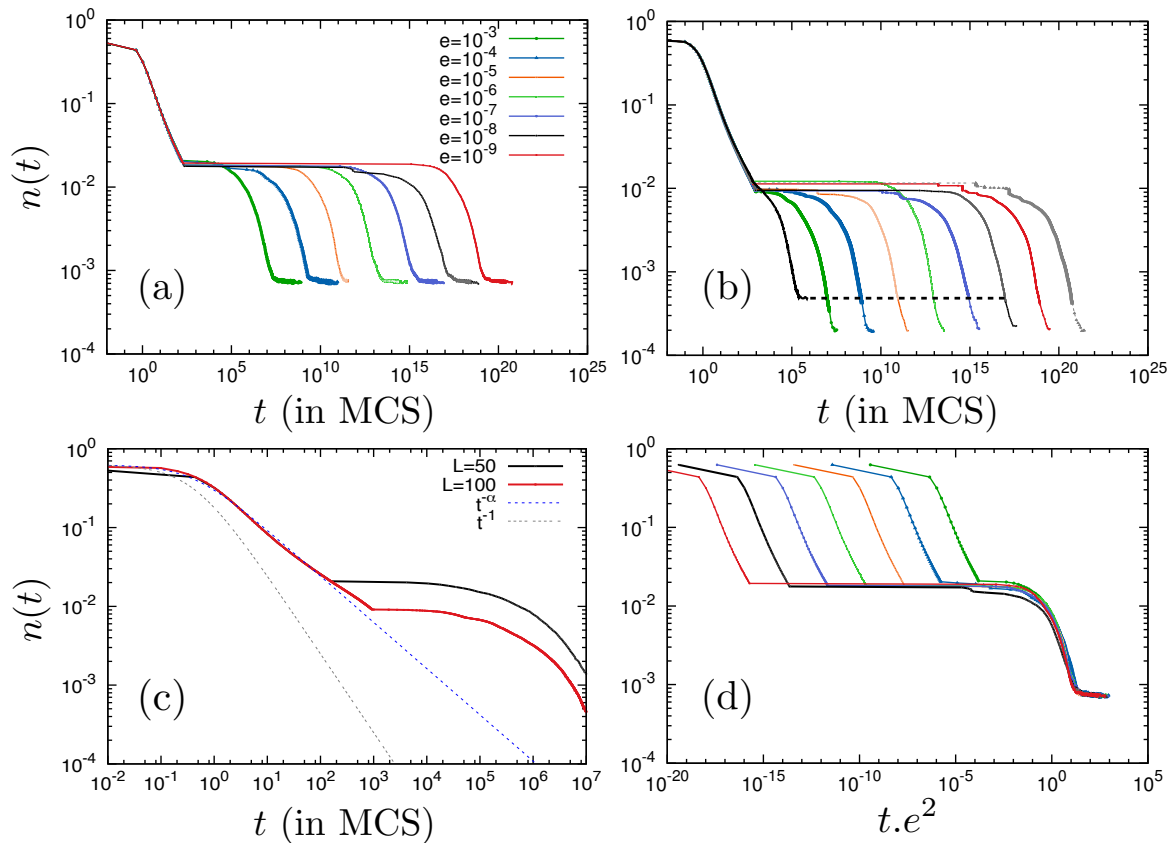
Figure VI.10: Time dependent density of defects after a quench from $a = b = d = e = 1$ to $a = 5$, $b = 1$ and $d = e^2$ for the different values of e. (a) $L = 50$ and $e = 10^{-3}, 10^{-4}, ..., 10^{-9}$ (as shown in the key). (b) $L = 100$ for $e = 10^{-2}$ (in black), $10^{-3}, ..., 10^{-10}$. For $e = 10^{-2}$ the system saturates to its equilibrium value shown with a dotted black line. (c) Short-time behaviour for $e = 10^{-3}$, $L = 50$ and $L = 100$. The decay is confronted to a $\rho_0/(1 + \Omega t)$ decay (grey dashed line) and the fit $\rho_0/(1 + \Omega t)^\alpha$ with $\alpha = 0.59$ (blue dashed line). (d) Test of scaling with $t.e^2$ for $L = 50$.

anisotropically and we choose the $\parallel$ and $\perp$ directions to be parallel and perpendicular to the diagonal joining the lower-left and upper-right corners in the pictures, respectively.

During a short transient ($t \lesssim 0.01$ MCs) all densities remain roughly constant (regime I). Suddenly, a large number of defects are transformed into divergence-free vertices by a few single spin-flips: n_d decays while n_a, n_b and n_c increase (regime II) independently of a. A typical configuration at this stage is the left-most snapshot and there is no visual ordering as corroborated by the small values taken by $L_{\parallel,\perp}$ and displayed in the inset in a log-linear scale for three values of the system size, $L = 100$, $L = 200$ and $L = 300$. Subsequently the system sets into a slow relaxation regime in which the dominant mechanism is the one of growing anisotropic domains with FM order, see the central snapshot (regime III); n_κ depend upon a and there are as many domains with $m_+^{x;y} = 1$ (vertices 1) as $m_+^{x;y} = -1$ (vertices 2) respecting symmetry. In this regime $L_\parallel$ grows faster than $L_\perp$ and tends to saturate to an L-dependent value when the stripes are fully formed. For the largest sample size, $L = 300$, our numerical data are consistent with a $t^{1/2}$ growth that is shown with a dotted black line. Instead order in the $\perp$ direction has not yet percolated. The full equilibration of the sample needs the percolation of order in the $\perp$ direction which is achieved by a still much slower mechanism (regime IV).
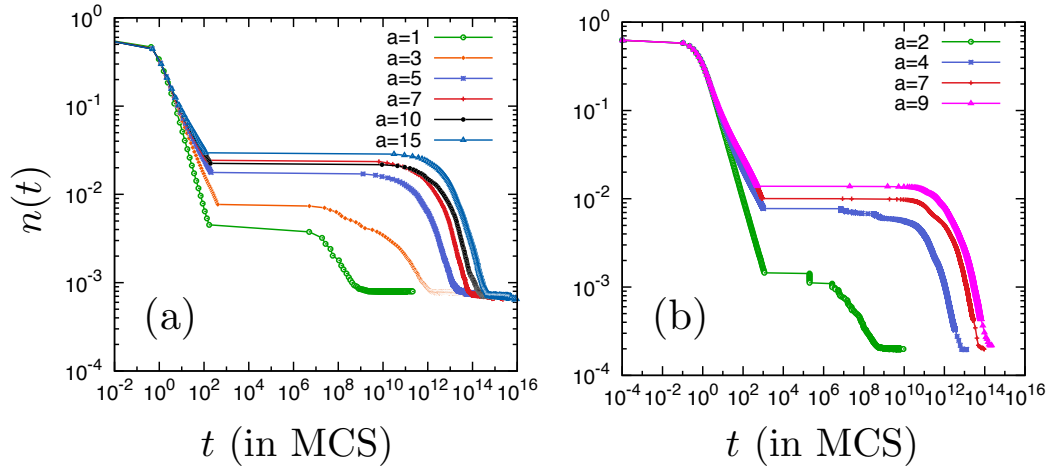
Figure VI.11: Time dependent density of defects after a quench from $a = b = d = e = 1$ to $b = 1$, $d = 10^{-18}$, $e = 10^{-6}$ and different values of a. (a) $L = 50$ for $a = 1, 3, 4, 7, 10$ (as shown in the key). (b) $L = 100$ for $a = 2, 4, 7, 9$. The data has been averaged over 300 independent runs.

The behaviour of the space-time correlation functions confirm this growth. As shown in Fig. VI.13 the correlations along the direction of the stripes (a) grow faster than in the orthogonal direction (b). The function $G^{\parallel}$ does not vanish at any point of the system for times larger than $\approx 10^5$ MCs. Instead, the correlations along $\vec{u}_{\perp}$ vanish at distances smaller than the system size in the simulated time window. The growth is highly anisotropic because of the choice $a > b$. For $b > a$ correlations along $\vec{u}_{\perp}$ develop faster than along $\vec{u}_{\parallel}$, forming stripes perpendicular to the ones shown in Fig. VI.12. The relevant parameter characterising the anisotropy of the ordering process is the ratio a/b. As shown in Fig. [VI.13 (c)] in the regime where anisotropic domains grow, the correlation function along the $\parallel$ direction depends on space and time through the ratio $r/t^{1/2}$:

$$G^{\parallel}(r, t) \simeq F^{\parallel}\left(\frac{r}{t^{1/2}}\right) \, , \tag{VI.32}$$

which confirms the expected growth $L_{\parallel}(t) \sim t^{1/2}$. In order to study the growth in the $\perp$ direction one needs to study larger samples since $L_{\perp}(t) \ll L_{\parallel}(t)$. This makes the estimation of the growth law for $L_{\perp}(t)$ unavailable in our simulations: heavier numerics are needed.

VI.5.3 Microscopic ordering mechanisms

A better understanding of the processes involved in the ordering dynamics is reached from the analysis of the snapshots.

(a) Domain walls are made of c-vertices and plaquettes of divergence-free vertices, as shown in the left and central panels in Fig. VI.14, respectively. The latter are 'loop' fluctuations in which all the spins on the plaquette are sequentially flipped. Interfaces between FM states tend to be parallel to the main diagonal, which one depending on which FM phase one quenches into.

(b) Quasi-one-dimensional paths made of b- and c-vertices (loop fluctuation can be attached to them) act as bridges between two domains of the same type and run through a region with the opposite order. These structures are similar to the ones found in the kinetically constrained spiral model [73]. In order to further increase the density of a-vertices and develop the FM order the
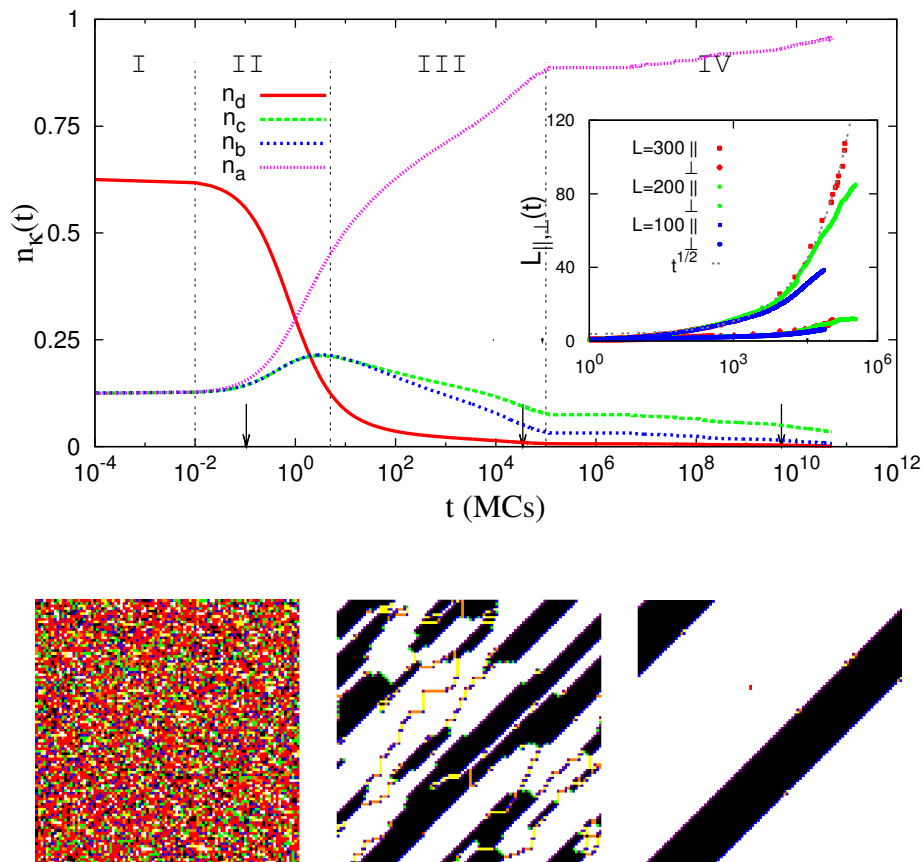
Figure VI.12: FM ordering. Upper panel: time evolution of the density of vertices with weight a, b, c, d for $a = 5$, $b = 1$, $d = 10^{-5}$ and $L = 100$ averaged over 300 samples. The snapshots are typical configurations at the dates indicated by the arrows. Black/white points are vertices 1/2 and the rest are shown in grey (color) scale. Inset: time-dependence of the longitudinal (upper curves) and transverse (lower curves) growing lengths for three system sizes, $L = 100, 200, 300$. A fit to $t^{1/2}$ is shown with a dotted black line.

domain walls and bridges have to be eliminated. The latter disappear first via the following mechanism. 'Corners' made of b (or, less commonly, d) vertices sit on a curved domain wall. Such b vertices cannot be surrounded by more than two type 1 or 2 vertices (only defects can, see the third panel in Fig. VI.14). The string progressively disappears eaten by the attached domains that grow from the corner or, alternatively, it is first cut by the creation of two defects and the two strands subsequently shrink, an extremely slow process. Once the path has been eliminated one is left with two defects sitting on the walls of the now detached domains, that move along the interface and eventually annihilate with their anti-partner.

(c) Once parallel bands are created (third configuration in Fig. VI.12) the mechanism in Fig. VI.15 takes over (regime IV). After the creation of a pair of defects on the interface, the sequence of steps in the figure shrink the vertex 1 stripe on a time scale that diverges with L.
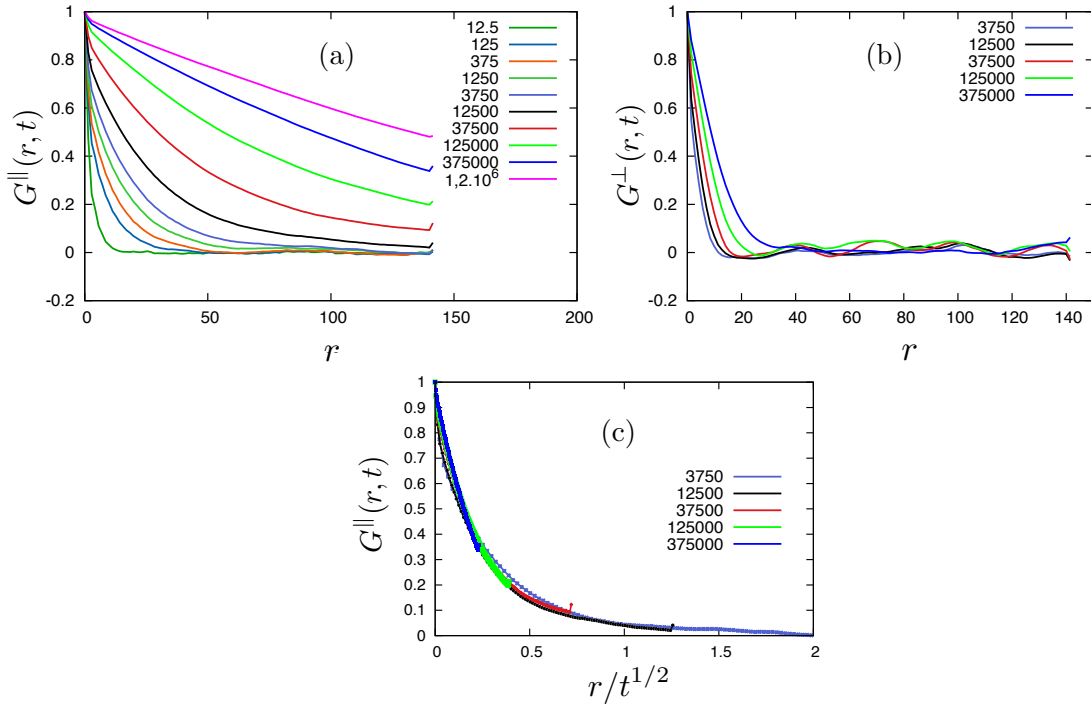
Figure VI.13: Space-time correlation function along the longitudinal (a)-(c) and orthogonal (b) directions for $L = 200$, $a = 5$, $b = 1$, $d = e = 10^{-5}$ and different times t given in the key. The data has been obtained after averaging over 100 runs. (c) $G^{\parallel}$ as a function of the rescaled variable $r/t^{1/2}$ for different times in the regime III (coarsening regime).

VI.6 Quench into the c-AF phase

Now we turn on the anti-ferromagnetic phase. We follow the evolution of the system after a quench from a random initial condition into the AF phase dominated by c-vertices (i.e. $1 \lesssim a + b + d + 3e$).

VI.6.1 Coarsening dynamics

The evolution of the vertex population is shown in the main panel in Fig. VI.16 for $a = b = 0.1$ and $d = e = 10^{-5}$. This data is illustrated by four snapshots of the system token at instants indicated with vertical arrows. The ordering process proceeds by growing isotropic domains of opposite staggered magnetisation $m_-^{x,y} = \pm 1$.

Similarly to what has been found in the FM quenches, in regime I all densities remain approximately constant. This is followed by regime II with a rapid annihilation of defects into divergence-free vertices. The creation of a, b and c-vertices occurs with a rate that depends on a while, surprisingly, n_d does not, at least within our numerical accuracy. In regime III the system increases the AF order by growing domains of staggered magnetisation ± 1 with c vertices. Since a is very close to b for our choice of parameters, domains are quite isotropic. This is explicitly shown in Fig. VI.17. The space-time self correlation functions along the $\parallel$ and $\perp$ direction are almost identical and the associated growing lengths are, within numerical accuracy, $t^{1/2}$. Regime IV follows next and it is characterised by a strong slowing-down although there is no obvious extended structure blocking the evolution. In regime V the system finally reaches equilibrium.
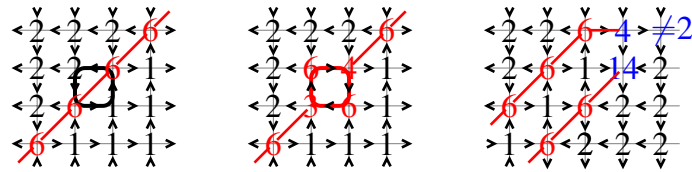
Figure VI.14: Interfaces between FM domains. Local vertices and spins on the bonds are shown. Left panel: diagonal wall (red solid line). Central panel: a 'loop' fluctuation on the plaquette highlighted in the left panel. Right panel: a b corner vertex cannot be neighbour of an a-vertex, explaining the presence of strings.
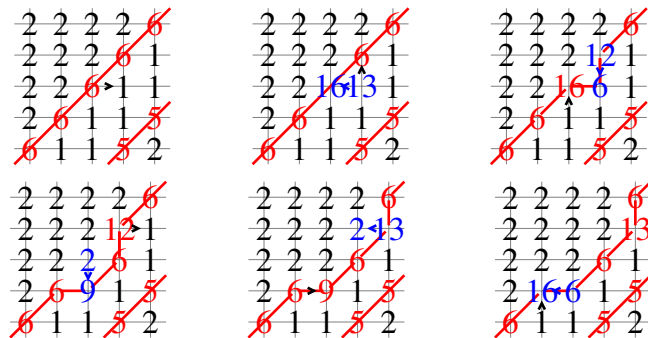

Figure VI.15: Schematic representation of FM stripe motion. Vertices on each site are specified. Diagonal (red) lines delimit domains of opposite magnetization. Black arrows indicate the spins that flip to get the new configuration (represented in blue after the flip).

VI.6.2 Domains and contour lines

A better understanding of the processes involved in the ordering dynamics is reached from the analysis of the snapshots.

(a) Domain walls are made of a- and b-vertices. Contrarily to the FM case, domains of any shape can be constructed without defects. As shown in the left and central panels in Fig. VI.18, horizontal and vertical walls are made by alternating a- and b-vertices. Diagonal walls are exclusively made by a- or b-vertices depending on their orientation. Therefore, domain walls without defects (energetically favoured) form loops of spins pointing along the same direction. In the SOS representation, each domain can be interpret as a contour line delimiting regions with different height. The ordering then proceeds by growing or shrinking regions of constant height. Note that the KT phase transition of the F model can be mapped into the roughening transition.

(b) Once isotropic domains are created, one has to eliminate small domains in order to further increase the density of c-vertices and develop the AF order. Fig. VI.19 illustrates the mechanism taking place. After the creation of a pair of defects in a typical time $\sim 1/e^2$, their motion along the wall shrinks the domain. This is done without any energy cost and the sequence of steps needed to make a domain disappear should scale with its size. The same kind of mechanism takes place for horizontal domain walls.
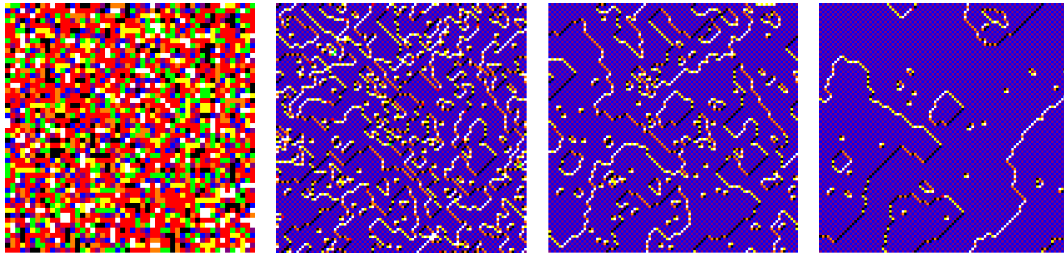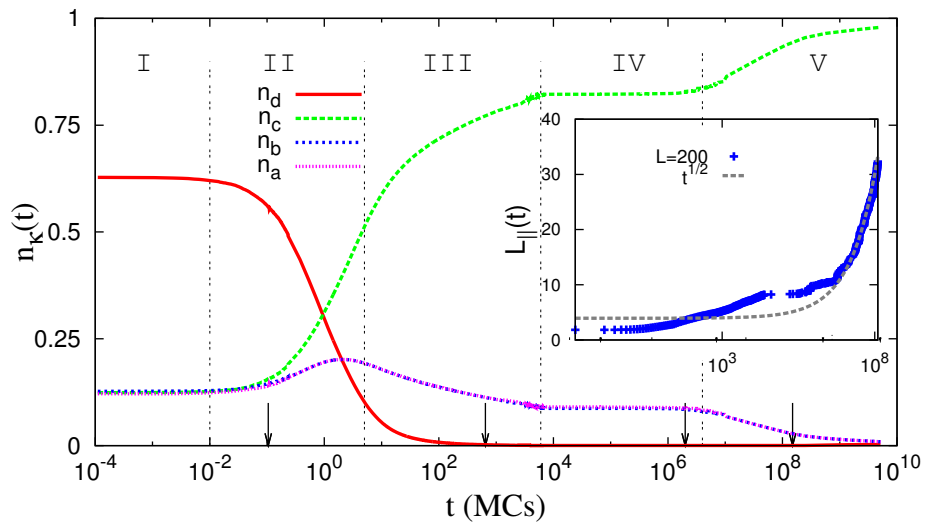
Figure VI.16: AF ordering. Time evolution of the density of vertices in a system with $L = 100$ after a quench to $a = 0.1$, $b = 0.1$, $d = 10^{-5}$ averaged over 300 runs. Inset: the time-dependent growing length $L_\parallel$ confronted to $t^{1/2}$ (dotted black line). Typical configurations are shown.

Usually domain walls in magnetic models with NCOP are curved and smooth interfaces which display a variety of shapes. In this model, AF domains have the tendency to form domain walls made by FM vertices. This kind of domain wall pattern has been observed in artificial spin ice samples with thermal ordering [197].
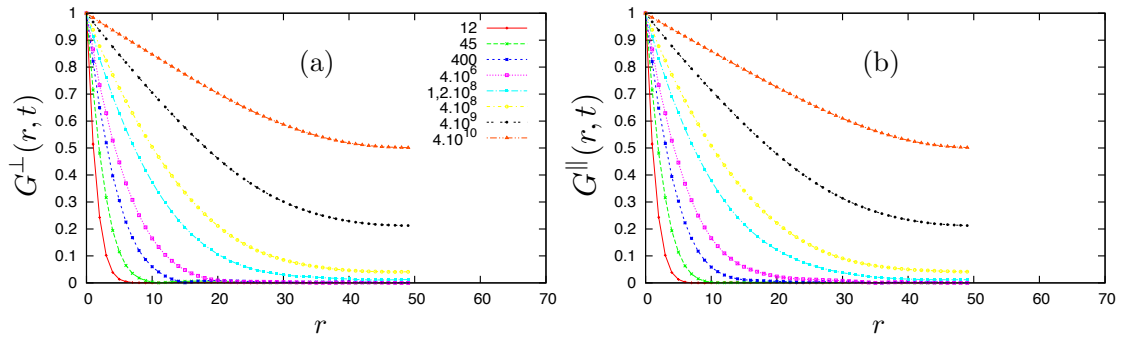
Figure VI.17: Space-time correlations after a quench from a random initial condition into $a = 0.1 = b = 0.1$, $d = e^2 = 10^{-10}$ and $L = 50$ averaged over 500 runs. (a) Correlations along the $\perp$ direction as a function of the distance r between sites for different times (shown in the key). (b) Correlations along the $\parallel$ direction as a function of r for the same times as in (a).
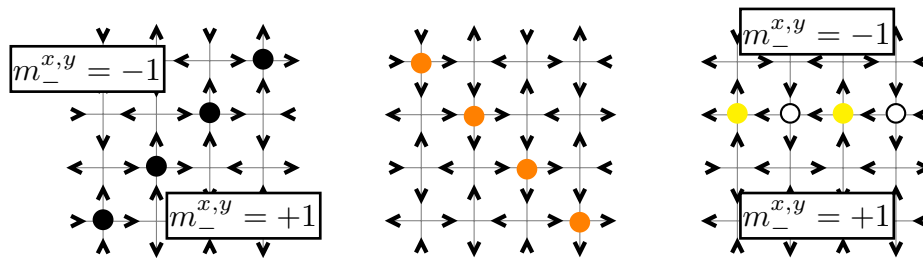
Figure VI.18: Domain walls between AF domains of opposite staggered order. The configuration of arrows is shown. We use the colour rule defined in Fig. VI.2. Left panel: diagonal walls in the $\parallel$ direction are made of a-vertices. Central panel: diagonal walls in the $\perp$ direction are made of b-vertices. Right panel: horizontal (and vertical, by symmetry) walls are made of an alternating chain of a- and b-vertices.
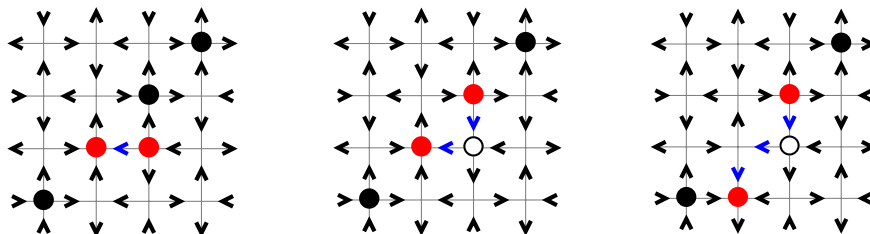
Figure VI.19: Schematic representation of the annihilation of AF domains. Vertices on the walls are represented by the colour rule defined in Fig. VI.2. Blue arrows indicate the spins that have been flipped to get the new configuration. As monopoles diffuse along the domain wall the ordered region on the right-bottom side of the figure shrinks.

VII

Conclusions and open questions

In this thesis we presented a thorough study of the sixteen-vertex model. Both its equilibrium and out-of-equilibrium dynamics following different quenches have been analysed in detail. We used a Continuous Time Monte Carlo algorithm to avoid the difficulties raised by the slowing down of the dynamics when a small weight of the defects is chosen. Thanks to this algorithm we were able to simulate the equilibrium phases of the model and its long-time dynamical behaviour. We extended the model to be defined on oriented trees of vertices and square plaquettes made by four vertices (Bethe-Peierls approximation). Then, we established the equilibrium phase diagram using numerical simulations of the $2D$ model and we compare this results with the ones obtained by approximating the model by the two before mentioned trees. By comparing our theoretical results with the vertex population measurements done in artificial spin-ice samples, we showed the relevance of the sixteen-vertex model for the study of $2D$ spin-ices.

The main equilibrium results obtained during this thesis can be summarised as follows:

(i) The criticality of the paramagnetic phase is broken as soon as the ice-rules constraint is relaxed. The a, b-FM–SL 'frozen-to-critical' phase transition and the c-AF–PM infinite order phase transitions of the six-vertex model both become continuous phase transitions when defects are allowed. We established the phase diagram of the unconstrained model numerically and we conjectured the existence of an generalised anisotropy parameter Δ_{16} characterising the phases of the model.

(ii) Our Bethe-Peierls (BP) approximation gives the exact location of the transition lines for the (integrable) six- and eight-vertex model. When defects are rare, our BP approach using a tree of plaquettes turns out to be an accurate approximation of the equilibrium phases of the sixteen-vertex model on the square lattice. In artificial spin-ice samples the weight of the defects is small. Therefore, our BP calculation gives results in quasi-quantitative agreement with the numerical simulations and with the experiments when choosing the parameters of the model accordingly. We argue that, away from the AF-PM critical point, as-grown artificial spin-ice samples are in thermal equilibrium. This explains the discrepancy between our (numerical and analytical) calculations and the experimental data close to the transition temperature.

(iii) Using a finite-size and a non-equilibrium relaxation analysis of the simulation data, we measured the value of the critical exponents of the sixteen-vertex model. We found that, similarly to what is known from the exact solution of the eight-vertex model, the value of the critical exponents depend on the external parameters of the model. A set of critical exponents can be defined in terms of the divergence of the correlation length close to the transition, instead of using the deviation to the critical point as the scaling variable. The values of these new set of critical exponents, which are identical for the six- and eight-vertex model, are also identical for the sixteen-vertex model. Moreover, the value of these exponents coincide for the six-, eight-, sixteen-, $2D$ Ising and $2D$ XY models.

(iv) We proposed some extensions of known mappings for constrained models to the un-constrained case. The presence of a hard local constraint in a lattice model allows us to define a height function and a gauge structure emerges naturally from that. The situation is less clear when the constraint is relaxed and thermal fluctuations are allowed. We propose the introduction of a multivalued height function where defects are interpreted as dislocations of the surface field. Once the extended strings which links two defects have been fixed arbitrarily, a unique height configuration can be associated to a vertex configuration. Within this framework a $2D$ Coulomb interaction between defects emerges as a many-body effect.

Once the equilibrium properties of these extended problems have been characterised, we moved to its dynamical properties. We followed the evolution of the system after different quenches: from a disordered initial state into its PM, a-FM and c-AF phases.

Let us summarise the results obtained for the out-of-equilibrium dynamics of the sixteen-vertex model:

(i) We analysed the evolution of the density of defects following all kind of quenches. The initial decay follows a power-law. Different algebraic decays are obtained for different special values of the Boltzmann weights. The exponent characterising the annihilation of defects is found to depend on the choice of the parameters in a non-trivial manner. We recover the $1/t$ decay found in $3D$ dipolar spin-ice in the PM phase when the weight of doubly charged defects d is smaller that the square of the weight of the single charged defects e.

(ii) After the initial power law decay, the density of topological defects take a finite density for long periods of time. The existence of these long-lived metastable states have been observed in numerical simulations of $3D$ dipolar spin-ice. This dynamical arrest is observed in our model for all kind on quenches. We discuss the persistence of the metastable state for different choices of the defects' weights, and found that the presence of 4in and 4out vertices are not responsible for the emergence of such slowing down of the dynamics. We analyse the effect of the boundary conditions and found that the plateau remains for fixed boundary conditions. After analysing the evolution of the density of defects for different system sizes we argued that the dynamical plateau vanishes at the thermodynamic limit.

(iii) We identified the microscopic mechanisms leading the dynamics during the evolution through the ordered phases. We evaluated the anisotropic growing lengths and showed that the ordering dynamics proceeds through coarsening. The evolution of the system conforms to the domain growth dynamical scaling picture. The interplay between extended topological defects in the form of domain walls and localised defects makes the coarsening dynamics of this model specially rich.

The following is a partial list of possible further research directions inspired by the work done during this thesis:

1. The connection between a quantum model in $1D$ and a classical lattice model in $2D$ allows to study quantum and classical phase transitions by a unified framework. The equivalence between the XXZ and XYZ quantum spin-1/2 chains and the six- and eight-vertex model has been proved to be closely related to the integrability of the model. We proposed a candidate that might be the quantum analog of the sixteen-vertex model. The mapping has, however, not been demonstrated and we should try (harder) to find a way to relate the parameters of the quantum problem with the weight of the vertices. Then, it would be possible to relate the phase diagram of the sixteen-vertex model with the quantum phases of the chain.

2. One could easily include an external magnetic field and study the equilibrium of the sixteen-vertex model with the cavity method and CTMC. Although for the six-vertex problem exact results are available, the phase diagram of the eight- and sixteen-vertex model in an external field is not known yet.

3. Our Bethe-Peierls approach should give accurate results for other constrained lattice models - for the same reasons that the transition lines are exactly reproduced for the six- and eight-vertex models. For instance, one could define Kagome Ice (or the AF Ising model in the triangular lattice, three-colouring model, etc.) on an appropriate chosen tree with coordination number $c = 3$. Then I expect that the zero point entropy, and the transitions lines obtained by the BP calculation be extremely close to the ones of the finite dimensional model.

4. In the six-vertex model, boundary conditions (i.e. the topology of the space where the model is defined) affect the thermodynamics of the system. I expect boundary conditions to have important dynamical consequences in hardly constrained models. Some work has been done recently on the dynamical properties of these kind of models with periodic boundary conditions (PBC). The presence of a hard constraint in a lattice model with PBC splits the phase space into different topological sectors. This gives rise to an ergodicity breaking which has motivated several groups to talk about 'topological glasses'. In the six-vertex model, one expects a strong slowing down of the dynamics due to the extended loop updates needed in order to explore all possible configurations. One could study the dynamics of the six-vertex model (or ice-model for simplicity) with Domain Wall Boundary Conditions for which the whole phase space can be sampled by local updates. Quantities of interest in this problem are time correlations and in particular, the equilibrium relaxation time as a function of the parameters of the model.

5. In section V.5 we compared the equilibrium results obtained for the sixteen-vertex model with experiments on artificial spin-ice (ASI). In these experimental samples the islands grow during fabrication until they freeze. It would be interesting to simulate the thermal annealing occurring during the fabrication of ASI samples with our model, in order to try to understand better the relationship between the canonical temperature, and the effective temperature extracted from population measurements. The effect of boundary conditions in this context should also be investigated, since usual experimental realisations do not verify PBC.

6. The dynamics of the defects in $3D$ spin-ice materials has attracted (and still does) much attention in recent years. The possibility to create currents of magnetic charges and then

realise an effective 'magnetricity' in spin-ice has been shown experimentally. We plan to investigate defect's motion in our model under different external conditions and the possibility to generate persistent currents. Starting from the study of two oppositely charged defects, one should ask whether a collective motion of a large density of defects is possible in $2D$ samples. In usual ASI realisations of square lattices, c-vertices are favoured, leading to a string tension connecting two oppositely charged defects. However, starting from a polarised initial configuration, defects would have the tendency to move apart of each other leaving behind a string made by a strong fraction of c-vertices. I expect that the polarisation background will affect monopole's motion. One should then study in detail the transport properties of the system at different time regimes and thermodynamic phases.

7. Following the same line of reasoning, one could study the dynamics of artificial Kagome ice. In this system, all the kind of vertices are equivalent such that monopoles' motion does not give rise to an energetic string. The evolution of the defects in this geometry has been recently studied experimentally by applying magnetic fields [236]. Domains made by an ordered arrangement of defects have been observed in these samples. A possible direction of research could be to study the statistics of these domains and the dynamical mechanisms which leads to these structures.

8. In the seventies, Kadanoff and Wegner showed the equivalence between the eight-vertex model and an Ising model with multi-spin interactions. This mapping was originally introduced in order to understand the critical singularities of Baxter's exact solution: the critical exponents are continuous functions of the interactions parameters. Using scaling arguments Kadanoff and Wegner were able to reproduce this result. A few years later van Leeuwen proposed a real-space Renormalisation Group (RG) procedure to treat the eight-vertex model. He explained by RG arguments the mechanism responsible for the emergence of continuously varying exponents. In order to give support to the numerical results, it would be interesting to treat the sixteen-vertex model by a real-space RG procedure and extend van Leeuwen's results. We expect to find a marginal scaling field and a line of fixed points where the critical exponents vary. The existence of exact solutions for the six- and eight-vertex model can be used as a guide to test the accuracy of the procedure. However, the exact critical exponents associated to the sixteen-vertex model are unknown.

The CTMC algorithm

In this Appendix we give some details on the implementation of the Continuous Time Monte Carlo algorithm that we used to study the phase diagram of the sixteen vertex model.

We chose to use single spin updates. The time needed to flip an arrow is computed by

$$\Delta t = \text{Int} \left(\frac{\ln \xi}{\ln \left(1 - \sum_{I=1}^{2N} W\left(\mu \to \mu^I \right) \right)} \right) + 1 \qquad \text{(A.1)}$$

and the transition probabilities defining the dynamics of the system are

$$W(\mu \to \mu^I) = \frac{1}{2L^2} \min \left(1, e^{-\beta(E(\mu^I) - E(\mu))} \right) \qquad \text{(A.2)}$$

satisfying detailed balance and ergodicity. This transition probabilities are expressed as a function of the state of the chosen spin I. We have to compute the probability to stay in the same state $W(\mu \to \mu) = 1 - \sum_{I=1}^{2N} W(\mu \to \mu^I)$ to obtain Δt using eq. (A.1) and then we need to know every possible energy change a single flip can produce. In the sixteen-vertex model there is a finite number of such possible processes (and then a finite number of possible transition probabilities) independently of the system size. This procedure can then be applied by making a list of all the arrows classified by their state, noted from now on l and defined by its neighbourhood (i.e. the type of its two adjacent vertices). Since each vertex can take sixteen different configurations, there are 8×8 such states for vertical and horizontal arrows, so a total of 64 states for each type of arrow. Following the original name of this method [41, 17] this algorithm is a 256-fold way. The transition probability of the process $\mu \to \mu^I$ only depends on the state l of the I-th arrow before the flip. This can be clearly seen by rewriting

$$\exp\left[-\beta(E_{\mu^{(I)}} - E_\mu) \right] = \exp\left[-\beta \left(E\left[V_{1,I}^{\mu^{(I)}} \right] + E\left[V_{2,I}^{\mu^{(I)}} \right] - E\left[V_{1,I}^{\mu} \right] - E\left[V_{2,I}^{\mu} \right] \right) \right]$$

here $E\left[V_{1,I}^{\mu^{(I)}} \right]$ is the energy of the first adjacent vertex of the I-th arrow after the flip from the state μ. To know the type of the neighbouring vertices $V_{1,I}$ and $V_{2,I}$ at state μ is equivalent to

l	$V_{L,I}^{\mu} \longleftrightarrow V_{R,I}^{\mu}$	$V_{L,I}^{\mu^{(I)}} \longleftrightarrow V_{R,I}^{\mu^{(I)}}$	$e^{-\beta\epsilon_l}$
0	1-1	11-16	$e^2/a^2 \lll 1$
1	1-4	11-12	$e^2/a.b \lll 1$
...	...	...	...
64	16-16	3-1	$a.b/e^2 \ggg 1$

Table A.1: Partial classification of the 64 possible sates of an horizontal arrows pointing to the right, corresponding to each one of all the transitions that can occur by a single flip. The second and third columns corresponds to the left and right vertices adjacent to the I-th arrow before and after the flip.

know the state of the concerned arrow before the flip (the vertex types of the neighbouring vertices after the flip are determined by the vertex types before the flip): the energy change after a flip depends only in its initial state. We define

$$P_l = \frac{1}{2N} \min\left(1, e^{-\beta\varepsilon_l}\right)$$

where ε_l is the energy difference after flipping an arrow in state l. It is useful for the implementation to note that we can compute Δt by counting the number of arrows occupying each one of the different possible states at each step. We substitute the latter equation by

$$Q = \sum_{I=1}^{2N} W(\mu \to \mu^{(I)}) = \sum_{l=1}^{256} g_l P_l \tag{A.3}$$

where g_l is the number of arrows in state l. We then need to keep record of the state of every arrow on a list at each step. After a transition this list must be updated. The main steps of the computation are implemented by Alg. (1).

Algorithm 1 Continuous Time Monte Carlo algorithm.

– **for** $l = 1..256$ **do**
    $P_l \leftarrow e^{-\beta\varepsilon_l}$
– **for** $i = 1..\#\text{steps}$ **do**
    input: t, state μ
    $\widetilde{Q} \leftarrow 1 - \sum_l g_l P_l$.
    $\Delta t \leftarrow 1 + \text{Int}\left(\frac{\ln(\text{ran}\in[0,1])}{\ln\widetilde{Q}}\right)$;
    $t \leftarrow t + \Delta t$
    $l \leftarrow$ random with a probability distribution $g_l P_l$.
    $k \leftarrow$ random uniformly between 1 and g_l.
    flip arrow I
    update the list
    output: t, state $\mu^{(I)}$, arrows classified

Bibliography

[1] ABOU-CHACRA, R., ANDERSON, P. W., AND THOULESS, D. J. A selfconsistent theory of localization. *Journal of Physics C: Solid State Physics 6* (1973), 1973.

[2] ALBANO, E. Monte Carlo simulations of the short time dynamics of a first-order irreversible phase transition. *Physics Letters A 288* (2001), 73.

[3] ALBANO, E. V., BAB, M. A., BAGLIETTO, G., BORZI, R. A., GRIGERA, T. S., LOSCAR, E. S., RODRÍGUEZ, D. E., PUZZO, M. L. R., AND SARACCO, G. P. Study of phase transitions from short-time non equilibrium behaviour. *Reports on Progress in Physics 74* (2011), 26501.

[4] ALET, F., JACOBSEN, J., MISGUICH, G., PASQUIER, V., MILA, F., AND TROYER, M. Interacting Classical Dimers on the Square Lattice. *Physical Review Letters 94* (June 2005), 235702.

[5] ALLEN, S. M., AND CAHN, J. W. A microscopic ry for antiphase boundary motion and its application to antiphase domain coarsening. *Acta Metallurgica 27* (1979), 1085.

[6] ALLISON, D., AND RESHETIKHIN, N. Numerical study of the 6-vertex model with domain wall boundary conditions. *Annales de l'institut Fourier 55* (2005), 1847.

[7] ANDERSON, P. W. Ordering and antiferromagnetism in ferrites. *Physical Review 325* (1956), 1008.

[8] ANDERSON, P. W. Resonating valence bonds: a new kind of insulator? *Materials Research Bulletin 8* (1973), 153.

[9] ANDERSON, P. W. The Resonating Valence Bond State in La2CuO4 and Superconductivity. *Science 235* (1987), 1196.

[10] ARENZON, J., BRAY, A., CUGLIANDOLO, L., AND SICILIA, A. Exact Results for Curvature-Driven Coarsening in Two Dimensions. *Physical Review Letters 98* (Apr. 2007), 145701.

[11] ARNOLD, V. I. *Mathematical Methods of Classical Mechanics*, 2nd ed. Springer, 1989.

[12] BABELON, O., BERNARD, D., AND TALON, M. *Introduction to classical integrable systems*. Cambridge University Press, 2003.

[13] BADER, S. Colloquium: Opportunities in nanomagnetism. *Reviews of Modern Physics 78* (Jan. 2006), 1.

[14] BALENTS, L. Spin liquids in frustrated magnets. *Nature 464* (2010), 199.

[15] BARBER, M. N. Finite-size scaling. In *Phase transitions and critical phenomena Vol. 8*, J. L. Lebowitz and C. Domb, Eds. Academic Press, 1983.

[16] BARKEMA, G. T., AND NEWMAN, M. E. J. Monte Carlo simulation of ice models. *Physical Review E 57* (1998), 1155.

[17] BARKEMA, G. T., AND NEWMAN, M. E. J. *Monte Carlo Methods in Statistical Mechanics*. Oxford University Press, 1999.

[18] BARRAT, A., KURCHAN, J., LORETO, V., AND SELLITTO, M. Edwards measures: A thermodynamic construction for dense granular media and glasses. *Physical Review E 63* (Apr. 2001), 051301.

[19] BAXTER, R. J. Colorings of a hexagonal lattice. *Journal of Mathematical Physics 11* (1970), 784.

[20] BAXTER, R. J. Exact Isotherm for the F Model in Direct and Staggered Electric Fields. *Physical Review B 1* (1970), 2199.

[21] BAXTER, R. J. Three Colorings of the Square Lattice: A Hard Squares Model. *Journal of Mathematical Physics 11* (1970), 3116.

[22] BAXTER, R. J. Eight Vertex Model in Lattice Statistics. *Physical Review Letters 26* (1971), 832.

[23] BAXTER, R. J. Partition function of the Eight-Vertex lattice model. *Annals of Physics 70* (1972), 193.

[24] BAXTER, R. J. Spontaneous Staggered Polarization of the F-Model. *Journal of Physics C: Solid State Physics 6* (1973), L94.

[25] BAXTER, R. J. *Exactly solved models in statistical mechanics*, vol. 9. Dover, 1982.

[26] BEIJEREN, H. V. Exactly Solvable Model for Roughening Transition of a Crystal Surface. *Physical Review Letters 38* (1977), 993.

[27] BENFATTO, G., AND MASTROPIERO, V. Renormalization Group, hidden symmetries and approximate Ward identities in the XYZ model. *Reviews in Mathematical Physics 13* (2001), 1323.

[28] BENGUIGUI, L. Critical point of infinite type. *Physical Review B 16* (1977), 1266.

[29] BEREZINSKII, V. L. Destruction of long-range order in one-dimensional and two-dimensional systems having a Continuous Symmetry Group I. Classical systems. *Soviet Journal of Experimental and Theoretical Physics 34* (July 1971), 610.

[30] BERNAL, J. D., AND FOWLER, R. H. A Theory of Water and Ionic Solution, with Particular Reference to Hydrogen and Hydroxyl Ions. *The Journal of Chemical Physics 1* (1933), 515.

[31] BERTHIER, L., AND BIROLI, G. A theoretical perspective on the glass transition and nonequilibrium phenomena in disordered materials. *Reviews of Modern Physics 83* (Nov. 2011), 587.

[32] BETHE, H. A. Statistical Theory of Superlattices. *Proceedings of the Royal Society of London. Series A. 150* (1935), 552.

[33] BHATTACHARJEE, S. M., NAGLE, J. F., HUSE, D. A., AND FISHE, M. E. Critical Behavior of a Three-Dimensional Dimer Model. *Journal of Statistical Physics 32* (1983), 361.

[34] BINDER, K. Finite size scaling analysis of ising model block distribution functions. *Zeitschrift fur Physik B Condensed Matter 43* (June 1981), 119.

[35] BINDER, K. Theory of first-order phase transitions. *Reports on Progress in Physics 50* (1987), 783.

[36] BINDER, K., AND LANDAU, P. D. Finite-size scaling at first-order phase transitions. *Physical Review B 30* (1984), 1477.

[37] BIROLI, G., AND KURCHAN, J. Metastable states in glassy systems. *Physical Review E 64* (June 2001), 016101.

[38] BLOTE, H., AND HILBORST, H. Roughening transitions and the zero-temperature triangular Ising antiferromagnet. *Journal of Physics A: Mathematical and General 15* (1982), L631.

[39] BLOTE, H. W. J., AND NIGHTINGALE, M. P. Antiferromagnetic triangular Ising model: Critical behaviour of the ground state. *Physical Review B 47* (1993), 15046.

[40] BOGOLIUBOV, N. M., PRONKO, A. G., AND ZVONAREV, M. B. Boundary correlation functions of the six-vertex model. *Journal of Physics A: Mathematical and General 35* (2002), 5525.

[41] BORTZ, A. B., KALOS, M. H., AND LEBOWITZ, J. L. A New Algorithm for Monte Carlo Simulation of Ising Spin Systems. *Journal of Computational Physics 17* (1975), 10.

[42] BRAGG, W. L., AND WILLIAMS, E. J. The Effect of Thermal Agitation on Atomic Arrangement in Alloys. *Proceedings of the Royal Society A: Mathematical, Physical and Engineering Sciences 145* (July 1934), 699.

[43] BRAMWEL, S. T., GINGRAS, M. J. P., AND HOLDSWORTH, P. C. W. Spin ice. In *Frustrated spin systems*, H. Diep, Ed. World Scientific, 2004, ch. 7.

[44] BRAMWELL, S. T., GIBLIN, S. R., CALDER, S., ALDUS, R., PRABHAKARAN, D., AND FENNELL, T. Measurement of the charge and current of magnetic monopoles in spin ice. *Nature 461* (2009), 956.

[45] BRAMWELL, S. T., GINGRAS, M. J. P., AND HOLDSWORTH, P. C. W. Frustrated Spin Systems. In *Frustrated spin systems*, H. T. Diep, Ed. World Scientific, 2004, ch. 7.

[46] BRAMWELL, S. T., HARRIS, M. J., DEN HERTOG, B. C., GINGRAS, M. J. P., GARDNER, J. S., McMORROW, D. F., WILDES, A. R., CORNELIUS, A. L., CHAMPION, J. D. M., MELKO, R. G., AND FENNELL, T. Spin Correlations in Ho_{2}Ti_{2}O_{7}: A Dipolar Spin Ice System. *Physical Review Letters 87* (July 2001), 047205.

[47] BRANFORD, W. R., LADAK, S., READ, D. E., ZEISSLER, K., AND COHEN, L. F. Emerging chirality in artificial spin ice. *Science 335* (Mar. 2012), 1597.

[48] BRAY, A. J. Non equilibrium statistical mechanics in one dimension. In *Non equilibrium statistical mechanics in one dimension*, V. Privman, Ed. Cambridge University Press, 1997.

[49] BRAY, A. J. Theory of phase ordering kinetics. *Advances in Physics 51* (2002), 481.

[50] BUDRIKIS, Z., LIVESEY, K. L., MORGAN, J. P., AKERMAN, J., STEIN, A., LANGRIDGE, S., MARROWS, C. H., AND STAMPS, R. L. Domain dynamics and fluctuations in artificial square ice at finite temperatures. *New Journal of Physics 14* (Dec. 2012), 035014.

[51] BUDRIKIS, Z., POLITI, P., AND STAMPS, R. L. Vertex dynamics in finite two dimensional square spin ices. *Physical Review Letters 105* (2010), 17201.

[52] BUZANO, C., AND PRETTI, M. Cluster variation approach to the Ising square lattice with two- and four-spin interactions. *Physical Review B 56* (July 1997), 636.

[53] CALABRESE, P., GAMBASSI, A., AND KRZAKALA, F. Critical ageing of Ising ferromagnets relaxing from an ordered state. *Journal of Statistical Mechanics: Theory and Experiment* (June 2006), P06016.

[54] CALABRESE, P., AND PARRUCCINI, P. Critical thermodynamics of a three-dimensional chiral model for N>3. *Physical Review B 68* (2003), 094415.

[55] CARDY, J. *Finite-size scaling*. Elsevier, 1988.

[56] CASTELNOVO, C. Private communication. 2011.

[57] CASTELNOVO, C., AND CHAMON, C. Topological order and topological entropy in classical systems. *Physical Review B 76* (Nov. 2007), 174416.

[58] CASTELNOVO, C., MOESSNER, R., AND SONDHI, S. L. Magnetic monopoles in spin ice. *Nature 451* (2008), 42.

[59] CASTELNOVO, C., MOESSNER, R., AND SONDHI, S. L. Thermal quenches in spin ice. *Physical Review Letters 104* (2010), 107201.

[60] CASTELNOVO, C., PUJOL, P., AND CHAMON, C. Dynamical obstruction in a constrained system and its realization in lattices of superconducting devices. *Physical Review B 69* (Mar. 2004), 104529.

[61] CAUX, J.-S., AND MOSSEL, J. Remarks on the notion of quantum integrability. *Journal of Statistical Mechanics: Theory and Experiment* (Feb. 2011), P02023.

[62] CAVAGNA, A. Supercooled liquids for pedestrians. *Physics Reports 476* (June 2009), 51.

[63] CEPAS, O., AND CANALS, B. Heterogeneous freezing in a geometrically frustrated spin model without disorder: spontaneous generation of two time-scales. *Physical Review B 86* (2012), 024434.

[64] CHAIKIN, P., AND LUBENSKY, T. C. *Principles of condensed matter physics.* Cambridge University Press, 1995.

[65] CHAKRABORTY, B., DAS, D., AND KONDEV, J. Topological jamming and the glass transition in a frustrated system. *The European physical journal. E, Soft matter 9* (Nov. 2002), 227.

[66] CHALLA, M. S. S., LANDAU, D. P., AND BINDER, K. Finite-size effects at temperature-driven first-order transitions. *Physical Review B 34* (1986), 1841.

[67] CHALUPA, J., LEATH, P. L., AND REICH, G. R. Bootstrap percolation on a Bethe lattice. *Journal of Physics C: Solid . . . 12* (1979), 31.

[68] CHANDRA, P., AND DOUCOT, B. Spin liquids on the Husimi cactus. *Journal of Physics A: Mathematical and . . . 27* (1994), 1541.

[69] CHEN, Z.-Y., AND KARDAR, M. Elastic antiferromagnets on a triangular lattice. *Journal of Physics C: Solid State Physics 19* (1986), 6825.

[70] CHERN, G.-W., MELLADO, P., AND TCHERNYSHYOV, O. Two-Stage Ordering of Spins in Dipolar Spin Ice on the Kagome Lattice. *Physical Review Letters 106* (May 2011), 207202.

[71] CHOU, S. Y., KRAUSS, P. R., AND KONG, L. Nanolithographically defined magnetic structures and quantum magnetic disk (invited). *Journal of Applied Physics 79* (1996), 6101.

[72] COLIZZA, V., BARRAT, A., AND LORETO, V. Definition of temperature in dense granular media. *Physical Review E 65* (May 2002), 050301.

[73] CORBERI, F., AND CUGLIANDOLO, L. F. Out-of-equilibrium dynamics of the spiral model. *Journal of Statistical Mechanics: Theory and Experiment* (Sept. 2009), P09015.

[74] CORBERI, F., LIPPIELLO, E., AND ZANNETTI, M. Slow relaxation in the large-N model for phase ordering. *Physical Review E 65* (Apr. 2002), 046136.

[75] COWBURN, R. P., AND WELLAND, M. E. Room Temperature Magnetic Quantum Cellular Automata. *Science 287* (Feb. 2000), 1466.

[76] CUGLIANDOLO, L. F. Topics in coarsening phenomena. *Physica A: Statistical Mechanics and its Applications 389* (Oct. 2010), 4360.

[77] CUGLIANDOLO, L. F., KURCHAN, J., AND PELITI, L. Energy flow, partial equilibration, and effective temperatures in systems with slow dynamics. *Physical Review E 55* (Apr. 1997), 3898.

[78] D. FRENKEL, AND SMIT, B. *Understanding molecular simulation: from algorithms to applications*. Academic Press, 2002.

[79] D. J. AMIT. *Field theory, the renormalization group, and critical phenomena*. World Scientific, 1984.

[80] DE GENNES, P.-G., AND PROST, J. *The physics of liquid crystals*. Clarendon Press, 1993.

[81] DEBENEDETTI, P. G., AND STILLINGER, F. H. Supercooled liquids and the glass transition. *Nature 410* (Mar. 2001), 259.

[82] DELAMOTTE, B., AND MOUHANNA, D. Nonperturbative renormalization-group approach to frustrated magnets. *Physical Review B 69* (Apr. 2004), 134413.

[83] DHAR, D., AND MAJUMDAR, S. N. Abelian sandpile model on the Bethe lattice. *Journal of Physics A: Mathematical and . . . 23* (1990), 4333.

[84] DIEP, H. T., Ed. *Frustrated spin systems*. World Scientific, 2004.

[85] DIRAC, P. A. M. Quantised Singularities in the Electromagnetic Field. *Proceedings of the Royal Society of London. 133* (1931), 60.

[86] DOMB, C. On the theory of cooperative phenomena in crystals. *Advances in Physics 9* (July 1960), 245.

[87] EDWARDS, S. Theory of powders. *Physica A: Statistical and Theoretical 157* (1989), 1080.

[88] EDWARDS, S. F. The role of entropy in the specification of a powder. In *Granular Matter: An interdisciplinary approach*, A. Mehta, Ed. 1994, ch. 4.

[89] ELORANTA, K. Diamond Ice. *Journal of Statistical Physics 96* (1999), 1091.

[90] EVERTZ, H. G., LANA, G., AND MARCU, M. Cluster Algorithm for Vertex models. *Physical Review Letters 70* (1993), 875.

[91] EVERTZ, H. G., AND MARCU, M. The Loop-Cluster Algorithm for the Case of the 6 Vertex Model. 1–5.

[92] FAN, C., AND WU, F. Y. General Lattice Model of Phase Transitions. *Physical Review B 2* (1970), 723.

[93] FENNELL, T., BRAMWELL, S. T., MCMORROW, D. F., MANUEL, P., AND WILDES, A. R. Pinch points and Kasteleyn transitions in kagome ice. *Nature Physics 3* (June 2007), 566.

[94] FENNELL, T., DEEN, P. P., WILDES, A. R., SCHMALZ, PRABHAKARAN, D., BOOTHROYD, A. T., ALDUS, R. J., MCMORROW, D. F., AND BRAMWELL, S. T. Magnetic Coulomb Phase in the Spin Ice Ho2Ti2O7. *Science 326* (2009), 415.

[95] FENNELL, T., PETRENKO, O., FÅ K, B., GARDNER, J., BRAMWELL, S., AND OULAD-DIAF, B. Neutron scattering studies of the spin ices Ho2Ti2O7 and Dy2Ti2O7 in applied magnetic field. *Physical Review B 72* (Dec. 2005), 224411.

[96] FISHER, M. Renormalization group theory: Its basis and formulation in statistical physics. *Reviews of Modern Physics 70*, 2 (Apr. 1998), 653.

[97] FISHER, M. E. Statistical Mechanics of Dimers on a Plane Lattice. *Physical Review 124* (1961), 1664.

[98] FISHER, M. E., AND BARBER, M. N. Scaling theory for Finite-size Effects in the Critical Region. *Physical Review Letters 28* (1972), 1516.

[99] FLORY, P. Molecular Size Distribution in Three Dimensional Polymers. I. Gelation1. *Journal of the American Chemical Society 63* (1941), 3083.

[100] FOINI, L., LEVIS, D., TARZIA, M., AND CUGLIANDOLO, L. F. Static properties of 2D spin-ice as a sixteen-vertex model. *arXiv:1210.8361* (2012).

[101] FUKAZAWA, H., MELKO, R., HIGASHINAKA, R., MAENO, Y., AND GINGRAS, M. Magnetic anisotropy of the spin-ice compound Dy2Ti2O7. *Physical Review B 65* (Jan. 2002), 054410.

[102] GARDNER, J. S., AND GREEDAN, J. E. Magnetic pyrochlore oxides. *Reviews of Modern Physics 82* (Jan. 2010), 53.

[103] GIAUQUE, W., AND STOUT, J. The Entropy of Water and the Third Law of Thermodynamics. The Heat Capacity of Ice from 15 to 273 K. *Journal of the American Chemical Society 58* (1936), 1144.

[104] GIAUQUE, W. F., AND ASHLEY, M. F. Molecular Rotation in ice at 10K. Free Energy of Formation and Entropy of Water. *Physical Review 43* (Aug. 1932), 81.

[105] GIBLIN, S. R., BRAMWELL, S. T., HOLDSWORTH, P. C. W., PRABHAKARAN, D., AND TERRY, I. Creation and measurement of long-lived magnetic monopole currents in spin ice. *Nature Physics 7* (Feb. 2011), 252.

[106] GLAUBER, R. J. Time-dependent statistics of the Ising model. *Journal of Mathematical Physics 4* (1963), 294.

[107] GOLDENFELD, N. *Lectures on phase transitions and the renormalization group*. Perseus Books Publishing, 1992.

[108] GRAF, E. H., JOHN, D. M., AND REPPY, J. D. Phase separation and the superfluid transition in liquid He3-He4 mixtures. *Physical Review Letters 19* (1967), 417.

[109] GUJRATI, P. D. Ordering field, order parameter, and Self-Avoiding Walks. *Physical Review Letters 53* (1984), 2453.

[110] HAN, Y. Phase-space networks of the six-vertex model under different boundary conditions. *Physical Review E 81* (Apr. 2010), 041118.

[111] HAN, Y., SHOKEF, Y., ALSAYED, A. M., YUNKER, P., LUBENSKY, T. C., AND YODH, A. G. Geometric frustration in buckled colloidal monolayers. *Nature 456* (Dec. 2008), 898.

[112] HARRIS, M., BRAMWELL, S., HOLDSWORTH, P., AND CHAMPION, J. Liquid-Gas Critical Behavior in a Frustrated Pyrochlore Ferromagnet. *Physical Review Letters 81* (Nov. 1998), 4496.

[113] HARRIS, M. J., BRAMWELL, S. T., MCMORROW, D. F., ZEISKE, T., AND GODFREY, K. W. Geometrical Frustration in the Ferromagnetic Pyrochlore Ho2Ti2O7. *Physical Review Letters 79* (1997), 2554.

[114] HENLEY, C. Classical height models with topological order. *Journal of Physics: Condensed Matter 23* (2011), 164212.

[115] HENLEY, C. L. The "Coulomb phase" in frustrated systems. *Annual Review of Condensed Matter Physics 1* (Dec. 2009), 179.

[116] HIGASHINAKA, R., FUKAZAWA, H., DEGUCHI, K., AND MAENO, Y. A Kagome ice state in the spin ice compound Dy 2 Ti 2 O 7. *Journal of Physics: Condensed Matter 16* (Mar. 2004), S679.

[117] HOHENBERG, P. C., AND HALPERIN, B. I. Theory of dynamic critical phenomena. *Reviews of Modern Physics 49* (1977), 435.

[118] HOUTAPPEL, R. Order-disorder in hexagonal lattices. *Physica 16* (May 1950), 425.

[119] HUANG, K. *Statistical mechanics*, 1st editio ed. Wiley, 1963.

[120] HURST, C. A., AND GREEN, H. S. New solution of the Ising problem for a rectangular lattice. *Journal of Chemical Physics 33* (1960), 1059.

[121] HUSE, D. A. Corrections to late-stage behaviour in spinodal decomposition: Lifshitz-Slyozov scaling and Monte Carlo simulations. *Physical Review B 34* (1986), 7845.

[122] HUSE, D. A., KRAUTH, W., MOESSNER, R., AND SONDHI, S. L. Coulomb and liquid dimer models in three dimensions. *Physical Review Letters 91* (2003), 167004.

[123] IMRE, A., CSABA, G., BERNSTEIN, G. H., POROD, W., AND METLUSHKO, V. Investigation of shape-dependent switching of coupled nanomagnets. *Superlattices and Microstructures 34* (Sept. 2003), 513.

[124] ISAKOV, S., GREGOR, K., MOESSNER, R., AND SONDHI, S. Dipolar Spin Correlations in Classical Pyrochlore Magnets. *Physical Review Letters 93* (Oct. 2004), 167204.

[125] JACOBSEN, J., AND KONDEV, J. Field theory of compact polymers on the square lattice. *Nuclear Physics B 532* (1998), 635.

[126] JAEGER, G. The Ehrenfest classification of phase transitions: introduction and evolution. *Archive for history of exact sciences 53* (1998), 51.

[127] JAEGER, H., NAGEL, S., AND BEHRINGER, R. Granular solids, liquids, and gases. *Reviews of Modern Physics 68* (Oct. 1996), 1259.

[128] JANSSEN, H. K., SCHAUB, B., AND SCHMITTMANN, B. New universal short-time scaling behaviour of critical relaxation processes. *Zeitschrift fur Physik B Condensed Matterr Physik B Condensed Matter 73* (Dec. 1989), 539.

[129] JASTER, A., MAINVILLE, J., SCHÜLKE, L., AND ZHENG, B. No Title. *Journal of Physics A 32* (1999), 1395.

[130] JAUBERT, L., CHALKER, J., HOLDSWORTH, P., AND MOESSNER, R. Three-Dimensional Kasteleyn Transition: Spin Ice in a [100] Field. *Physical Review Letters 100* (Feb. 2008), 067207.

[131] JAUBERT, L. D. C., CHALKER, J. T., HOLDSWORTH, P. C. W., AND MOESSNER, R. Spin ice under pressure: symmetry enhancement and infinite order multicriticality.

[132] JAUBERT, L. D. C., AND HOLDSWORTH, P. C. W. Signature of magnetic monopole and Dirac string dynamics in spin ice. *Nature Physics 5* (Mar. 2009), 258.

[133] KADANOFF, L. P., AND WEGNER, F. J. Some Critical properties of the eight-vertex model. *Physical Review B 4* (1971), 3989.

[134] KANDEL, D., AND DOMANY, E. General cluster Monte Carlo dynamics. *Physical Review B 43* (1991), 8539.

[135] KANO, K., AND NAYA, S. Antiferromagnetism. The Kagome Ising Net. *Progress of Theoretical Physics 10*, 2 (1953), 158.

[136] KAPAKLIS, V., ARNALDS, U., AND HARMAN-CLARKE, A. Melting artificial spin ice. *New Journal of Physics 14* (2012), 035009.

[137] KASTELEYN, P. W. The statistics of dimers on a lattice. *Physica 27* (1961), 1209.

[138] KASTELEYN, P. W. Dimer Statistics and Phase Transitions. *Journal of Mathematical Physics 4* (1963), 287.

[139] KE, X., LI, J., NISOLI, C., LAMMERT, P., MCCONVILLE, W., WANG, R., CRESPI, V., AND SCHIFFER, P. Energy Minimization and ac Demagnetization in a Nanomagnet Array. *Physical Review Letters 101* (July 2008), 18.

[140] KENYON, R., OKOUNKOV, A., AND SHEFFIELD, S. Dimers and amoebae. *Annals of mathematics 163* (2006), 1019.

[141] KITTEL, C. *Introduction to Solid State Physics*, 7th editio ed. Wiley, 1996.

[142] KLEIN, A. Extended States in the Anderson Model on the Bethe Lattice. *Advances in Mathematics 133* (Jan. 1998), 163.

[143] KLEINERT, H. *Gauge Fields in Condensed Matter.* World Scientific, 1989.

[144] KONDEV, J., GIER, J. D., AND NIENHUIS, B. Operator spectrum and exact exponents of the fully packed loop model. *Journal of Physics A: Mathematical and General 29* (1996), 6489.

[145] KOREPIN, V., AND ZINN-JUSTIN, P. Thermodynamic limit of the six-vertex model with domain wall boundary conditions. *Journal of Physics A: Mathematical and General 33* (2000), 7053.

[146] KOREPIN, V. E. Calculation of norms of Bethe wave functions. *Communications in Mathematical Physics 86* (Sept. 1982), 391.

[147] KOREPIN, V. E., BOGOLIUBOV, N. M., AND IZERGIN, A. G. *Quantum inverse scattering method and correlation functions.* Cambridge University Press, 1997.

[148] KOSTERLITZ, J. M. The critical properties of the two-dimensional xy model. *Journal of Physics C: Solid State Physics 7* (1974), 1046.

[149] KOSTERLITZ, J. M., AND THOULESS, D. J. Long range order and metastability in two dimensional solids and superfluids. *Journal of Physics C: Solid State Physics 5* (1972), 125.

[150] KOSTERLITZ, J. M., AND THOULESS, D. J. Ordering, metastability and phase transitions in two-dimensional systems. *Journal of Physics C: Solid State . . . 6* (1973), 1181.

[151] KRAUTH, W. *Statistical Mechanics: Algorithms and Computations.* Oxford University Press, 2006.

[152] KUPERBERG, G. Another proof of the alternative-sign matrix conjecture. *International Mathatematics Research Notes 3* (1996), 139.

[153] LADAK, S., READ, D. E., PERKINS, G. K., COHEN, L. F., AND BRANFORD, W. R. Direct observation of magnetic monopole defects in an artificial spin-ice system. *Nature Physics 6* (Apr. 2010), 359.

[154] LADAK, S., WALTON, S. K., ZEISSLER, K., TYLISZCZAK, T., READ, D. E., BRANFORD, W. R., AND COHEN, L. F. Disorder-independent control of magnetic monopole defect population in artificial spin-ice honeycombs. *New Journal of Physics 14* (2012), 045010.

[155] LAI, Z. W., MAZENKO, G. F., AND VALLS, O. T. Classes for growth kinetics problems at low temperatures. *Physical Review B 37* (1988), 9481.

[156] LAMMERT, P. E., KE, X., LI, J., NISOLI, C., GARAND, D. M., CRESPI, V. H., AND SCHIFFER, P. Direct entropy determination and application to artificial spin ice. *Nature Physics 6* (July 2010), 786.

[157] LANDAU, L. Theory of Elasticity, 1975.

[158] LEE, P. A., AND WEN, X.-G. Doping a Mott insulator: Physics of high-temperature superconductivity. *Reviews of Modern Physics 78* (Jan. 2006), 17.

[159] LEE, T. D., AND YANG, C. N. Statistical Theory of equations of State and phase transitions. 2. Lattice gas and Ising Model. *Physical Review 87* (1953), 410.

[160] LEVIS, D., AND CUGLIANDOLO, L. F. Out-of-equilibrium dynamics in the bidimensional spin-ice model. *Europhysics Letters 97* (Feb. 2012), 30002.

[161] LEVIS, D., CUGLIANDOLO, L. F., FOINI, L., AND TARZIA, M. -. *In preparation* (2012).

[162] LIBÁL, A., REICHHARDT, C., AND REICHHARDT, C. J. O. Realizing Colloidal Artificial Ice on Arrays of Optical Traps. *Physical Review Letters 97* (Nov. 2006), 228302.

[163] LIEB, E. H. Exact solution of the F model of an antiferroelectric. *Physical Review Letters 18* (1967), 1046.

[164] LIEB, E. H. Exact Solution of the Two-Dimensional Slater KDP Model of a Ferroelectric. *Physical Review Letters 19* (1967), 108.

[165] LIEB, E. H. Residual Entropy of Square Ice. *Physical Review 162* (1967), 162.

[166] LIEB, E. H., AND WU, F. Y. Two-dimensional ferroelectric models. In *Phase transitions and critical phenomena Vol. 1*, C. Domb and J. L. Lebowitz, Eds. Academic Press, 1972, ch. 8, p. 331.

[167] LIEBMANN, R. *Statistical mechanics of periodic frustrated Ising systems*, vol. 251. Springer-Verlag, 1986.

[168] LOSCAR, E. S., FERRERO, E. E., GRIGERA, T. S., AND CANNAS, S. a. Nonequilibrium characterization of spinodal points using short time dynamics. *The Journal of chemical physics 131* (July 2009), 024120.

[169] MAKSE, H. a., AND KURCHAN, J. Testing the thermodynamic approach to granular matter with a numerical model of a decisive experiment. *Nature 415* (Feb. 2002), 614.

[170] MARINARI, E., AND PARISI, G. Phase structure of the three-dimensional Edwards-Anderson spin glass. *Physical Review B 58* (1998), 14852.

[171] MASTROPIETRO, V. Non Universality in Ising Models with Four Spin interaction. *Journal of statistical physics 111* (2003), 201.

[172] MASTROPIETRO, V. Ising Models with Four Spin Interaction at Criticality. *Communications in Mathematical Physics 244* (Feb. 2004), 595.

[173] MATSUHIRA, K., HIROI, Z., AND TAYAMA, T. A new macroscopically degenerate ground state in the spin ice compound Dy2Ti2O7 under a magnetic field. *Journal of Physics C: Solid State Physics 14* (2002), L559.

[174] MEHTA, A., Ed. *Granular Matter: An interdisciplinary approach*. No. May. Springer-Verlag, 1994.

[175] MELKO, R. G., AND GINGRAS, M. J. P. Monte Carlo studies of the dipolar spin ice model. *Journal of Physics: Condensed Matter 16* (Nov. 2004), R1277.

[176] MELLADO, P., PETROVA, O., SHEN, Y., AND TCHERNYSHYOV, O. Dynamics of magnetic charges in artificial spin ice. *Physical Review Letters 105* (June 2010), 187206.

[177] MENGOTTI, E., HEYDERMAN, L., FRAILE RODRÍGUEZ, A., BISIG, A., LE GUYADER, L., NOLTING, F., AND BRAUN, H. B. Building blocks of an artificial kagome spin ice: Photoemission electron microscopy of arrays of ferromagnetic islands. *Physical Review B 78* (Oct. 2008), 1444.

[178] MENGOTTI, E., HEYDERMAN, L. J., RODRÍGUEZ, A. F., NOLTING, F., HÜGLI, R. V., AND BRAUN, H.-B. Real-space observation of emergent magnetic monopoles and associated Dirac strings in artificial kagome spin ice. *Nature Physics 7* (Oct. 2011), 68.

[179] MERMIN, N. D. The topological theory of defects in ordered media. *Reviews of Modern Physics 51* (1979), 591.

[180] MERMIN, N. D., AND WAGNER, H. Absence of ferromagnetism or antiferromagnetism in one- or two-dimensional isotropic Heisenberg models. *Physical Review Letters 17* (1966), 1133.

[181] METCALF, B. D. Ground state spin orderings of the triangular Ising model. *Physics Letters 46A* (1974), 325.

[182] MEZARD, M., AND MONTANARI, A. *Information, physics and computation*. No. 2042. Oxford University Press, 2009.

[183] MEZARD, M., PARISI, G., AND VIRASORO, M. A. SK Model : The Replica Solution without Replicas . *Europhysics Letters 1* (1986), 77.

[184] MEZARD, M., PARISI, G., AND VIRASORO, M. A. *Spin glass theory and beyond*. World Scientific, 1987.

[185] MILTON, K. A. Theoretical and experimental status of magnetic monopoles. *Reports on Progress in Physics 69* (June 2006), 1637.

[186] MISGUISH, G., AND LHUILLIER, C. Two-dimensional Quantum Antiferromagnets. In *Frustrated spin systems*, H. T. Diep, Ed., vol. 52. World Scientific, Jan. 2004, ch. 5.

[187] MITO, M., KUWABARA, S., MATSUHIRA, K., DEGUCHI, H., TAKAGI, S., AND HIROI, Z. Uniaxial pressure effects on spin-ice compound Dy2Ti2O7. *Journal of Magnetism and Magnetic Materials 310* (Mar. 2007), e432.

[188] MOESSNER, R., AND RAMIREZ, A. P. Geometrical frustration. *Physics Today* (2006), 24.

[189] MÓL, L., SILVA, R., SILVA, R., PEREIRA, A., MOURA-MELO, W., AND COSTA, B. Magnetic monopole and string excitations in two-dimensional spin ice. *Journal of Applied Physics 106* (2009), 063913.

[190] MÖLLER, G., AND MOESSNER, R. Artificial Square Ice and Related Dipolar Nanoarrays. *Physical Review Letters 96* (2006), 237202.

[191] MÖLLER, G., AND MOESSNER, R. Magnetic multipole analysis of kagome and artificial spin-ice dipolar arrays. *Physical Review B 80* (Oct. 2009), 140409.

[192] MONASSON, R. Introduction to phase transitions in random optimization problems. In *Complex Systems*, J. Bouchaud, M. Mezard, and J. Dalibard, Eds., no. 1. Elsevier, Les Houches, 2007.

[193] MONROE, J. Frustrated Ising systems on Husimi trees. *Physica A: Statistical Mechanics and its Applications 256* (1998), 217.

[194] MONROE, J. L. Phase diagrams of Ising models on Husimi trees. I. Pure multisite interaction systems. *Journal of statistical physics 65* (1991), 255.

[195] MOORE, C., AND NEWMAN, M. E. J. Height representation, critical exponents, and ergodicity in the four-state triangular Potts antiferromagnet. *Journal of Statistical Mechanics: Theory and Experiment 99* (2000), 629.

[196] MORGAN, J. P., AND MARROWS, C. H. Private Communication.

[197] MORGAN, J. P., STEIN, A., LANGRIDGE, S., AND MARROWS, C. H. Thermal ground-state orderins and elementary excitations in artificial magnetic square ice. *Nature Physics 7* (2010), 75.

[198] MORRIS, D. J. P., TENNANT, D. A., GRIGERA, S. A., KLEMKE, B., CASTELNOVO, C., MOESSNER, R., CZTERNASTY, C., MEISSNER, M., RULE, K. C., HOFFMANN, J.-U., KIEFER, K., GERISCHER, S., SLOBINSKY, D., AND PERRY, R. S. Dirac strings and magnetic monopoles in the spin ice Dy2Ti2O7. *Science 326* (Oct. 2009), 411.

[199] NABARRO, F. R. N., Ed. *Dislocations in Solids Vol. 1*. Elsevier, 1979.

[200] NAGLE, J. F. Lipid Bilayer Phase Transition : Density Measurements and Theory. *Proceedings of the National Academy of Sciences of the United States of America 70* (1973), 3443.

[201] NAGLE, J. F. Theory of biomembrane phase transitions. *The Journal of Chemical Physics 58* (1973), 252.

[202] NAKATSUJI, S., NAMBU, Y., TONOMURA, H., SAKAI, O., JONAS, S., BROHOLM, C., TSUNETSUGU, H., QIU, Y., AND MAENO, Y. Spin disorder on a triangular lattice. *Science 309* (Sept. 2005), 1697.

[203] NELSON, D., AND HALPERIN, B. Dislocation-mediated melting in two dimensions. *Physical Review B 19* (1979), 2457.

[204] NELSON, D. R. *Geometry and defects in condensed matter*. Cambridge University Press, 2002.

[205] NIENHUIS, B. Coulomb gas formulation of two-diemnsional phase transitions. In *Phase Transitions and Critical Phenomena Vol 11*, C. Domb and J. L. Lebowitz, Eds. Academic Press, 1987, ch. 1.

[206] NISOLI, C., LI, J., KE, X., GARAND, D., SCHIFFER, P., AND CRESPI, V. Effective Temperature in an Interacting Vertex System: Theory and Experiment on Artificial Spin Ice. *Physical Review Letters 105* (July 2010), 047205.

[207] NISOLI, C., WANG, R., LI, J., MCCONVILLE, W., LAMMERT, P., SCHIFFER, P., AND CRESPI, V. Ground State Lost but Degeneracy Found: The Effective Thermodynamics of Artificial Spin Ice. *Physical Review Letters 98* (May 2007), 217203.

[208] ÓDOR, G. Universality classes in nonequilibrium lattice systems. *Reviews of Modern Physics 76* (2004), 663.

[209] ONSAGER, L. Deviations from Ohm's Law in Weak Electrolytes. *The Journal of Chemical Physics 2* (1934), 599.

[210] ONSAGER, L. Crystal Statistics. I. A two-dimensional model with an order-disorder transition. *Physical Review 65* (1944), 117.

[211] OZEKI, Y., AND ITO, N. Nonequilibrium relaxation method. *Journal of Physics A: Mathematical and Theoretical 40* (Aug. 2007), R149.

[212] OZEKI, Y., KASONO, K., ITO, N., AND MIYASHITA, S. Nonequilibrium relaxation analysis for first-order phase transitions. *Physica A: Statistical Mechanics and its Applications 321* (Apr. 2003), 271.

[213] OZEKI, Y., OGAWA, K., AND ITO, N. Nonequilibrium relaxation analysis of Kosterlitz-Thouless phase transition. *Physical Review E 67* (Feb. 2003), 026702.

[214] PALMER, S., AND CHALKER, J. Order induced by dipolar interactions in a geometrically frustrated antiferromagnet. *Physical Review B 62* (July 2000), 488.

[215] PAULING, L. The Structure and Entropy of Ice and of Other Crystals with Some Randomness of Atomic Arrangement. *Journal of Chemical Physics 57* (1935), 2680.

[216] PEARL, J. *Probabilistic reasoning in intelligent systems: networks of plausible inference*, vol. 600093. Morgan Kaufman, 1988.

[217] POLKOVNIKOV, A., SENGUPTA, K., SILVA, A., AND VENGALATTORE, M. Colloquium: Nonequilibrium dynamics of closed interacting quantum systems. *Reviews of Modern Physics 83* (Aug. 2011), 863.

[218] POLLARD, S., VOLKOV, V., AND ZHU, Y. Propagation of magnetic charge monopoles and Dirac flux strings in an artificial spin-ice lattice. *Physical Review B 85* (May 2012), 180402.

[219] POLYAKOV, A. M. Particle spectrum in quantum field theory. *JETP Letters 20* (1974), 194.

[220] PRETTI, M. A Note on Cactus Trees : Variational vs. Recursive Approach. *Journal of Statistical Physics 111* (2003), 993.

[221] PRIVMAN, V., AND FISHER, M. Finite-size effects at first-order transitions. *Journal of statistical physics 33* (Nov. 1983), 385.

[222] PROZOROV, R., FIDLER, A. F., HOBERG, J. R., AND CANFIELD, P. C. Suprafroth in type-I superconductors. *Nature Physics 4* (Mar. 2008), 327.

[223] QI, Y., BRINTLINGER, T., AND CUMINGS, J. Direct observation of the ice rule in an artificial kagome spin ice. *Physical Review B 77* (Mar. 2008), 094418.

[224] RAMIREZ, A., HAYASHI, A., CAVA, R., SIDDHARTHAN, R., AND SHASTRY, B. Zero-point entropy in spin ice. *Nature 399* (1999), 333.

[225] RAMIREZ, A., HESSEN, B., AND WINKLEMANN, M. Entropy balance and evidence for local spin singlets in a Kagome-like magnet. *Physical Review Letters 84* (Mar. 2000), 2957.

[226] RAMIREZ, A. P. Strongly Geometrically Frustrated Magnets. *Annual Review of Materials Science 24* (Aug. 1994), 453.

[227] REICHHARDT, O., LIBÁL, A., AND REICHHARDT, C. Multi-Step Ordering in Kagome and Square Artificial Spin Ice. *New Journal of Physics 14* (2011), 025006.

[228] REIMERS, J., BERLINSKY, A., AND SHI, A. Mean-field approach to magnetic ordering in highly frustrated pyrochlores. *Physical Review B 43* (1991), 865.

[229] RITORT, F., AND SOLLICH, P. Glassy dynamics of kinetically constrained models. *Advances in Physics 52* (June 2003), 219.

[230] ROUGEMAILLE, N., MONTAIGNE, F., CANALS, B., DULUARD, A., LACOUR, D., HEHN, M., BELKHOU, R., FRUCHART, O., EL MOUSSAOUI, S., BENDOUNAN, A., AND MACCHEROZZI, F. Artificial Kagome Arrays of Nanomagnets: A Frozen Dipolar Spin Ice. *Physical Review Letters 106* (Feb. 2011), 4.

[231] RYS, F. Ueber ein zweidimensionales klassisches Konfigurationsmodell. *Helvetica Physica Acta 36* (1963), 537.

[232] SACHDEV, S. Kagome and triangular-lattice Heisenberg antiferromagnets: Ordering from quantum fluctuations. *Physical Review B 45* (1992), 377.

[233] SADOC, J.-F., AND MOSSERI, R. *Geometrical Frustration*, vol. 79. Cambridge University Press, 1999.

[234] SANDVIK, A., AND MOESSNER, R. Correlations and confinement in nonplanar two-dimensional dimer models. *Physical Review B 73* (Apr. 2006), 144504.

[235] SCHULTZ, T. D., MATTIS, D. C., AND LIEB, E. H. Two-dimensional Ising model as a soluble problem of many fermions. *Reviews of Modern Physics 36* (1964), 856.

[236] SCHUMANN, A., SZARY, P., VEDMEDENKO, E. Y., AND ZABEL, H. Magnetic dipole configurations in honeycomb lattices: order and disorder. *New Journal of Physics 14* (Mar. 2012), 035015.

[237] SEMERJIAN, G., TARZIA, M., AND ZAMPONI, F. Exact solution of the Bose-Hubbard model on the Bethe lattice. *Physical Review B 80* (2009), 014524.

[238] SHORE, J. D., HOLZER, M., AND SETHNA, J. P. Logarithmically slow domain growth in nonrandomly frustrated systems: Ising models with competing interactions. *Physical Review B 46* (1992), 11376.

[239] SICILIA, A., ARENZON, J. J., BRAY, A. J., AND CUGLIANDOLO, L. F. Domain growth morphology in curvature driven two dimensional coarsening. *Physical Review E 76* (2007), 061116.

[240] SIDDHARTHAN, R., SHASTRY, B., AND RAMIREZ, A. Spin ordering and partial ordering in holmium titanate and related systems. *Physical Review B 63* (Apr. 2001), 184412.

[241] SIGGIA, E. D. Late stages of spinodal decomposition in binary mixtures. *Physical Review A 20* (1979), 595.

[242] SILVA, R. C., NASCIMENTO, F. S., MÓL, L. A. S., MOURA-MELO, W. A., AND PEREIRA, A. R. Thermodynamics of elementary excitations in artificial magnetic square ice. *New Journal of Physics 14*, 015008 (Oct. 2012), 7.

[243] SLATER, J. C. Theory of the transition in KH2PO4. *Journal of Chemical Physics 9* (1941), 16.

[244] SNYDER, J., UELAND, B., SLUSKY, J., KARUNADASA, H., CAVA, R., AND SCHIFFER, P. Low-temperature spin freezing in the Dy2Ti2O7 spin ice. *Physical Review B 69* (Feb. 2004), 064414.

[245] STAUFFER, D., AND AHARONY, A. *Introduction to Percolation Theory*. Taylor & Francis, 1991.

[246] STEPHENSON, J. Ising-Model Spin Correlations on the Triangular Lattice. III. Isotropic Antiferromagnetic Lattice. *Journal of Mathematical Physics 11* (1970), 413.

[247] STILLINGER, F. H., AND COTTER, M. A. Local orientational order in ice. *Journal of Chemical Physics 58* (1973), 2532.

[248] SUTHERLAND, B. Exact solution of a two-dimensional model for hydrogen-bonded crystals. *Physical Review Letters 19* (1967), 103.

[249] SUTHERLAND, B. Two-Dimensional Hydrogen Bonded Crystals without the Ice Rule. *Journal of Mathematical Physics 11* (1970), 3183.

[250] SUZUKI, M. New Universality of Critical Exponents. *Progress of Theoretical Physics 51* (1974), 1992.

[251] SUZUKI, M. Relationship between d-Dimensional Quantal Spin Systems and (d+1)-Dimensional Ising Systems. *Progress of Theoretical Physics 56* (1976), 1454.

[252] SUZUKI, M. Transfer-matrix method and Monte Carlo simulation in quantum spin systems. *Physical Review B 31* (1985), 2957.

[253] SYLJUÅ SEN, O., AND ZVONAREV, M. Directed-loop Monte Carlo simulations of vertex models. *Physical Review E 70* (July 2004), 016118.

[254] SYLJUASEN, O. F., AND ZVONAREV, M. B. Directed-loop Monte Carlo simulations of vertex models. *Physical Review E 70* (2008), 016118.

[255] 'T HOOFT, G. Magnetic monopoles in Unified Gauge Theories. *Nuclear Physics B 79* (1974), 276.

[256] TEMPERLEY, H. N. V., AND FISHER, M. E. Dimer problem in statistical mechanics-an exact result. *Philosophical Magazine T 6* (1961), 1061.

[257] THOMAS, G., DE ALMEIDA, R., AND GRANER, F. Coarsening of three-dimensional grains in crystals, or bubbles in dry foams, tends towards a universal, statistically scale-invariant regime. *Physical Review E 74* (Aug. 2006), 21.

[258] TORQUATO, S. *Random heterogeneous materials: microstructure and macroscopic properties*. Springer-Verlag, 2002.

[259] TOULOUSE, G. Theory of the frustration effect. I. Ising spins on a square lattice. *Journal of Physics C: Solid State Physics 2* (1977), 115.

[260] VAN LEEUWEN, J. M. J. Singularities in the critical surface and universality for Ising-like spin systems. *Physical Review Letters 34* (1975), 1056.

[261] VILENKIN, A., AND SHELLARD, E. P. S. *Cosmic Strings and Other Topological Defects*. Cambridge University Press, 1994.

[262] VILLAIN, J., BIDAUX, R., CARTON, J. P., AND R., C. Order as an effect of disorder. *Journal de Physique 41* (1980), 1263.

[263] VOLLMAYR, K., REGER, J. D., SCHENCHER, M., AND BINDER, K. Finite size effects at thermally-driven first order phase transitions : a phenomenological theory of the order parameter distribution. *Zeitschrift fur Physik B Condensed Matter 91* (1993), 113.

[264] WANG, R. F., NISOLI, C., FREITAS, R. S., LI, J., McCONVILLE, W., COOLEY, B. J., LUND, M. S., SAMARTH, N., LEIGHTON, C., CRESPI, V. H., AND SCHIFFER, P. Artificial 'spin ice' in a geometrically frustrated lattice of nanoscale ferromagnetic islands. *Nature 439* (2006), 303.

[265] WANNIER, G. H. Antiferromagnetism. The Triangular Ising Net. *Physical Review 79* (1950), 357.

[266] WATSON, G. I. Symmetry Relations for the Six-Vertex Model. *Journal of Statistical Physics 94* (1999), 1045.

[267] WEIGERT, S. The problem of quantum integrability. *Physica D 56* (1992), 107.

[268] WIDOM, B. Degree of the Critical Isotherm. *Journal of Chemical Physics 41* (1964), 1633.

[269] WU, F. Dimers on two-dimensional lattices. *International Journal of Modern Physics B 20* (2006), 5357.

[270] WU, F. Y. Remarks on the modified Potassium Dihydrogen Phosphate Model of a Ferro-electric. *Physical Review 168*, 2 (1968), 10–14.

[271] WU, F. Y. Critical Behaviour of two-dimensional Hydrogen-bonded Antiferroelectrics. *Physical Review Letters 22*, 22 (1969).

[272] WU, F. Y. Critical behaviour of hydrogen-bonded ferroelectrics. *Physical Review Letters 25*, 13 (1970).

[273] YANG, C. N. Some exact results for the many-body problem in one dimension with repulsive delta-function interaction. *Physical Review Letters 19* (1967), 1312.

[274] YANG, C. N., AND YANG, C. P. One-Dimensional Chain of Anisotropic Spin-Spin Interactions. I. Proof of Bethe's Hypothesis for Ground State in a Finite System. *Physical Review 150*, 1 (1966), 321.

[275] YEDIDIA, J. S., FREEMAN, W. T., AND WEISS, Y. Understanding belief propagation and its generalizations. *Exploring artificial intelligence . . .* (2003).

[276] YOSHIDA, S.-I., AND NEMOTO, K. Application of the cluster variation method to spin ice systems on the pyrochlore lattice. *Journal of the Physical Society of Japan 73* (2004), 1619.

[277] YOUNG, A. P. Melting and vector Coulomb gas in two dimensions. *Physical Review B 19* (1979), 1855.

[278] YOUNGBLOOD, R., AXE, J. D., AND MCCOY, B. M. Correlations in ice-rule ferro-electrics. *Physical Review B 21*, 11 (1980).

[279] YURKE, B., PARGELLIS, A. N., KOVACS, T., AND HUSE, D. A. Coarsening dynamics of the XY model. *Phys. Rev. E 47*, 3 (1993), 1525.

[280] ZHU, J.-G., ZHENG, Y., AND PRINZ, G. A. Ultrahigh density vertical magnetoresistive random access memory (invited). *Journal of Applied Physics 87*, 9 (2000), 6668.

[281] ZINN-JUSTIN, P. Six-Vertex model with DWBC and one-matrix model. *Physical Review E 62*, 3 (2000), 3411–3418.

[282] ZIRNBAUER, M. Localization transition on the Bethe lattice. *Physical review. B, Condensed matter 34*, 9 (Nov. 1986), 6394–6408.